

THE UNIVERSITY OF CHICAGO

SPATIO-ANGULAR FLUORESCENCE MICROSCOPY

A DISSERTATION SUBMITTED TO
THE FACULTY OF THE DIVISION OF THE BIOLOGICAL SCIENCES
AND THE PRITZKER SCHOOL OF MEDICINE
IN CANDIDACY FOR THE DEGREE OF
DOCTOR OF PHILOSOPHY

COMMITTEE ON MEDICAL PHYSICS

BY
TALON CHANDLER

CHICAGO, ILLINOIS

AUGUST 2020

Copyright © 2020 by Talon Chandler
All Rights Reserved

To the Chandlers.

The nice thing about having a brain is that one can learn,
that ignorance can be supplanted by knowledge,
and that small bits of knowledge
can gradually pile up into
substantial heaps.

— DOUGLAS HOFSTADTER, *Le Ton beau de Marot* (1997)

Contents

LIST OF FIGURES	vii
LIST OF TABLES	ix
ACKNOWLEDGMENTS	x
ABSTRACT	xiii
1 INTRODUCTION	1
1.1 Background: Polarized fluorescence spectroscopy	6
1.2 Background: Fluorescence microscopy	11
1.3 Background: Image science	15
1.4 Dissertation themes	16
1.5 Chapter descriptions	17
2 BASIC THEORY	19
2.1 Introduction	19
2.2 Theory	23
2.3 Monopole imaging	24
2.4 Dipole imaging	31
2.5 Discussion	41
2.6 Conclusions	46
2.7 Appendix: Spherical harmonics and the spherical Fourier transform	46
2.8 Appendix: Spatio-angular dynamics	48
3 PARAXIAL $4f$ IMAGING	52
3.1 Introduction	52
3.2 Theory	53
3.3 Results	60
3.4 Discussion	75
3.5 Conclusions	80
3.6 Appendix: Relationships between special functions	81
3.7 Appendix: Spherical Fourier transform of a double cone	84
4 CONSTRAINED ANGULAR DIFFUSION, POLARIZED EXCITATION, AND HIGH-NA IMAGING	87
4.1 Introduction	87
4.2 Theory	89
4.3 Results	111
4.4 Discussion and conclusions	117

5	INVERSE PROBLEMS, SINGULAR-VALUE DECOMPOSITIONS, AND RECONSTRUCTION ALGORITHMS	123
5.1	Inverse problems	127
5.2	SVD of uniform excitation with epi-detection	131
5.3	SVD of polarized excitation with uniform detection	141
5.4	SVD of polarized illumination and epi-detection	153
5.5	Reconstruction algorithms	159
5.6	Discussion and conclusions	169
6	DUAL-VIEW SPATIO-ANGULAR MICROSCOPY	172
6.1	Forward model and transfer functions	172
6.2	Singular value decomposition	182
6.3	Optimal polarization sampling	184
6.4	Reconstruction algorithm	189
6.5	Reconstructions and discussion	192
6.6	Appendix: Flat-field detection transfer function	203
7	MODELING EMERGING SPATIO-ANGULAR MICROSCOPES	206
7.1	Spatio-angular structured illumination	207
7.2	Detection-side polarization splitters, pupil splitters, and phase masks	210
7.3	Light-field detection	215
7.4	Discussion	224
8	CONCLUSIONS AND OUTLOOK	226
	BIBLIOGRAPHY	230
	INDEX	248

List of Figures

1.1 A comparison of monopole and dipole emission patterns.	3
2.1 The mapping between the object and data spaces of a monopole fluorescence microscope in two bases.	29
2.2 Relationships between monopole transfer functions.	31
2.3 The mapping between the object and data spaces of a dipole fluorescence microscope in four bases.	40
2.4 Relationships between dipole transfer functions.	41
2.5 Comparison of the $\ell = 0$ and $\ell = 2$ spherical harmonics with the second moment functions.	45
2.6 Square-integrable functions on the sphere can be written as a weighted sum of spherical harmonics.	48
3.1 Schematic of an aplanatic imaging system in a $4f$ geometry with a paraxial tube lens.	56
3.2 Paraxial dipole point spread function as a function of the scaled radial coordinate $\nu_c r$, the dipole inclination angle ϑ , and NA/n_o	65
3.3 Comparison of paraxial models for monopole radiators and dipole radiators.	66
3.4 Paraxial simulation of a spatially and angularly sparse phantom.	68
3.5 Dipole spatial transfer function as a function of the scaled spatial frequency ν/ν_c , the dipole inclination angle ϑ , and NA/n_o	69
3.6 Paraxial simulation of a dense and angularly sparse phantom.	70
3.7 Paraxial dipole angular transfer function in terms of a scaled radial detection coordinate $\nu_c r$, the spherical harmonic degree ℓ , and NA/n_o	72
3.8 Paraxial simulation of a spatially sparse and angularly dense phantom.	73
3.9 Spatio-angular dipole transfer function as a function of the scaled spatial frequency ν/ν_c , the spherical harmonic degree ℓ , and NA/n_o	74
3.10 Paraxial simulation of a spatially and angularly dense phantom.	76
3.11 Relationships between chat and jinc functions.	82
3.12 Geometric construction for evaluating an autocorrelation.	83
4.1 Diffusion-free steady-state excited-state probability $w^{(\text{ex})}$ as a function of the angle from the incident polarization θ and the detection rate to excitation rate ratio $\kappa^{(\text{d})}/\kappa^{(\text{ex})}$	103
4.2 Weak-excitation emission density for a free dipole w as a function of the angle from the incident polarization θ and the diffusion rate to decay rate constant ratio $6D/\kappa^{(\text{d})}$	106
4.3 Simulation of a spatio-angular phantom undergoing fast angular diffusion under illumination by $(\hat{\mathbf{x}} + \hat{\mathbf{y}})$ and $(\hat{\mathbf{x}} - \hat{\mathbf{z}})$ polarized light.	115
4.4 Simulation of a spatio-angular phantom undergoing slow angular diffusion under illumination by $(\hat{\mathbf{x}} + \hat{\mathbf{y}})$ and $(\hat{\mathbf{x}} - \hat{\mathbf{z}})$ polarized light.	116
4.5 Simulation of a spatio-angular phantom consisting of free dipoles under illumination by $(\hat{\mathbf{x}} + \hat{\mathbf{y}})$ and $(\hat{\mathbf{x}} - \hat{\mathbf{z}})$ polarized light.	118

5.1	The spatio-angular transfer function $H_{\ell m}^{(\text{det})}(\boldsymbol{\nu})$ for two defocus positions.	134
5.2	The singular system of $\mathcal{H}^{(\text{det})}$ for two defocus positions.	142
5.3	Two optimal icosahedral sampling schemes.	149
5.4	The in-focus transfer function $H_{j,\ell m}^{(\text{epi})}(\boldsymbol{\nu})$ for six icosahedral illuminations.	155
5.5	The singular system of $\mathcal{H}^{(\text{epi})}$ for in-focus objects measured with six icosahedral illumination polarizations.	158
5.6	Demonstration of angular visualization schemes.	164
6.1	A dual-view light sheet microscope with asymmetric detection objectives, computer-controlled illumination-side liquid crystal polarizers, and tiltable light sheets.	173
6.2	Dual-view light sheet microscope coordinates.	175
6.3	Optimized diSPIM polarization samples.	190
6.4	A three-dimensional spatio-angular reconstruction of a GUV measured with six optimal tilting polarization samples.	197
6.5	Sliced spatio-angular reconstructions of GUV peaks with and without tilting polarization samples.	198
6.6	A simulation study and an experimental study of a GUV imaged with a light-sheet tilting sampling scheme.	199
6.7	A simulated GUV with four simulated reconstructions under different sampling conditions.	200
6.8	Regularization study of GUV reconstructions with tilted light-sheet sampling.	201
6.9	A three-dimensional spatio-angular reconstruction of U2OS cells labeled with Alexa Fluor 488 phalloidin.	202
8.1	The proposed orientation-based molecular force sensor.	229

List of Tables

3.1	Summary of relevant quantities for in-focus fluorescence microscopy under the monopole approximation.	54
3.2	Summary of relevant quantities for in-focus fluorescence microscopy under the dipole approximation.	55
5.1	Summary of the reconstruction algorithm for a polarized illumination spatio-angular microscope.	168

ACKNOWLEDGMENTS

Carrying out this work has been one of the major pleasures of my life. Many people have played a role in making it so enjoyable, and I would like to thank:

- PATRICK LA RIVIÈRE for being a truly extraordinary mentor, role model, and friend; for relentless encouragement and support; and for sharing your enthusiasm.
- RUDOLF OLDENBOURG for hosting me in your lab for a year, in your home many times, and in your ear as much as I needed; and for enthusiastic discussions and support.
- HARI SHROFF for unrelenting support, generosity, and kindness; and for encouraging and displaying a steady-state 11/10.
- XIAOCHUAN PAN and CHIEN-MIN KAO for serving on my committee, for valuable suggestions, and for constant encouragement.
- SCOTT TRINKLE for discussing every idea in this dissertation before it was put to paper (and usually after), and for your friendship.
- COREY SMITH for early guidance, for Thanksgiving meals, and for your friendship.
- PHIL VARGAS, DIMPLE MODGIL, DAVE RIGIE, BRYAN QUIGLEY, BEN PREUSSER, CALDER SHEAGREN and all of the rotating students in the La Rivière lab for helpful suggestions and support.
- MAI TRAN, AMITABH VERMA, TOMOMI TANI, MAKI KOIKE-TANI, MICHAEL SHRIBAK, GRANT HARRIS, GREENFIELD (KIP) SLUDER, and TOBIAS BASKIN for stimulating discussions and friendship at the MBL. Special thanks to TOBIAS BASKIN for sharing an office and valuable samples.
- MIN GUO for unmatched enthusiasm and leg speed, for collecting all of the data presented in this dissertation, and for assistance with Fig. 6.1.

- YIJUN (PLUTO) SU for assistance with GUV sample preparation.
- SHALIN MEHTA and ABHISHEK KUMAR for hosting visits to CZI and NIST, helpful conversations, and for early polarized diSPIM prototypes.
- JOE FOY, KAYLA ROBINSON, NEVILLE ECLOV, BRITTANY BRODER, ANDREW MCVEA, NATHANIEL HOLDERMAN, EMIL SIDKY, SEAN ROSE, EYJÓLFUR GUÐMUNDSSON, JENNIE CROSBY, SAM HENDLEY, ISABELLE HU, JORDAN FUHRMAN, INNA GERTSENSHTEYN, MADELEINE DURKEE and HADLEY SMITH for sharing offices, for your friendship, and for sharing many laughs.
- HARRISON BARRETT and KYLE MYERS for writing the book that laid the foundation for this dissertation [1], and for kind encouragement.
- JEROME MERTZ, SCOTT CARNEY, LUKE PFISTER, SJOERD STALLINGA, MIKAEL BACKLUND, MATTHEW LEW, PETER BASSER, MARC LEVOY, MICHAEL BROXTON, GORDON WETZSTEIN, HAYATO IKOMA, LAURA WALLER, REN NG, DAN FLETCHER, EVA SCHMID, LUKE LAVIS, KASPAR PODGORSKI, SATYAJIT MAYOR, ANKITA JHA, ANDREW YORK and MARTIN SCHWARTZ for valuable discussions and encouragement.
- SOREN JENSEN, JULIE O'KEANE, SARAH HORMOZI, YAEL PETEL, ALAN MANNING, CARL MICHAL, ALEX MACKAY, ANDRE MARZIALI, JON NAKANE and STEVEN SHECHTER for early encouragement.
- RUTH MAGAÑA, JULIE HLAVATY, HOANG NGO, MAYA SURAJ and ELENA RIZZO for administrative support.
- JONATHAN BARRY and JACKIE MACDIARMID for friendship and much-needed breaks.
- JIANHUA GONG for friendship, encouragement, and lots of math.
- TIQUE, ECHO, and REECE for love and support at every step.

This work was supported by funds from the following sources: the University of Chicago Biological Sciences Division Graduate Fellowship, the O'Brien–Hasten Scholarship Fund, the Marine Biological Laboratory Whitman Center Fellowship, the Intramural Research Programs of the National Institute of Biomedical Imaging and Bioengineering, National Institutes of Health grants R01GM114274, R01EB017293, and R35GM131843.

This work benefited from the contributions of volunteers to free and open-source software. I'd like to thank contributors to (in approximate order of time used during this work) GNU Emacs, L^AT_EX, Python, VTK, Matplotlib, ImageJ, Fiji, Dipy, MayaVi, and μ Manager.

ABSTRACT

Fluorescent molecules move and rotate as they transition between states and emit photons that we can detect. How much information can we recover about the position, orientation, and motion of fluorescent molecules by measuring these photons? Can we design imaging systems that recover as much information as possible by making optimal measurements?

In this dissertation, we develop mathematical models of this class of experiments, efficient reconstruction and visualization schemes, and methods for designing instruments that acquire optimal samples. We use these methods to propose and demonstrate the first spatio-angular imaging system that can measure the three-dimensional position and orientation of fluorescent molecules that densely label biological structures. We validate our techniques by successfully reconstructing known spatio-angular objects, and we are beginning to use spatio-angular microscopy to explore new biological structures.

Our proof of concept paves the way towards microscopes that can encode, measure, and reconstruct fundamentally new information from fluorescent molecules. We discuss existing applications and speculate on future directions.

CHAPTER 1

INTRODUCTION

THIS dissertation introduces a new approach for designing imaging systems that can measure the position, orientation, and rotational mobility of dense ensembles of fluorescent molecules. Existing design approaches are disparate and *ad hoc*—polarized fluorescence imaging systems are designed by a combination of intuition and iteration. Instead, we study the physical limits that all fluorescence microscopes face, and we find that no existing designs measure all of the information available from fluorescent samples. We begin to close this gap by proposing and demonstrating the first fluorescence imaging system that can measure the three-dimensional position and orientation of fluorescent objects, and we show that there remains room for improvement. This dissertation shows that designing new instruments to saturate physical limits leads to fluorescence imaging systems that can measure fundamentally new information from biological samples.

To understand the physical limits that fluorescence microscopes face, it is worthwhile to understand that fluorescence microscopes fall into the broader class of *emission tomography imaging systems*—systems that image self-luminous objects. The task of the emission tomography designer is to arrange detectors and emission-modifying elements around the sample so that useful information about the sample is encoded into the detector measurements. Examples of emission tomography imaging systems include single-photon emission computed tomography (SPECT), positron emission tomography (PET), and seismic tomography. A good emission tomography design will encode as much information as possible into measurements while ensuring that information about the sample is recoverable.

In fluorescence microscopy, we begin with a sample that has been labeled with fluorescent molecules. To first order, these fluorescent molecules emit fields that we can model as a

scalar-valued monochromatic spherical wave

$$U(\mathbf{r}) = \frac{1}{|\mathbf{r}|} \exp\left(\frac{-2\pi i n |\mathbf{r}|}{\lambda}\right), \quad (1.1)$$

where \mathbf{r} is a three-dimensional coordinate measured from the emitter's position, n is the index of refraction of the medium, and λ is the emission wavelength—see Fig. 1.1a) for an illustration. Detectors cannot measure these fields directly, but with a bright enough emitter they can measure the absolute square of these fields (the *irradiance*, or commonly the *intensity*). If we arrange unadorned detectors around the emitter, then we can measure the irradiance pattern

$$I(\mathbf{r}) = |U(\mathbf{r})|^2 = \frac{1}{|\mathbf{r}|^2}. \quad (1.2)$$

In reality, we cannot even measure the irradiance pattern directly; we can only measure discrete photons with probabilities proportional to the irradiance. Readers familiar with quantum mechanics will recognize that the scalar fields in Eq. (1.1) play the role of the wave function, the irradiance in Eq. (1.2) plays the role of an unnormalized detection probability, and photon measurements consist of discrete events that “collapse the wavefunction”.

Equation (1.2) is the deterministic *point-spread function* for this simple fluorescence imaging system, and studying this function is essential for understanding the limits of any linear imaging system. The breadth of the point-spread function indicates how much information about the emitter's position is encoded into our measurements, and in this case the point-spread function has a broad $1/r^2$ dependence. To make this point-spread function narrower, we need to introduce elements that modify the emitted fields. Phase-modifying elements are available, so we can use *interference* to shape the point-spread function into a spot that is much narrower than Eq. (1.2). A back-of-the-envelope calculation reveals the minimum size of this spot. The emitted waves have spatial frequency n/λ , and we would like to find the

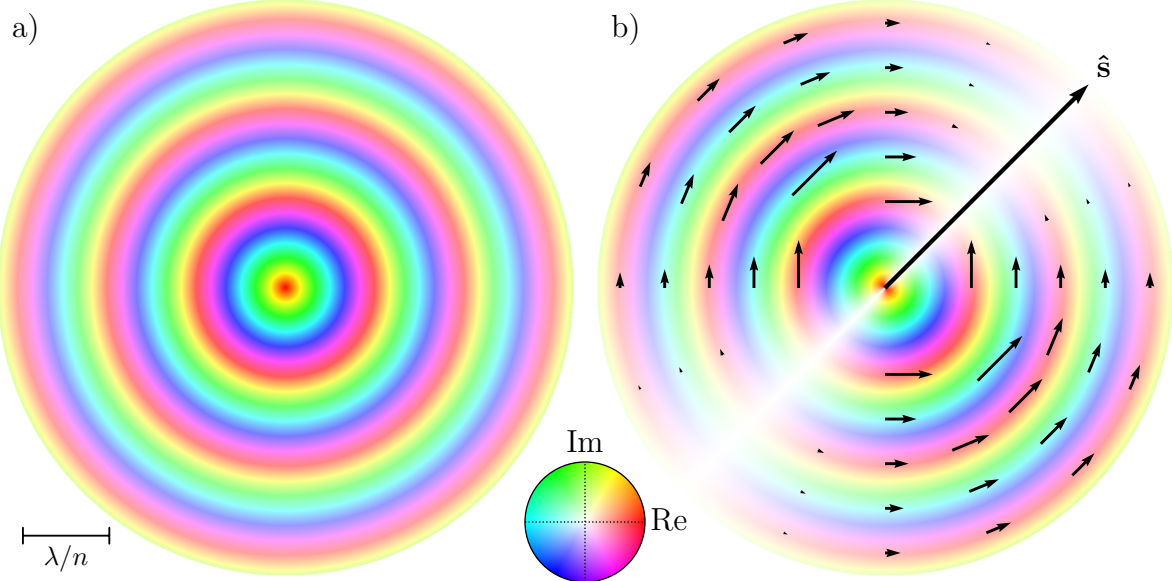


Figure 1.1: A comparison of monopole and dipole far-field emission patterns at a single instant in time. a) A monopole emits monochromatic isotropic scalar-valued waves with wavelength λ/n . The hue and saturation encode the complex phase and magnitude of the emitted wave, respectively (see color wheel). b) A dipole emitter with transition moment \hat{s} emits monochromatic vector-valued waves with wavelength λ/n and electric field orientation $\mathbf{r} \times \hat{s} \times \mathbf{r}$. The direction and length of each small black arrow encodes the orientation and magnitude of the emitted electric field at the arrow's tail, respectively.

spatial frequency content of arbitrary sums of these waves squared. Summing and squaring waves in the spatial domain is equivalent to summing and autocorrelating in the frequency domain, so the maximum spatial frequency of the irradiance pattern is $2n/\lambda$. Therefore, the minimum irradiance spot size is approximately $\lambda/(2n)$. This spot size represents a *physical limit* on fluorescence microscopes—we can never hope to recover information about the sample in object volumes smaller than $[\lambda/(2n)]^3$ without prior information.

In practice, real instruments cannot interfere all of the plane waves emitted by a sample into a single irradiance spot, so real irradiance spots sizes do not saturate the physical limit. A paraxial imaging system that interferes all of the waves emitted within a cone of half angle

α onto a two-dimensional detector creates an irradiance spot of the form

$$I^{(2D)}(\mathbf{r}) = \left| \frac{J_1(\pi\nu_c|\mathbf{r}|)}{\nu_c|\mathbf{r}|} \right|^2, \quad \nu_c = \frac{2n \sin \alpha}{\lambda}, \quad (1.3)$$

where \mathbf{r} is a two-dimensional coordinate measured from the center of the irradiance spot, and $J_1(x)$ is a first-order Bessel function of the first kind. Notice that Eq. (1.3) decays with a $1/r^3$ dependence (since $|J_1(x)| \sim x^{-1/2}$ for large x), so this point-spread function is much narrower than Eq. (1.2). This function is called an *Airy pattern*, and it serves to illustrate several of the design choices that fluorescence microscopists face. First, the value $\lambda/(2n \sin \alpha)$ is proportional to the width of the Airy pattern, so microscopes that encode the most spatial information use a large index of refraction n , a large collection angle α , and a short wavelength λ . Every microscope designer uses the value $\lambda/(2n \sin \alpha)$ to choose the size of their detector elements so that they are sampling at the physical limit. Second, real imaging systems miss the physical limit by a factor of $1/\sin \alpha$, which highlights the importance of interfering waves from a wide range of angles. Finally, the value $n \sin \alpha$ simultaneously controls the width of the irradiance spot and serves as an invariant quantity for rays traveling through layered media with different indices of refraction $n_0 \sin \alpha_0 = n_1 \sin \alpha_1$ (Snell's law). Together, these properties merit $n \sin \alpha$ a special name: the *numerical aperture*

$$\text{NA} = n \sin \alpha. \quad (1.4)$$

We briefly note that increasing the collection angle α has an additional benefit: collecting more of the emitted wave results in larger irradiances and proportionally larger numbers of measured photons.

The quantity $\lambda/(2n \sin \alpha)$ is of such importance to microscopy that it earned a place on Ernst Abbe's stone memorial in Jena, Germany. We want to reemphasize that this quantity represents the combination of two different limits: the physical limit $\lambda/(2n)$ and

the *instrumental limit* $1/\sin \alpha$. The physical limit is set by how much structure the emitted signal has, while the instrumental limit is set by the design of our imaging system. The physical limit is the more fundamental limit, and the instrument can saturate but not exceed the physical limit.

Although Eq. (1.1) is a reasonable way to start modeling fluorescent emitters, it does not meet all of our expectations for an emitted electromagnetic wave. Readers familiar with electrodynamics will recall that electromagnetic radiation consists of *vector-valued transverse waves*, not scalar-valued waves like Eq. (1.1). Additionally, electromagnetic radiation is always created by accelerated charges, and the isotropic emissions modeled in Eq. (1.1) imply that charges have been accelerated in a way that violates the conservation of charge [2]. Clearly, a more accurate model of emission is required.

The fields emitted by most fluorescent molecules can be modeled by

$$\mathbf{E}(\mathbf{r}) = \frac{\mathbf{r} \times \hat{\mathbf{s}} \times \mathbf{r}}{|\mathbf{r}|^3} \exp\left(\frac{-2\pi in|\mathbf{r}|}{\lambda}\right), \quad (1.5)$$

where $\hat{\mathbf{s}}$ is the dipole emission moment of the molecule—see Fig. 1.1b) for an illustration. This emission pattern is vector-valued (polarized) and anisotropic, so it meets our baseline expectations. The fact that Eq. (1.5) is a more accurate model for emission than Eq. (1.1) implies that the emitted fields have more angular structure than we initially realized. This raises the possibility of encoding angular information into the emitted signals.

A key result of this dissertation is that the vector-valued signal in Eq. (1.5) can carry exactly six times as much information as the scalar-valued signal in Eq. (1.1). This realization raises the physical limit of all fluorescence microscopes to include six angular components, and it is now up to the instrument designer to build microscopes that can saturate this new limit. We pursue these improvements throughout the dissertation.

The six-fold improvement of the physical limit is surprising. Why an integer? Why six? Both of these questions have answers that lead to deep insights about this class of imaging.

The improvement is integer-valued because of the *topology* of the configuration space of a dipole emitter—the configuration space is compact, so operators that act on it have discrete spectra. The improvement factor is six because we live in three dimensions, and photon detection probabilities scale with the square of the fields. The vector space of homogeneous polynomials of degree two in three variables is six-dimensional, which leads directly to the six-fold improvement we predict.

We have been careful to specify that all of the physical and instrumental limits discussed so far are for imaging emitting objects when no priors are available. Exploiting priors allows us to encode even more information into the measurements we make. For example, *structured illumination* can be used to excite fluorescent molecules in specific positions and orientations within the sample, and this approach allows us to design and encode prior information about where fluorescent emissions originate. In other words, we can *alias* high-frequency information about the sample into the passband of the system, and this capability allows us to improve the spatial and angular resolution of fluorescence imaging systems.

This dissertation builds on the work of three fields: polarized fluorescence spectroscopy, fluorescence microscopy, and image science. In the remainder of this introduction we give brief histories of these fields and highlight the key ideas that have helped inform this dissertation. We conclude with a summary of this dissertation’s themes and its chapter-by-chapter contributions.

1.1 Background: Polarized fluorescence spectroscopy

The first written account of fluorescent emissions appeared in Nicolás Bautista Monardes’ 1565 book *Historia Medicinal*—an encyclopedia of medicinal plants imported to Spain from Mexico [3]. Monardes described how the Aztecs would soak thin slices of a white wood in water, and the water would turn pale blue in sunlight. The Aztecs used this solution as a diuretic, and an early Latin translation of Monardes’ work by Charles de L’Écluse gave the

wood its widely used name *Lignum nephriticum*—literally, kidney wood.

Samples of *Lignum nephriticum* circulated in 16th to 18th century Europe, and bowls and cups turned from the wood were given as gifts to royalty [4, 5]. Many early scientists attempted to explain the origin of the pale-blue color, but even giants missed the mark. In the same book where he coined the word “diffraction”, Francesco Maria Grimaldi described his investigation of *Lignum nephriticum* and concluded that the color was due to reflection within the solution [6]. Robert Boyle drew similar conclusions and demonstrated that the blue color could be made to disappear and reappear by changing the acidity of the solution—the first fluorescence pH sensor [7]. Isaac Newton wrote of several investigations [8, 9], and he echoed Grimaldi when he wrote that the solution was “apt to reflect one sort of light and transmit another” [10]. It appears that Isaac Newton’s definitive accounts (and his later stature) concluded the scientific investigation of *Lignum nephriticum* among early scientists.

In the 19th century, *Lignum nephriticum* was absent from the scientific literature as samples of the wood were unavailable. In 1915, the Smithsonian Institution sent William Edwin Safford, a botanist, to Mexico to find the source of the wood and investigate its medicinal properties [4]. Safford found that wood from the species *Eysenhardtia polystachya* created blue solutions that matched earlier descriptions, but he noted that the tree was too thin limbed to be turned into a cup or bowl. Safford investigated further and found that the national tree of the Philippines, *Pterocarpus indicus* or commonly *narra*, created blue solutions, had thick limbs, and was accessible to Europe after 1565 via Filipino–Mexican–Spanish trades routes. Monardes performed his investigations before 1565, so his samples must have come directly from Mexico. However, the cups and bowls that Boyle and Newton studied were likely misattributed to Mexico since they traveled through Mexico on their way to Spain. More recently, Acuña and coworkers have identified the fluorescent compound in *Eysenhardtia polystachya* as Coatline B [11] and have assembled a more complete account of this wood’s history [12].

The credit for the first modern description of fluorescence goes to George Gabriel Stokes in 1852 [13]. Starting his investigation with John Herschel’s observation of blue light from a quinine sulphate solution [14], Stokes arrived at two principal conclusions: (1) fluorescent emissions originate from within the solution “as if the fluid were self-luminous”, and (2) fluorescent emissions always have a longer wavelength than the incident light (the so-called Stokes shift). Stokes listed many other solutions that displayed fluorescence, and noted that fluorescent light could be used to test for the presence of fluorescent substances (although he notes that “unfortunately, these observations for the most part require sunlight”). Stokes also observed that illuminating his samples with polarized light did not change the emitted light, and the emitted light was always unpolarized. We will discuss this observation, which we now know to be true only under certain conditions, further in chapter 4.

Fluorescent emitters found early applications in lighting (Edmond Becquerel, father of better-known Henri, conceived of fluorescent light bulbs in 1857; Becquerel also has a potential priority claim for discovering the Stokes shift [15]), analytical chemistry (Göppelsröder made the progress of a chemical reaction visible with fluorescence in 1868 [16]), and hydrogeology (the Danube’s underground flow was fluoresently traced in 1877 [17]). In the 1920s Weigert studied the polarization of fluorescent emissions [18], Wawilow and Lewschin studied the differences of polarization between different dyes [19], and Francis Perrin synthesized all of the existing data by accounting for the fluorescence lifetime of the emitting molecules [20].

During his studies of polarized fluorescence Perrin introduced a quantity called the *polarization*, which he defined as

$$p = \frac{I_{\parallel} - I_{\perp}}{I_{\parallel} + I_{\perp}}, \quad (1.6)$$

where I_{\parallel} (I_{\perp}) is the irradiance measured by a low collection-angle detector ($\alpha \approx 0$) behind a polarizing filter that is oriented parallel (perpendicular) to the polarization of the illumina-

tion light. Note that the word *polarization* is overloaded: it can refer to a property of light or the result of the specific experiment described above. Perrin used this definition to derive a fundamental relationship in polarized fluorescence spectroscopy called the *Perrin equation*

$$\frac{1}{p} = \frac{1}{p_0} + \left(\frac{1}{p_0} - \frac{1}{3} \right) \frac{\tau_F}{\tau_R}, \quad (1.7)$$

where p_0 is the *fundamental polarization*, τ_F is the fluorescence lifetime of the molecule, and τ_R is the rotational correlation time of the molecule. When the molecule is approximately spherical, the rotational correlation time is related to other physical quantities by

$$\tau_R = \frac{\eta V}{k_B T}, \quad (1.8)$$

where k_B is Boltzmann's constant, T is the absolute temperature, η is the viscosity of the solution, and V is the volume of the fluorescent molecule. The fundamental polarization is the polarization that would be observed if the fluorescent molecules do not rotate between excitation and emission. Finding the fundamental polarization of a fluorescent molecule is simple using the Perrin equation: measure the polarization p as the temperature or viscosity of the solution varies, plot $1/p$ against the varied parameter and draw the line of best fit (a *Perrin plot*), then find the y -intercept as the value of $1/p_0$. Perrin's work provided a strong theoretical foundation for the field of polarized fluorescence spectroscopy: he described a linear relationship between a fundamental property of a fluorescent molecule (the fundamental polarization) and the observed data $\{I_{\parallel}, I_{\perp}\}$, then he used a graphical method as a linear reconstruction algorithm.

In 1960, Jabłoński introduced the *emission anisotropy* to simplify Perrin's expressions [21]

$$r = \frac{I_{\parallel} - I_{\perp}}{I_{\parallel} + 2I_{\perp}}. \quad (1.9)$$

Rewriting the Perrin equation in terms of the emission anisotropy leads to the simpler expression

$$\frac{r_0}{r} = 1 + \frac{\tau_F}{\tau_R}, \quad (1.10)$$

where r_0 is the *fundamental anisotropy*. All of Perrin's conclusions and methods remain qualitatively unchanged; we start with data $\{I_{\parallel}, I_{\perp}\}$ then use a linear model-based reconstruction to estimate the fundamental anisotropy. Once again, the word *anisotropy* is overloaded: it can describe a non-uniform angular distribution of fluorophores or the result of the specific experiment described above.

The polarization and the emission anisotropy are extremely useful quantities for analyzing and characterizing fluorescent molecules in solution, but their utility diminishes as soon as we consider ensembles of fluorescent molecules that are not oriented isotropically. For example, consider an ensemble of fluorescent dipole emitters that are oriented along a single direction. The measured values of I_{\parallel} and I_{\perp} now depend on the orientation of the dipole emitters with respect to the polarizer orientations. Of course, we can still calculate a value for the polarization or emission anisotropy, but these values are *rotation variant*—they change when we rotate the sample or the instrument. Clearly, one pair of measurements is not enough to characterize fluorescent samples that are not oriented isotropically.

More recent work by Weber [22, 23], Albrecht [24], Lakowicz [25], and many others have moved polarized fluorescence spectroscopy from physics labs into much broader use. Lakowicz' comprehensive book *Principles of Fluorescence Spectroscopy* covers much of the field of polarized fluorescence spectroscopy, and it highlights many useful applications. Although the field appears to be nearly mature, we think there is room for growth in both instrumentation and applications. In particular, we are interested in building instruments that can help us understand fluorescent molecules that are distributed anisotropically. In this dissertation we generalize Perrin's work to cases where fluorescent molecules are angularly

constrained, then design instruments and linear reconstruction schemes that can recover more information than existing polarized fluorescence spectroscopy experiments.

1.2 Background: Fluorescence microscopy

The early transmitted-light microscopes of Galileo Galilei, Antonie van Leeuwenhoek, and Robert Hooke were difficult to use and improve before the contributions of Ernst Abbe in the late 19th century. In addition to his aforementioned theory of resolution in microscopy, Abbe calculated the specific conditions that an optical system must meet to form a two dimensionally shift-invariant image—the *Abbe sine condition* [26, 27]. The improved resolution and extended field of view of Abbe’s imaging systems enabled too many applications to count. Essentially every optical microscope since 1900 has used Abbe’s designs.

In 1911, Heimstädt imaged autofluorescent bacteria by focusing ultraviolet light onto the sample with darkfield illumination—illumination that does not enter the detection objective—to minimize background [28]. Haitinger improved on the dim autofluorescent signals by labeling with extrinsic dyes, and he introduced the widefield epi-illumination configuration where the same objective is used for both illumination and detection [29]. The development of dichroic mirrors allowed the background to be reduced even further [30]. Combined with the flexibility and specificity of immunofluorescent labeling [31], the widefield epi-illumination fluorescent microscope became one of the most useful tools in the modern biology lab.

In 1834 Talbot published the first use of polarized light in a compound microscope [32] although Brewster performed simple investigations of minerals and plants as early as 1814 [33]. Polarized light microscopy found its first major use in live-cell imaging in work by Schmidt [34] and Inoué [35] in their studies of the mitotic spindle. The \sim 25-nm diameter microtubules of the mitotic spindle are invisible to typical transmission microscopes, but the addition of polarizing elements provided a new contrast mechanism that enabled early glimpses down to the nanometer scale.

In the late 1970s the first pair of quantitative polarized fluorescence microscopy studies was published [36, 37]. Interestingly, the authors of both studies are better known for their later contributions: two-photon microscopy for Watt Webb and total-internal reflection microscopy for Daniel Axelrod. Both studies used models for polarized excitation, angular diffusion, and polarized detection to interpret their measurements and recover physically meaningful parameters that describe biological samples. A broad range of developments in wide-field fluorescence polarization techniques occurred in the following decades: improved angular diffusion models [38], studies of myosin and muscle fibers [38, 39], and studies of fluorophores near interfaces [40].

Another major milestone occurred in 1994 when green fluorescent protein (GFP) was first expressed in a genetically modified organism [41]. This work spawned an enormous field devoted to developing fluorescent proteins that can report on biological pathways and gene expression *in situ* and in living samples. In 2002, Inoué and colleagues showed that GFP crystals display anisotropic absorption and emission [42], and Rosell and Boxer reported the orientations of the dipole absorption and emission moments with respect to the GFP molecule [43]. Genetically encoded fluorophores that exhibit anisotropic absorption and emission have been used in many widefield polarized light microscopy applications since: studies of lipid rafts [44, 45], septins [46–49], integrins [50], the nuclear pore complex [51, 52], and actin [53] have been reported.

Widefield polarized fluorescence techniques have been combined with many other illumination and detection techniques: two-photon excitation [54–56], Föster resonance energy transfer (FRET) [57], and fluorescence lifetime imaging (FLIM) [58–60]. Polarized-light FLIM often uses the name time-resolved fluorescence anisotropy imaging (TR-FAIM) to distinguish itself from steady-state fluorescence anisotropy imaging (SS-FAIM). Time-resolved measurements give access to even more information about the sample including anisotropic angular diffusion and fluorescence lifetimes. We will consider time-resolved measurements

briefly in chapter 4, but this dissertation mostly focuses on extending steady-state anisotropy imaging.

The ability to image single molecules has led to extremely valuable new ways of imaging biological samples. The Weiss lab reported the first experiments that used polarized excitation to track the orientation and state of single molecules [61, 62], and more recent work has exploited detection-side polarizers to the same effect [63–65]. These polarizing-filter single-molecule techniques have been applied to study molecular motors [66], actin dynamics [67], forces on single strands of DNA [68], and protein conformation changes at the ångstrom scale [69].

Although polarizing filters can be used to measure the orientation of fluorescent molecules, these filters are not strictly necessary. The Novotny and Enderlein labs demonstrated that the orientation of a fluorescent dipole is encoded in its irradiance pattern [70–73], and the Enderlein lab showed that two images at different defocus positions can be used to recover the three-dimensional position and orientation of single fluorescent molecules [74]. The Rieger, Stallinga, and Moerner labs realized that these irradiance patterns could introduce bias into typical Gaussian-fit single-molecule localization algorithms [75–78], and the Moerner group reported algorithms and meta-surface masks designed to reduce these biases [79–81]. Most recently, the Lew lab has been developing methods to measure the angular information emitted by single molecules using optimized phase masks that achieve fundamental limits [82–86].

To date, all polarized fluorescence studies of ensembles of molecules have implicitly assumed that a fluorescent dipole creates an Airy pattern-shaped irradiance patterns independent of the dipole’s orientation. The single molecule community has shown that this assumption is not true—the irradiance pattern is strongly dependent on the dipole’s orientation. One of the major goals of this dissertation is to show how the information encoded in orientation-dependent irradiance patterns can be exploited during reconstructions.

Many improvements can be made to fluorescence microscopes by modifying a standard instrument, taking multiple images, then combining the results optically or computationally into a final result. In 1957, Minsky demonstrated the first confocal design which used scanned-spot illumination with a confocal pinhole to remove light from out-of-focus planes [87, 88]. The confocal fluorescence microscope was the first to create *optically sectioned images*, and this property enabled many applications in material science and biology [89, 90].

Although confocal microscopes are still the workhorse of microscopy core facilities, the scanned spot bathes the entire sample in damaging light and the pinhole blocks a large fraction of the emissions. One way to reduce the light dose is to replace the pinhole with a detector then computationally [91–93] or optically [94] combine the images into a final result. A different option is to illuminate the sample with a light sheet that only illuminates in-focus regions of the sample [95, 96]. Light-sheet microscopes found their quintessential application in developmental biology where long imaging experiments require extremely low illumination levels to keep the sample alive [97, 98]. Light-sheet imaging systems generate optically sectioned images, but the resolution is still poor along the detection optical axis. Therefore, multiview light sheets with isotropic spatial resolution were developed [99, 100]. Many multiview light-sheet microscopes image samples in a cuvette, which creates a major barrier for many model organisms. To image specimens with isotropic resolution on a coverslip, the dual-view inverted selective plane illumination microscope (diSPIM) was developed [101] and later extended to exploit a third [102] and (effective) fourth view [103]. Researchers continue to search for illumination strategies that minimize the light dose to the sample: lattice light sheet designs reduce the peak irradiance, which decreases bleaching [104], and field synthesis approaches provide flexibility to reduce bleaching rates even further [105].

In chapter 5, we describe how we have outfitted the diSPIM instrument with polarized illumination to create the first instrument that can measure the three-dimensional position and orientation of densely labeled fluorescent molecules. Two reports of light-sheet anisotropy

imaging have appeared in the literature [106, 107], but anisotropy is a rotation-variant quantity so these instruments have not fully sampled the underlying signals.

In the same way that single-molecule studies do not require polarizing filters to recover molecular orientations, polarization filters are not necessary to recover all of the available angular information from densely labeled fluorescent samples. For this reason, we feel justified in dropping the word “polarized” and naming the class of techniques discussed in this dissertation *spatio-angular fluorescence microscopy*. The position and orientation of fluorescent ensembles is encoded in every fluorescence microscopy image, and our goal is to design systems that can measure this information in an invertible way.

1.3 Background: Image science

Image science is a field that attempts to improve imaging systems in a principled way. The standard approach is to start with a task—usually a decision or estimation task—then optimize the imaging system to achieve that task. The major thread of research in image science has consisted of finding ways to objectively define these tasks and measure the performance of imaging systems at achieving them.

Early image science monographs restricted their attention to two-dimensional imaging with film detectors [108, 109]. By studying the complete imaging chain in parts and as a whole—deterministic image formation, noise, detection, and decision making—these works laid an early foundation for defining and evaluating image quality. Later works began to expand to three-dimensional imaging including SPECT imaging systems [110].

The essential work on image science is Barrett and Myers’ book *Foundations of Image Science* [1]. This work provides a general linear systems approach to modeling imaging systems, to modeling their noise properties, to making decisions based on their results, and to evaluating and improving their design. This book sparked so many of the ideas in this dissertation that many parts of it are nearly prerequisite. For essential reading that

is used directly throughout this dissertation, we recommend chapter 1 and chapter 7. For intermediate topics that are used regularly including Fourier analysis, physical modeling, and inverse problems, we recommend chapters 2, 3, 4, 9, and 15. For advanced topics including almost all of the group theory used in this work, we recommend chapters 6 and 7.2.8–7.2.10.

Foundations provides a set of insights and mathematical tools that we use throughout this dissertation to analyze spatio-angular imaging systems. The first major insight is that objects and images can be represented as members of infinite- and finite-dimensional vector spaces, respectively. Before doing anything else, the imaging system designer should understand their object and data spaces—what is the “shape” and dimensionality of the data, and what exactly are we trying to reconstruct? Next, an imaging system can be represented as a mapping between these vector spaces, and studying this mapping, its null space, and its symmetries can provide deep insights into the imaging system’s behavior. If the mapping is linear, then the singular value decomposition (SVD) of the imaging operator is the tool of choice since it can show us the measurement space, null space, and what we can reconstruct without applying any priors. In this dissertation we calculate the SVD for many different spatio-angular imaging systems to help us understand if our designs achieve physical limits.

1.4 Dissertation themes

Several themes appear throughout this dissertation:

- **Spatio-angular fluorescence microscopy unifies polarized fluorescence spectroscopy, microscopy, and image science.** We construct a mathematical framework that combines the essential elements of all three fields to design optimal spatio-angular fluorescence instruments.
- **Geometry first, symmetry second, basis third.** Choosing the correct geometry for object space and data space, understanding the symmetries of the imaging system, then

choosing a basis that exploits the symmetries pays enormous dividends. Every imaging system we analyze follows this path.

- **Spatio-angular imaging is approximately linear.** General spatio-angular imaging problems are non-linear, but we find the specific conditions under which the imaging process is linear and pursue designs under these conditions.
- **Spatio-angular, not spatial and angular.** Microscopy is primarily spatial, and polarized fluorescence spectroscopy is primarily angular. Existing approaches to polarized fluorescence microscopy have taken a “spatial and angular” approach that leaves information on the table. A combined spatio-angular approach to modeling and reconstruction leads to the best results.
- **Design to the limit.** Whenever possible, we find the physical limits that the imaging system faces before developing designs that saturate these limits.

1.5 Chapter descriptions

- Chapter 2 introduces the basic elements of the theory of spatio-angular imaging systems, including spatio-angular point-spread functions and spatio-angular transfer functions. This chapter is a minimally modified version of the paper *Spatio-angular fluorescence microscopy I. Basic theory*, which appeared in the Journal of the Optical Society of America A [111].
- Chapter 3 applies spatio-angular imaging theory to the simplest possible optical system—a paraxial $4f$ system. Approximations in this chapter yield closed-form expressions for many relevant point-spread functions and transfer functions. This chapter is a minimally modified version of the paper *Spatio-angular fluorescence microscopy II. Paraxial 4f imaging*, which appeared in the Journal of the Optical Society of America A [112].

- Chapter 4 completes the forward model for single-view polarized illumination microscopes with unobstructed high-NA detection paths. We calculate the effects of constrained angular diffusion, polarized excitation, and high-NA objectives, and we find closed-form solutions in several experimentally relevant parameter spaces. This chapter is under review at the Journal of the Optical Society of America A under the name *Spatio-angular fluorescence microscopy III. Constrained angular diffusion, polarized excitation, and high-NA imaging* [113].
- Chapter 5 formulates a general spatio-angular fluorescence inverse problem, finds the conditions under which this inverse problem is linear, and describes a practical and efficient reconstruction algorithm based on the singular value decomposition. As a bonus, we find a class of optimal sampling schemes for single-view spatio-angular microscopes. This chapter is in preparation for submission.
- Chapter 6 uses the single-view model from chapter 4 as a building block to model and optimize a novel polarized light-sheet illumination dual-view microscope. We include reconstructions of two samples that give clear evidence that this instrument is the first to recover the three-dimensional position and orientation of densely labeled fluorescent molecules. This chapter is in preparation for submission as part of a larger project.
- Chapter 7 presents models and reconstruction algorithms for emerging spatio-angular microscopes including structured illumination, split-aperture, split-polarization, and light-field microscopes. We compare these designs and speculate on optimal combinations.
- Chapter 8 summarizes what we have learned and speculates on how basic scientists might exploit spatio-angular microscopy to ask and answer fundamentally new questions in biology.

CHAPTER 2

BASIC THEORY

Let no one who cannot think geometrically enter.
—*Above the entrance to PLATO’s Academy* (circa 350 BC)

We introduce the basic elements of a spatio-angular theory of fluorescence microscopy, providing a unified framework for analyzing systems that image single fluorescent dipoles and ensembles of overlapping dipoles that label biological molecules. We model an aplanatic microscope imaging an ensemble of fluorescent dipoles as a linear Hilbert-space operator, and we show that the operator takes a particularly convenient form when expressed in a basis of complex exponentials and spherical harmonics—a form we call the dipole spatio-angular transfer function. We discuss the implications of our analysis for all quantitative fluorescence microscopy studies and lay out a path towards a complete theory.

2.1 Introduction

Fluorescence microscopes are widely used in the biological sciences for imaging fluorescent molecules that label specific proteins and biologically important molecules. While most fluorescence microscopy experiments are designed to measure only the spatial distribution of fluorophores, a growing number of experiments seek to measure both the spatial and angular distributions of fluorophores by the use of polarizers [46, 51, 67, 114, 115] or point spread function engineering [85, 116].

Meanwhile, single-molecule localization microscopy (SMLM) experiments use spatially sparse fluorescent samples to localize single molecules with precision that surpasses the diffraction limit. Noise limits the precision of this localization [117, 118], and several studies have shown that model mismatch (e.g. ignoring the effects of vector optics, dipole orientation [77], and dipole rotation [76]) can introduce localization bias as well. Therefore, the

most precise and accurate SMLM experiments must use an appropriate model and jointly estimate both the position and orientation of each fluorophore. Several studies have successfully used vector optics and dipole models to estimate the position and orientation of single molecules [71, 72, 74, 119, 120], and there is growing interest in designing optical systems for measuring the position, orientation, and rotational dynamics of single molecules [78, 80, 84, 85, 116].

While many studies have focused on improving imaging models for spatially sparse fluorescent samples, we consider the more general case and aim to improve imaging models for arbitrary samples including those containing ensembles of fluorophores within a resolvable volume. In particular, we examine the effects of two widely used approximations in fluorescence microscopy—the *monopole approximation* and the *scalar approximation*.

We use the term *monopole* to refer to a model of a fluorescent object that treats it as an isotropic absorber/emitter. Although the term *monopole approximation* is not in widespread use, we think it accurately describes the way many models of fluorescence microscopy treat fluorescent objects, and we use the term to distinguish the monopole model from more realistic dipole and higher-order models. Despite their use in models, electromagnetic monopole absorber/emitters do not exist in nature. All physical fluorescent objects absorb and emit radiation with dipole or higher-order moments, and these moments are always oriented in space. For a classical mental model of fluorescent objects we imagine each dipole as a small oriented antenna where electrons are constrained to move along a single direction.

All fluorescence microscopy models that use an *optical point spread function* or an *optical transfer function* to describe the propagation of light through the microscope implicitly make the monopole approximation. The optical point spread function is the irradiance response of an optical system to an isotropic point source, so it cannot model the response due to an anisotropic dipole radiator. In this chapter we define *monopole and dipole transfer functions* that describe the mapping between fluorescent emissions and the measured

irradiance. Although optical systems are an essential part of microscopes, fluorescence microscopists are interested in measuring the properties of fluorophores (not optics), so the monopole and dipole transfer functions are more directly useful than the optical transfer function for the problems that fluorescence microscopists are interested in solving.

While the monopole approximation applies to the fluorescent object, the *scalar approximation* applies to the fields that propagate through the microscope. Modeling the electric fields in a region requires a three-dimensional vector field, but if the electric fields are random or completely parallel to one another, a scalar field is sufficient, and we can replace the vector-valued electric field, \mathbf{E} , with a scalar-valued field, U .

The scalar approximation is often made together with the monopole approximation. For example, the Born–Wolf model [121] and the Gibson–Lanni model [122] make both the monopole and scalar approximations when applied to fluorescence microscopes. However, some models make the monopole approximation but not the scalar approximation. For example, the Richards–Wolf model [123] considers the role of vector-valued fields in the optical system, but it is implicitly an optical model so when it is applied to fluorescence microscopes the monopole approximation is assumed.

This work lies at the intersection of three subfields of fluorescence microscopy: (1) spatial ensemble imaging where each resolvable volume contains many fluorophores and the goal is to find the concentration of fluorophores as a function of position in the sample, (2) spatio-angular ensemble imaging where each resolvable volume contains many fluorophores and the goal is to find the concentration and average orientation of fluorophores as a function of position in the sample, and (3) SMLM imaging where fluorophores are sparse in the sample and the goal is to find the position and orientation of each fluorophore. We briefly review how these three subfields use the monopole and scalar approximations.

The large majority of fluorescence microscopes are used to image ensembles of fluorophores, and most existing modeling techniques make use of the monopole approximation,

the scalar approximation, or both. As discussed above, the Gibson–Lanni model, the Born–Wolf model, and the Richards–Wolf model are approximate when applied to fluorescence microscopy data because they only model monopole emitters. Deconvolution algorithms that use these models may make biased estimates of fluorophore concentrations since they ignore the dipole excitation and emission of fluorophores.

A small but growing group of microscopists is interested in measuring the orientation and position of ensembles of fluorophores [46, 51, 67, 114, 115]. These techniques typically use polarizers to make multiple measurements of the same object with different polarizer orientations, then they use a model of the dipole excitation and emission processes [63] to recover the orientation of fluorophores using pixel-wise arithmetic. Although these studies do not adopt the scalar or monopole approximations for the angular part of the problem, they adopt both approximations when they consider the spatial part of the problem. Existing works either ignore the spatial reconstruction problem [46, 51, 67, 114] or assume that the spatial and angular reconstruction problems can be solved sequentially [115].

The most precise experiments in SMLM imaging do not adopt the scalar or monopole approximations. Many works have applied dipole models with vector optics, and several works have considered the effects of rotational and spatial diffusion on the images of single molecules [66, 82, 85, 124, 125]. We will see that the dipole transfer functions are useful tools for incorporating angular and spatial diffusion into SMLM simulations and reconstructions.

In this chapter we begin to place these three subfields on a common theoretical footing. First, in section 2.2, we consider arbitrary fluorescence imaging models and lay out a plan for developing a model for spatio-angular imaging. In section 2.3 we review the familiar monopole imaging model, and in section 2.4 we extend the model to dipoles. Finally, in section 2.5 we discuss the results and their broader implications.

In this chapter we focus on modeling a single-view fluorescence microscope with neither polarized excitation nor detection. In subsequent chapters of this dissertation we will extend

our models to include polarized excitation, polarized detection, and multi-view microscopes. Additionally, we have restricted this chapter to the forward problem—the mapping between a known object and the data. In later chapters we will consider the inverse problem, and the singular value decomposition (SVD) will play a central role.

2.2 Theory

We begin our analysis with the abstract Hilbert space formalism of Barrett and Myers [1, ch. 1.3]. Our first task is to formulate the imaging process as a mapping between two Hilbert spaces $\mathcal{H} : \mathbb{U} \rightarrow \mathbb{V}$, where \mathbb{U} is a set that contains all possible objects, \mathbb{V} is a set that contains all (possibly noise-corrupted) datasets, and \mathcal{H} is a model of the instrument that maps between these two spaces. We denote (possibly infinite-dimensional) Hilbert-space vectors in \mathbb{U} with \mathbf{f} , Hilbert-space vectors in \mathbb{V} with \mathbf{g} , and the mapping between the spaces with

$$\mathbf{g} = \mathcal{H}\mathbf{f}. \quad (2.1)$$

Throughout this dissertation we will use the letters g , h , and f with varying fonts, capitalizations, and arguments to represent the data, the instrument, and the object, respectively.

Once we have identified the spaces \mathbb{U} and \mathbb{V} , we can start expressing the mapping between the spaces in a specific object-space and data-space basis. In most cases the easiest mapping to find uses a delta-function basis—we expand object and data space into delta functions, then express the mapping as an integral transform. After finding this mapping we can start to investigate the same mapping in different bases.

The above discussion is quite abstract, but it is a powerful point of view that will enable us to unify the analysis of spatio-angular fluorescence imaging. In section 2.3 we will demonstrate the formalism by examining a familiar monopole imaging model, and we will

demonstrate the mapping between object and data space in two different bases. In section 2.4 we will extend the monopole imaging model to dipoles and examine the mapping in four different bases.

2.3 Monopole imaging

We start by modeling the imaging process for a field of dynamic fluorescent monopoles. We have split our model into two pieces: (1) the dynamics of excitation, decay, and diffusion processes, and (2) the emission and detection processes. This section treads familiar ground, but it serves to establish the concepts and notation that will be necessary when we extend to the dipole case.

2.3.1 Monopole dynamics

We begin by considering a spatial distribution of monopoles that can occupy just two states—a ground state and an excited state. We use $f^{(\text{gr})}(\mathbf{r}_o, t)$ to represent the number of monopoles in the ground state at position \mathbf{r}_o per unit volume at time t per unit time. Similarly, we use $f^{(\text{ex})}(\mathbf{r}_o, t)$ to represent the number of monopoles in the excited state.

Next, we describe all of the transitions between states. If we excite the monopoles with an illumination pattern that is uniform in space and time, then the rate of excitation will be the product of an excitation constant $\kappa^{(\text{ex})}$ with the number of monopoles in the ground state. Similarly, the rate of molecules decaying from the excited state to the ground state will be the product of a decay constant $\kappa^{(\text{d})}$ with the number of monopoles in the excited state (assuming that stimulated emission is negligible).

Finally, we describe the effect of diffusion within each state. If the diffusion is homogeneous (independent of position) and isotropic (independent of direction) then the rate of change of the spatial distribution will be proportional to a diffusion constant D_R multiplied by the Laplacian operator $\Delta_{\mathbb{R}^3} = \frac{\partial^2}{\partial x^2} + \frac{\partial^2}{\partial y^2} + \frac{\partial^2}{\partial z^2}$ acting on the spatial distribution of

monopoles at that point.

Bringing the effects of excitation, decay, and diffusion together yields a pair of coupled partial differential equations

$$\frac{\partial f^{(\text{gr})}(\mathbf{r}_o, t)}{\partial t} = -\kappa^{(\text{ex})} f^{(\text{gr})}(\mathbf{r}_o, t) + \kappa^{(\text{d})} f^{(\text{ex})}(\mathbf{r}_o, t) + D_R \Delta_{\mathbb{R}^3} f^{(\text{gr})}(\mathbf{r}_o, t), \quad (2.2)$$

$$\frac{\partial f^{(\text{ex})}(\mathbf{r}_o, t)}{\partial t} = \kappa^{(\text{ex})} f^{(\text{gr})}(\mathbf{r}_o, t) - \kappa^{(\text{d})} f^{(\text{ex})}(\mathbf{r}_o, t) + D_R \Delta_{\mathbb{R}^3} f^{(\text{ex})}(\mathbf{r}_o, t). \quad (2.3)$$

Equations (2.2) and (2.3) serve as a minimal model of monopole dynamics, and these equations can be generalized to model a broad class of fluorescence imaging techniques. For example, space- and time-varying excitation patterns $\kappa^{(\text{ex})}(\mathbf{r}_o, t)$ are useful for modeling structured illumination microscopes (SIM); space- and time-varying decay constants $\kappa^{(\text{d})}(\mathbf{r}_o, t)$ are of interest in fluorescence lifetime imaging microscopy (FLIM); space-, time-, and direction-varying (tensor-valued) diffusion coefficients are of interest in diffusion imaging; and extra states and transitions can be added to model single-molecule techniques, stimulated emission and depletion (STED) techniques, Forster resonance energy transfer (FRET), and photobleaching.

2.3.2 Monopole detection

Next, we model the monopole emission and detection processes independent of the underlying dynamics. In our simple two-state model we can only measure the photons radiated during transitions from the excited state to the ground state, which occur at a rate $\kappa^{(\text{d})} f^{(\text{ex})}(\mathbf{r}_o, t)$. If we expose a detector for a period t_e , then the most we can hope to recover from our data without knowing more about the dynamics of the system is the quantity

$$f(\mathbf{r}_o) = \int_0^{t_e} dt \kappa^{(\text{d})} f^{(\text{ex})}(\mathbf{r}_o, t). \quad (2.4)$$

The function $f(\mathbf{r}_o)$ represents the number of monopole emissions during the exposure time from position \mathbf{r}_o per unit volume. A complete name for $f(\mathbf{r}_o)$ would be the *time-integrated monopole emission density rate*, but for brevity we will refer to it as the *monopole emission density*.

We identify the set of all possible monopole emission densities as our object space $\mathbb{U} = \mathbb{L}_2(\mathbb{R}^3)$ —the set of square-integrable functions in three-dimensional space. If we measure the irradiance on a two-dimensional detector then data space is $\mathbb{V} = \mathbb{L}_2(\mathbb{R}^2)$ and the data can be represented by a function $g'(\mathbf{r}'_d)$ called the *irradiance*—the power received by a surface per unit area at position \mathbf{r}'_d . Note that we have adopted a slightly unusual convention of using primes to denote unscaled coordinates. Later in this section we will introduce unprimed scaled coordinates that we will use throughout the rest of the dissertation.

A reasonable starting point is to assume that the relationship between the object and the data is *linear*—this is true in many fluorescence microscopes because fluorophores emit incoherently, so a scaled sum of emissions result in a scaled sum of the irradiance patterns created by the individual emissions.

If the mapping is linear, we can write the irradiance as a weighted integral over the monopole emission density

$$g'(\mathbf{r}'_d) = \int_{\mathbb{R}^3} d\mathbf{r}_o h'(\mathbf{r}'_d, \mathbf{r}_o) f(\mathbf{r}_o), \quad (2.5)$$

where $h'(\mathbf{r}'_d, \mathbf{r}_o)$ is the irradiance at two-dimensional position \mathbf{r}'_d (roman font) created by a point source at three-dimensional position \mathbf{r}_o (gothic font).

Next, we assume that the optical system is *aplanatic*—Abbe's sine condition is satisfied and on-axis points are imaged without aberration. Abbe's sine condition guarantees that off-axis points are imaged without spherical aberration or coma [27, ch. 1], so the imaging system can be modeled within the field of view of the optical system as a transverse magnifier with shift-invariant blur. We split the three-dimensional object coordinate \mathbf{r}_o into a two-

dimensional transverse coordinate \mathbf{r}_o^\perp and a one-dimensional axial coordinate r_o^{\parallel} to write the forward model as

$$g'(\mathbf{r}'_d) = \int_{\mathbb{R}} dr_o^{\parallel} \int_{\mathbb{R}^2} d\mathbf{r}_o^\perp h'(\mathbf{r}'_d - m\mathbf{r}_o^\perp, r_o^{\parallel}) f(\mathbf{r}_o^\perp, r_o^{\parallel}), \quad (2.6)$$

where m is a transverse magnification factor. Note that non-paraxial imaging systems that satisfy Abbe's sine condition cannot simultaneously satisfy the Herschel condition when $m \neq 1$ [126, 127], so non-paraxial magnifying imaging systems cannot be shift-invariant in three dimensions. For paraxial imaging systems the Abbe sine and Herschel conditions are approximately the same, and the imaging system can be described as approximately shift invariant in three dimensions.

We can simplify our analysis by changing coordinates and writing Eq. (2.6) as a transverse convolution [1, ch. 7.2.7]. We define a demagnified detector coordinate $\mathbf{r}_d = \mathbf{r}'_d/m$ and a normalization factor that corresponds to the total power incident on the detector plane due to an in-focus point source $P_{\text{mono}} = \int_{\mathbb{R}^2} d\mathbf{r} h'(\mathbf{r}, 0)$ where $\mathbf{r} = \mathbf{r}_d - \mathbf{r}_o^\perp$. We use these scaling factors to define the *monopole point spread function* as

$$h(\mathbf{r}_d - \mathbf{r}_o^\perp, r_o^{\parallel}) = \frac{h'(m[\mathbf{r}_d - \mathbf{r}_o^\perp], r_o^{\parallel})}{P_{\text{mono}}}, \quad (2.7)$$

and the *scaled irradiance* as

$$g(\mathbf{r}_d) = \frac{g'(m\mathbf{r}_d)}{P_{\text{mono}}}. \quad (2.8)$$

With these definitions we can express the mapping between the object and the data as a familiar transverse convolution

$$g(\mathbf{r}_d) = \int_{\mathbb{R}} dr_o^{\parallel} \int_{\mathbb{R}^2} d\mathbf{r}_o^\perp h(\mathbf{r}_d - \mathbf{r}_o^\perp, r_o^{\parallel}) f(\mathbf{r}_o^\perp, r_o^{\parallel}). \quad (2.9)$$

We have chosen to normalize the monopole point spread function so that

$$\int_{\mathbb{R}^2} d\mathbf{r} h(\mathbf{r}, 0) = 1. \quad (2.10)$$

The monopole point spread function corresponds to a measurable irradiance, so it is always real and positive.

The mapping between the object and the data in a linear shift-invariant imaging system takes a particularly simple form in a complex exponential (i.e. Fourier) basis. If we apply the Fourier convolution theorem to Eq. (2.9) we find that

$$G(\boldsymbol{\nu}) = \int_{\mathbb{R}} dr_o^\parallel H(\boldsymbol{\nu}, r_o^\parallel) F(\boldsymbol{\nu}, r_o^\parallel), \quad (2.11)$$

where we define the *scaled irradiance spectrum* as

$$G(\boldsymbol{\nu}) = \int_{\mathbb{R}^2} d\mathbf{r} g(\mathbf{r}) \exp(-2\pi i \mathbf{r} \cdot \boldsymbol{\nu}), \quad (2.12)$$

the *monopole transfer function* as

$$H(\boldsymbol{\nu}, r_o^\parallel) = \int_{\mathbb{R}^2} d\mathbf{r} h(\mathbf{r}, r_o^\parallel) \exp(-2\pi i \mathbf{r} \cdot \boldsymbol{\nu}), \quad (2.13)$$

and the *monopole spectrum* as

$$F(\boldsymbol{\nu}, r_o^\parallel) = \int_{\mathbb{R}^2} d\mathbf{r} f(\mathbf{r}, r_o^\parallel) \exp(-2\pi i \mathbf{r} \cdot \boldsymbol{\nu}). \quad (2.14)$$

The monopole point spread function is normalized and real, so we know that the monopole transfer function is normalized, $H(\mathbf{0}, 0) = 1$, and conjugate symmetric, $H(-\boldsymbol{\nu}, 0) = H^*(\boldsymbol{\nu}, 0)$, where z^* denotes the complex conjugate of z .

Notice that Eqs. (2.9) and (2.11) are expressions of the same mapping between object

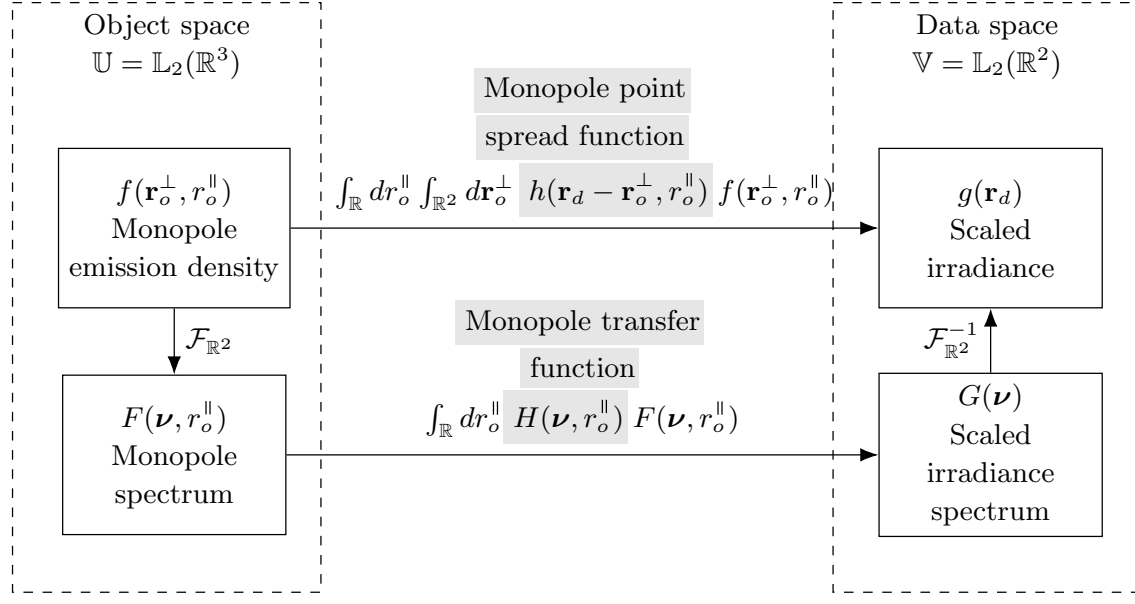


Figure 2.1: The mapping between the object and data space of a monopole fluorescence microscope can be computed in two different bases—a delta function basis and a complex exponential basis. The change of basis can be computed with a two-dimensional Fourier transform denoted $\mathcal{F}_{\mathbb{R}^2}$. Gray highlighting indicates which part of each expression is being named.

and data space in different bases. Figure 2.1 summarizes the relationship between object and data space in both bases.

We have been careful to use the term *monopole transfer function* instead of the commonly-used term *optical transfer function*. We reserve the term *optical transfer function* for optical systems—the optical transfer function maps between an input irradiance spectrum and an output irradiance spectrum in an optical system. We can use optical transfer functions to model the propagation of light through a microscope, but ultimately we are always interested in the object, not the light emitted by the object. We will find the distinction between the optical transfer function and the object transfer function to be especially valuable when we consider dipoles in section 2.4.

2.3.3 Monopole coherent transfer functions

Although the Fourier transform can be used to calculate the monopole transfer function directly from the monopole point spread function, there is a well-known alternative that exploits coherent transfer functions. The key idea is that the monopole point spread function can always be written as the absolute square of a scalar-valued *monopole coherent spread function*, $c(\mathbf{r}_d - \mathbf{r}_o^\perp, r_o^\parallel)$, defined by

$$|c(\mathbf{r}_d - \mathbf{r}_o^\perp, r_o^\parallel)|^2 = h(\mathbf{r}_d - \mathbf{r}_o^\perp, r_o^\parallel). \quad (2.15)$$

Physically, the monopole coherent spread function corresponds to the scalar-valued electro-magnetic field on the detector with appropriate scaling.

We can plug Eq. (2.15) into Eq. (2.13) and use the autocorrelation theorem to rewrite the monopole transfer function as

$$H(\boldsymbol{\nu}, r_o^\parallel) = \int_{\mathbb{R}^2} d\boldsymbol{\tau} C(\boldsymbol{\tau}, r_o^\parallel) C^*(\boldsymbol{\tau} - \boldsymbol{\nu}, r_o^\parallel), \quad (2.16)$$

where we have introduced the *monopole coherent transfer function* as the two-dimensional Fourier transform of the monopole coherent spread function:

$$C(\boldsymbol{\tau}, r_o^\parallel) = \int_{\mathbb{R}^2} d\mathbf{r} c(\mathbf{r}, r_o^\parallel) \exp[-2\pi i \mathbf{r} \cdot \boldsymbol{\tau}]. \quad (2.17)$$

Physically, the monopole coherent transfer function corresponds to the scalar-valued field in a Fourier plane of the detector with appropriate scaling.

The coherent transfer function provides a valuable shortcut for analyzing microscopes since it is often straightforward to calculate the field in a Fourier plane of the detector. A typical approach for calculating the transfer functions is to (1) calculate the field in a Fourier plane of the detector, (2) scale the field to find the monopole coherent transfer

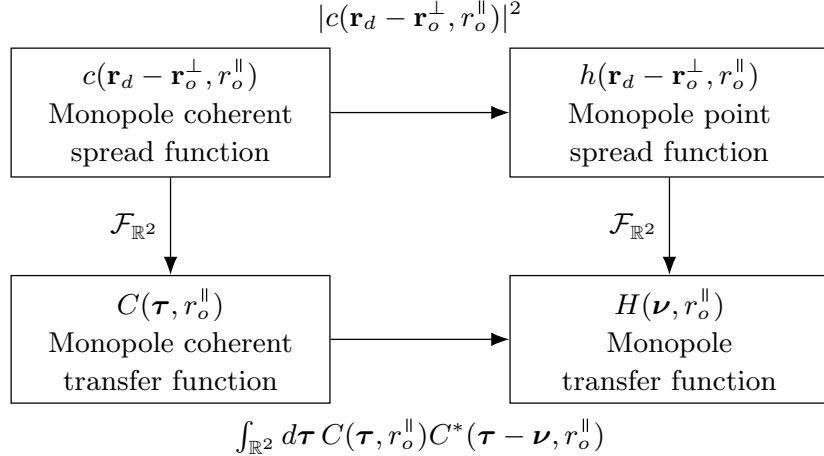


Figure 2.2: The monopole transfer functions are related by a two-dimensional Fourier transform (right column). The coherent monopole transfer functions (left column) can be used to simplify the calculation of the remaining transfer functions.

function, then (3) use the relationships in Fig. 2.2 to calculate the other transfer functions.

2.4 Dipole imaging

Now we consider a microscope imaging a field of dipoles by recording the irradiance on a two-dimensional detector. Similar to the monopole case, we split our model in two pieces: a dynamics model and an imaging model.

2.4.1 Dipole dynamics

We consider a distribution of dipoles that can occupy a ground state and an excited state. A function that assigns a real number to each point in space \mathbf{r}_o and time t is not enough to specify a dynamic field of dipoles because the dipoles can have different orientations. Therefore, we introduce an orientation coordinate $\hat{\mathbf{s}}_o$ and use the function $f^{(\text{gr})}(\mathbf{r}_o, \hat{\mathbf{s}}_o, t)$ to represent the number of dipoles in the ground state at position \mathbf{r}_o per unit volume oriented along $\hat{\mathbf{s}}_o$ per steradian at time t per unit time. Similarly, we use $f^{(\text{ex})}(\mathbf{r}_o, \hat{\mathbf{s}}_o, t)$ to represent the number of dipoles in the excited state.

We can model the transitions between states in the same way that we did with monopoles. If we excite the dipoles with an illumination pattern that is uniform in space, orientation, and time, then the rate of excitation will be $\kappa^{(\text{ex})} f^{(\text{gr})}(\mathbf{r}_o, \hat{\mathbf{s}}_o, t)$. Similarly, the rate of decay from the excited state to the ground state will be $\kappa^{(\text{d})} f^{(\text{ex})}(\mathbf{r}_o, \hat{\mathbf{s}}_o, t)$ (assuming that stimulated emission is negligible).

We can model homogeneous and isotropic spatial diffusion in the same way that we did for monopoles—the rate of change of the spatial distribution will be the product of a spatial diffusion coefficient D_R multiplied by the Laplacian $\Delta_{\mathbb{R}^3}$ acting on the dipole distribution at that point. Similarly, if angular diffusion is homogeneous (independent of orientation $\hat{\mathbf{s}}_o$) and isotropic (independent of angular diffusion direction) then the rate of the change of angular distribution will be the product of an angular diffusion coefficient D_S multiplied by the spherical Laplacian $\Delta_{\mathbb{S}^2}$ acting on the dipole distribution at that orientation. If we choose a set of spherical coordinates $\hat{\mathbf{s}}_o = (\theta, \phi)$ where θ is the inclination angle and ϕ is the azimuthal angle, then the spherical Laplacian takes the form $\Delta_{\mathbb{S}^2} = \frac{1}{\sin^2 \theta} \frac{\partial^2}{\partial \phi^2} + \frac{1}{\sin \theta} \frac{\partial}{\partial \theta} \left(\sin \theta \frac{\partial}{\partial \theta} \right)$.

Bringing everything together yields a pair of coupled partial differential equations

$$\begin{aligned} \frac{\partial f^{(\text{gr})}(\mathbf{r}_o, \hat{\mathbf{s}}_o, t)}{\partial t} &= -\kappa^{(\text{ex})} f^{(\text{gr})}(\mathbf{r}_o, \hat{\mathbf{s}}_o, t) + \kappa^{(\text{d})} f^{(\text{ex})}(\mathbf{r}_o, \hat{\mathbf{s}}_o, t) + D_R \Delta_{\mathbb{R}^3} f^{(\text{gr})}(\mathbf{r}_o, \hat{\mathbf{s}}_o, t) \\ &\quad + D_S \Delta_{\mathbb{S}^2} f^{(\text{gr})}(\mathbf{r}_o, \hat{\mathbf{s}}_o, t), \end{aligned} \quad (2.18)$$

$$\begin{aligned} \frac{\partial f^{(\text{ex})}(\mathbf{r}_o, \hat{\mathbf{s}}_o, t)}{\partial t} &= \kappa^{(\text{ex})} f^{(\text{gr})}(\mathbf{r}_o, \hat{\mathbf{s}}_o, t) - \kappa^{(\text{d})} f^{(\text{ex})}(\mathbf{r}_o, \hat{\mathbf{s}}_o, t) + D_R \Delta_{\mathbb{R}^3} f^{(\text{ex})}(\mathbf{r}_o, \hat{\mathbf{s}}_o, t) \\ &\quad + D_S \Delta_{\mathbb{S}^2} f^{(\text{ex})}(\mathbf{r}_o, \hat{\mathbf{s}}_o, t). \end{aligned} \quad (2.19)$$

Variants of Eqs. (2.18) and (2.19) can be used to model a wide range of more realistic dynamics. For example, a space-, orientation-, and time-varying excitation pattern $\kappa^{(\text{ex})}(\mathbf{r}_o, \hat{\mathbf{s}}_o, t)$ can be used to model spatio-angular structured illumination patterns. Specifically, an orientation-dependent excitation pattern can be used to model selective excitation with polarized light. There is also the possibility of modeling space-, orientation-, and time-varying

decay constants and diffusion constants.

Finally, we note that many fluorescent molecules have excitation and emission dipole moments that are not collinear. We can model these types of molecules by choosing the orientation coordinate $\hat{\mathbf{s}}_o$ to be along the emission dipole moment, then accounting for the excitation moment in the excitation rate function $\kappa^{(\text{ex})}(\mathbf{r}_o, \hat{\mathbf{s}}_o, t)$.

2.4.2 Dipole detection

Next, we model the dipole emission and detection processes independent of the underlying dynamics. We can only measure photons radiated during transitions from the excited state to the ground state, which occur at rate $\kappa^{(\text{d})} f^{(\text{ex})}(\mathbf{r}_o, \hat{\mathbf{s}}_o, t)$. If we expose a detector for a period t_e then the most we can hope to recover from our data without knowing more about the underlying dynamics is the quantity

$$f(\mathbf{r}_o, \hat{\mathbf{s}}_o) = \int_0^{t_{\text{det}}} dt \kappa^{(\text{d})} f^{(\text{ex})}(\mathbf{r}_o, \hat{\mathbf{s}}_o, t). \quad (2.20)$$

The function $f(\mathbf{r}_o, \hat{\mathbf{s}}_o)$ represents the number of dipole emissions during the exposure time from position \mathbf{r}_o per unit volume and orientation $\hat{\mathbf{s}}_o$ per unit steradian. A complete name for $f(\mathbf{r}_o, \hat{\mathbf{s}}_o)$ would be the *time-integrated dipole emission density rate*, but for brevity we will refer to it as the *dipole emission density*. We identify the set of all possible dipole emission densities as our object space $\mathbb{U} = \mathbb{L}_2(\mathbb{R}^3 \times \mathbb{S}^2)$ —the set of square-integrable functions on the product space of a volume and a two-dimensional spherical surface (the usual spherical surface embedded in \mathbb{R}^3). To visualize functions in object space we imagine a sphere at every point in a three-dimensional volume with a scalar value assigned to every surface point on each sphere.

Predicting the dipole emission density for a specific experiment requires (1) a model of the underlying dynamics (a variant of Eqs. (2.18) and (2.19)), (2) a set of initial/boundary

conditions, (3) a solution of the coupled partial differential equations $f^{(\text{ex})}(\mathbf{r}_o, \hat{\mathbf{s}}_o, t)$ (either an analytic or a numerical solution), then (4) the computation of the dipole emission density using Eq. (2.20). In Appendix 2.8 we demonstrate this procedure for an experiment with an instantaneous excitation pulse.

Similar to the monopole case, we model the mapping between the object and the irradiance as an integral transform

$$g'(\mathbf{r}'_d) = \int_{\mathbb{S}^2} d\hat{\mathbf{s}}_o \int_{\mathbb{R}^3} d\mathbf{r}_o h'(\mathbf{r}'_d, \mathbf{r}_o, \hat{\mathbf{s}}_o) f(\mathbf{r}_o, \hat{\mathbf{s}}_o), \quad (2.21)$$

where $h'(\mathbf{r}'_d, \mathbf{r}_o, \hat{\mathbf{s}}_o)$ is the irradiance at position \mathbf{r}'_d created by a point source at \mathbf{r}_o with orientation $\hat{\mathbf{s}}_o$. Notice that we have considered all possible orientations $\hat{\mathbf{s}}_o$ and integrated over the sphere \mathbb{S}^2 . The dipole emission density is always symmetric under angular inversion, $f(\mathbf{r}_o, \hat{\mathbf{s}}_o) = f(\mathbf{r}_o, -\hat{\mathbf{s}}_o)$, so we could have chosen to integrate over a hemisphere and adjusted the definition of the dipole emission density by a factor of two. For convenience we will continue to integrate over the complete sphere. We note that all functions in this chapter with $\hat{\mathbf{s}}_o$ as an independent variable are symmetric under angular inversion, $\hat{\mathbf{s}}_o \rightarrow -\hat{\mathbf{s}}_o$.

If the optical system is aplanatic, then we can split the three-dimensional object coordinate \mathbf{r}_o into a transverse coordinate \mathbf{r}_o^\perp and an axial coordinate r_o^\parallel and write the forward model as

$$g'(\mathbf{r}'_d) = \int_{\mathbb{S}^2} d\hat{\mathbf{s}}_o \int_{\mathbb{R}} dr_o^\parallel \int_{\mathbb{R}^2} d\mathbf{r}_o^\perp h'(\mathbf{r}'_d - m\mathbf{r}_o \mathbf{r}_o^\perp, r_o^\parallel, \hat{\mathbf{s}}_o) f(\mathbf{r}_o^\perp, r_o^\parallel, \hat{\mathbf{s}}_o). \quad (2.22)$$

We define the same demagnified detector coordinate $\mathbf{r}_d = \mathbf{r}'_d/m$ and a new normalization factor that corresponds to the total power incident on the detector due to an in-focus spatial point source with an angularly uniform distribution of dipoles

$$P_{\text{dip}} = \int_{\mathbb{S}^2} d\hat{\mathbf{s}}_o \int_{\mathbb{R}^2} d\mathbf{r} h'(m\mathbf{r}, 0, \hat{\mathbf{s}}_o).$$

We use these scaling factors to define the *dipole point spread function* as

$$h(\mathbf{r}_d - \mathbf{r}_o^\perp, r_o^{\parallel}, \hat{\mathbf{s}}_o) = \frac{h'(m[\mathbf{r}_d - \mathbf{r}_o^\perp], r_o^{\parallel}, \hat{\mathbf{s}}_o)}{P_{\text{dip}}}, \quad (2.23)$$

and the *scaled irradiance* as

$$g(\mathbf{r}_d) = \frac{g'(\mathbf{r}_d)}{P_{\text{dip}}}. \quad (2.24)$$

With these definitions we can express the mapping between the object and the data as

$$g(\mathbf{r}_d) = \int_{\mathbb{S}^2} d\hat{\mathbf{s}}_o \int_{\mathbb{R}} dr_o^{\parallel} \int_{\mathbb{R}^2} d\mathbf{r}_o^\perp h(\mathbf{r}_d - \mathbf{r}_o^\perp, r_o^{\parallel}, \hat{\mathbf{s}}_o) f(\mathbf{r}_o^\perp, r_o^{\parallel}, \hat{\mathbf{s}}_o). \quad (2.25)$$

Equation (2.25) is a key result because it represents the mapping between object space and data space in a delta function basis. The integrals in Eq. (2.25) would be extremely expensive to compute for an arbitrary object, but the integrals simplify to an efficient sum if the object is spatially and angularly sparse. For example, Eq. (2.25) would reduce to a superposition of dipole point spread functions if the object consisted of immobile dipole emitters.

Similar to the monopole case, we have chosen to normalize the dipole point spread function so that

$$\int_{\mathbb{S}^2} d\hat{\mathbf{s}}_o \int_{\mathbb{R}^2} d\mathbf{r} h(\mathbf{r}, 0, \hat{\mathbf{s}}_o) = 1. \quad (2.26)$$

The dipole point spread function is a measurable irradiance, so it is real and positive.

2.4.3 Dipole spatial transfer function

We can make our first change of basis by applying the Fourier-convolution theorem to Eq. (2.25), which yields

$$G(\boldsymbol{\nu}, r_o^{\parallel}) = \int_{\mathbb{S}^2} d\hat{\mathbf{s}}_o \int_{\mathbb{R}} dr_o^{\parallel} H(\boldsymbol{\nu}, r_o^{\parallel}, \hat{\mathbf{s}}_o) F(\boldsymbol{\nu}, r_o^{\parallel}, \hat{\mathbf{s}}_o), \quad (2.27)$$

where we define the *dipole spatial transfer function* as

$$H(\boldsymbol{\nu}, r_o^{\parallel}, \hat{\mathbf{s}}_o) = \int_{\mathbb{R}^2} d\mathbf{r} h(\mathbf{r}, r_o^{\parallel}, \hat{\mathbf{s}}_o) \exp(-2\pi i \mathbf{r} \cdot \boldsymbol{\nu}), \quad (2.28)$$

and the *dipole spatial spectrum* as

$$F(\boldsymbol{\nu}, r_o^{\parallel}, \hat{\mathbf{s}}_o) = \int_{\mathbb{R}^2} d\mathbf{r} f(\mathbf{r}, r_o^{\parallel}, \hat{\mathbf{s}}_o) \exp(-2\pi i \mathbf{r} \cdot \boldsymbol{\nu}). \quad (2.29)$$

Since the dipole point spread function is normalized and real, we know that the dipole spatial transfer function is normalized, $\int_{\mathbb{S}^2} d\hat{\mathbf{s}} H(\mathbf{0}, 0, \hat{\mathbf{s}}_o) = 1$, and conjugate symmetric, $H(-\boldsymbol{\nu}, 0, \hat{\mathbf{s}}_o) = H^*(\boldsymbol{\nu}, 0, \hat{\mathbf{s}}_o)$.

This basis is efficient for simulating and analyzing objects that are angularly sparse and spatially dense; e.g. rod-like structures that contain fluorophores in a fixed orientation, or rotationally fixed fluorophores that are undergoing spatial diffusion.

2.4.4 Dipole angular transfer function

The spherical harmonics are another set of convenient basis functions that play the same role as complex exponentials in spatial transfer functions—see Appendix 2.7 for an introduction to the spherical harmonics. We can change basis from spherical delta functions to spherical

harmonics by applying the generalized Plancherel theorem for spherical functions

$$\int_{\mathbb{S}^2} d\hat{\mathbf{s}} p(\hat{\mathbf{s}}) q^*(\hat{\mathbf{s}}) = \sum_{\ell=0}^{\infty} \sum_{m=-\ell}^{\ell} P_{\ell}^m Q_{\ell}^{m*}, \quad (2.30)$$

where $p(\hat{\mathbf{s}})$ and $q(\hat{\mathbf{s}})$ are arbitrary functions on the sphere, P_{ℓ}^m and Q_{ℓ}^m are their spherical Fourier transforms defined by

$$P_{\ell}^m = \int_{\mathbb{S}^2} d\hat{\mathbf{s}} p(\hat{\mathbf{s}}) Y_{\ell}^{m*}(\hat{\mathbf{s}}), \quad (2.31)$$

and $Y_{\ell}^m(\hat{\mathbf{s}})$ are the spherical harmonic functions defined in Appendix 2.7. Equation (2.30) expresses the fact that scalar products are invariant under a change of basis [1, Eq. 3.78]. The left-hand side of Eq. (2.30) is the scalar product of $\mathbb{L}_2(\mathbb{S}^2)$ functions in a delta function basis and the right-hand side is the scalar product of $\mathbb{L}_2(\mathbb{S}^2)$ functions in a spherical harmonic function basis. Applying Eq. (2.30) to Eq. (2.25) yields

$$g(\mathbf{r}_d) = \sum_{\ell=0}^{\infty} \sum_{m=-\ell}^{\ell} \int_{\mathbb{R}} dr_o^{\parallel} \int_{\mathbb{R}^2} d\mathbf{r}_o^{\perp} H_{\ell}^m(\mathbf{r}_d - \mathbf{r}_o^{\perp}, r_o^{\parallel}) F_{\ell}^m(\mathbf{r}_o^{\perp}, r_o^{\parallel}), \quad (2.32)$$

where we have defined the *dipole angular transfer function* as

$$H_{\ell}^m(\mathbf{r}_d - \mathbf{r}_o^{\perp}, r_o^{\parallel}) = \int_{\mathbb{S}^2} d\hat{\mathbf{s}}_o h(\mathbf{r}_d - \mathbf{r}_o^{\perp}, r_o^{\parallel}, \hat{\mathbf{s}}_o) Y_{\ell}^{m*}(\hat{\mathbf{s}}_o), \quad (2.33)$$

and the *dipole angular spectrum* as

$$F_{\ell}^m(\mathbf{r}_o^{\perp}, r_o^{\parallel}) = \int_{\mathbb{S}^2} d\hat{\mathbf{s}}_o f(\mathbf{r}_o^{\perp}, r_o^{\parallel}, \hat{\mathbf{s}}_o) Y_{\ell}^{m*}(\hat{\mathbf{s}}_o). \quad (2.34)$$

Since the dipole point spread function is normalized and real, we know that the dipole angular transfer function is normalized, $\int_{\mathbb{R}^2} d\mathbf{r} H_0^0(\mathbf{r}, 0) = 1$, and conjugate symmetric, $H_{\ell}^{-m}(\mathbf{r}, 0) = (-1)^m H_{\ell}^{m*}(\mathbf{r}, 0)$.

This basis is efficient for simulating and analyzing objects that are spatially sparse and angularly dense; e.g. single fluorophores that are undergoing angular diffusion, or many fluorophores that are within a resolvable volume with varying orientations.

2.4.5 Spatio-angular dipole transfer function

We can arrive at our final basis in two ways: by applying the generalized Plancherel theorem for spherical functions to Eq. (2.27) or by applying the Fourier convolution theorem to Eq. (2.32). We follow the first path and find that

$$G(\boldsymbol{\nu}, r_o^{\parallel}) = \sum_{\ell=0}^{\infty} \sum_{m=-\ell}^{\ell} \int_{\mathbb{R}} dr_o^{\parallel} \mathsf{H}_{\ell}^m(\boldsymbol{\nu}, r_o^{\parallel}) \mathsf{F}_{\ell}^m(\boldsymbol{\nu}, r_o^{\parallel}), \quad (2.35)$$

where we have defined the *dipole spatio-angular transfer function* as

$$\mathsf{H}_{\ell}^m(\boldsymbol{\nu}, r_o^{\parallel}) = \int_{\mathbb{S}^2} d\hat{\mathbf{s}}_o H(\boldsymbol{\nu}, r_o^{\parallel}, \hat{\mathbf{s}}_o) Y_{\ell}^{m*}(\hat{\mathbf{s}}_o), \quad (2.36)$$

and the *dipole spatio-angular spectrum* as

$$\mathsf{F}_{\ell}^m(\boldsymbol{\nu}, r_o^{\parallel}) = \int_{\mathbb{S}^2} d\hat{\mathbf{s}}_o F(\boldsymbol{\nu}, r_o^{\parallel}, \hat{\mathbf{s}}_o) Y_{\ell}^{m*}(\hat{\mathbf{s}}_o). \quad (2.37)$$

Since the dipole point spread function is normalized and real, we know that the dipole spatio-angular transfer function is normalized, $\mathsf{H}_0^0(\mathbf{0}, 0) = 1$, and conjugate symmetric, $\mathsf{H}_{\ell}^{-m}(-\boldsymbol{\nu}, 0) = (-1)^m \mathsf{H}_{\ell}^m(\boldsymbol{\nu}, 0)$.

This basis is efficient for simulating and analyzing arbitrary samples because it exploits the band limit of the imaging system. We note that most single molecule imaging experiments are efficiently described in this basis because of the effects of spatial and rotational diffusion—see Appendix 2.8 for an example.

Figure 2.3 summarizes the relationships between the four bases that we can use to com-

pute the image of a field of dipoles. We reiterate that all four bases may be useful depending on the sample.

2.4.6 Dipole coherent transfer functions

Similar to the monopole case, there is an efficient way to calculate the transfer functions using coherent transfer functions. The dipole point spread function can always be written as the absolute square of a vector-valued function, $\mathbf{c}(\mathbf{r}_d - \mathbf{r}_o^\perp, r_o^\parallel, \hat{\mathbf{s}}_o)$, called the *dipole coherent spread function*:

$$|\mathbf{c}(\mathbf{r}_d - \mathbf{r}_o^\perp, r_o^\parallel, \hat{\mathbf{s}}_o)|^2 = h(\mathbf{r}_d - \mathbf{r}_o^\perp, r_o^\parallel, \hat{\mathbf{s}}_o). \quad (2.38)$$

Physically, the dipole coherent spread function corresponds to the vector-valued electric field on the detector with appropriate scaling. We need a vector-valued coherent transfer function since the polarization of the field plays a significant role in dipole imaging, so the dipole point spread function cannot be written as an absolute square of a scalar-valued function.

We can plug Eq. (2.38) into Eq. (2.28) and use the autocorrelation theorem to rewrite the dipole spatial transfer function as

$$H(\boldsymbol{\nu}, r_o^\parallel, \hat{\mathbf{s}}_o) = \int_{\mathbb{R}^2} d\boldsymbol{\tau} \mathbf{C}(\boldsymbol{\tau}, r_o^\parallel, \hat{\mathbf{s}}_o) \mathbf{C}^\dagger(\boldsymbol{\tau} - \boldsymbol{\nu}, r_o^\parallel, \hat{\mathbf{s}}_o), \quad (2.39)$$

where we have introduced the *dipole coherent transfer function* $\mathbf{C}(\boldsymbol{\tau}, r_o^\parallel, \hat{\mathbf{s}}_o)$ as the two-dimensional Fourier transform of the dipole coherent spread function:

$$\mathbf{C}(\boldsymbol{\tau}, r_o^\parallel, \hat{\mathbf{s}}_o) = \int_{\mathbb{R}^2} d\mathbf{r} \mathbf{c}(\mathbf{r}, r_o^\parallel, \hat{\mathbf{s}}_o) \exp[-2\pi i \mathbf{r} \cdot \boldsymbol{\tau}]. \quad (2.40)$$

Physically, the dipole coherent transfer function corresponds to the vector-valued electric field created by a dipole oriented along $\hat{\mathbf{s}}_o$ in a Fourier plane of the detector with appropriate

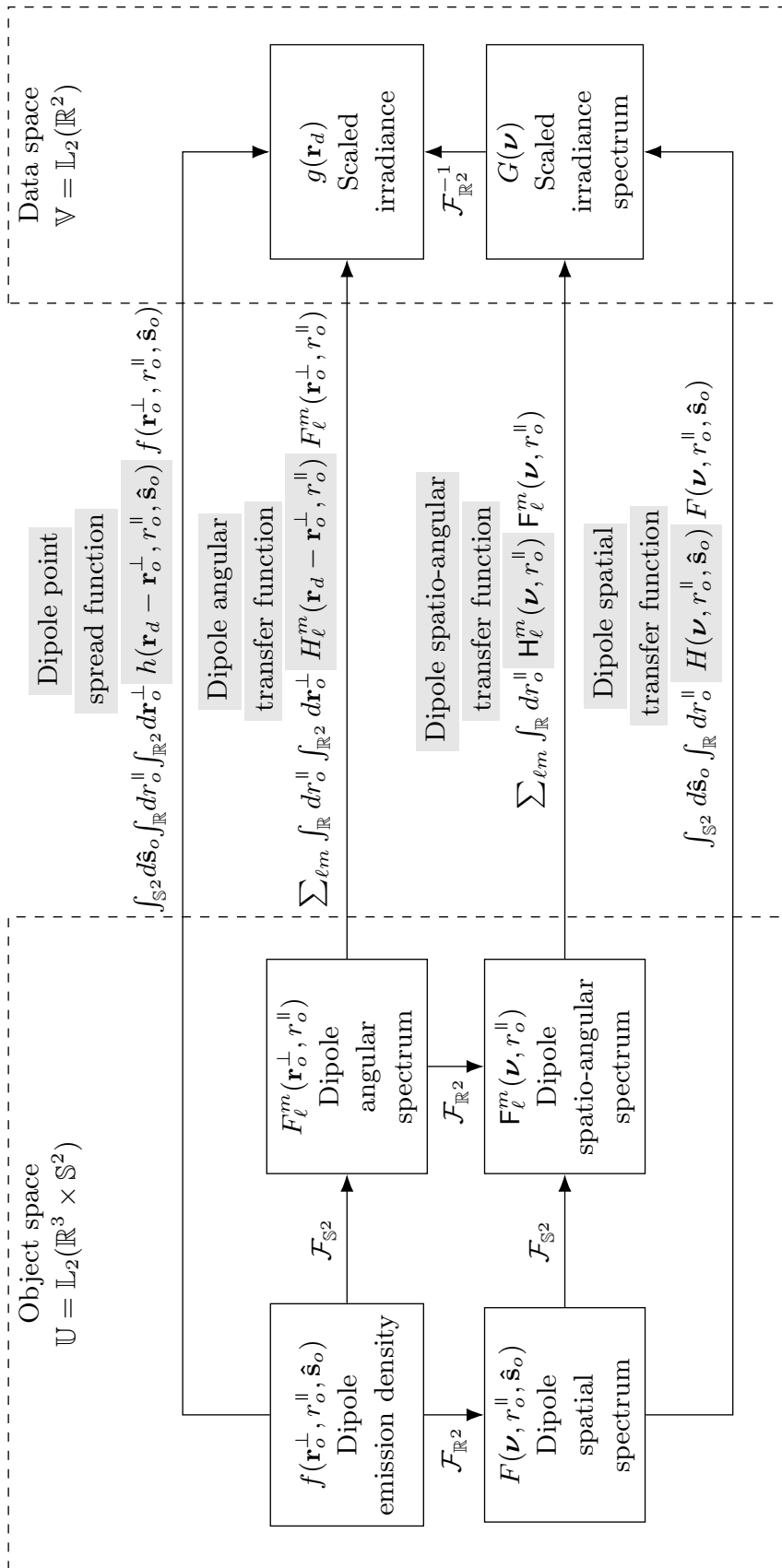


Figure 2.3: The mapping between the object space and data space of a dipole imaging system can be computed in four different bases—a delta function basis, a complex-exponential/angular-delta basis, a spatial-delta/spherical-harmonic basis, and a complex-exponential/spherical-harmonic basis. The changes of basis can be computed with the two-dimensional Fourier transform denoted $\mathcal{F}_{\mathbb{R}^2}$, and the spherical Fourier transform denoted $\mathcal{F}_{\mathbb{S}^2}$. Gray highlighting indicates which part of each expression is being named.

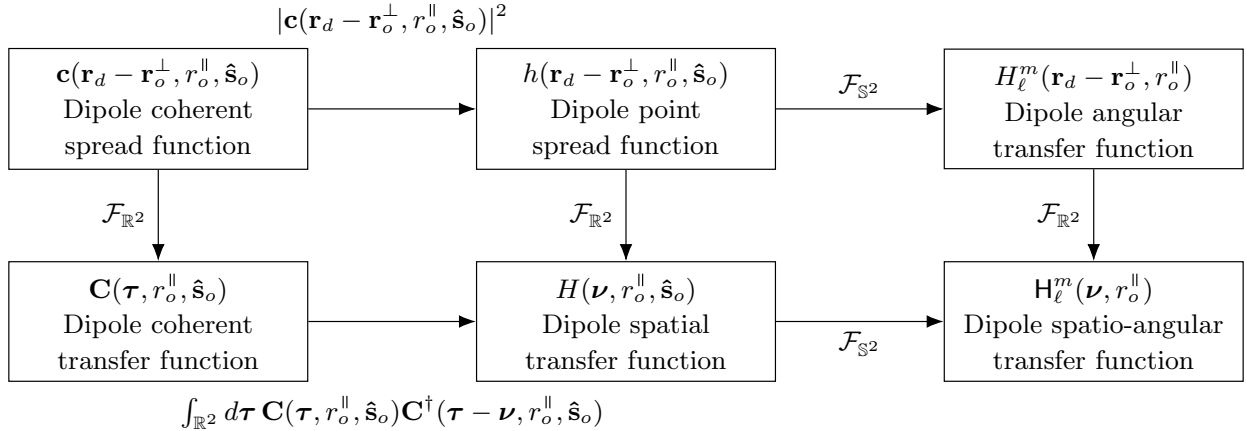


Figure 2.4: There is one transfer function for each set of object-space basis functions, and these transfer functions are related by two-dimensional and spherical Fourier transforms—see center and right columns. There is an additional pair of coherent transfer functions—see left column.

scaling. Similar to the monopole case, we can calculate the dipole-orientation-dependent fields in a Fourier plane of the detector, scale appropriately to find the dipole coherent transfer function, then use the relationships in Fig. 2.4 to calculate the other transfer functions. Finally, we note that the dipole coherent transfer function is identical (up to scaling factors) to what Agrawal et al. call the *Green’s tensor* [116] and Novotny and Hecht’s *dyadic point spread function* multiplied by the dipole moment vector [73].

2.5 Discussion

2.5.1 When are alternative bases useful?

Describing a sample \mathbf{f} , an imaging system \mathcal{H} , or data \mathbf{g} in a basis other than a delta function basis is useful when the signal is sparse or band-limited in the new basis. Expressing a signal in a sparser basis is particularly useful for improving intuition about the signal and for reducing computation time.

Throughout this chapter we have emphasized examples of samples that are sparse in alternative bases. For example, dipoles that are undergoing spatial and angular diffusion

give rise to dipole emission densities that are sparse in a basis of complex exponentials and spherical harmonics. In the next chapter we describe how a common imaging system—a single-view aplanatic microscope—can be described sparsely in the same basis, and this will lead us to a natural definition of the angular band-limit of the imaging system that augments the widely known spatial band-limit.

2.5.2 Alternatives to the spherical harmonics

Throughout this chapter we have used the spherical harmonic functions as a basis for functions on the sphere, but there are other basis functions that can be advantageous in some cases. Several works [55, 80, 82, 84, 85, 119] have used the second moments of the Cartesian unit vectors in orientation space (or second moments for brevity) as basis functions for the sphere because they arise naturally when computing the dipole point spread function. These works use an alternative to the dipole angular transfer function that uses the second moments as basis functions so the forward model can be written as

$$g(\mathbf{r}_d) = \sum_{j=1}^6 \int_{\mathbb{R}} dr_o^{\parallel} \int_{\mathbb{R}^2} d\mathbf{r}_o^{\perp} H_j(\mathbf{r}_d - \mathbf{r}_o^{\perp}, r_o^{\parallel}) F_j(\mathbf{r}_o^{\perp}, r_o^{\parallel}), \quad (2.41)$$

where

$$H_j(\mathbf{r}_d - \mathbf{r}_o^{\perp}, r_o^{\parallel}) = \int_{\mathbb{S}^2} d\hat{\mathbf{s}}_o h(\mathbf{r}_d - \mathbf{r}_o^{\perp}, r_o^{\parallel}, \hat{\mathbf{s}}_o) Z_j(\hat{\mathbf{s}}_o), \quad (2.42)$$

$$F_j(\mathbf{r}_o^{\perp}, r_o^{\parallel}) = \int_{\mathbb{S}^2} d\hat{\mathbf{s}}_o f(\mathbf{r}_o^{\perp}, r_o^{\parallel}, \hat{\mathbf{s}}_o) Z_j(\hat{\mathbf{s}}_o), \quad (2.43)$$

and $Z_j(\hat{\mathbf{s}}) = \{s_x^2, s_y^2, s_z^2, s_x s_y, s_y s_z, s_x s_z\}$ are the second moments. This formulation is convenient because it can exploit the spatial sparsity of the sample, the angular sparsity of diffusing samples in the basis of second moments, and the angular band-limit of common imaging systems. Additionally, the second moments approach does not require an expansion of the dipole point spread function onto spherical harmonics.

The spherical harmonics provide the same conveniences as the second moments: samples undergoing angular diffusion can be efficiently described using the spherical harmonics, and common imaging systems have an angular band-limit. Additionally, the spherical harmonics provide several potential advantages over the second moments. First, the spherical harmonics form a complete basis for functions on the sphere, while the second moments span a much smaller function space. Descoteaux et al. show that the even order spherical harmonics up to order ℓ and the degree- ℓ homogeneous polynomials restricted to the sphere span the same $\frac{1}{2}(\ell+1)(\ell+2)$ -dimensional function space [128]. Therefore, the spherical harmonic basis can be extended by adding an extra order of spherical harmonics to the existing set of spherical harmonics. Meanwhile, extending the basis of homogeneous polynomials without redundant basis vectors requires a completely new set of functions. Second, the spherical harmonics are orthogonal, which will allow us to deploy invaluable tools from linear algebra—linear subspaces, rank, SVD, etc.—to analyze and compare microscope designs. Finally, using the spherical harmonics provides access to a set of fast algorithms. The naive expansion of an arbitrary discretized N point spherical function onto spherical harmonics (or second moments) requires a $\mathcal{O}(N^2)$ matrix multiplication, while pioneering work by Driscoll and Healy [129] showed that the forward discrete fast spherical harmonic transform can be computed with a $\mathcal{O}(N(\log N)^2)$ algorithm and its inverse can be computed with a $\mathcal{O}(N^{3/2})$ algorithm. To our knowledge no similarly fast algorithms exist for expansion onto the higher-order moments.

Zhang et al. [85] have used the second moments to optimize a phase mask that creates a tri-spot point spread function. The authors formulate a system model as a 6×6 matrix that maps the six second moments that describe a rotating single molecule to the six intensity measurements from each lobe and polarization of the tri-spot point spread function. They show that the measurement matrices for existing phase mask designs are rank 4 or 5, and they implement a new rank 6 design that can measure all six second moments. The spherical harmonics can be used to similar effect in this problem by rewriting the system matrix

in a basis of spherical harmonics instead of second moments. Additionally, the spherical harmonics form an orthogonal basis, so optimizing the system will be slightly easier (for example, the Fisher information matrix will be diagonal in a spherical harmonic basis).

Backer et al. [130] have used the transverse second moments $\{s_x^2, s_y^2, s_x s_y\}$ to design a polarized-excitation imaging system and reconstruction algorithm that can recover the transverse distribution of fluorescent molecules. Similarly, Zhanghao et al. [115] have used the circular harmonics to design a polarized structured illumination imaging system and reconstruction scheme that can recover the transverse distribution of fluorescent molecules. The transverse second moments and the circular harmonics share the same relationship as the three-dimensional second moments and the spherical harmonics—each pair spans the same function space but only the circular/spherical harmonics are orthogonal. The transverse second moments and the circular harmonics are useful design tools for restricting the number of parameters to estimate, but these approaches artificially restrict the reconstructed dipole distributions to the transverse plane. Finally, we note that the relationship between 2D and 3D estimation problems is slightly simpler in a second moment basis than a spherical/circular harmonic basis. In a second moment basis the six second moments that describe the 3D problem can be truncated to the three second moments that describe the 2D problem. Meanwhile, the spherical harmonics that describe the 3D problem require a matrix multiplication (not a truncation) to map to the circular harmonics.

The diffusion magnetic resonance imaging community uses both the second moments (or second-order tensor) basis functions [131] and the spherical harmonic basis functions [132]. Descoteaux et al. have provided an explicit invertible transformation matrix to convert between the second moments and the zeroth- and second-order spherical harmonics [128]. Since the transformation between these two bases is invertible, functions on the sphere can be described with equal accuracy in either basis.

Another difference between the spherical harmonics and the second moments is that the

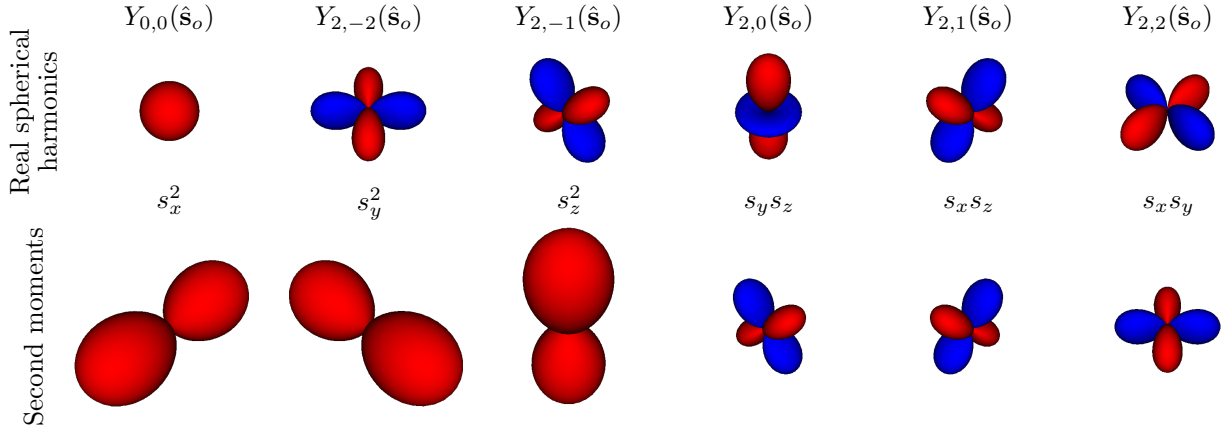


Figure 2.5: **Top row:** Real spherical harmonic basis functions for $\ell = 0$ and $\ell = 2$. **Bottom row:** Second moments of the Cartesian unit vectors in orientation space. The radius of each glyph indicates the value of the function along that direction. Red surfaces indicate positive values and blue surfaces indicate negative values. The two sets of basis functions span the same function space, but only the real spherical harmonics form an orthogonal basis.

spherical harmonics are complex-valued functions while the second moments are real-valued. Complex-valued spherical harmonics are convenient for mathematical manipulations, but we can also work with real-valued spherical harmonics for cheaper numerical manipulations or for improving our intuition. One possible definition of real-valued spherical harmonics is

$$Y_{\ell m}(\hat{s}_o) = \begin{cases} \sqrt{2} (-1)^m \operatorname{Im} [Y_\ell^{|m|}(\hat{s}_o)] & \text{if } m < 0, \\ Y_\ell^0(\hat{s}_o) & \text{if } m = 0, \\ \sqrt{2} (-1)^m \operatorname{Re} [Y_\ell^m(\hat{s}_o)] & \text{if } m > 0, \end{cases} \quad (2.44)$$

where the pair of lower indices imply that these are real-valued spherical harmonic functions. In Fig. 2.5 we directly compare the real-valued spherical harmonic functions to the second moment functions.

2.5.3 Towards spatio-angular reconstructions

We have focused on modeling the mapping between the object and the data in this chapter, but ultimately we are interested in reconstructing the object from the data. Considering in-focus objects and applying the monopole approximation simplifies the reconstruction problem because both object and data space are $\mathbb{L}_2(\mathbb{R}^2)$, so we can directly apply regularized inverse filters and maximum likelihood methods. The complete three-dimensional dipole model expands object space to $\mathbb{L}_2(\mathbb{R}^3 \times \mathbb{S}^2)$, so the inverse problem becomes much more challenging. In upcoming chapters we will use the singular value decomposition to find inverse filters, and we will consider using polarizers and multiple views to increase the size of data space.

2.6 Conclusions

Many models of fluorescence microscopes use the monopole and scalar approximations, but complete models need to consider dipole and vector optics effects. In this chapter we have introduced several transfer functions that simplify the mapping between the dipole emission density and the irradiance pattern on the detector. In the upcoming chapters we will calculate these transfer functions for specific instruments and use the results to simulate and analyze data collected by these instruments.

2.7 Appendix: Spherical harmonics and the spherical Fourier transform

The spherical harmonic function of degree ℓ and order $|m| \leq \ell$ is defined as [133]

$$Y_\ell^m(\vartheta, \varphi) = \sqrt{\frac{2\ell+1}{4\pi}} \sqrt{\frac{(\ell-|m|)!}{(\ell+|m|)!}} P_\ell^m(\cos \vartheta) \exp(im\varphi), \quad (2.45)$$

where $P_\ell^m(\cos \vartheta)$ are the associated Legendre polynomials with the Condon–Shortley phase

$$P_\ell^m(x) = (-1)^m (1-x^2)^{|m|/2} \frac{d^{|m|}}{dx^{|m|}} P_\ell(x), \quad (2.46)$$

and $P_\ell(x)$ are the Legendre polynomials defined by the recurrence

$$P_0(x) = 1, \quad (2.47)$$

$$P_1(x) = x, \quad (2.48)$$

$$\ell P_\ell(x) = (2\ell - 1)x P_{\ell-1}(x) - (\ell - 1)P_{\ell-2}(x). \quad (2.49)$$

The spherical harmonics are orthonormal, which means that

$$\int_{\mathbb{S}^2} d\hat{\mathbf{s}} Y_\ell^m(\hat{\mathbf{s}}) Y_{\ell'}^{m'*}(\hat{\mathbf{s}}) = \delta_{\ell\ell'} \delta_{mm'}, \quad (2.50)$$

where $\delta_{\ell\ell'}$ denotes the Kronecker delta. The spherical harmonics form a complete basis for $L_2(\mathbb{S}^2)$, so an arbitrary square-integrable function on the sphere $f(\hat{\mathbf{s}})$ can be expanded into a sum of weighted spherical harmonic functions

$$f(\hat{\mathbf{s}}) = \sum_{\ell=0}^{\infty} \sum_{m=-\ell}^{\ell} F_\ell^m Y_\ell^m(\hat{\mathbf{s}}). \quad (2.51)$$

We can find the spherical harmonic coefficients F_ℓ^m for a given function using Fourier's trick—multiply both sides by $Y_\ell^{m*}(\hat{\mathbf{s}})$, integrate over the sphere, and exploit orthogonality to find that

$$F_\ell^m = \int_{\mathbb{S}^2} d\hat{\mathbf{s}} f(\hat{\mathbf{s}}) Y_\ell^m(\hat{\mathbf{s}}). \quad (2.52)$$

The coefficients F_ℓ^m are called the *spherical Fourier transform* of a spherical function.

We can build an intuition for the spherical harmonics by building several spherical func-

$$Y_{0,0}(\hat{\mathbf{s}}_o) = \text{Red Sphere} \quad Y_{0,0}(\hat{\mathbf{s}}_o) + \frac{1}{8}Y_{2,0}(\hat{\mathbf{s}}_o) = \text{Elliptical Sphere} \quad Y_{0,0}(\hat{\mathbf{s}}_o) - \frac{1}{16}Y_{2,0}(\hat{\mathbf{s}}_o) + \frac{\sqrt{3}}{16}Y_{2,2}(\hat{\mathbf{s}}_o) = \text{Non-rotational Symmetric Sphere}$$

Figure 2.6: Square-integrable functions on the sphere can be written as a weighted sum of spherical harmonics. The $\ell = 0, m = 0$ spherical harmonic can represent a constant function (left), $m = 0$ spherical harmonics can represent rotationally symmetric functions (center), and $m \neq 0$ spherical harmonics can represent non-rotationally symmetric functions (right).

tions from their spherical harmonic components—see Fig. 2.6. We can build a constant function on the sphere with the $\ell = 0, m = 0$ spherical harmonic $Y_{0,0}(\vartheta, \varphi) = \sqrt{1/4\pi}$. The $\ell = 2, m = 0$ spherical harmonic $Y_{2,0}(\vartheta, \varphi) = \sqrt{5/16\pi} (3\cos^2 \vartheta - 1)$ is independent of the azimuthal angle φ , so the function is rotationally symmetric about the $\vartheta = 0$ axis (see the fourth column of the top row of Fig. 2.5). $Y_{2,0}(\vartheta, \varphi)$ is negative for $55^\circ < \vartheta < 125^\circ$, zero for $\vartheta = 55^\circ, 125^\circ$, and positive otherwise. The weighted sum of these two spherical harmonics $Y_{0,0}(\vartheta, \varphi) + \frac{1}{8}Y_{2,0}(\vartheta, \varphi)$ results in a rotationally symmetric function that is relatively large near the $\vartheta = 0$ axis (the poles) and relatively small near $\vartheta = \pi/2$ (the equator). The real-valued $\ell = 2, m = 2$ spherical harmonic $Y_{2,2}(\vartheta, \varphi) = \sqrt{15/16\pi} \sin^2 \vartheta \cos(2\varphi)$ (see Eq. (2.44)) depends on both the polar angle ϑ and the azimuthal angle φ , so it is not a rotationally symmetric function (see the sixth column of the top row of Fig. 2.5). The weighted sum of these three spherical harmonics $Y_{0,0}(\vartheta, \varphi) + \frac{1}{8}Y_{2,0}(\vartheta, \varphi) + \frac{1}{8}Y_{2,2}(\vartheta, \varphi)$ results in a non-rotationally symmetric function that is relatively large near the $\vartheta = 0$ axis (the poles) and the $(\vartheta, \varphi) = (\pi/2, 0)$ axis, and relatively small near the $(\vartheta, \varphi) = (\pi/2, \pi/2)$ axis. By adding spherical harmonics with suitable prefactors, arbitrary square-integrable spherical functions can be built using the spherical harmonics (see Eq. (2.51)).

2.8 Appendix: Spatio-angular dynamics

In this appendix we will demonstrate the calculation of the dipole emission density from a simple underlying dynamic model. Our analysis is related to Stallinga’s [78], but here

we consider an ensemble of dipoles diffusing both spatially and rotationally with homogeneous and isotropic diffusion coefficients. We start by considering a sample with all of its fluorescent molecules in the ground state. At $t = 0$ an instantaneous pulse excites a spatio-angular distribution of dipoles so that the initial condition is given by a known function $f^{(\text{ex})}(\mathbf{r}_o, \hat{\mathbf{s}}_o, t = 0)$. As time evolves, we assume the fluorescent molecules decay at a constant rate $\kappa^{(\text{d})}$, diffuse spatially with a constant coefficient D_R , and diffuse angularly with a constant coefficient D_S so that the dynamics are governed by the partial differential equation

$$\frac{\partial f^{(\text{ex})}(\mathbf{r}_o, \hat{\mathbf{s}}_o, t)}{\partial t} = [-\kappa^{(\text{d})} + D_R \Delta_{\mathbb{R}^3} + D_S \Delta_{\mathbb{S}^2}] f^{(\text{ex})}(\mathbf{r}_o, \hat{\mathbf{s}}_o, t). \quad (2.53)$$

As written this equation is difficult to solve, but in a basis of complex exponentials and spherical harmonics this equation reduces to an ordinary differential equation. We start by expanding $f^{(\text{ex})}(\mathbf{r}_o, \hat{\mathbf{s}}_o, t)$ into its frequency components using

$$f^{(\text{ex})}(\mathbf{r}_o, \hat{\mathbf{s}}_o, t) = \sum_{\ell=0}^{\infty} \sum_{m=-\ell}^{\ell} \int_{\mathbb{R}^3} d\mathbf{v} F_{\ell}^{(\text{ex}),m}(\mathbf{v}, t) \exp[i2\pi\mathbf{v} \cdot \mathbf{r}_o] Y_{\ell}^m(\hat{\mathbf{s}}_o). \quad (2.54)$$

Plugging this expansion into Eq. (2.53) we find that

$$\begin{aligned} & \sum_{\ell=0}^{\infty} \sum_{m=-\ell}^{\ell} \int_{\mathbb{R}^3} d\mathbf{v} \frac{\partial F_{\ell}^{(\text{ex}),m}(\mathbf{v}, t)}{\partial t} \exp[i2\pi\mathbf{v} \cdot \mathbf{r}_o] Y_{\ell}^m(\hat{\mathbf{s}}_o) = \\ & [-\kappa^{(\text{d})} + D_R \Delta_{\mathbb{R}^3} + D_S \Delta_{\mathbb{S}^2}] \sum_{\ell=0}^{\infty} \sum_{m=-\ell}^{\ell} \int_{\mathbb{R}^3} d\mathbf{v} F_{\ell}^{(\text{ex}),m}(\mathbf{v}, t) \exp[i2\pi\mathbf{v} \cdot \mathbf{r}_o] Y_{\ell}^m(\hat{\mathbf{s}}_o). \end{aligned} \quad (2.55)$$

We can simplify this equation using the eigenvectors and eigenvalues of the spatial and spherical Laplacian operators

$$\Delta_{\mathbb{R}^3} \exp[2\pi i \mathbf{v} \cdot \mathbf{r}_o] = -(2\pi |\mathbf{v}|)^3 \exp[2\pi i \mathbf{v} \cdot \mathbf{r}_o], \quad (2.56)$$

$$\Delta_{\mathbb{S}^2} Y_{\ell}^m(\hat{\mathbf{s}}_o) = -\ell(\ell+1) Y_{\ell}^m(\hat{\mathbf{s}}_o), \quad (2.57)$$

to find that

$$\begin{aligned} & \sum_{\ell=0}^{\infty} \sum_{m=-\ell}^{\ell} \int_{\mathbb{R}^3} d\mathbf{v} \frac{\partial F_{\ell}^{(\text{ex}),m}(\mathbf{v}, t)}{\partial t} \exp[i2\pi\mathbf{v} \cdot \mathbf{r}_o] Y_{\ell}^m(\hat{\mathbf{s}}_o) = \\ & \sum_{\ell=0}^{\infty} \sum_{m=-\ell}^{\ell} \int_{\mathbb{R}^3} d\mathbf{v} \left[-\kappa^{(\text{d})} - D_R(2\pi|\mathbf{v}|)^3 - D_S \ell(\ell+1) \right] F_{\ell}^{(\text{ex}),m}(\mathbf{v}, t) \exp[i2\pi\mathbf{v} \cdot \mathbf{r}_o] Y_{\ell}^m(\hat{\mathbf{s}}_o). \end{aligned} \quad (2.58)$$

Comparing both sides we find that

$$\frac{\partial F_{\ell}^{(\text{ex}),m}(\mathbf{v}, t)}{\partial t} = \left[-\kappa^{(\text{d})} - D_R(2\pi|\mathbf{v}|)^3 - D_S \ell(\ell+1) \right] F_{\ell}^{(\text{ex}),m}(\mathbf{v}, t). \quad (2.59)$$

The solution of this equation is given by

$$F_{\ell}^{(\text{ex}),m}(\mathbf{v}, t) = F_{\ell}^{(\text{ex}),m}(\mathbf{v}, 0) \exp[\alpha t], \quad (2.60)$$

where $\alpha = -\kappa^{(\text{d})} - D_R(2\pi|\mathbf{v}|)^3 - D_S \ell(\ell+1)$.

Eq. (2.60) shows that as time evolves the initial spectrum $F_{\ell}^{(\text{ex}),m}(\mathbf{v}, 0)$ decays to the ground state while undergoing an effective decay of the high spatial- and angular-frequency components. In other words, we can interpret diffusion as a filtering operation applied to the spatio-angular spectrum.

$F_{\ell}^{(\text{ex}),m}(\mathbf{v}, t)$ is the excited state spectrum, but we can only detect photons emitted as molecules decay to the ground state during the exposure time t_e . In other words, we can only measure the quantity

$$F_{\ell}^m(\mathbf{v}) = \int_0^{t_e} dt \kappa^{(\text{d})} F_{\ell}^{(\text{ex}),m}(\mathbf{v}, t) = F_{\ell}^{(\text{ex}),m}(\mathbf{v}, 0) \frac{\kappa^{(\text{d})}}{\alpha} \{ \exp[\alpha t_e] - 1 \}. \quad (2.61)$$

The main conclusion of this appendix is that spatial and angular diffusion can be efficiently described in a basis of complex exponentials and spherical harmonics. Although we have only considered homogeneous and isotropic diffusion with constant diffusion coefficients,

the complex exponentials and spherical harmonics can be used to simplify the analysis of inhomogeneous and anisotropic diffusion as well. Stallinga has used the spherical harmonics to model angular diffusion in rotationally symmetric potentials [78], and his approach can be generalized to arbitrary spatial and angular diffusion potentials. We will consider more general angular diffusion models in chapter 4.

CHAPTER 3

PARAXIAL $4f$ IMAGING

I shall speak in round numbers, not absolutely accurate,
yet not so wide from truth as to vary the result materially.

— THOMAS JEFFERSON (1824)

We investigate the properties of a single-view fluorescence microscope in a $4f$ geometry when imaging fluorescent dipoles without using the monopole or scalar approximations. We show that this imaging system has a spatio-angular band limit, and we exploit the band limit to perform efficient simulations. Notably, we show that information about the out-of-plane orientation of ensembles of in-focus fluorophores is recorded by paraxial fluorescence microscopes. Additionally, we show that the monopole approximation may cause biased estimates of fluorophore concentrations, but these biases are small when the sample contains either many randomly oriented fluorophores in each resolvable volume or unconstrained rotating fluorophores.

3.1 Introduction

In the previous chapter we developed a new set of transfer functions that can be used to analyze spatio-angular fluorescence microscopes. In this chapter we will demonstrate these transfer functions by analyzing a single-view fluorescence microscope in a $4f$ geometry.

The central goal of this chapter is to understand how much angular information an unmodified $4f$ microscope transmits to the detector. Fluorescence microscopists know that without structured illumination or single molecule techniques they can only hope to recover spatial frequencies up to the spatial band limit of the optical system $2NA/\lambda$. In this chapter we will find a similar limit for angular frequencies and understand what design factors affect this limit.

A secondary goal of this chapter is to examine the validity of the monopole approximation in fluorescence microscopy. Although many works implicitly apply the monopole approximation, we have encountered two explicit justifications: (1) the sample contains many randomly oriented fluorophores within a resolvable volume or (2) the sample contains unconstrained rotating fluorophores. While both of these situations yield monopole-like emitters, neither yields emitters that are perfectly described by the monopole model. We investigate the dipole model of fluorophores in detail and find the conditions under which the monopole approximation is justified.

We begin in section 3.2 by specifying the imaging geometry and defining *pupil functions* for imaging systems with and without the monopole approximation. We explicitly relate the pupil functions to the coherent transfer functions to establish a connection between physical calculations and the transfer functions. Next, in section 3.3 we calculate the monopole and dipole transfer functions in closed form, and we use these transfer functions to perform efficient simulations with four numerical phantoms. Finally, in section 3.4 we discuss the results and expand on how the pupil functions can be used to develop improved models for spatio-angular microscopes.

3.2 Theory

During our initial modeling we considered an aplanatic optical system imaging a sample of fluorescent emissions—either a monopole emission density, $f(\mathbf{r}_o)$, or a dipole emission density, $f(\mathbf{r}_o, \hat{\mathbf{s}}_o)$ —by recording the scaled irradiance on a two-dimensional detector, $g(\mathbf{r}_d)$. A central result was that we could express the relationship between the object (the emission densities) and the data (the irradiance) as a linear Hilbert-space operator, and we showed that these operators took the form of an integral transform in a delta function basis. In this chapter we will restrict our attention to in-focus objects, so we will split \mathbf{r}_o into \mathbf{r}_o^\perp and r_o^\parallel

Quantity	Symbol	Relationships
Monopole emission density	$f(\mathbf{r}_o^\perp)$	—
Monopole spectrum	$F(\boldsymbol{\nu})$	$= \mathcal{F}_{\mathbb{R}^2} \{ f(\mathbf{r}_o^\perp) \}$
Monopole coherent spread function	$c(\mathbf{r}_d - \mathbf{r}_o^\perp)$	—
Monopole coherent transfer function	$C(\boldsymbol{\tau})$	$= \mathcal{F}_{\mathbb{R}^2} \{ c(\mathbf{r}_d - \mathbf{r}_o^\perp) \}$
Monopole point spread function	$h(\mathbf{r}_d - \mathbf{r}_o^\perp)$	$= c(\mathbf{r}_d - \mathbf{r}_o^\perp) ^2$
Monopole transfer function	$H(\boldsymbol{\nu})$	$= \mathcal{F}_{\mathbb{R}^2} \{ h(\mathbf{r}_d - \mathbf{r}_o^\perp) \}$ $= \int_{\mathbb{R}^2} d\boldsymbol{\tau} C(\boldsymbol{\tau}) C^*(\boldsymbol{\tau} - \boldsymbol{\nu})$
Scaled irradiance	$g(\mathbf{r}_d)$	$= \int_{\mathbb{R}^2} d\mathbf{r}_o^\perp h(\mathbf{r}_d - \mathbf{r}_o^\perp) f(\mathbf{r}_o^\perp)$
Scaled irradiance spectrum	$G(\boldsymbol{\nu})$	$= \mathcal{F}_{\mathbb{R}^2} \{ g(\mathbf{r}_d) \} = H(\boldsymbol{\nu}) F(\boldsymbol{\nu})$

Table 3.1: Summary of relevant quantities for in-focus fluorescence microscopy under the monopole approximation—see chapter 2 for derivations. $\mathcal{F}_{\mathbb{R}^2}$ denotes a two-dimensional Fourier transform.

and set $r_o^\parallel = 0$. For in-focus monopole emissions the integral transform takes the form

$$g(\mathbf{r}_d) = \int_{\mathbb{R}^2} d\mathbf{r}_o^\perp h(\mathbf{r}_d - \mathbf{r}_o^\perp) f(\mathbf{r}_o^\perp), \quad (3.1)$$

where $h(\mathbf{r}_d - \mathbf{r}_o^\perp)$ is the monopole point spread function. For dipole emissions the integral transform takes the form

$$g(\mathbf{r}_d) = \int_{\mathbb{S}^2} d\hat{\mathbf{s}}_o \int_{\mathbb{R}^2} d\mathbf{r}_o^\perp h(\mathbf{r}_d - \mathbf{r}_o^\perp, \hat{\mathbf{s}}_o) f(\mathbf{r}_o^\perp, \hat{\mathbf{s}}_o), \quad (3.2)$$

where $h(\mathbf{r}_d - \mathbf{r}_o^\perp, \hat{\mathbf{s}}_o)$ is the dipole point spread function. Note that we have written Eqs. (3.1) and (3.2) in their demagnified forms. We will use primes to denote the unscaled detector coordinate, \mathbf{r}'_d , and unscaled point spread functions, h' .

After expressing the operators in a delta function basis we explored the form of the operators with several other choices of basis functions. Tables 3.1 and 3.2 summarize our results.

Our task is to calculate the form of the monopole and dipole transfer functions for a

Quantity	Symbol	Relationships
Dipole emission density	$f(\mathbf{r}_o^\perp, \hat{\mathbf{s}}_o)$	—
Dipole spatial spectrum	$F(\boldsymbol{\nu}, \hat{\mathbf{s}}_o)$	$= \mathcal{F}_{\mathbb{R}^2} \{ f(\mathbf{r}_o^\perp, \hat{\mathbf{s}}_o) \}$
Dipole angular spectrum	$F_\ell^m(\mathbf{r}_o^\perp)$	$= \mathcal{F}_{\mathbb{S}^2} \{ f(\mathbf{r}_o^\perp, \hat{\mathbf{s}}_o) \}$
Dipole spatio-angular spectrum	$\mathsf{F}_\ell^m(\boldsymbol{\nu})$	$= \mathcal{F}_{\mathbb{R}^2} \{ F_\ell^m(\mathbf{r}_o^\perp) \} = \mathcal{F}_{\mathbb{S}^2} \{ F(\boldsymbol{\nu}, \hat{\mathbf{s}}_o) \}$
Dipole coherent spread function	$\mathbf{c}(\mathbf{r}_d - \mathbf{r}_o^\perp, \hat{\mathbf{s}}_o)$	—
Dipole coherent transfer function	$\mathbf{C}(\boldsymbol{\tau}, \hat{\mathbf{s}}_o)$	$= \mathcal{F}_{\mathbb{R}^2} \{ \mathbf{c}(\mathbf{r}_d - \mathbf{r}_o^\perp, \hat{\mathbf{s}}_o) \}$
Dipole point spread function	$h(\mathbf{r}_d - \mathbf{r}_o^\perp, \hat{\mathbf{s}}_o)$	$= \mathbf{c}(\mathbf{r}_d - \mathbf{r}_o^\perp, \hat{\mathbf{s}}_o) ^2$
Dipole spatial transfer function	$H(\boldsymbol{\nu}, \hat{\mathbf{s}}_o)$	$= \mathcal{F}_{\mathbb{R}^2} \{ h(\mathbf{r}_d - \mathbf{r}_o^\perp, \hat{\mathbf{s}}_o) \}$ $= \int_{\mathbb{R}^2} d\boldsymbol{\tau} \mathbf{C}(\boldsymbol{\tau}, \hat{\mathbf{s}}_o) \mathbf{C}^\dagger(\boldsymbol{\tau} - \boldsymbol{\nu}, \hat{\mathbf{s}}_o)$
Dipole angular transfer function	$H_\ell^m(\mathbf{r}_d - \mathbf{r}_o^\perp)$	$= \mathcal{F}_{\mathbb{S}^2} \{ h(\mathbf{r}_d - \mathbf{r}_o^\perp, \hat{\mathbf{s}}_o) \}$
Dipole spatio-angular tran. func.	$\mathsf{H}_\ell^m(\boldsymbol{\nu})$	$= \mathcal{F}_{\mathbb{R}^2} \{ H_\ell^m(\mathbf{r}_d - \mathbf{r}_o^\perp) \} = \mathcal{F}_{\mathbb{S}^2} \{ H(\boldsymbol{\nu}, \hat{\mathbf{s}}_o) \}$
Scaled irradiance	$g(\mathbf{r}_d)$	$= \int_{\mathbb{S}^2} d\hat{\mathbf{s}}_o \int_{\mathbb{R}^2} d\mathbf{r}_o^\perp h(\mathbf{r}_d - \mathbf{r}_o^\perp, \hat{\mathbf{s}}_o) f(\mathbf{r}_o^\perp, \hat{\mathbf{s}}_o)$ $= \sum_{\ell m} \int_{\mathbb{R}^2} d\mathbf{r}_o^\perp H_\ell^m(\mathbf{r}_d - \mathbf{r}_o^\perp) F_\ell^m(\mathbf{r}_o^\perp)$
Scaled irradiance spectrum	$G(\boldsymbol{\nu})$	$= \mathcal{F}_{\mathbb{R}^2} \{ g(\mathbf{r}_d) \}$ $= \int_{\mathbb{S}^2} d\hat{\mathbf{s}}_o H(\boldsymbol{\nu}, \hat{\mathbf{s}}_o) F(\boldsymbol{\nu}, \hat{\mathbf{s}}_o)$ $= \sum_{\ell m} \mathsf{H}_\ell^m(\boldsymbol{\nu}) \mathsf{F}_\ell^m(\boldsymbol{\nu})$

Table 3.2: Summary of relevant quantities for in-focus spatio-angular dipole imaging—see chapter 2 for derivations. $\mathcal{F}_{\mathbb{R}^2}$ denotes a two-dimensional Fourier transform, and $\mathcal{F}_{\mathbb{S}^2}$ denotes a spherical Fourier transform.

specific imaging geometry. In this chapter we will consider an aplanatic optical system in a *4f configuration* with an arbitrary first lens (the objective lens) and a *paraxial second lens* (the tube lens) as shown in Fig. 3.1. A lens can be considered paraxial if the angle α between the optical axis of the lens and the marginal ray is small enough that $\sin \alpha \approx \alpha$. As a rule of thumb, non-paraxial effects only become significant when the numerical aperture of a lens exceeds 0.7 [126, ch. 6], but this is only a rough guideline. Commercial microscopes with infinity-corrected objectives can almost always be modeled by considering the tube lens as paraxial.

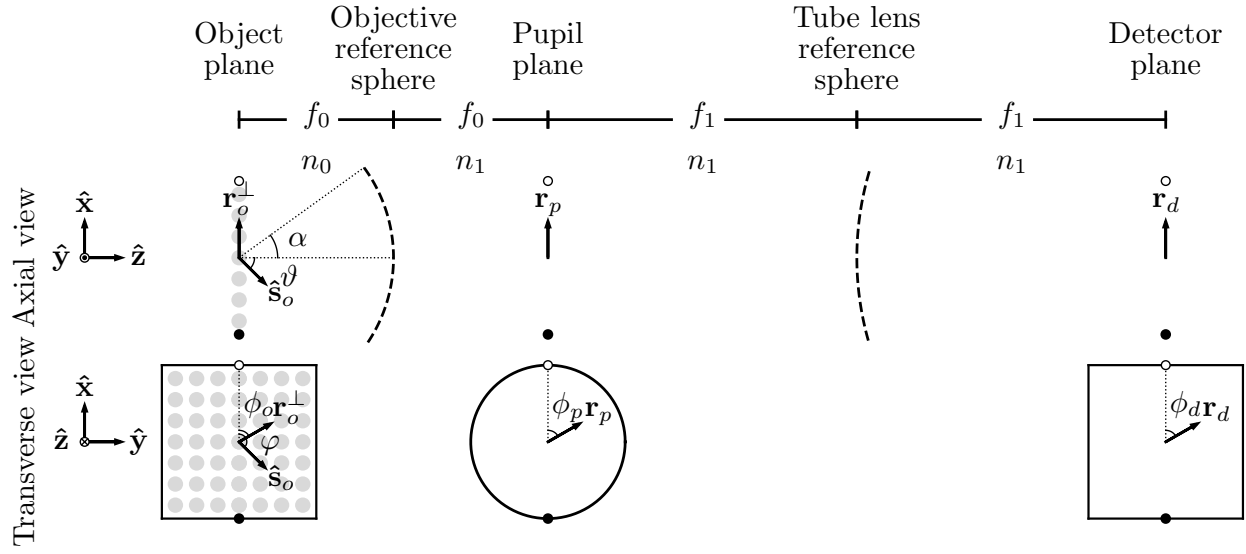


Figure 3.1: Schematic of an aplanatic imaging system in a $4f$ geometry with a paraxial tube lens. We are considering an aplanatic optical system, so we only need to consider the image created by on-axis objects. The fluorescent object consists of ensembles of monopoles or dipoles embedded in a medium with index of refraction n_0 . An objective with focal length f_0 and numerical aperture $\text{NA} = n_0 \sin \alpha$ is trained on the object. A paraxial tube lens with focal length f_1 and a detector complete the $4f$ geometry, and all components except the object are embedded in a medium with index of refraction n_1 . The object, pupil, and detector planes are parameterized by vectors \mathbf{r}_o^\perp , \mathbf{r}_p , and \mathbf{r}_d with polar coordinates (r_o, ϕ_o) , (r_p, ϕ_p) , and (r_d, ϕ_d) , respectively. At each position \mathbf{r}_o^\perp in the object there is a sphere parameterized by a unit vector $\hat{\mathbf{s}}_o$ with spherical coordinates (ϑ, φ) .

3.2.1 Monopole pupil functions

We define the *monopole pupil function* $p(\mathbf{r}_p)$ of the imaging system as the field immediately following the pupil plane created by an on-axis monopole, where \mathbf{r}_p is an unscaled two-dimensional coordinate in the pupil plane. In this section we will relate the monopole pupil function to the monopole transfer functions by adapting the treatment in Barrett and Myers [1, ch. 9.7].

Since monopoles emit scalar fields, the monopole pupil function is a scalar-valued function. The optical system is aplanatic, so we can write the field, $U_p(\mathbf{r}_p, \mathbf{r}_o^\perp)$, created at a point

in the pupil plane \mathbf{r}_p by a monopole at position \mathbf{r}_o^\perp as

$$U_p(\mathbf{r}_p, \mathbf{r}_o^\perp) \propto p(\mathbf{r}_p) \exp \left[-2\pi i \frac{n_0}{\lambda f_0} \mathbf{r}_p \cdot \mathbf{r}_o^\perp \right], \quad (3.3)$$

where λ is the emission wavelength, and f_0 is the focal length of the objective. Equation (3.3) is a restatement of the aplanatic condition for a $4f$ optical system—the fields in the pupil plane can be written as the pupil function multiplied by a linear phase factor that encodes the position of the object.

Since the second lens is paraxial, we can model the relationship between the field in the pupil plane and the field on the detector with a scaled Fourier transform [80, 134, 135]:

$$U_d(\mathbf{r}'_d, \mathbf{r}_o^\perp) \propto \int_{\mathbb{R}^2} d\mathbf{r}_p p(\mathbf{r}_p) \exp \left[-2\pi i \frac{n_0}{\lambda f_0} \mathbf{r}_p \cdot \mathbf{r}_o^\perp \right] \exp \left[-2\pi i \frac{n_1}{\lambda f_1} \mathbf{r}_p \cdot \mathbf{r}'_d \right], \quad (3.4)$$

where \mathbf{r}'_d is an unscaled detector coordinate, and f_1 is the focal length of the tube lens.

If we define $P(\boldsymbol{\tau})$ as the two-dimensional Fourier transform of the pupil function then we can rewrite Eq. (3.4) as

$$U_d(\mathbf{r}'_d, \mathbf{r}_o^\perp) \propto P \left(\frac{n_0}{\lambda f_0} \mathbf{r}_o^\perp + \frac{n_1}{\lambda f_1} \mathbf{r}'_d \right), \quad (3.5)$$

which we can simplify further by writing in terms of the magnification $m = -\frac{f_1 n_0}{f_0 n_1}$:

$$U_d(\mathbf{r}'_d - m \mathbf{r}_o^\perp) \propto P \left(\frac{n_1}{\lambda f_1} [\mathbf{r}'_d - m \mathbf{r}_o^\perp] \right). \quad (3.6)$$

The irradiance on the detector is the absolute square of the field so

$$h'(\mathbf{r}'_d - m \mathbf{r}_o^\perp) \propto \left| P \left(\frac{n_1}{\lambda f_1} [\mathbf{r}'_d - m \mathbf{r}_o^\perp] \right) \right|^2. \quad (3.7)$$

If we demagnify the coordinates with $\mathbf{r}_d = \mathbf{r}'_d/m$ and demagnify the irradiance with

$h(\mathbf{r}_d - \mathbf{r}_o^\perp) \propto h'(m[\mathbf{r}_d - \mathbf{r}_o^\perp])$, we find that the monopole point spread function is related to the Fourier transform of the monopole pupil function by

$$h(\mathbf{r}_d - \mathbf{r}_o^\perp) \propto \left| P\left(-\frac{n_o}{\lambda f_o} [\mathbf{r}_d - \mathbf{r}_o^\perp]\right) \right|^2. \quad (3.8)$$

The monopole point spread function is the absolute square of the monopole coherent spread function so

$$c(\mathbf{r}_d - \mathbf{r}_o^\perp) \propto P\left(-\frac{n_o}{\lambda f_o} [\mathbf{r}_d - \mathbf{r}_o^\perp]\right). \quad (3.9)$$

Finally, the monopole coherent transfer function is the Fourier transform of the monopole coherent spread function so

$$C(\boldsymbol{\tau}) \propto p\left(\frac{\lambda f_o}{n_o} \boldsymbol{\tau}\right). \quad (3.10)$$

Equation (3.10) is the key result of this section—the monopole coherent transfer function is a scaled monopole pupil function.

3.2.2 Dipole pupil function

We define the *dipole pupil function* $\mathbf{p}(\mathbf{r}_p, \hat{\mathbf{s}}_o)$ of the imaging system as the electric field immediately following the pupil plane created by an on-axis dipole oriented along $\hat{\mathbf{s}}_o$. Since dipoles emit vector-valued electric fields, the dipole pupil function is a vector-valued function. Almost all of the arguments in the previous section carry over to the dipole case. Briefly, we can write the electric field created at a point in the pupil \mathbf{r}_p by a dipole at \mathbf{r}_o^\perp oriented along $\hat{\mathbf{s}}_o$ as

$$\mathbf{E}_p(\mathbf{r}_p, \mathbf{r}_o^\perp, \hat{\mathbf{s}}_o) \propto \mathbf{p}(\mathbf{r}_p, \hat{\mathbf{s}}_o) \exp\left[-2\pi i \frac{n_0}{\lambda f_0} \mathbf{r}_p \cdot \mathbf{r}_o^\perp\right]. \quad (3.11)$$

The second lens is paraxial, so we can find the field on the detector with a Fourier transform

$$\mathbf{E}_d(\mathbf{r}'_d, \mathbf{r}_o^\perp, \hat{\mathbf{s}}_o) \propto \int_{\mathbb{R}^2} d\mathbf{r}_p \mathbf{p}(\mathbf{r}_p, \hat{\mathbf{s}}_o) \exp \left[-2\pi i \frac{n_0}{\lambda f_0} \mathbf{r}_p \cdot \mathbf{r}_o^\perp \right] \exp \left[-2\pi i \frac{n_1}{\lambda f_1} \mathbf{r}_p \cdot \mathbf{r}'_d \right]. \quad (3.12)$$

Note that the Fourier transform of a vector field is the Fourier transform of its scalar-valued orthogonal components, so Eq. (3.12) specifies three two-dimensional Fourier transforms. We follow the same manipulations as the previous section and find that the dipole coherent transfer function is a scaled dipole pupil function

$$\mathbf{C}(\boldsymbol{\tau}, \hat{\mathbf{s}}_o) \propto \mathbf{p} \left(\frac{\lambda f_o}{n_o} \boldsymbol{\tau}, \hat{\mathbf{s}}_o \right). \quad (3.13)$$

We have restricted our analysis to paraxial tube lenses, but non-paraxial tube lenses (or a non-infinity-corrected objective) can be modeled with vector-valued three-dimensional pupil functions [126, 136–138].

3.2.3 Special functions

We adopt and generalize Bracewell’s notation [139] for several special functions which will simplify our calculations. First, we define a *rectangle function* as

$$\Pi(x) = \begin{cases} 1 & \text{if } |x| < \frac{1}{2}, \\ 0 & \text{else.} \end{cases} \quad (3.14)$$

We also define the n^{th} -order *jinc function* as

$$\text{jinc}_n(r) = \frac{J_{n+1}(\pi r)}{2r}, \quad (3.15)$$

where $J_{n+1}(r)$ is the $(n + 1)^{th}$ -order Bessel function of the first kind.

Although the rectangle and jinc functions are defined in one dimension, we will usually apply them in two dimensions. In Appendix 3.6 we derive the following two-dimensional Fourier transform relationships between the jinc functions and the weighted rectangle functions

$$i^n \begin{Bmatrix} \exp(in\phi_r) \\ \cos(n\phi_r) \\ \sin(n\phi_r) \end{Bmatrix} \text{jinc}_n(r) \xrightarrow{\mathcal{F}_{\mathbb{R}^2}} (2\nu)^n \begin{Bmatrix} \exp(in\phi_\nu) \\ \cos(n\phi_\nu) \\ \sin(n\phi_\nu) \end{Bmatrix} \Pi(\nu), \quad (3.16)$$

where the entries inside the curly braces are to be taken one at a time and $\{r, \phi_r\}/\{\nu, \phi_\nu\}$ are conjugate sets of polar coordinates.

Finally, we define the n^{th} -order *chat function* as the two-dimensional Fourier transform of the squared n^{th} -order jinc function

$$\text{jinc}_n^2(r) \xrightarrow{\mathcal{F}_{\mathbb{R}^2}} \text{chat}_n(\nu). \quad (3.17)$$

In Appendix 3.6 we show that the zeroth- and first-order chat functions can be written in closed form as

$$\text{chat}_0(x) = \frac{1}{2} \left[\cos^{-1}|x| - |x|\sqrt{1-x^2} \right] \Pi\left(\frac{x}{2}\right), \quad (3.18)$$

$$\text{chat}_1(x) = \frac{1}{2} \left[\cos^{-1}|x| - |x|(3-2x^2)\sqrt{1-x^2} \right] \Pi\left(\frac{x}{2}\right). \quad (3.19)$$

3.3 Results

3.3.1 Monopole transfer functions

Our first step towards the monopole transfer functions is to calculate the monopole pupil function and coherent transfer function. Several works [140, 141] have modeled an aplanatic

fluorescence microscope imaging monopole emitters with the scalar pupil function

$$p(\mathbf{r}_p) \propto \tilde{C} \left(\frac{r_p}{f_o} \right) \Pi \left(\frac{r_p}{2f_o \sin \alpha} \right), \quad (3.20)$$

where

$$\tilde{C}(x) = (1 - x^2)^{-1/4} = 1 + \frac{x^2}{4} + \frac{5x^4}{32} + \dots \quad (3.21)$$

The $\tilde{C}(x)$ function models the radial dependence of the field and ensures that power is conserved on either side of an aplanatic objective, and the rectangle function models the aperture stop of the objective. Applying Eq. (3.10) and collecting constants we find that the coherent monopole transfer function is

$$C(\boldsymbol{\tau}) \propto \tilde{C} \left(\frac{2\text{NA}}{n_o} \frac{\tau}{\nu_c} \right) \Pi \left(\frac{\tau}{\nu_c} \right), \quad (3.22)$$

where $\text{NA} = n_o \sin \alpha$ and $\nu_c = 2\text{NA}/\lambda$. This coherent transfer function models objectives with an arbitrary numerical aperture, but for our initial analysis we restrict ourselves to the paraxial regime. We drop second- and higher-order radial terms to find that

$$C(\boldsymbol{\tau}) \stackrel{(p)}{\propto} \Pi \left(\frac{\tau}{\nu_c} \right), \quad (3.23)$$

where (p) indicates that we have used the paraxial approximation for the objective lens.

We can find the monopole coherent spread function by taking the inverse Fourier transform of the monopole coherent transfer function

$$c(\mathbf{r}) \stackrel{(p)}{\propto} \text{jinc}_0(\nu_c r). \quad (3.24)$$

The monopole point spread function is the (normalized) absolute square of the monopole

coherent spread function so

$$h(\mathbf{r}) \stackrel{(p)}{=} \frac{4}{\pi} \text{jinc}_0^2(\nu_c r), \quad (3.25)$$

which is the well-known *Airy disk*.

Finally, we can calculate the monopole transfer function as the two-dimensional Fourier transform of the monopole point spread function (or the autocorrelation of the coherent transfer function) and find that

$$H(\boldsymbol{\nu}) \stackrel{(p)}{=} \frac{4}{\pi} \text{chat}_0\left(\frac{\nu}{\nu_c}\right). \quad (3.26)$$

3.3.2 Dipole transfer functions

To calculate the dipole transfer function we proceed similarly to the monopole case—we find the pupil function, scale to find the coherent dipole transfer function, then calculate the remaining transfer functions.

Several works [71, 72, 80] have calculated the dipole pupil function for a high-NA objective. Using Backer and Moerner’s notation we find that the dipole pupil function is given by

$$\mathbf{p}(\mathbf{r}_p, \hat{\mathbf{s}}_o) \propto \begin{bmatrix} \tilde{C}_0\left(\frac{r_p}{f_o}\right) + \tilde{C}_2\left(\frac{r_p}{f_o}\right)c(2\phi_p) & \tilde{C}_2\left(\frac{r_p}{f_o}\right)s(2\phi_p) & \tilde{C}_1\left(\frac{r_p}{f_o}\right)c(\phi_p) \\ \tilde{C}_2\left(\frac{r_p}{f_o}\right)s(2\phi_p) & \tilde{C}_0\left(\frac{r_p}{f_o}\right) - \tilde{C}_2\left(\frac{r_p}{f_o}\right)c(2\phi_p) & \tilde{C}_1\left(\frac{r_p}{f_o}\right)s(\phi_p) \\ 0 & 0 & 0 \end{bmatrix} \begin{bmatrix} s_x \\ s_y \\ s_z \end{bmatrix} \Pi\left(\frac{r_p}{2f_o s(\alpha)}\right), \quad (3.27)$$

where $c(x)$ and $s(x)$ are shorthand for $\cos(x)$ and $\sin(x)$, $\{s_x, s_y, s_z\}$ are the Cartesian

components of $\hat{\mathbf{s}}_o$ when $\hat{\mathbf{z}}$ is aligned with the optical axis, and

$$\tilde{C}_0(x) = \frac{1}{2} \left(\sqrt{1-x^2} + 1 \right) (1-x^2)^{-1/4} = 1 + \frac{x^4}{32} + \frac{x^6}{32} + \dots, \quad (3.28)$$

$$\tilde{C}_1(x) = x(1-x^2)^{-1/4} = x + \frac{x^3}{4} + \frac{5x^5}{32} + \dots, \quad (3.29)$$

$$\tilde{C}_2(x) = \frac{1}{2} \left(\sqrt{1-x^2} - 1 \right) (1-x^2)^{-1/4} = -\frac{x^2}{4} - \frac{x^4}{8} - \frac{11x^6}{128} - \dots. \quad (3.30)$$

Similar to the monopole case, the dipole pupil function conserves power and has a cutoff at the objective aperture, but the dipole pupil function is vector-valued to model the complete electric field in the pupil plane.

Scaling the dipole pupil function using Eq. (3.13) yields the dipole coherent transfer function

$$\mathbf{C}(\tau, \hat{\mathbf{s}}_o) \propto \begin{bmatrix} \tilde{C}_0\left(\frac{\lambda r_p \tau}{n_0}\right) + \tilde{C}_2\left(\frac{\lambda r_p \tau}{n_0}\right)c(2\phi_\tau) & \tilde{C}_2\left(\frac{\lambda r_p \tau}{n_0}\right)s(2\phi_\tau) & \tilde{C}_1\left(\frac{\lambda r_p \tau}{n_0}\right)c(\phi_\tau) \\ \tilde{C}_2\left(\frac{\lambda r_p \tau}{n_0}\right)s(2\phi_\tau) & \tilde{C}_0\left(\frac{\lambda r_p \tau}{n_0}\right) - \tilde{C}_2\left(\frac{\lambda r_p \tau}{n_0}\right)c(2\phi_\tau) & \tilde{C}_1\left(\frac{\lambda r_p \tau}{n_0}\right)s(\phi_\tau) \\ 0 & 0 & 0 \end{bmatrix} \begin{bmatrix} s_x \\ s_y \\ s_z \end{bmatrix} \Pi\left(\frac{\tau}{\nu_c}\right). \quad (3.31)$$

We restrict our analysis to the paraxial regime of the objective lens by dropping second- and higher-order radial terms to find that

$$\mathbf{C}(\tau, \hat{\mathbf{s}}_o) \stackrel{(p)}{\propto} \begin{bmatrix} 1 & 0 & \frac{2\text{NA}}{n_o} \frac{\tau}{\nu_c} \cos \phi_\tau \\ 0 & 1 & \frac{2\text{NA}}{n_o} \frac{\tau}{\nu_c} \sin \phi_\tau \\ 0 & 0 & 0 \end{bmatrix} \begin{bmatrix} s_x \\ s_y \\ s_z \end{bmatrix} \Pi\left(\frac{\tau}{\nu_c}\right). \quad (3.32)$$

Under the paraxial approximation applied to the objective lens the transverse components of the dipole $\{s_x, s_y\}$ create purely parallel fields in the pupil plane and the axial component of the dipole $\{s_z\}$ creates purely radial fields in the pupil plane. Applying the paraxial approximation to the objective lens may seem crude compared to Backer and Moerner's

numerical results, but the approximation will allow us to calculate the transfer functions in closed form so that we can build an intuition for the limits of the microscope. We also note that many existing works in ensemble polarized fluorescence microscopy make stronger approximations than ours. For example, Fourkas only considers the total irradiance in the pupil plane while ignoring the propagation of fields to the detector [63].

The dipole coherent spread function is the inverse Fourier transform of the dipole coherent transfer function. Applying Eq. (3.16) in reverse yields

$$\mathbf{c}(\mathbf{r}, \hat{\mathbf{s}}_o) \stackrel{(p)}{\propto} \begin{bmatrix} \text{jinc}_0(\nu_c r) & 0 & \frac{\text{NA}}{n_o} i \cos \phi \text{jinc}_1(\nu_c r) \\ 0 & \text{jinc}_0(\nu_c r) & \frac{\text{NA}}{n_o} i \sin \phi \text{jinc}_1(\nu_c r) \\ 0 & 0 & 0 \end{bmatrix} \begin{bmatrix} s_x \\ s_y \\ s_z \end{bmatrix}. \quad (3.33)$$

Notice that the radial component of the dipole coherent spread function has a $\pi/2$ phase shift relative to the parallel component. This phase factor arises because the Fourier transform of a real and odd function is purely imaginary.

Paraxial dipole point spread function

The dipole point spread function is the (normalized) absolute square of the coherent dipole spread function

$$h(\mathbf{r}, \hat{\mathbf{s}}_o) \propto \mathbf{c}(\mathbf{r}, \hat{\mathbf{s}}_o) \mathbf{c}^\dagger(\mathbf{r}, \hat{\mathbf{s}}_o). \quad (3.34)$$

Plugging in the paraxial dipole coherent spread function and normalizing yields

$$h(\mathbf{r}, \hat{\mathbf{s}}_o) \stackrel{(p)}{=} N \left[\text{jinc}_0^2(\nu_c r) \sin^2 \vartheta + \left(\frac{\text{NA}}{n_o} \right)^2 \text{jinc}_1^2(\nu_c r) \cos^2 \vartheta \right], \quad (3.35)$$

where $\sin^2 \vartheta = s_x^2 + s_y^2$, $\cos^2 \vartheta = s_z^2$, and the normalization factor is

$$N = 6\nu_c^2\pi^{-3/2} \left[2 + \left(\frac{\text{NA}}{n_o} \right)^2 \right]^{-1}. \quad (3.36)$$

As discussed above, the parallel and radial fields are out of phase on the detector, so the total irradiance is the sum of the contributions from the parallel and radial components. In Fig. 3.2 we plot the dipole point spread function for several dipole orientations and numerical apertures, and in Fig. 3.3 we compare the monopole point spread function to the dipole point spread function. The paraxial monopole and dipole models are only equivalent when the sample consists of transverse dipoles, which is clear if we notice that Eq. (3.35) reduces to an Airy disk when $\vartheta = \pi/2$ —see Novotny and Hecht for a similar observation [73, ch. 4].

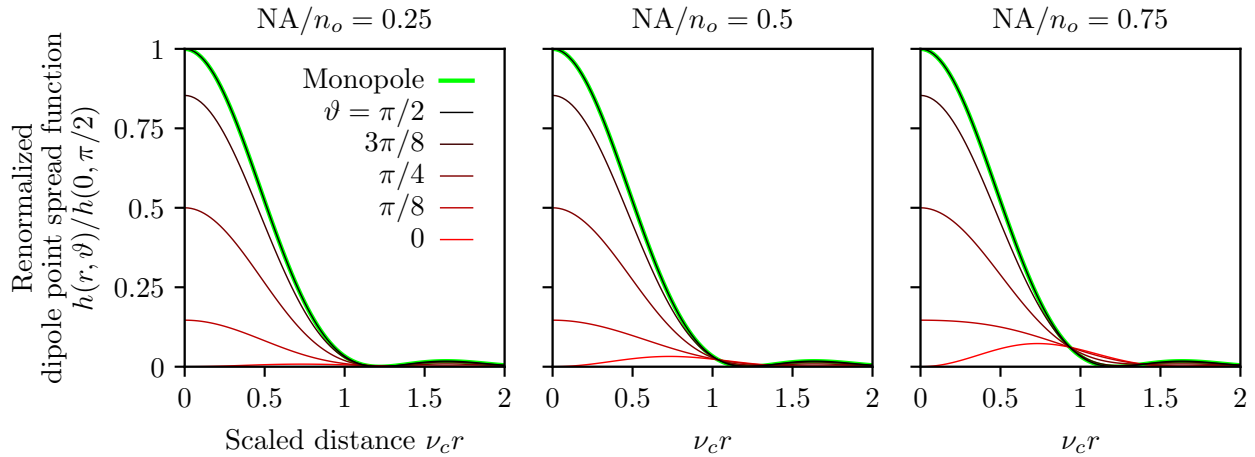


Figure 3.2: Renormalized paraxial dipole point spread function as a function of the scaled radial coordinate ν_{cr} , the dipole inclination angle ϑ , and NA/n_o . For small numerical apertures (left) the irradiance pattern created by axial dipoles (red) is small compared to transverse dipoles (black), but the relative contribution of axial dipoles increases with the numerical aperture (see red lines from left to right). Additionally, we plot the monopole point spread function (green) and observe that the paraxial monopole and dipole models are identical for transverse dipoles (the green and black lines are coincident).

All of the figures in this chapter use the paraxial approximation applied to the objective lens. We estimated the error introduced by this approximation by numerically calculating the dipole point spread function using the exact pupil function in Eq. (3.27) and

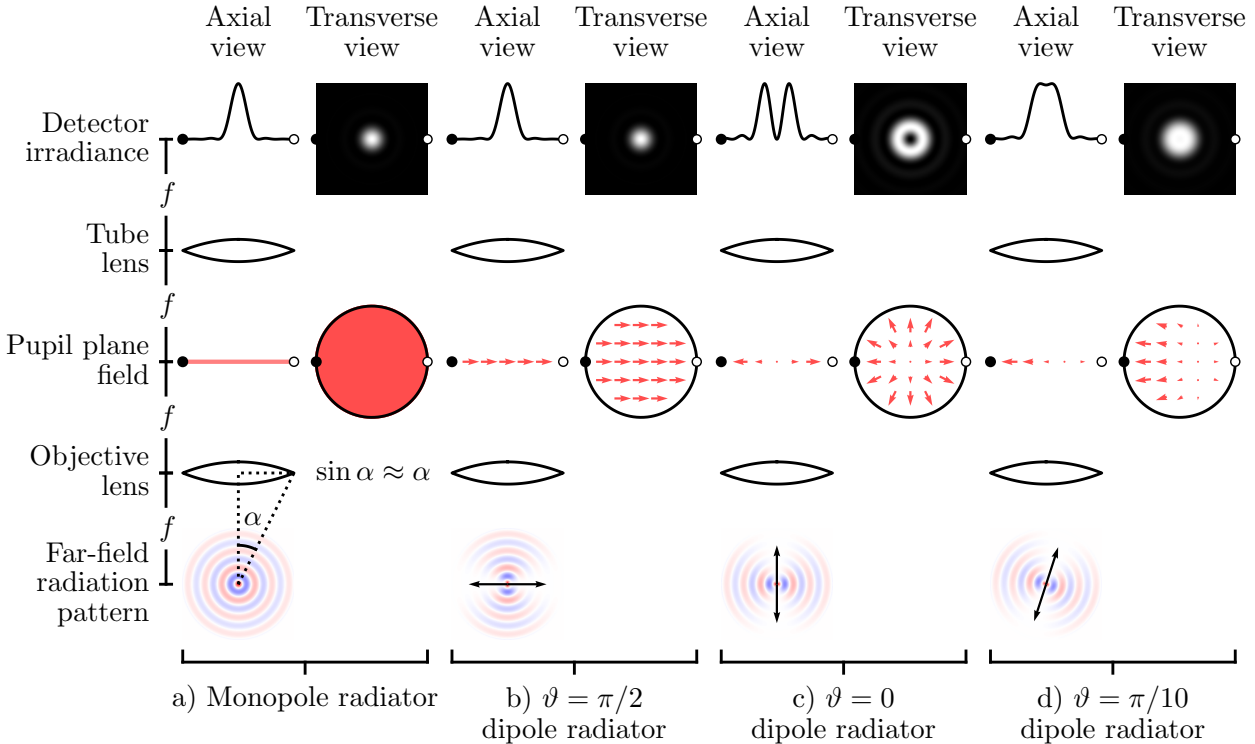


Figure 3.3: Comparison of paraxial models for monopole radiators a) and dipole radiators b)–d). a) Monopole radiators fill the pupil plane with a uniform scalar field which gives rise to an Airy disk on the detector. b) A transverse dipole radiator also creates an Airy disk, but the pupil plane is filled with a uniform vector field. c) An axial dipole radiator creates a radial electric field pattern in the back focal plane that creates a $jinc_1^2(r)$ pattern on the detector. d) Dipoles that are not transverse or axial still create radially symmetric irradiance patterns under the paraxial approximation. Fields from transverse dipoles are real and even while fields from axial dipoles are real and odd, which causes a relative $\pi/2$ phase shift for the fields on the detector. This phase shift means that the fields from transverse and axial components of the dipole do not interfere, which causes radially symmetric irradiance patterns.

comparing the result to the analytic dipole point spread function in Eq. (3.35). We found that the maximum irradiance error (root mean square irradiance error) in the image plane for $NA/n_o = 0.25, 0.5$ and 0.75 was $1\%(0.02\%)$, $5\%(0.05\%)$, and $12\%(0.12\%)$, respectively. Although the paraxial approximation introduces relatively large errors in the fields near the edge of the pupil function, the irradiance errors are modest for $NA/n_o < 0.75$ because the paraxial pupil function is accurate near the optical axis, every point in the pupil contributes

to the irradiance, and the irradiance is the absolute square of fields. However, note that the paraxial approximation introduces increasingly large errors as NA/n_o approaches 1. Additionally, the paraxial approximation on the objective imposes radial symmetry on the dipole point spread function. This radial symmetry is approximate, and the symmetry disappears for high-NA objectives.

To demonstrate the paraxial dipole point spread function we simulate a set of equally spaced dipoles with varying orientation:

$$f_{(ph1)}(r_x, r_y, \vartheta, \varphi) = \sum_{j=0}^3 \sum_{k=0}^3 \delta(r_x - j) \delta(r_y - k) \delta(\cos \vartheta - \cos \vartheta_j) \delta(\varphi - \varphi_k), \quad (3.37)$$

where $\vartheta_j = j\frac{\pi}{6}$, $\varphi_k = k\frac{\pi}{4}$, the subscript $(ph1)$ indicates that this is the first phantom, and the spatial coordinates are expressed in μm . To find the irradiance pattern created by the phantom we plug Eq. (3.37) into Eq. (3.2) and use the sifting property to find that

$$g_{(ph1)}(r_x, r_y) = \sum_{j=0}^3 \sum_{k=0}^3 h\left(\sqrt{(r_x - j)^2 + (r_y - k)^2}, \vartheta_j\right). \quad (3.38)$$

In Fig. 3.4 we plot the phantom and scaled irradiance for an imaging system with $\text{NA} = 0.75$, $\lambda = 500 \text{ nm}$, and $n_o = 1.33$. For these parameters the maximum irradiance error introduced by the paraxial approximation is 6%. We sample and plot the scaled irradiance at $20 \times$ the Nyquist rate, $\Delta x = 1/[20(2\nu_c)]$, so the irradiance patterns are free of aliasing. The output demonstrates that the irradiance pattern depends on the dipole inclination, but not its azimuth.

Paraxial dipole spatial transfer function

The dipole spatial transfer function is the spatial Fourier transform of the dipole point spread function (or the complex autocorrelation of the dipole coherent transfer function). Applying

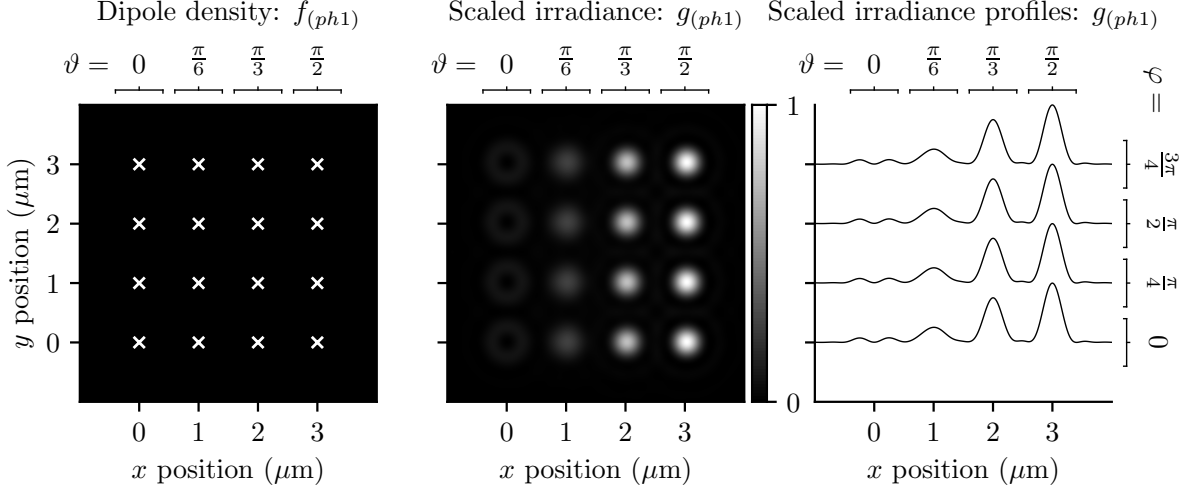


Figure 3.4: **Left:** A spatially and angularly sparse phantom—uniformly spaced single dipoles with varying orientations (increasing ϑ from left to right and increasing φ from bottom to top). White crosses mark the positions of the dipoles. **Center:** Scaled irradiance for an imaging system with $\text{NA} = 0.75$, $\lambda = 500 \text{ nm}$, and $n_o = 1.33$ sampled at $20\times$ the Nyquist rate. **Right:** x profiles through the scaled irradiance. The response is independent of the azimuth angle and strongly dependent on the inclination angle.

the Fourier transform to Eq. (3.35) we find that

$$H(\boldsymbol{\nu}, \vartheta) \stackrel{(p)}{=} \frac{N}{\nu_c^2} \left[\text{chat}_0 \left(\frac{\nu}{\nu_c} \right) \sin^2 \vartheta + \left(\frac{\text{NA}}{n_o} \right)^2 \text{chat}_1 \left(\frac{\nu}{\nu_c} \right) \cos^2 \vartheta \right]. \quad (3.39)$$

In Fig. 3.5 we plot the dipole spatial transfer function for several dipole orientations and numerical apertures. We find that the dipole spatial transfer function is negative for axial dipoles at high spatial frequencies, especially for larger numerical apertures. The negative dipole spatial transfer function corresponds to a contrast inversion for high-frequency patterns of axial dipoles because the irradiance minimum corresponds to the position of the dipole.

To demonstrate the dipole spatial transfer function we simulate a set of equally spaced disks with varying diameter containing fluorophores with varying orientation

$$f_{(ph2)}(r_x, r_y, \vartheta) = \sum_{j=0}^3 \sum_{k=0}^3 \frac{1}{D_k^2} \Pi \left(\frac{1}{D_k} \sqrt{(r_x - j)^2 + (r_y - k)^2} \right) \delta (\cos \vartheta - \cos \vartheta_j) \quad (3.40)$$

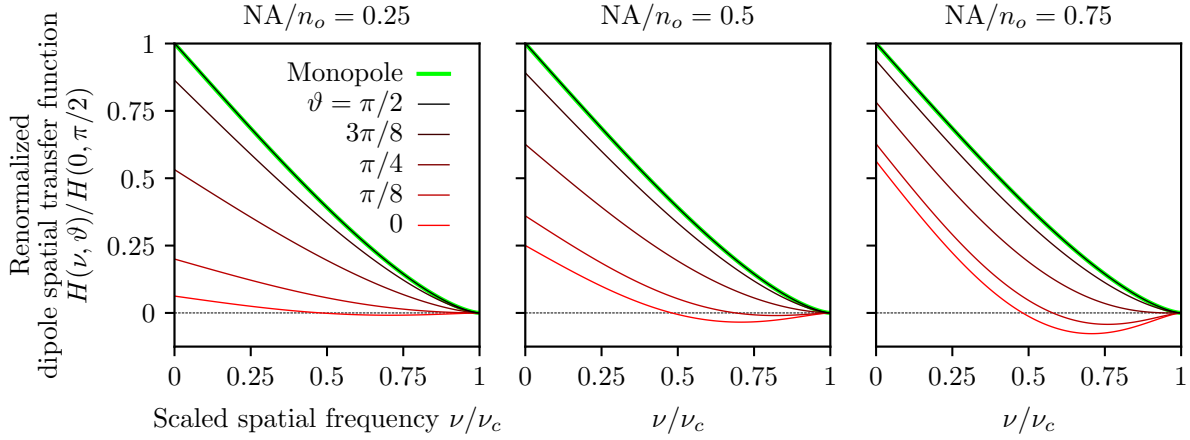


Figure 3.5: Dipole spatial transfer function as a function of the scaled spatial frequency ν/ν_c , the dipole inclination angle ϑ , and NA/n_o . For small numerical apertures (left) the dipole spatial transfer function for axial dipoles (red) is small compared to transverse dipoles (black), but the relative contribution of axial dipoles increases with the numerical aperture (see red lines from left to right). The spatial dipole transfer function of axial dipoles is negative at high spatial frequencies because the central minimum of the axial dipole point spread function corresponds to the position of the dipole. Equivalently, a high-spatial-frequency pattern of axial dipoles will generate an irradiance pattern where the minimum irradiance corresponds to the peak of the axial dipole emission density. Additionally, we plot the monopole transfer function (green) and observe that the paraxial monopole and dipole models are identical for transverse dipoles (the green and black lines are coincident).

where $D_k = 0.15(1 + k) \mu\text{m}$ and $\vartheta_j = j\frac{\pi}{6}$. Notice that we have scaled the disks so that the total number of fluorophores in each disk is constant. Also notice that the disk can model a spatial distribution of many fluorophores or a single molecule undergoing spatial diffusion within a well.

We can calculate the scaled irradiance by taking the spatial Fourier transform of each orientation in the phantom, multiplying the result with the dipole spatial transfer function, summing over the orientations, then taking the inverse spatial Fourier transform

$$g_{(ph2)}(r_x, r_y) = \mathcal{F}_{\mathbb{R}^2}^{-1} \left\{ \sum_j H(\nu, \vartheta_j) \mathcal{F}_{\mathbb{R}^2} \left\{ f_{(ph2)}(r_x, r_y, \vartheta_j) \right\} \right\}. \quad (3.41)$$

In Fig. 3.6 we plot the phantom and scaled irradiance with the same imaging parameters as the previous section. The small disks create irradiance patterns that are similar to the

point sources in the previous section, while larger disks create increasingly uniform irradiance patterns that hide the orientation of the fluorophores.

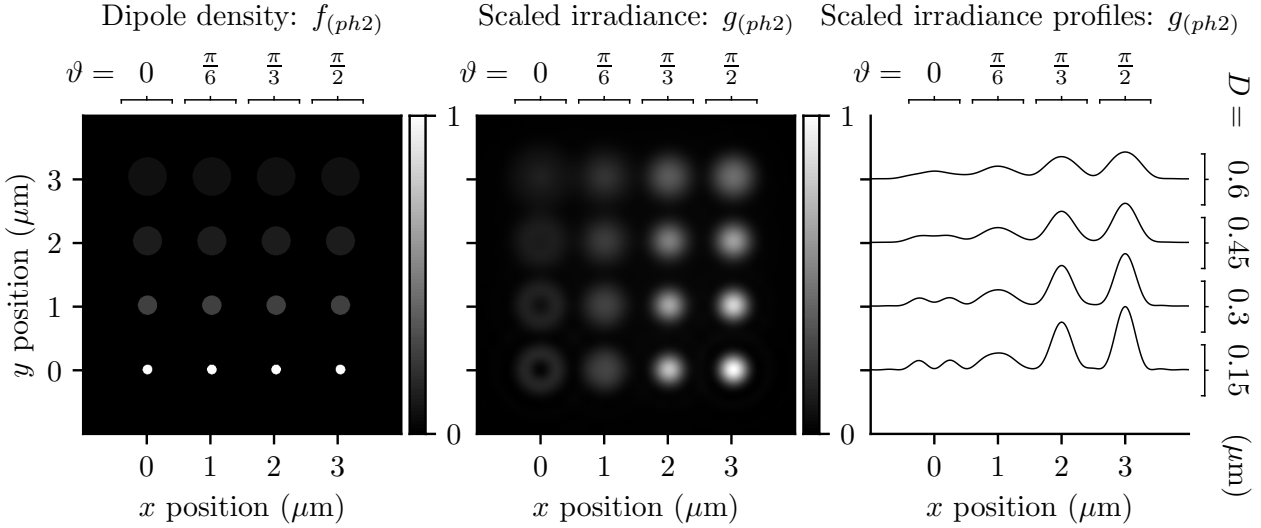


Figure 3.6: **Left:** A spatially dense and angularly sparse phantom—uniformly spaced disks with varying size (increasing D from bottom to top) and dipole orientation (increasing ϑ from left to right) **Center:** Scaled irradiance for an imaging system with $\text{NA} = 0.75$, $\lambda = 500 \text{ nm}$, and $n_o = 1.33$ sampled at $20\times$ the Nyquist rate. **Right:** x profiles through the scaled irradiance. Larger disks generate increasingly uniform irradiance patterns with fewer details that may indicate the orientation of fluorophores.

Paraxial dipole angular transfer function

To calculate the angular dipole transfer function we take the spherical Fourier transform of the dipole point spread function

$$H_l^m(\mathbf{r}) = \int_{\mathbb{S}^2} d\hat{\mathbf{s}}_o h(\mathbf{r}, \hat{\mathbf{s}}_o) Y_l^{m*}(\hat{\mathbf{s}}_o). \quad (3.42)$$

After evaluating the integrals and normalizing, the angular dipole transfer function is

$$\begin{aligned} H_l^m(\mathbf{r}) &\stackrel{(p)}{=} \frac{N}{3} \left[2\text{jinc}_0^2(\nu_c r) + \left(\frac{\text{NA}}{n_o} \right)^2 \text{jinc}_1^2(\nu_c r) \right] \Lambda_0 \delta_{\ell 0} \delta_{m0} + \\ &\quad \frac{N}{3} \left[-2\text{jinc}_0^2(\nu_c r) + 2 \left(\frac{\text{NA}}{n_o} \right)^2 \text{jinc}_1^2(\nu_c r) \right] \Lambda_2 \delta_{\ell 2} \delta_{m0}, \end{aligned} \quad (3.43)$$

where $\Lambda_\ell = \sqrt{4\pi/(2\ell+1)}$. Notice that the dipole angular transfer function only has two non-zero terms that correspond to $m = 0$ spherical harmonics. These spherical harmonics are rotationally symmetric about the optical axis, and this symmetry is imposed by the paraxial approximation. When the paraxial approximation is not applied to low-NA imaging systems, the higher-order m terms will be very small. As the NA increases, the relative size of the higher-order m terms increases. The root mean square error introduced by the paraxial approximation is conserved under a change of basis, so the paraxial approximation introduces a 0.02%, 0.05%, 0.12% RMS error for $\text{NA}/n_o = 0.25, 0.5$ and 0.75 , respectively.

In Fig. 3.7 we plot the dipole angular transfer function for both spherical harmonic terms and several numerical apertures. Note that the dipole angular transfer function can be negative because the spherical harmonics can take negative values. The $\ell = 0$ term shows that angularly uniform distributions of dipoles create spatial irradiance patterns that are similar but not identical to the Airy disk, while the $\ell = 2$ term shows a negative pattern because of the large contribution of the transverse negative values in the Y_2^0 spherical harmonic.

To demonstrate the dipole angular transfer function we simulate a set of equally spaced fluorophore distributions with varying orientation and angular distributions

$$f_{(ph3)}(r_x, r_y, \vartheta) = \sum_{j=0}^3 \sum_{k=0}^3 \delta(r_x - j) \delta(r_y - k) f_{(\text{cone})}(\vartheta, \varphi; \vartheta_j, 0, \Delta_k), \quad (3.44)$$

where

$$f_{(\text{cone})}(\hat{\mathbf{s}}_o; \hat{\mathbf{s}}'_o, \Delta) = f_{(\text{cone})}(\vartheta, \varphi; \vartheta', \varphi', \Delta) = \frac{1}{4\pi(1 - \cos \Delta)} \Pi\left(\frac{\hat{\mathbf{s}} \cdot \hat{\mathbf{s}}'}{2 \cos \Delta}\right) \quad (3.45)$$

is an angular double cone distribution with central direction $\hat{\mathbf{s}}'$ and cone half-angle Δ ; $\vartheta_j = j\frac{\pi}{6}$; and $\Delta_k = k\frac{\pi}{6}$. Notice that when $\Delta = 0$ the angular double cone reduces to a single direction, and when $\Delta = \pi/2$ the angular double cone reduces to an angularly uniform distribution. Also notice that the double cone can model angular diffusion or the angular

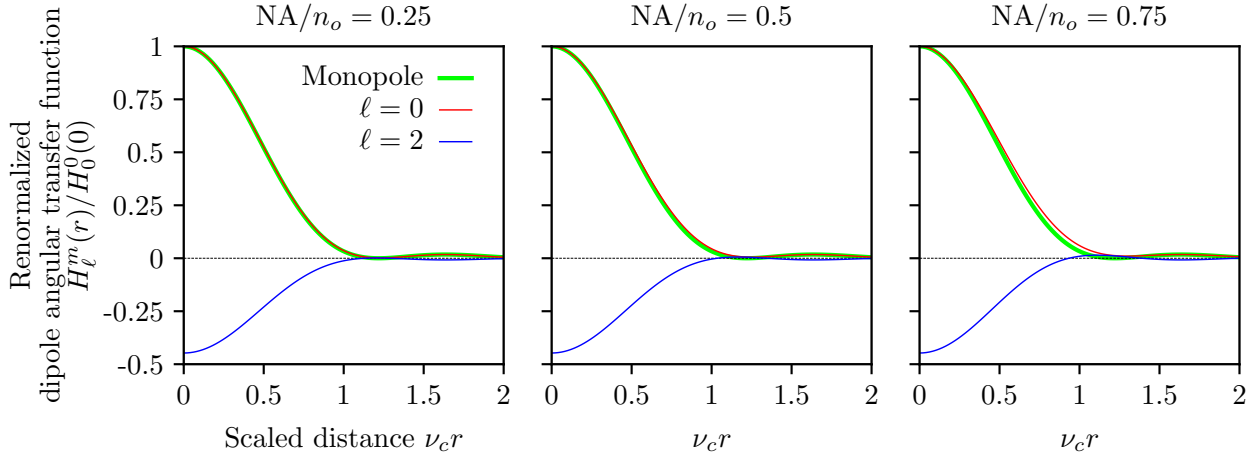


Figure 3.7: Paraxial dipole angular transfer function in terms of a scaled radial detection coordinate ν_cr , the spherical harmonic degree ℓ , and NA/n_o . Angularly uniform distributions of dipoles $\ell = 0$ generate a spatial pattern that is similar but not identical to the Airy disk created by a monopole (green), and this discrepancy increases with the numerical aperture. $\ell = 2$ distributions have a negative response because $Y_2^0(\hat{s})$ is negative for transverse directions. As the numerical aperture increases, the relative contribution of positive axial dipoles in the $\ell = 2$ distribution increases.

distribution of many fluorophores within a resolvable volume.

Our first step towards the irradiance pattern is to calculate the dipole angular spectrum of the phantom. In Appendix 3.7 we calculate the spherical Fourier transform of the double cone distribution $F_{\ell,(\text{cone})}^m(\vartheta', \varphi'; \Delta)$ which we can use to express the dipole angular spectrum as

$$F_{\ell,(ph3)}^m(r_x, r_y, \vartheta) = \sum_{j=0}^3 \sum_{k=0}^3 \delta(r_x - j) \delta(r_y - k) F_{\ell,(\text{cone})}^m(\vartheta_j, 0, \Delta_k). \quad (3.46)$$

To calculate the scaled irradiance we multiply the dipole angular spectrum by the dipole angular transfer function and sum over the dipoles and spherical harmonics

$$g_{(ph3)}(r_x, r_y) = \sum_{\ell m} \sum_{j=0}^3 \sum_{k=0}^3 H_\ell^m \left(\sqrt{(r_x - j)^2 + (r_y - k)^2} \right) F_{\ell,(\text{cone})}^m(\vartheta_j, 0, \Delta_k). \quad (3.47)$$

In Fig. 3.8 we plot the phantom and scaled irradiance with the same imaging parameters

as the previous sections. For small cone angles the irradiance patterns are similar to the point sources in the previous sections, while larger cone angles create increasingly uniform irradiance patterns that hide the angular information about the distributions.

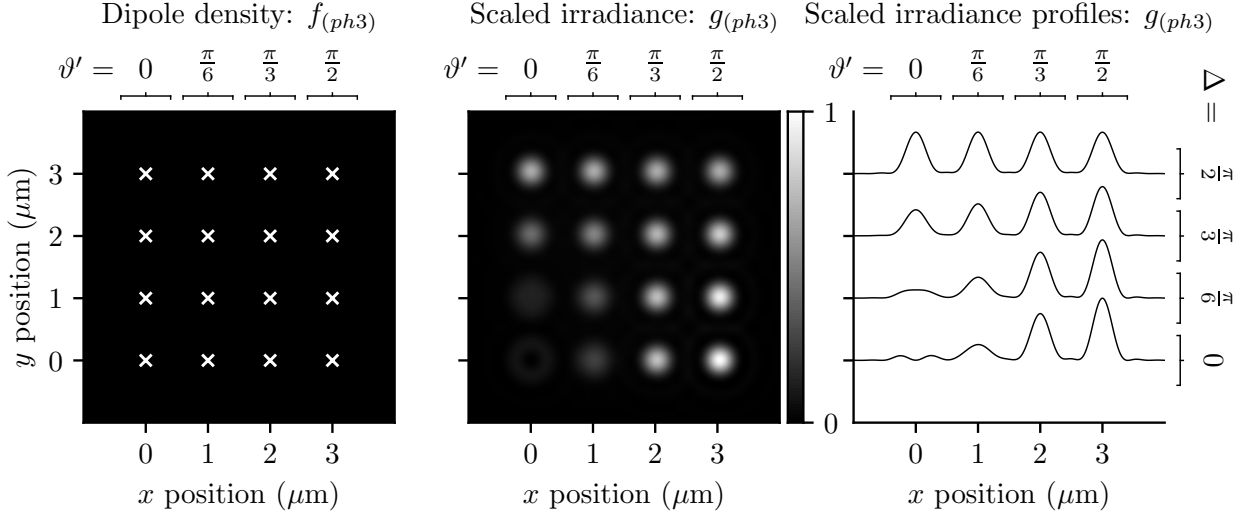


Figure 3.8: **Left:** A spatially sparse and angularly dense phantom—uniformly spaced double cone distributions of fluorophores with varying central direction (increasing ϑ' from left to right) and varying cone half-angle (increasing Δ from bottom to top). **Center:** Scaled irradiance for an imaging system with $\text{NA} = 0.75$, $\lambda = 500 \text{ nm}$, and $n_o = 1.33$ sampled at $20\times$ the Nyquist rate. **Right:** x profiles through the scaled irradiance. Small cone angles have irradiance patterns that vary with the central direction, while larger cones angles have increasingly uniform irradiance patterns that hide angular information.

Paraxial dipole spatio-angular transfer function

We can calculate the dipole spatio-angular transfer function by taking the spatial Fourier transform of the dipole angular transfer function (or the spherical Fourier transform of the dipole spatial transfer function) to find that

$$\begin{aligned} H_\ell^m(\nu) &\stackrel{(p)}{=} \frac{N}{3\nu_c^2} \left[2\text{chat}_0\left(\frac{\nu}{\nu_c}\right) + \left(\frac{\text{NA}}{n_o}\right)^2 \text{chat}_1\left(\frac{\nu}{\nu_c}\right) \right] \Lambda_0 \delta_{\ell 0} \delta_{m 0} + \\ &\quad \frac{N}{3\nu_c^2} \left[-2\text{chat}_0\left(\frac{\nu}{\nu_c}\right) + 2\left(\frac{\text{NA}}{n_o}\right)^2 \text{chat}_1\left(\frac{\nu}{\nu_c}\right) \right] \Lambda_2 \delta_{\ell 2} \delta_{m 0}. \end{aligned} \quad (3.48)$$

In Fig. 3.9 we plot the dipole spatio-angular transfer function for both spherical harmonic terms and several numerical apertures. The $\ell = 0$ term shows that an angularly uniform distribution of dipoles has a transfer function that is similar but not identical to the monopole transfer function with high frequencies increasingly suppressed as the numerical aperture increases. The $\ell = 2$ term shows a negative pattern because of the large contribution of the transverse negative values in the Y_2^0 spherical harmonic. As the numerical aperture increases the relative contribution of the positive axial values increases and the $\ell = 2$ term becomes less negative.

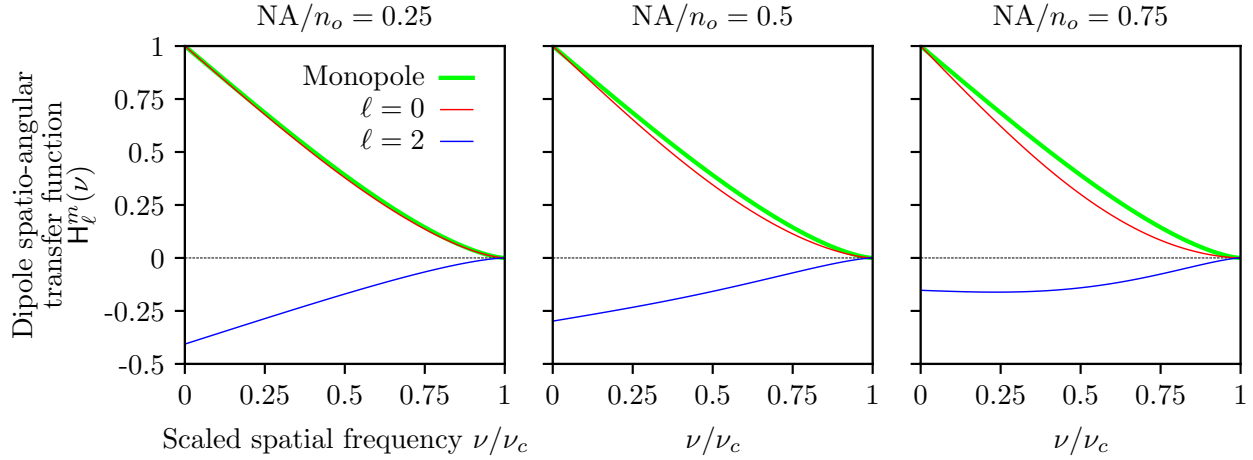


Figure 3.9: Spatio-angular dipole transfer function as a function of the scaled spatial frequency ν/ν_c , the spherical harmonic degree ℓ , and NA/n_o . When the numerical aperture is small the transverse dipoles contribute the most to the signal which gives rise to a positive $\ell = 0$ component and a negative $\ell = 2$ component. As the numerical aperture increases, the relative contribution of axial dipoles increases and the $\ell = 2$ component becomes less negative. Additionally, we plot the monopole transfer function (green) and observe that the $\ell = 0$ term is similar but not identical to the monopole transfer function, and this discrepancy increases with the numerical aperture.

To demonstrate the spatio-angular transfer function, we simulate a set of equally spaced disks of fluorophores with varying radius and angular distributions

$$f_{(ph4)}(r_x, r_y, \vartheta, \varphi) = \sum_{j=0}^3 \sum_{k=0}^3 \frac{1}{D_k^2} \Pi \left(\frac{1}{D_k} \sqrt{(r_x - j)^2 + (r_y - k)^2} \right) f_{(\text{cone})} \left(\vartheta, \varphi; \frac{\pi}{2}, 0, \Delta_j \right), \quad (3.49)$$

where $D_k = 0.15(1 + k) \mu\text{m}$, and $\Delta_j = j\frac{\pi}{6}$.

Our first step towards calculating the irradiance pattern is to calculate the dipole spatio-angular spectrum given by the spatial Fourier transform of the dipole angular spectrum

$$\mathcal{F}_{\ell,(ph4)}^m(\nu_x, \nu_y) = \mathcal{F}_{\mathbb{R}^2} \left\{ \sum_{j=0}^3 \sum_{k=0}^3 \frac{1}{D_k^2} \Pi \left(\frac{1}{D_k} \sqrt{(r_x - j)^2 + (r_y - k)^2} \right) F_{\ell,\text{cone}}^m \left(\frac{\pi}{2}, 0, \Delta_j \right) \right\}. \quad (3.50)$$

To calculate the scaled irradiance we multiply the dipole spatio-angular spectrum by the dipole spatio-angular transfer function, sum over the spherical harmonics, then take an inverse Fourier transform

$$g_{(ph4)}(r_x, r_y) = \mathcal{F}_{\mathbb{R}^2}^{-1} \left\{ \sum_{\ell m} H_{\ell}^m(\nu_x, \nu_y) \mathcal{F}_{\ell,(ph4)}^m(\nu_x, \nu_y) \right\}. \quad (3.51)$$

In Fig. 3.10 we plot the phantom and scaled irradiance with the same imaging parameters as the previous sections. Small cone angles and small disks create relatively unique irradiance patterns, while increasing the cone angle or disk size creates increasingly similar irradiance patterns.

3.4 Discussion

3.4.1 Interpreting the spherical harmonics

Before we interpret the spherical harmonics it is worthwhile to review the interpretation of complex exponentials in monopole fluorescence imaging. We can think of complex exponential functions $\exp[i2\pi\mathbf{r}_o^\perp \cdot \boldsymbol{\nu}]$ as functions on the plane with coordinates \mathbf{r}_o^\perp indexed by spatial frequencies $\boldsymbol{\nu}$. Complex exponentials with small spatial frequencies $|\boldsymbol{\nu}|$ can be used to build smooth functions, and complex exponentials with higher spatial frequencies can be added to build sharp edge-like functions. Note that the complex exponentials themselves do not have

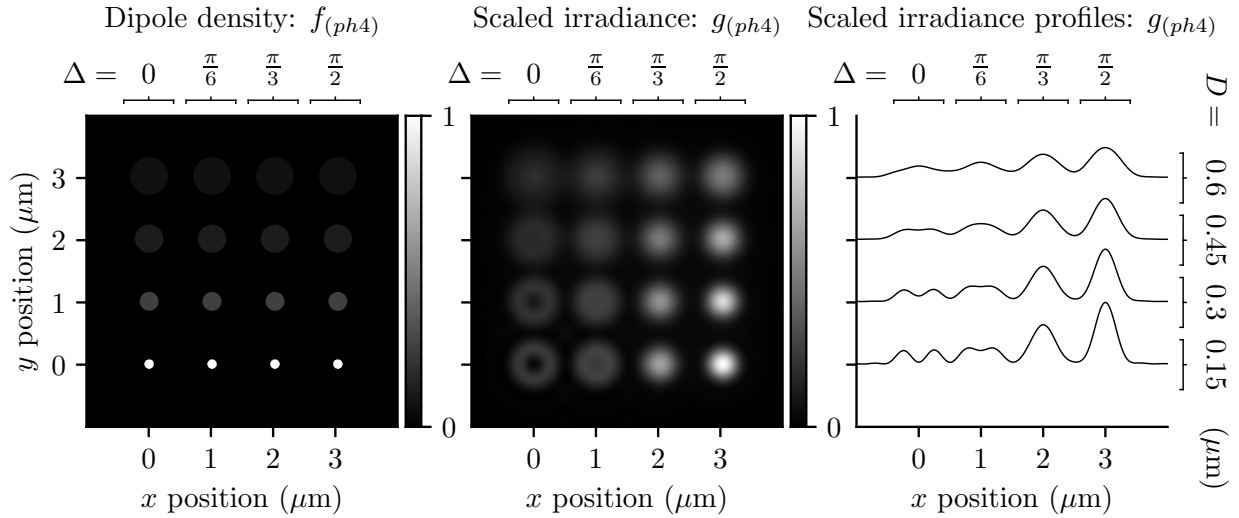


Figure 3.10: **Left:** A spatially and angularly dense phantom—uniformly spaced disks with varying size (increasing D from bottom to top) and double cone half angle (increasing Δ from left to right) **Center:** Scaled irradiance for an imaging system with $\text{NA} = 0.75$, $\lambda = 500 \text{ nm}$, and $n_o = 1.33$ sampled at $20\times$ the Nyquist rate. **Right:** x profiles through the scaled irradiance.

a direct physical interpretation—they are purely a mathematical convenience for efficiently describing and interpreting imaging systems. A direct physical interpretation would require us to interpret negative- and complex-valued “densities”. However, each complex exponential component of the emission density creates a single physically interpretable plane wave that propagates through the imaging system. This indirect physical interpretation of the complex exponentials is valuable for building an intuition for the effects of pupil apertures and phase masks.

Similarly, the spherical harmonics $Y_\ell^m(\hat{\mathbf{s}}_o)$ are functions on the sphere with coordinates $\hat{\mathbf{s}}_o$ indexed by angular frequencies ℓ and m . Spherical harmonics with small ℓ can be used to build smooth spherical functions (for example the $\ell = 0$ spherical harmonic is a constant function), and spherical harmonics with higher ℓ can be added to build sharp edge-like spherical functions. Spherical harmonics with $m = 0$ (the zonal harmonics) can be used to build spherical functions that are rotationally symmetric about the optical axis, and spherical harmonics with non-zero m can be used to build non-rotationally symmetric functions. Once

again, the spherical harmonics do not have a direct physical interpretation, but they are useful for efficiently describing and interpreting angular imaging systems.

A single spatio-angular component of the dipole emission density (parameterized by a spatial frequency ν and angular frequency ℓ and m) creates a single plane wave that propagates through the imaging system along a path in accordance with its spatial frequency. When multiple angular components are present at a single spatial frequency, each angular component contributes a plane wave traveling along the same path through the imaging system. We emphasize that this interpretation is indirect—the complex exponentials and spherical harmonics do not have a direct physical interpretation.

3.4.2 What determines the angular bandwidth?

Spatial imaging systems have a spatial bandwidth that characterizes the highest spatial frequency that the system can transfer between object and data space. Similarly, angular imaging systems have an angular bandwidth that characterizes the highest angular frequency that the system can transfer, but in the angular case there are two different types of angular bandwidths that we call the ℓ - and m -bandwidth. The ℓ -bandwidth can be interpreted in a similar way to the spatial bandwidth—it characterizes the smallest angular features that the imaging system can measure. The m -bandwidth does not have a direct analog in the spatial domain—it characterizes the angular uniformity of the imaging system. If the ℓ - and m -bandwidths are equal then the imaging system can be said to have an *isotropic angular bandwidth*.

The spatial bandwidth of a fluorescence microscope is well known to be $\nu_c = 2\text{NA}/\lambda$. In other words, we can increase the spatial resolution of a fluorescence microscope by increasing the NA of the instrument or by choosing a fluorophore with a shorter emission wavelength. Similarly, the angular bandwidth of a fluorescence microscope depends on both the instrument and the choice of fluorophore.

The paraxial microscope we considered in this chapter has an ℓ -bandwidth of $\ell_c = 2$ and an m -bandwidth of $m_c = 0$, so it does not have an isotropic angular bandwidth. The ℓ -bandwidth of the imaging system is constant for dipole imaging systems because dipole radiators only emit in the $\ell = 0$ and $\ell = 2$ bands. Increasing the ℓ -bandwidth requires us to use quadrupole/higher-order emitters [142], structured/polarized illumination [39, 115], or multi-photon excitation [55]. The m -bandwidth of the imaging system is 0 for paraxial microscopes because these imaging systems are only sensitive to the inclination angle of dipoles. Therefore, paraxial microscopes only transfer information about dipole emission distributions that are rotationally symmetric about the optical axis. Increasing the m -bandwidth requires a non-paraxial optical system or polarizers in the illumination/detection path.

3.4.3 Comparing monopole and dipole models

The only case when the dipole and monopole transfer functions match exactly is when the sample consists of dipoles that are completely constrained to the transverse plane of a paraxial imaging system. Dipole radiators that do not lie in the transverse plane are not well described by the monopole approximation, and the monopole approximation is worst for axial dipoles (see Fig. 3).

Applying the monopole approximation to dipoles that are not constrained to the transverse plane can lead to biased estimates of the fluorophore concentrations. To see how these biases manifest, consider the irradiance pattern created by a disk of dipoles oriented along the optic axis—see Figs. 3.6 or 3.10. Any reconstruction scheme that uses the monopole approximation would attribute the irradiance pattern created by a disk of axially oriented dipoles to a lower concentration of monopoles, which is a clear example of a biased estimate caused by model mismatch.

However, the common justifications for the monopole approximation—that the fluo-

rophores are rotationally unconstrained or that there are many randomly oriented fluorophores in a resolvable volume—are good approximations. In both of these cases the irradiance contribution from axial dipoles is small compared to the contribution from transverse dipoles, and the irradiance patterns are very similar to the pattern created by a monopole (within 5% at $\text{NA}/n_0 = 0.75$ —compare the $\ell = 0$ line to the monopole line in Fig. 7).

3.4.4 Towards more realistic models

The theoretical model we presented in this chapter is an extreme simplification of a real microscope. We have ignored the effects of thick samples, refractive-index mismatch, aberration, scattering, and interactions between fluorophores among others. Because of this long list of unconsidered effects, real experiments will likely require extensions of the models developed here.

The dipole pupil function provides the simplest way to create more realistic models from the simple model in this chapter. Phase aberrations can be added to the dipole pupil function with Zernike polynomials, and refractive index boundaries can be modeled by applying the work of Gibson and Lanni to the dipole pupil function [122]. These additions will model phase aberrations, but modeling polarization aberrations will also be necessary, and we anticipate that vector Zernike polynomials and the Jones pupil [143–145] will be essential tools for modeling dipole imaging systems. We will use the dipole pupil function to include the effects of non-paraxial objectives, polarizers, and defocus in subsequent chapters.

The dipole pupil function also provides an enormous set of design opportunities. The dipole imaging problem may benefit from spatially varying diattenuating and birefringent masks [76, 81]—a much larger set of possibilities than the well-explored design space of amplitude and phase masks [70, 74, 80, 81, 146–148]. The dipole pupil function is a step towards Green’s tensor engineering [116], and the dipole transfer functions provide a strong framework for evaluating dipole imaging designs.

In the simple case considered here we focused on the emission path of the microscope, but the excitation path is equally important. Complete models will need to consider the spatio-angular dependence of excitation. Zhenghao et al. [115] have taken steps in this direction by considering polarized structured illumination microscopy. Rotational dynamics and the fluorescence lifetime are also important to consider when incorporating models of the excitation process [76, 84, 85].

Finally, we have only considered incoherent dipole radiators in this chapter, but coherent dipole radiators have been modeled in detail by Khadir et al. [149]. We expect that extensions of the dipole transfer functions will help simplify and generalize the coherent dipole radiation point response function, especially when multiple coherent dipole radiators are considered.

3.5 Conclusions

We have calculated the monopole and dipole transfer functions for paraxial $4f$ imaging systems and demonstrated these transfer functions with efficient simulations. We have found that dipole radiators have an angular frequency cutoff of $\ell_c = 2$, and paraxial imaging systems have an angular frequency cutoff of $m_c = 0$. We also found that the monopole and scalar approximations are good approximations when the sample consists of unconstrained rotating fluorophores or many randomly oriented fluorophores within a resolvable volume. Finally, we found that dipole and vector optics effects become larger as rotational order increases, and in these cases the dipole transfer functions become valuable tools.

3.6 Appendix: Relationships between special functions

Our first task is to show that

$$i^n \begin{Bmatrix} \exp(in\phi_r) \\ \cos(n\phi_r) \\ \sin(n\phi_r) \end{Bmatrix} \text{jinc}_n(r) \xrightarrow{\mathcal{F}_{\mathbb{R}^2}} (2\nu)^n \begin{Bmatrix} \exp(in\phi_\nu) \\ \cos(n\phi_\nu) \\ \sin(n\phi_\nu) \end{Bmatrix} \Pi(\nu). \quad (3.52)$$

Writing the inverse Fourier transform in polar coordinates yields

$$= 2^n \int_0^{1/2} d\nu \nu^{n+1} \int_0^{2\pi} d\phi_\nu \begin{Bmatrix} \exp(in\phi_\nu) \\ \cos(n\phi_\nu) \\ \sin(n\phi_\nu) \end{Bmatrix} \exp[2\pi i\nu r \cos(\phi_\nu - \phi_r)]. \quad (3.53)$$

The azimuthal integral can be evaluated in terms of an n^{th} order Bessel function (for the complex case see [1, ch. 4.111]).

$$= 2^n 2\pi i^n \begin{Bmatrix} \exp(in\phi_r) \\ \cos(n\phi_r) \\ \sin(n\phi_r) \end{Bmatrix} \int_0^{1/2} d\nu \nu^{n+1} J_n(2\pi\nu r). \quad (3.54)$$

We can use the following identity [150, ch. 6.561-5]

$$\int_0^1 du u^{n+1} J_n(au) = a^{-1} J_{n+1}(a) \quad (3.55)$$

with a change of variable $u = 2\nu$ to find the final result

$$\begin{aligned} &= 2^n 2\pi i^n \begin{Bmatrix} \exp(in\phi_r) \\ \cos(n\phi_r) \\ \sin(n\phi_r) \end{Bmatrix} \int_0^1 \frac{du}{2} \left(\frac{u}{2}\right)^{n+1} J_n(\pi ur) = i^n \begin{Bmatrix} \exp(in\phi_r) \\ \cos(n\phi_r) \\ \sin(n\phi_r) \end{Bmatrix} \frac{J_{n+1}(\pi r)}{2r} \\ &= i^n \begin{Bmatrix} \exp(in\phi_r) \\ \cos(n\phi_r) \\ \sin(n\phi_r) \end{Bmatrix} \text{jinc}_n(r). \end{aligned} \quad (3.56)$$

We can use the relationship in Eq. (3.52) to express the chat functions in terms of a complex autocorrelation—see the diagram in Fig. 3.11. Starting with the definition of the

$$\begin{array}{ccc}
i^n \exp[in\phi_r] \text{jinc}_n(r) & \xrightarrow{|\cdot|^2} & \text{jinc}_n^2(r) \\
\downarrow \mathcal{F}_{\mathbb{R}^2} & & \downarrow \mathcal{F}_{\mathbb{R}^2} \\
(2\tau)^n \exp[in\phi_\tau] \Pi(\tau) & \xrightarrow{\star_2} & \text{chat}_n(\nu)
\end{array}$$

Figure 3.11: The relationships between special functions. The chat functions are defined as the two-dimensional Fourier transform of the squared jinc functions, and they can be calculated with the two-dimensional complex autocorrelations (denoted by \star_2) of the complex-weighted rectangle functions.

n^{th} -order chat function

$$\text{chat}_n(\nu) = \int_{\mathbb{R}^2} d\mathbf{r} \text{jinc}_n^2(|\mathbf{r}|) \exp[-2\pi i \mathbf{r}\nu], \quad (3.57)$$

we can rewrite the integrand in terms of the absolute square of a simpler function with a known Fourier transform

$$\text{chat}_n(\nu) = \int_{\mathbb{R}^2} d\mathbf{r} |t_n(\mathbf{r})|^2 \exp[-2\pi i \mathbf{r}\nu]. \quad (3.58)$$

$$t_n(\mathbf{r}) = i^n \exp[in\phi_r] \text{jinc}_n(r). \quad (3.59)$$

Now we can apply the autocorrelation theorem to rewrite the Fourier transform as

$$\text{chat}_n(\nu) = \int_{\mathbb{R}^2} d\boldsymbol{\tau} T_n(\boldsymbol{\tau}) T_n^*(\boldsymbol{\tau} - \nu), \quad (3.60)$$

where the function to be autocorrelated can be found with the help of Eq. (3.52)

$$T_n(\boldsymbol{\tau}) = \int_{\mathbb{R}^2} d\mathbf{r} t_n(\mathbf{r}) \exp[-2\pi i \mathbf{r} \cdot \boldsymbol{\tau}] = (2\tau)^n \exp[in\phi_\tau] \Pi(\tau). \quad (3.61)$$

It will be more convenient to set up the autocorrelation in Cartesian coordinates

$$T_n(\tau) = 2^n (\tau_x + i\tau_y)^n \Pi\left(\sqrt{\tau_x^2 + \tau_y^2}\right). \quad (3.62)$$

Plugging Eq. (3.62) into Eq. (3.60) gives

$$\text{chat}_n(\nu) = 4^n \int_{\mathbb{R}^2} d\tau (\tau_x^2 + \tau_y^2 - \nu\tau_x)^n \Pi\left(\sqrt{\tau_x^2 + \tau_y^2}\right) \Pi\left(\sqrt{(\tau_x - \nu)^2 + \tau_y^2}\right). \quad (3.63)$$

We can interpret the autocorrelation as an integral over a region of overlap between a circle centered at the origin and a circle shifted to the right by ν (a geometric lens). Using the construction in Fig. 3.12 we can express this region as

$$\begin{aligned} \text{chat}_n(\nu) &= 4^{n+1} \left[\int_0^{1/2} \tau d\tau \int_0^{\cos^{-1} \nu} d\phi_\tau (\tau^2 - \nu\tau \cos \phi_\tau)^n - \right. \\ &\quad \left. \int_0^{\nu/2} d\tau_x \int_0^{\frac{\tau_x}{\nu} \sqrt{1-\nu^2}} d\tau_y (\tau_x^2 + \tau_y^2 - \nu\tau_x)^n \right] \Pi\left(\frac{\nu}{2}\right). \end{aligned} \quad (3.64)$$

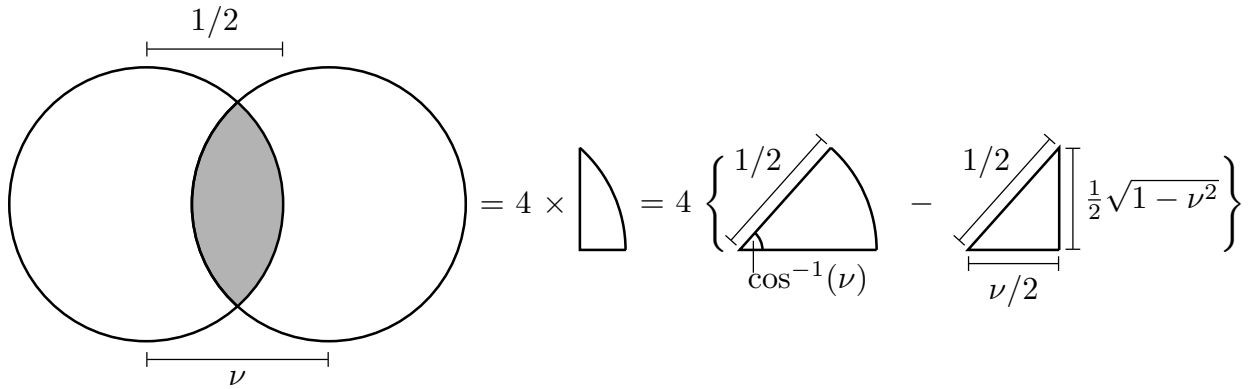


Figure 3.12: Geometric construction for evaluating the autocorrelation. We need to integrate over the overlapping region of two circles with radius $1/2$ and distance ν between their centers. The region is four times the difference in area between a sector of angle $\cos^{-1}(\nu)$ and radius $1/2$ and a right triangle with base $\nu/2$ and hypotenuse $1/2$.

For $n = 0$:

$$\text{chat}_0(\nu) = 4 \left[\int_0^{1/2} \tau d\tau \int_0^{\cos^{-1} \nu} d\phi_\tau - \int_0^{\nu/2} d\tau_x \int_0^{\frac{\tau_x}{\nu} \sqrt{1-\nu^2}} d\tau_y \right] \Pi\left(\frac{\nu}{2}\right), \quad (3.65)$$

$$\text{chat}_0(\nu) = \frac{1}{2} \left[\cos^{-1} |\nu| - |\nu| \sqrt{1 - \nu^2} \right] \Pi\left(\frac{\nu}{2}\right), \quad (3.66)$$

which is a well-known result [134, 139, 151]. For $n = 1$:

$$\begin{aligned} \text{chat}_1(\nu) &= 16 \left[\int_0^{1/2} \tau d\tau \int_0^{\cos^{-1} \nu} d\phi_\tau (\tau^2 - \nu\tau \cos \phi_\tau) - \right. \\ &\quad \left. \int_0^{\nu/2} d\tau_x \int_0^{\frac{\tau_x}{\nu} \sqrt{1-\nu^2}} d\tau_y (\tau_x^2 + \tau_y^2 - \nu\tau_x) \right] \Pi\left(\frac{\nu}{2}\right), \end{aligned} \quad (3.67)$$

$$\text{chat}_1(\nu) = \frac{1}{2} \left[\cos^{-1} |\nu| - |\nu|(3 - 2\nu^2)\sqrt{1 - \nu^2} \right] \Pi\left(\frac{\nu}{2}\right). \quad (3.68)$$

3.7 Appendix: Spherical Fourier transform of a double cone

In this appendix we evaluate the spherical Fourier transform of a normalized double-cone angular distribution with central direction $\hat{\mathbf{s}}'$ and cone half-angle Δ

$$f_{(\text{cone})}(\hat{\mathbf{s}}; \hat{\mathbf{s}}', \Delta) = \frac{1}{4\pi(1 - \cos \Delta)} \Pi\left(\frac{\hat{\mathbf{s}} \cdot \hat{\mathbf{s}}'}{2 \cos \Delta}\right). \quad (3.69)$$

The spherical Fourier transform is

$$F_{\ell(\text{cone})}^m(\hat{\mathbf{s}}', \Delta) = \int_{\mathbb{S}^2} d\hat{\mathbf{s}} f_{(\text{cone})}(\hat{\mathbf{s}}; \hat{\mathbf{s}}', \Delta) Y_\ell^{m*}(\hat{\mathbf{s}}). \quad (3.70)$$

The limits of integration will be difficult to find unless we change coordinates to exploit the axis of symmetry $\hat{\mathbf{s}}'$. Since the spherical function is rotationally symmetric about $\hat{\mathbf{s}}'$ we can rotate the function so that the axis of symmetry is aligned with $\hat{\mathbf{z}}$ and multiply by

$\sqrt{\frac{4\pi}{2l+1}} Y_\ell^{m*}(\hat{\mathbf{s}}')$ to account for the rotation [152]

$$F_{\ell(\text{cone})}^m(\hat{\mathbf{s}}', \Delta) = \sqrt{\frac{4\pi}{2l+1}} Y_\ell^{m*}(\hat{\mathbf{s}}') \int_{\mathbb{S}^2} d\hat{\mathbf{s}} f_{(\text{cone})}(\vartheta; \hat{\mathbf{z}}, \Delta) Y_\ell^0(\hat{\mathbf{s}}). \quad (3.71)$$

In this coordinate system the double cone is independent of the azimuthal angle, so we can evaluate the azimuthal integral and express the function in terms of an integral over ϑ :

$$F_{\ell(\text{cone})}^m(\hat{\mathbf{s}}', \Delta) = 2\pi Y_\ell^{m*}(\hat{\mathbf{s}}') \int_0^\pi d\vartheta \sin \vartheta f_{(\text{cone})}(\vartheta; \hat{\mathbf{z}}, \Delta) P_\ell(\cos \vartheta). \quad (3.72)$$

The function $f_{(\text{cone})}(\vartheta; \hat{\mathbf{z}}, \Delta)$ is only non-zero on the intervals $\vartheta \in [0, \Delta]$ and $\vartheta \in [\pi - \Delta, \pi]$ so

$$F_{\ell(\text{cone})}^m(\hat{\mathbf{s}}', \Delta) = \frac{Y_\ell^{m*}(\hat{\mathbf{s}}')}{2(1 - \cos \Delta)} \left[\int_0^\Delta d\vartheta \sin \vartheta P_\ell(\cos \vartheta) + \int_{\pi - \Delta}^\pi d\vartheta \sin \vartheta P_\ell(\cos \vartheta) \right]. \quad (3.73)$$

Applying a change of coordinates with $u = \cos \vartheta$ yields

$$F_{\ell(\text{cone})}^m(\hat{\mathbf{s}}', \Delta) = \frac{Y_\ell^{m*}(\hat{\mathbf{s}}')}{2(1 - \cos \Delta)} \left[\int_{\cos \Delta}^1 d\vartheta P_\ell(u) + \int_{-1}^{-\cos \Delta} d\vartheta P_\ell(u) \right]. \quad (3.74)$$

The Legendre polynomials $P_\ell(u)$ are even (odd) on the interval $[-1, 1]$ when ℓ is even (odd), so the pair of integrals will be identical when ℓ is even and cancel when ℓ is odd. For even ℓ ,

$$F_{\ell(\text{cone})}^m(\hat{\mathbf{s}}', \Delta) = \frac{Y_\ell^{m*}(\hat{\mathbf{s}}')}{1 - \cos \Delta} \int_{\cos \Delta}^1 d\vartheta P_\ell(u). \quad (3.75)$$

The integral evaluates to [150, ch. 7.111]

$$\int_{\cos \Delta}^1 d\vartheta P_\ell(u) = \begin{cases} 1 - \cos \Delta, & \ell = 0, \\ \sin \Delta P_l^{-1}(\cos \Delta), & \text{else,} \end{cases} \quad (3.76)$$

where $P_l^{-1}(\cos \Delta)$ is the associated Legendre polynomial with order $m = -1$, not an inverse Legendre polynomial. Bringing everything together

$$F_{\ell(\text{cone})}^m(\hat{\mathbf{s}}', \Delta) = \begin{cases} \sqrt{1/(4\pi)}, & \ell = 0, \\ 0, & \ell \text{ odd}, \\ Y_\ell^{m*}(\hat{\mathbf{s}}') \cot\left(\frac{\Delta}{2}\right) P_l^{-1}(\cos \Delta), & \ell > 0 \text{ even.} \end{cases} \quad (3.77)$$

CHAPTER 4

CONSTRAINED ANGULAR DIFFUSION, POLARIZED EXCITATION, AND HIGH-NA IMAGING

Burn the great sphere thou mov'st in!

— WILLIAM SHAKESPEARE, *Antony and Cleopatra* (1606)

We investigate rotational diffusion of fluorescent molecules in angular potential wells, the excitation and subsequent emissions from these diffusing molecules, and the imaging of these emissions with high-NA aplanatic optical microscopes. Although dipole emissions only transmit six low-frequency angular components, we show that angular structured illumination can alias higher frequency angular components into the passband of the imaging system. We show that the number of measurable angular components is limited by the relationships between three time scales: the rotational diffusion time, the fluorescence decay time, and the acquisition time. We demonstrate our model by simulating a numerical phantom in the limits of fast angular diffusion, slow angular diffusion, and weak potentials.

4.1 Introduction

Rotational diffusion plays an important role in every fluorescence experiment. Stokes' 1852 investigation of fluorescence (which led him to coin the word "fluorescence") reported no apparent polarization of the light emitted by a fluorescing solution of quinine [13]. We now understand that his observation reflects the relative time scales of angular diffusion, fluorescence decay, and measurement acquisition [153]. Angular diffusion of quinine (~ 0.3 ns rotational relaxation time) is fast compared to its fluorescence lifetime (~ 20 ns), which is fast compared to Stokes' acquisition time (~ 0.1 s for human vision). Even though each individual emission is polarized, diffusive reorientation of each fluorophore results in randomly polarized emissions that result in no apparent polarization when averaged over the measurement time.

These relationships were elucidated by several investigators in the 1920s. Weigert demonstrated that decreasing the rotational mobility of fluorescent molecules (by increasing the viscosity of the solvent or decreasing the temperature) resulted in increasingly polarized fluorescent emissions [18]. Wawilow and Lewschin observed that different dyes displayed varying relationships between the rotational mobility and the polarization of the fluorescent emissions [19], and Francis Perrin explained these variations by accounting for the fluorescence lifetime of the fluorophores [20]. Perrin’s synthesis inspired Weber to develop modern fluorescence polarization assays for biological applications [22, 23]. See Jameson’s review [153] for English summaries of the papers cited in this paragraph.

Since Weber’s work, fluorescence polarization assays have been used to deduce information from a wide range of samples in solution—see Lakowicz [25, chs. 10–12] for a review. More recently, fluorescence polarization imaging assays have been developed to image rotationally constrained fluorophores that label biological structures [37, 39, 48, 51, 55, 59, 115]. Furthermore, breakthroughs in single-molecule localization microscopy have led to assays that measure the position, orientation, and rotational dynamics of single molecules [61, 66, 68, 74, 85, 119]. All of these techniques use a model of rotational diffusion and the imaging process to interpret the collected data, and any mismatch between the model and the experiment could limit the accuracy of these interpretations.

Several recent works have modeled the images created by rotating single molecules under angular constraints [67, 76, 78, 82], and this chapter refines and extends these models. First, we consider angular potentials more general than those that are rotationally symmetric about a single axis. Modeling general potentials reduces the number of assumptions required to interpret data and creates opportunities for designing instruments that can draw new conclusions. Second, we consider in detail how the angular potential affects angular diffusion. Existing works have assumed that angular diffusion can be described by a monoexponential decay, while here we use the Smoluchowski equation to show that angular diffusion is multi-

exponential with time constants that depend on the potential. Third, we consider the effects of fluorescence saturation on the spatio-angular imaging process. We show that exploiting saturation can enable measurements of high-frequency angular components. Finally, we efficiently model arbitrary spatio-angular distributions of fluorescent emitters including but not limited to single molecules. These modeling improvements make several new predictions that may guide future experiments and improve the interpretation of existing data.

In chapters 2 and 3, we described the organization of our theory, described spatio-angular imaging operators and how they can be expressed in different bases, then calculated spatio-angular imaging operators for a paraxial $4f$ imaging system. In this chapter, we build on our framework and incorporate angular diffusion within a potential, polarized excitation, and high-NA imaging.

The chapter is organized as follows. In section 4.2 we develop models for spatio-angular diffusion, excitation, emission, and imaging. After introducing our notation (section 4.2.1), we build on the work of Jones [154] and Schulten et al. [155] to describe angular diffusion of one-state dipoles within asymmetric (section 4.2.2) and symmetric potentials (section 4.2.3). Next, we describe the diffusion of two-state molecules and their emissions under strong (section 4.2.4), and weak excitation (section 4.2.5–4.2.6). In section 4.3 we create a numerical phantom, specify an imaging system, then simulate imaging results. Finally, in section 4.4 we discuss our results and their implications.

4.2 Theory

4.2.1 Notation

We use roman fonts for scalars and functions (e.g. t, f), bold fonts for vectors (e.g. \mathbf{f}, \mathbf{s}), and blackboard bold for manifolds and vector spaces (e.g. $\mathbb{S}^2, \mathbb{R}^3$). We use hats to denote unit vectors (e.g. $\hat{\mathbf{s}}, \hat{\mathbf{e}}$), and we use $\{\hat{\mathbf{e}}_i\}$ to denote a set of orthonormal standard basis vectors.

We briefly review notation for functions that map points on the sphere \mathbb{S}^2 onto the real numbers \mathbb{R} . We denote these spherical functions by $f(\hat{\mathbf{s}})$ where $\hat{\mathbf{s}} \in \mathbb{S}^2$, and we denote their associated Hilbert-space vectors by $\mathbf{f} \in \mathbb{L}_2(\mathbb{S}^2)$. We define an inner product for this Hilbert space as

$$(\mathbf{f}_1, \mathbf{f}_2) = \int_{\mathbb{S}^2} d\hat{\mathbf{s}} f_1(\hat{\mathbf{s}}) f_2(\hat{\mathbf{s}}), \quad (4.1)$$

and we use this inner product to confirm that the non-denumerable set of standard basis vectors $\{\hat{\mathbf{e}}(\hat{\mathbf{s}})\} = \{[1, 0, 0 \dots], [0, 1, 0 \dots], \dots, [\dots, 0, 0, 1]\}$ satisfy

$$(\hat{\mathbf{e}}(\hat{\mathbf{s}}), \hat{\mathbf{e}}(\hat{\mathbf{s}}')) = \delta(\hat{\mathbf{s}} - \hat{\mathbf{s}}'), \quad (4.2)$$

where $\delta(\hat{\mathbf{s}} - \hat{\mathbf{s}}')$ is the Dirac delta on the sphere. We can construct an alternative orthonormal basis using the real-valued spherical harmonic functions $Y_{\ell m}(\hat{\mathbf{s}})$ which satisfy

$$\int_{\mathbb{S}^2} d\hat{\mathbf{s}} Y_{\ell m}(\hat{\mathbf{s}}) Y_{\ell' m'}(\hat{\mathbf{s}}) = \delta_{\ell \ell'} \delta_{m m'}, \quad (4.3)$$

where $\ell \in \{0, 1, 2, \dots\}$ and $m \in \{-\ell, -\ell + 1, \dots, \ell - 1, \ell\}$. The new basis vectors are

$$\hat{\mathbf{E}}_{\ell m} = \int_{\mathbb{S}^2} d\hat{\mathbf{s}} Y_{\ell m}(\hat{\mathbf{s}}) \hat{\mathbf{e}}(\hat{\mathbf{s}}), \quad (4.4)$$

which satisfy

$$(\hat{\mathbf{E}}_{\ell m}, \hat{\mathbf{E}}_{\ell' m'}) = \delta_{\ell \ell'} \delta_{m m'}, \quad (4.5)$$

$$(\hat{\mathbf{e}}(\hat{\mathbf{s}}), \hat{\mathbf{E}}_{\ell m}) = (\hat{\mathbf{E}}_{\ell m}, \hat{\mathbf{e}}(\hat{\mathbf{s}})) = Y_{\ell m}(\hat{\mathbf{s}}). \quad (4.6)$$

We can expand arbitrary Hilbert-space vectors $\mathbf{f} \in \mathbb{L}_2(\mathbb{S}^2)$ in either basis as

$$\mathbf{f} = \int_{\mathbb{S}^2} d\hat{\mathbf{s}} f(\hat{\mathbf{s}}) \hat{\mathbf{e}}(\hat{\mathbf{s}}) = \sum_{\ell=0}^{\infty} \sum_{m=-\ell}^{\ell} F_{\ell m} \hat{\mathbf{E}}_{\ell m}. \quad (4.7)$$

The coefficients $f(\hat{\mathbf{s}})$ can be found by taking the inner product of both sides of Eq. (4.7) with the basis vectors $\hat{\mathbf{e}}(\hat{\mathbf{s}})$ and exploiting orthonormality

$$f(\hat{\mathbf{s}}) = (\hat{\mathbf{e}}(\hat{\mathbf{s}}), \mathbf{f}). \quad (4.8)$$

We can proceed similarly for the coefficients $F_{\ell m}$ then write these coefficients in terms of $f(\hat{\mathbf{s}})$

$$F_{\ell m} = (\hat{\mathbf{E}}_{\ell m}, \mathbf{f}) = \int_{\mathbb{S}^2} d\hat{\mathbf{s}} (\hat{\mathbf{E}}_{\ell m}, \hat{\mathbf{e}}(\hat{\mathbf{s}})) (\hat{\mathbf{e}}(\hat{\mathbf{s}}), \mathbf{f}) = \int_{\mathbb{S}^2} d\hat{\mathbf{s}} Y_{\ell m}(\hat{\mathbf{s}}) f(\hat{\mathbf{s}}), \quad (4.9)$$

which is usually called the spherical Fourier transform.

We denote Hilbert-space operators with capital calligraphic letters \mathcal{H} . Hilbert-space operators act on Hilbert-space vectors to create other Hilbert-space vectors $\mathbf{g} = \mathcal{H}\mathbf{f}$, and we can express the action of \mathcal{H} concretely by choosing a basis for \mathbf{g} and \mathbf{f} . For example, if $\mathcal{H} : \mathbb{L}_2(\mathbb{S}^2) \rightarrow \mathbb{L}_2(\mathbb{R}^2)$ then we can choose the standard basis for both the input and output spaces and write

$$\mathbf{g} = \mathcal{H}\mathbf{f}, \quad (4.10)$$

$$(\hat{\mathbf{e}}(\mathbf{r}), \mathbf{g}) = \int_{\mathbb{S}^2} d\hat{\mathbf{s}} (\hat{\mathbf{e}}(\mathbf{r}), \mathcal{H}\hat{\mathbf{e}}(\hat{\mathbf{s}})) (\hat{\mathbf{e}}(\hat{\mathbf{s}}), \mathbf{f}), \quad (4.11)$$

$$g(\mathbf{r}) = \int_{\mathbb{S}^2} d\hat{\mathbf{s}} h(\mathbf{r}, \hat{\mathbf{s}}) f(\hat{\mathbf{s}}), \quad (4.12)$$

where $h(\mathbf{r}, \hat{\mathbf{s}}) = (\hat{\mathbf{e}}(\mathbf{r}), \mathcal{H}\hat{\mathbf{e}}(\hat{\mathbf{s}}))$ are the *standard entries* of \mathcal{H} .

We can calculate the entries of \mathcal{H} in a different basis by relating them to the standard entries. For example

$$H_{\ell m}(\mathbf{r}) \equiv (\hat{\mathbf{e}}(\mathbf{r}), \mathcal{H}\hat{\mathbf{E}}_{\ell m}) = \int_{\mathbb{S}^2} d\hat{\mathbf{s}} (\hat{\mathbf{e}}(\mathbf{r}), \mathcal{H}\hat{\mathbf{e}}(\hat{\mathbf{s}})) (\hat{\mathbf{e}}(\hat{\mathbf{s}}), \hat{\mathbf{E}}_{\ell m}) = \int_{\mathbb{S}^2} d\hat{\mathbf{s}} h(\mathbf{r}, \hat{\mathbf{s}}') Y_{\ell m}(\hat{\mathbf{s}}). \quad (4.13)$$

Finally, we denote adjoint operators with a dagger \dagger using the definition

$$(\mathbf{f}_1, \mathcal{H}\mathbf{f}_2) = (\mathcal{H}^\dagger \mathbf{f}_1, \mathbf{f}_2). \quad (4.14)$$

4.2.2 Dipole angular diffusion in arbitrary potentials

Consider a rigid molecule with orientation $\mathbf{R} \in \mathbb{SO}(3)$ —a 3×3 orthogonal matrix with determinant +1. We let $\omega(\mathbf{R}, t)$ denote the probability of finding the molecule in orientation \mathbf{R} at time t . Our goal is to develop a useful model for the time evolution of $\omega(\mathbf{R}, t)$ given an initial condition $\omega(\mathbf{R}, 0)$.

We start by assuming that the molecule's orientation can be completely described by a single absorption/emission dipole axis $\hat{\mathbf{s}}$. To apply this assumption, we parameterize the molecule's orientation using an axis-angle representation $\mathbf{R} = (\hat{\mathbf{s}}, \psi)$, where $\hat{\mathbf{s}} \in \mathbb{S}^2$ specifies the dipole axis and $\psi \in [0, 2\pi)$ specifies a rotation about $\hat{\mathbf{s}}$. With this parameterization we can apply the assumption by ignoring ψ and considering the time evolution of $\omega(\hat{\mathbf{s}}, t)$. We also know that dipole absorber/emitters are symmetric under inversion, so we constrain our distributions to be of the form $\omega(\hat{\mathbf{s}}, t) = \omega(-\hat{\mathbf{s}}, t)$. Finally, we normalize our probability distribution using

$$\int_{\mathbb{S}^2} d\hat{\mathbf{s}} \omega(\hat{\mathbf{s}}, t) = 1. \quad (4.15)$$

We can model the time evolution of $\omega(\hat{\mathbf{s}}, t)$ using the *Smoluchowski equation*

$$\frac{\partial \omega(\hat{\mathbf{s}}, t)}{\partial t} = \nabla \cdot \mathbf{D}(\hat{\mathbf{s}}) [\nabla \omega(\hat{\mathbf{s}}, t) + \beta \omega(\hat{\mathbf{s}}, t) \nabla v(\hat{\mathbf{s}})], \quad (4.16)$$

where $v(\hat{\mathbf{s}})$ is an arbitrary angular potential (for example, from an external field or a molecular bond), ∇ is the spherical gradient operator, $\nabla \cdot$ is the spherical divergence operator, $\mathbf{D}(\hat{\mathbf{s}})$ is an orientation-dependent angular diffusion tensor, and $\beta = 1/k_B T$ with k_B Boltzmann's constant and T temperature. Although we point readers elsewhere for a derivation [155–157], Eq. (4.16) is plausible at a glance. The first term in brackets models diffusion down a concentration gradient, and the second term models torques due to the potential. The orientation-dependent angular diffusion tensor scales and rotates the gradients. Next, the divergence sums over all neighboring orientations to find the total change in $\omega(\hat{\mathbf{s}}, t)$. We note that Eq. (4.16) assumes that inertial terms are negligible and that the torques can be related to a scalar potential.

Next, we assume that the molecule behaves like a *spherical rotor*—the diffusion tensor is homogeneous (independent of $\hat{\mathbf{s}}$) and isotropic (independent of angular diffusion direction)—so we can replace $\mathbf{D}(\hat{\mathbf{s}})$ with a single constant D

$$\frac{\partial \omega(\hat{\mathbf{s}}, t)}{\partial t} = D \nabla \cdot [\nabla \omega(\hat{\mathbf{s}}, t) + \beta \omega(\hat{\mathbf{s}}, t) \nabla v(\hat{\mathbf{s}})]. \quad (4.17)$$

This assumption is widely used in fluorescence microscopy [67, 76, 78, 82], and it provides a reasonable approximation for globular emitters like green fluorescent protein. Other investigators have modeled fluorescence from non-spherical rotors in solution [25, 158] and non-fluorescent diffusion of non-spherical rotors in a potential [157], while here we focus on modeling fluorescence from spherical rotors in a potential.

We can rewrite Eq. (4.17) in terms of Hilbert-space vectors and operators by collecting the $\hat{\mathbf{s}}$ dependence of $\omega(\hat{\mathbf{s}}, t)$ and $v(\hat{\mathbf{s}})$ into boldface vectors $\boldsymbol{\omega}(t) = \int_{\mathbb{S}^2} d\hat{\mathbf{s}} \omega(\hat{\mathbf{s}}, t) \hat{\mathbf{e}}(\hat{\mathbf{s}})$ and

$\mathbf{v} = \int_{\mathbb{S}^2} d\hat{\mathbf{s}} v(\hat{\mathbf{s}}) \hat{\mathbf{e}}(\hat{\mathbf{s}})$ then writing

$$\frac{\partial \boldsymbol{\omega}(t)}{\partial t} = D \nabla \cdot [\nabla \boldsymbol{\omega}(t) + \beta \boldsymbol{\omega}(t) \nabla \mathbf{v}] = -\mathcal{D}_{\mathbf{v}} \boldsymbol{\omega}(t), \quad (4.18)$$

where $\mathcal{D}_{\mathbf{v}} = -D \nabla \cdot [\nabla + \beta \nabla \mathbf{v}]$ is the Smoluchowski operator with arbitrary potential \mathbf{v} and the negative sign is included for convenience.

Eq. (4.18) is a homogeneous system of linear first-order differential equations. A typical approach is to expand $\boldsymbol{\omega}$ into a linear combination of eigenfunctions of $\mathcal{D}_{\mathbf{v}}$, but it is not obvious that a complete set of eigenfunctions exists. To show that a complete set of eigenfunctions does exist we follow Schulten et al. [155] and rewrite $\mathcal{D}_{\mathbf{v}}$ as

$$\mathcal{D}_{\mathbf{v}} = -D \nabla \cdot \exp(-\beta \mathbf{v}) \nabla \exp(\beta \mathbf{v}). \quad (4.19)$$

In this form it is straightforward to confirm that

$$\mathcal{W} \mathcal{D}_{\mathbf{v}} \mathcal{W}^{-1} = \mathcal{B}^\dagger \mathcal{B}, \quad (4.20)$$

where

$$\mathcal{W} = \exp(\beta \mathbf{v}/2), \quad (4.21)$$

$$\mathcal{B} = \sqrt{D} \exp(-\beta \mathbf{v}/2) \nabla \exp(\beta \mathbf{v}/2), \quad (4.22)$$

$$\mathcal{B}^\dagger = -\sqrt{D} \exp(\beta \mathbf{v}/2) \nabla \cdot \exp(-\beta \mathbf{v}/2), \quad (4.23)$$

and we have used the following operator identity (the adjoint of the gradient is the negative divergence)

$$\nabla^\dagger = -\nabla \cdot . \quad (4.24)$$

Eq. (4.20) shows that $\mathcal{D}_\mathbf{v}$ is similar to a Hermitian operator [1, ch. 1.4], and Hermitian operators have real non-negative eigenvalues $\lambda_{\mathbf{v},i}$ and a complete set of orthogonal eigenfunctions $\psi_{\mathbf{v},i}$ that satisfy

$$\mathcal{W}\mathcal{D}_\mathbf{v}\mathcal{W}^{-1}\psi_{\mathbf{v},i} = \lambda_{\mathbf{v},i}\psi_{\mathbf{v},i}. \quad (4.25)$$

Applying \mathcal{W}^{-1} to both sides yields

$$\mathcal{D}_\mathbf{v}\mathcal{W}^{-1}\psi_{\mathbf{v},i} = \lambda_{\mathbf{v},i}\mathcal{W}^{-1}\psi_{\mathbf{v},i}, \quad (4.26)$$

$$\mathcal{D}_\mathbf{v}\phi_{\mathbf{v},i} = \lambda_{\mathbf{v},i}\phi_{\mathbf{v},i}, \quad (4.27)$$

which shows that we can find a complete (though not necessarily orthogonal) set of eigenfunctions for $\mathcal{D}_\mathbf{v}$ by calculating $\phi_{\mathbf{v},i} = \mathcal{W}^{-1}\psi_{\mathbf{v},i}$. Additionally, we have shown that $\mathcal{D}_\mathbf{v}$ has real non-negative eigenvalues, so we can label its eigenvalues in order

$$0 \leq \lambda_{\mathbf{v},0} \leq \lambda_{\mathbf{v},1} \leq \lambda_{\mathbf{v},2} \leq \lambda_{\mathbf{v},3} \leq \dots. \quad (4.28)$$

Now that we have confirmed that $\mathcal{D}_\mathbf{v}$ has a complete set of eigenvectors, we can write the general solution of Eq. (4.18) as

$$\omega(t) = \sum_{i=0}^{\infty} c_{\mathbf{v},i} \phi_{\mathbf{v},i} \exp(-\lambda_{\mathbf{v},i} t), \quad (4.29)$$

where $c_{\mathbf{v},i}$ are constants determined by the initial condition.

From statistical mechanics we expect the Boltzmann distribution to be a steady-state solution. We can confirm this expectation by plugging the Boltzmann distribution

$$\phi_{\mathbf{v},0} = Z_\mathbf{v}^{-1} \exp(-\beta \mathbf{v}), \quad (4.30)$$

where $Z_{\mathbf{v}}$ is the partition function

$$Z_{\mathbf{v}} = \int_{\mathbb{S}^2} d\hat{\mathbf{s}} \exp(-\beta v(\hat{\mathbf{s}})), \quad (4.31)$$

into Eq. (4.18) and confirming that it is an eigenfunction of $\mathcal{D}_{\mathbf{v}}$ with a zero eigenvalue. We also expect the Boltzmann distribution to be the unique steady-state solution—the only eigenfunction with a zero eigenvalue. We point readers elsewhere for a physical argument that this is true [155], but we remark that a single steady-state solution depends on $v(\hat{\mathbf{s}})$ being square-integrable. For example, a non-square-integrable potential could have two potential wells separated by an infinite potential, and in this case we would expect multiple steady-state solutions.

Finally, we calculate the coefficients $c_{\mathbf{v},i}$ in terms of the initial condition $\omega(0)$. The naive approach of taking the inner product of both sides of Eq. (4.29) with the eigenfunctions $(\phi_{\mathbf{v},i}, \cdot)$ will fail because the eigenfunctions are not orthogonal. Instead, we construct a biorthogonal set by solving the eigenvalue problem for the adjoint Smoluchowski operator. If we write the adjoint Smoluchowski operator in the form

$$\mathcal{D}_{\mathbf{v}}^\dagger = -D \exp(\beta \mathbf{v}) \nabla \cdot \exp(-\beta \mathbf{v}) \nabla, \quad (4.32)$$

then it is straightforward to confirm that

$$\mathcal{D}_{\mathbf{v}}^\dagger \left(\frac{\phi_{\mathbf{v},i}}{\phi_{\mathbf{v},0}} \right) = \lambda_i \left(\frac{\phi_{\mathbf{v},i}}{\phi_{\mathbf{v},0}} \right), \quad (4.33)$$

where the division of Hilbert-space vectors is elementwise. Therefore, $(\phi_{\mathbf{v},i}/\phi_{\mathbf{v},0})$ are eigenfunctions of $\mathcal{D}_{\mathbf{v}}^\dagger$, and these functions form a biorthogonal set with the eigenfunctions of $\mathcal{D}_{\mathbf{v}}$.

We can normalize so that these functions form a biorthonormal set that satisfies

$$\left(\frac{\phi_{\mathbf{v},i}}{\phi_{\mathbf{v},0}}, \phi_{\mathbf{v},j} \right) = \delta_{ij}. \quad (4.34)$$

Now we can take the inner product of both sides of Eq. (2.60) with the eigenfunctions of $\mathcal{D}_{\mathbf{v}}^\dagger$ and solve for $c_{\mathbf{v},i}$ in terms of the initial condition

$$c_{\mathbf{v},i} = \left(\frac{\phi_{\mathbf{v},i}}{\phi_{\mathbf{v},0}}, \boldsymbol{\omega}(0) \right). \quad (4.35)$$

Therefore, the solution takes the form

$$\boldsymbol{\omega}(t) = \sum_{i=0}^{\infty} \left(\frac{\phi_{\mathbf{v},i}}{\phi_{\mathbf{v},0}}, \boldsymbol{\omega}(0) \right) \phi_{\mathbf{v},i} \exp(-\lambda_{\mathbf{v},i} t). \quad (4.36)$$

We can use these results to draw several conclusions for diffusion under arbitrary potentials. The fact that the eigenvalues are real implies that the solutions will never oscillate—this is expected since we are ignoring inertial effects. The fact that the eigenvalues are positive except for a single zero eigenvalue implies that our solutions will always decay to the Boltzmann distribution $\boldsymbol{\omega}(t \rightarrow \infty) = \phi_{\mathbf{v},0}$. The smallest non-zero eigenvalue $\lambda_{\mathbf{v},1}$ will set the time scale of the decay, so we know that $\boldsymbol{\omega}(t \gg 1/\lambda_{\mathbf{v},1}) \approx \phi_{\mathbf{v},0}$. Finally, the decay of $\boldsymbol{\omega}(t)$ will be monoexponential if the initial condition is either an eigenfunction of $\mathcal{D}_{\mathbf{v}}$ or a linear combination of eigenfunctions of $\mathcal{D}_{\mathbf{v}}$ that share an eigenvalue.

4.2.3 Dipole angular diffusion in symmetric potentials

Next, we consider how symmetric potentials can constrain the form of the solution. If the potential is rotationally symmetric ($v(\hat{s})$ is constant) then the Smulochowski equation

reduces to the diffusion equation

$$\frac{\partial \boldsymbol{\omega}(t)}{\partial t} = D\Delta\boldsymbol{\omega}(t) = -\mathcal{D}_c\boldsymbol{\omega}(t), \quad (4.37)$$

where Δ is the spherical Laplacian, and $\mathcal{D}_c = -D\Delta$. This equation has a well-known solution—the eigenfunctions of \mathcal{D}_c that satisfy the biorthonormality relation Eq. (4.34) are the renormalized spherical harmonics $\phi_{c,\ell m} = \hat{\mathbf{E}}_{\ell m}/\sqrt{4\pi}$ with eigenvalues $\lambda_{c,\ell m} = D\ell(\ell+1)$, which we can plug into Eq. (4.36) to find that

$$\boldsymbol{\omega}(t) = \sum_{\ell=0,2,4\dots}^{\infty} \sum_{m=-\ell}^{\ell} (\hat{\mathbf{E}}_{\ell m}, \boldsymbol{\omega}(0)) \hat{\mathbf{E}}_{\ell m} \exp(-D(\ell(\ell+1)t)). \quad (4.38)$$

Eq. (4.38) has a simple form when expressed in terms of the spherical harmonic coefficients $\Omega_{\ell m}$

$$(\hat{\mathbf{E}}_{\ell m}, \boldsymbol{\omega}(t)) \equiv \Omega_{\ell m}(t) = \Omega_{\ell m}(0) \exp(-D\ell(\ell+1)t). \quad (4.39)$$

An essential feature of this solution is that each eigenvalue $\lambda_{c,\ell m}$ forms a multiplet with $2\ell+1$ other eigenvalues indexed by m . This fact allows us to split the single eigenvalue index i in Eq. (4.36) into a pair of indices (ℓ, m) in Eq. (4.38).

The multiplicity of eigenvalues reduces the number of decay components in the solution. For example, if the initial condition is bandlimited to $\ell = 2$, that is $(\hat{\mathbf{E}}_{\ell m}, \boldsymbol{\omega}(0)) \neq 0$ for $\ell = 0$ and $\ell = 2$ only, then the 6-dimensional initial distribution will decay towards the Boltzmann distribution monoexponentially with time constant $(6D)^{-1}$.

We can predict eigenvalue multiplets by studying the *symmetry group of the operator* $\mathcal{D}_{\mathbf{V}}$ [1, ch. 6.7], and we will use the rotationally symmetric example \mathcal{D}_c to illustrate this process. First, we identify the symmetry group of the operator by finding the set of operators that commute with $\mathcal{D}_{\mathbf{V}}$. All three-dimensional rotation operators commute with \mathcal{D}_c because

rotating the potential leaves it unchanged. Therefore, we identify the symmetry group of \mathcal{D}_c as $\text{SO}(3)$. Next, we find the *irreducible representations* of the symmetry group—sets of irreducible matrices assigned to each group element where matrix multiplication reproduces the group composition rule. An irreducible representation that uses $N \times N$ matrices is said to be N -dimensional. Irreducible representations can be calculated from scratch, but in practice they can almost always be found in the literature [159, 160]. The irreducible representations of $\text{SO}(3)$ are the Wigner D-matrices $\mathbf{D}_\ell(\mathbf{R})$ where $\ell = 0, 1/2, 1, 3/2, 2, \dots$ indexes the $(2\ell + 1)$ -dimensional irreducible representations and \mathbf{R} indexes the elements of $\text{SO}(3)$. Finally, eigenvalue N -plets correspond to the N -dimensional irreducible representations of the symmetry group of \mathcal{D}_v . \mathcal{D}_c has irreducible representations of integer dimension, so there will be at most an N -plet for each natural number N .

Some of the multiplets may not appear in the solution due to symmetries of the distribution $\omega(\mathbf{R})$. For example, we expect $\omega(\hat{\mathbf{s}}, \psi) = \omega(\hat{\mathbf{s}}, \psi + 2\pi)$ which implies that $(\phi_{c,\ell m}, \boldsymbol{\omega}(0)) = 0$ for half-integer ℓ [1, ch. 6.7]. Similarly, we expect $\omega(\hat{\mathbf{s}}, \psi) = \omega(-\hat{\mathbf{s}}, \psi)$ which implies that $(\phi_{c,\ell m}, \boldsymbol{\omega}(0)) = 0$ for odd ℓ . The remaining multiplets correspond to even integer ℓ , which means we can expect a singlet, a 5-plet, a 9-plet, etc. This explains the multiplet structure of Eq. (4.38).

Several works have considered axially symmetric potentials that can be written in the form $v(\hat{\mathbf{s}} \cdot \hat{\mathbf{s}}_c)$, where $\hat{\mathbf{s}}_c$ is the axis of symmetry [78, 154]. In this case rotating the potential about the axis of symmetry commutes with the Smoluchowski operator. Additionally, rotating the potential by π about any axis orthogonal to the symmetry axis also commutes. We can identify this set of rotations as members of the group $\text{O}(2)$ — 2×2 orthogonal matrices. The irreducible representations of $\text{O}(2)$ are one- and two-dimensional [159], so multiplets can be at most doublets. Jones demonstrates how perturbing a rotationally symmetric potential to an axially symmetric potential splits the eigenvalue spectrum into singlets and doublets [154]—the original singlet is maintained, the 5-plet splits into a singlet and two doublets,

the 9-plet splits into a singlet and four doublets, etc.

Note that perturbing the potential also perturbs the eigenfunctions, so the spherical harmonics will not be eigenfunctions for an axially symmetric Smoluchowski operator. Perturbing the potential from complete rotational symmetry will always create eigenfunctions that are not bandlimited, so bandlimited initial conditions will decay via a superposition of an infinite number of exponentials.

4.2.4 Two-state diffusion and polarized excitation

Now we extend our model to a molecule that can be in two states. We define two functions $w^{(\text{gr})}(\hat{\mathbf{s}}, t)$ and $w^{(\text{ex})}(\hat{\mathbf{s}}, t)$ as the probabilities that the molecule is in the ground or excited state, respectively, in orientation $\hat{\mathbf{s}}$ at time t . We normalize so that

$$\int_{\mathbb{S}^2} d\hat{\mathbf{s}} \left[w^{(\text{gr})}(\hat{\mathbf{s}}, t) + w^{(\text{ex})}(\hat{\mathbf{s}}, t) \right] = 1. \quad (4.40)$$

Next, we define the associated Hilbert-space vectors $\mathbf{w}^{(\text{gr})}(t)$ and $\mathbf{w}^{(\text{ex})}(t)$, a molecular-species specific decay rate constant $\kappa^{(\text{d})}$, and a polarization-dependent excitation operator $\mathcal{K}_{\hat{\mathbf{p}}}^{(\text{ex})}$ (parameterized by an arbitrary polarization state $\hat{\mathbf{p}}$) that encodes the orientation-dependent excitation rate. We assume that the molecule diffuses in the same potential while it is in the ground and excited state, so we can model the time-evolution of the molecule as

$$\frac{\partial}{\partial t} \begin{bmatrix} \mathbf{w}^{(\text{ex})}(t) \\ \mathbf{w}^{(\text{gr})}(t) \end{bmatrix} = \begin{bmatrix} \mathcal{D}_{\mathbf{v}} - \kappa^{(\text{d})} & \mathcal{K}_{\hat{\mathbf{p}}}^{(\text{ex})} \\ \kappa^{(\text{d})} & \mathcal{D}_{\mathbf{v}} - \mathcal{K}_{\hat{\mathbf{p}}}^{(\text{ex})} \end{bmatrix} \begin{bmatrix} \mathbf{w}^{(\text{ex})}(t) \\ \mathbf{w}^{(\text{gr})}(t) \end{bmatrix}. \quad (4.41)$$

This model assumes that stimulated emission is negligible. This assumption is justified when the newly excited molecule undergoes fast vibrational relaxation to a state that is unaffected by stimulated emission from the original excitation beam. In this two-state model the mean excited-state lifetime is given by $\tau_e = 1/\kappa^{(\text{d})}$.

Our goal is to model the observable irradiance emitted by the molecule as it decays from the excited state to the ground state. If we expose a detector from $t = t_0$ to $t = t_1$, then the most we can hope to recover from our measurement is

$$\mathbf{w} = \int_{t_0}^{t_1} dt \kappa^{(d)} \mathbf{w}^{(\text{ex})}(t), \quad (4.42)$$

which we call the *point emission density*. Calculating \mathbf{w} will almost always require numerics, but we can find closed-form solutions in several specific cases.

For example, if we assume that diffusion is slow compared to the decay rate constant and the maximum excitation rate constant $D \ll \kappa^{(d)}, \kappa_{\max}^{(\text{ex})}$, then we can ignore \mathcal{D}_v and write

$$\frac{\partial}{\partial t} \begin{bmatrix} \mathbf{w}^{(\text{ex})}(t) \\ \mathbf{w}^{(\text{gr})}(t) \end{bmatrix} = \begin{bmatrix} -\kappa^{(d)} & \mathcal{K}_{\hat{\mathbf{p}}}^{(\text{ex})} \\ \kappa^{(d)} & -\mathcal{K}_{\hat{\mathbf{p}}}^{(\text{ex})} \end{bmatrix} \begin{bmatrix} \mathbf{w}^{(\text{ex})}(t) \\ \mathbf{w}^{(\text{gr})}(t) \end{bmatrix}. \quad (4.43)$$

If we excite with coherent light polarized linearly along direction $\hat{\mathbf{p}} \in \mathbb{S}^2$, then the standard entries of the excitation operator are

$$\left(\hat{\mathbf{e}}(\hat{\mathbf{s}}), \mathcal{K}_{\hat{\mathbf{p}}}^{(\text{ex})} \hat{\mathbf{e}}(\hat{\mathbf{s}}') \right) = \kappa^{(\text{ex})} |\hat{\mathbf{p}} \cdot \hat{\mathbf{s}}|^2 \delta(\hat{\mathbf{s}} - \hat{\mathbf{s}}'), \quad (4.44)$$

where $\kappa^{(\text{ex})}$ is the maximum excitation rate constant, which is proportional to the intensity of the excitation beam. Rewriting the whole system in a standard basis yields

$$\frac{\partial}{\partial t} \begin{bmatrix} w^{(\text{ex})}(\hat{\mathbf{s}}, t) \\ w^{(\text{gr})}(\hat{\mathbf{s}}, t) \end{bmatrix} = \begin{bmatrix} -\kappa^{(d)} & \kappa^{(\text{ex})} |\hat{\mathbf{p}} \cdot \hat{\mathbf{s}}|^2 \\ \kappa^{(d)} & -\kappa^{(\text{ex})} |\hat{\mathbf{p}} \cdot \hat{\mathbf{s}}|^2 \end{bmatrix} \begin{bmatrix} w^{(\text{ex})}(\hat{\mathbf{s}}, t) \\ w^{(\text{gr})}(\hat{\mathbf{s}}, t) \end{bmatrix}. \quad (4.45)$$

If the molecule starts in the ground state $w^{(\text{gr})}(\hat{\mathbf{s}}, 0) = 1/4\pi$ and $w^{(\text{ex})}(\hat{\mathbf{s}}, 0) = 0$, then the

solution is given by

$$\begin{bmatrix} w^{(\text{ex})}(\hat{\mathbf{s}}, t) \\ w^{(\text{gr})}(\hat{\mathbf{s}}, t) \end{bmatrix} = \frac{1}{\kappa^{(\text{ex})}|\hat{\mathbf{p}} \cdot \hat{\mathbf{s}}|^2 + \kappa^{(\text{d})}} \begin{bmatrix} \kappa^{(\text{ex})}|\hat{\mathbf{p}} \cdot \hat{\mathbf{s}}|^2 \\ \kappa^{(\text{d})} \end{bmatrix} + \frac{\kappa^{(\text{ex})}|\hat{\mathbf{p}} \cdot \hat{\mathbf{s}}|^2}{\kappa^{(\text{ex})}|\hat{\mathbf{p}} \cdot \hat{\mathbf{s}}|^2 + \kappa^{(\text{d})}} \begin{bmatrix} -1 \\ 1 \end{bmatrix} \exp[-(\kappa^{(\text{ex})}|\hat{\mathbf{p}} \cdot \hat{\mathbf{s}}|^2 + \kappa^{(\text{d})})t]. \quad (4.46)$$

A particularly interesting result is the steady-state probability of finding the molecule in the excited state

$$w^{(\text{ex})}(\theta, t \gg \kappa^{(\text{ex})} + \kappa^{(\text{d})}) = \frac{\cos^2 \theta}{\cos^2 \theta + [\kappa^{(\text{d})}/\kappa^{(\text{ex})}]}, \quad (4.47)$$

where θ is the angle between $\hat{\mathbf{p}}$ and $\hat{\mathbf{s}}$.

Figure 4.1 shows the behavior of Eq. (4.47) as θ and $\kappa^{(\text{d})}/\kappa^{(\text{ex})}$ are varied. For strong excitation, $\kappa^{(\text{d})}/\kappa^{(\text{ex})} \ll 1$ and the excited state saturates and contains high angular-frequency patterns. These patterns are directly analogous to the high spatial-frequency patterns generated in non-linear structured illumination microscopy [161].

For weak excitation, $\kappa^{(\text{d})}/\kappa^{(\text{ex})} \gg 1$ and the $\cos^2 \theta$ in the denominator of Eq. (4.47) is dwarfed, so the excited state probability is proportional to $\cos^2 \theta$. In this limit we are far from saturating the excited state, and the excited-state probability is linear in the excitation power.

4.2.5 Two-state diffusion under weak polarized excitation

In the weak excitation limit, $\kappa^{(\text{d})}/\kappa^{(\text{ex})} \gg 1$, we can approximate the two-state model using an effective one-state model. If the molecule starts in the ground state and the molecule has diffused to the steady state then $\mathbf{w}^{(\text{gr})}(0) = \phi_{\mathbf{v},0}$. Under weak excitation the probability of excitation is small, so the ground state probability will stay approximately constant

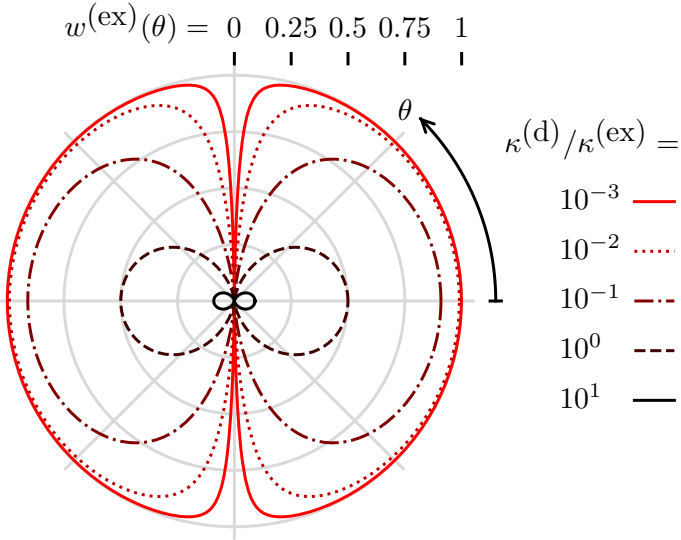


Figure 4.1: Diffusion-free steady-state excited-state probability $w^{(\text{ex})}$ (radius from center) as a function of the angle from the incident polarization θ (clockwise angle from positive x axis) and the detection rate to excitation rate ratio $\kappa^{(\text{d})}/\kappa^{(\text{ex})}$ (color). For weak excitation $\kappa^{(\text{d})}/\kappa^{(\text{ex})} \gg 1$ the excited-state probability is small and only contains low angular-frequency components. For strong excitation $\kappa^{(\text{d})}/\kappa^{(\text{ex})} \ll 1$ the excited state is saturated and contains high angular-frequency components.

$\mathbf{w}^{(\text{gr})}(t) \approx \phi_{\mathbf{v},0}$. Our remaining task is to solve for the excited-state probability, which evolves according to

$$\frac{\partial \mathbf{w}^{(\text{ex})}(t)}{\partial t} = - (\mathcal{D}_{\mathbf{v}} + \kappa^{(\text{d})}) \mathbf{w}^{(\text{ex})}(t) + \mathcal{K}_{\hat{\mathbf{p}}}^{(\text{ex})} \phi_{\mathbf{v},0}. \quad (4.48)$$

Eq. (4.48) is an inhomogeneous system of linear first-order differential equations. To solve Eq. (4.48), we start by noticing that the operator $(\mathcal{D}_{\mathbf{v}} + \kappa^{(\text{d})})$ has the same eigenfunctions as $\mathcal{D}_{\mathbf{v}}$ with larger eigenvalues $\lambda_{\mathbf{v},i} + \kappa^{(\text{d})}$. Next, we find the steady-state solution by setting the left-hand side to zero

$$\mathbf{w}^{(\text{ex})}(\infty) = (\mathcal{D}_{\mathbf{v}} + \kappa^{(\text{d})})^{-1} \mathcal{K}_{\hat{\mathbf{p}}}^{(\text{ex})} \phi_{\mathbf{v},0} = \sum_{i=0}^{\infty} \frac{1}{\lambda_{\mathbf{v},i} + \kappa^{(\text{d})}} \left(\frac{\phi_{\mathbf{v},i}}{\phi_{\mathbf{v},0}}, \mathcal{K}_{\hat{\mathbf{p}}}^{(\text{ex})} \phi_{\mathbf{v},0} \right) \phi_{\mathbf{v},i}. \quad (4.49)$$

We can find the homogeneous solution $\mathbf{w}_h^{(\text{ex})}(t)$ by ignoring the constant term to find

$$\mathbf{w}_h^{(\text{ex})}(t) = \sum_{i=0}^{\infty} c_{\mathbf{v},i} \phi_{\mathbf{v},i} \exp \left[-(\lambda_{\mathbf{v},i} + \kappa^{(\text{d})}) t \right]. \quad (4.50)$$

The complete solution is given by the sum of the homogenous solution and the steady-state solution

$$\mathbf{w}^{(\text{ex})}(t) = \mathbf{w}_h^{(\text{ex})}(t) + \mathbf{w}^{(\text{ex})}(\infty). \quad (4.51)$$

If we begin exposing a detector for a period t_e after the system has reached a steady state at $t_1 \gg 1/\kappa^{(\text{d})}$ then the point emission density is given by

$$\mathbf{w} = \int_{t_1}^{t_1+t_e} dt \kappa^{(\text{d})} \mathbf{w}^{(\text{ex})}(\infty) \quad (4.52)$$

$$\mathbf{w} = \sum_{i=0}^{\infty} \frac{t_e \kappa^{(\text{d})}}{\lambda_{\mathbf{v},i} + \kappa^{(\text{d})}} \left(\frac{\phi_{\mathbf{v},i}}{\phi_{\mathbf{v},0}}, \mathcal{K}_{\hat{\mathbf{p}}}^{(\text{ex})} \phi_{\mathbf{v},0} \right) \phi_{\mathbf{v},i}. \quad (4.53)$$

Eq. (4.53) is the main result of this section, and we briefly consider it more closely for cases when diffusion is very slow and very fast.

In the fast diffusion limit ($\lambda_{\mathbf{v},i} \gg \kappa^{(d)}$ for all $i > 0$) all of the terms in Eq. (4.53) are negligible except for the $i = 0$ term and the result simplifies to

$$\mathbf{w} \stackrel{(\text{fast})}{=} t_e \left(1, \mathcal{K}_{\hat{\mathbf{p}}}^{(\text{ex})} \phi_{\mathbf{v},0} \right) \phi_{\mathbf{v},0}, \quad (4.54)$$

which means that the measurable angular distribution is the Boltzmann distribution weighted by a constant excitation efficiency. Informally, Eq. (4.54) says that a fast diffusing dipole reaches the Boltzmann distribution before emission, so the emission density is the Boltzmann distribution multiplied by a constant excitation efficiency.

In the slow diffusion limit ($\lambda_{\mathbf{v},i} \ll \kappa^{(d)}$ for all i), every term in Eq. (4.53) contributes

and the sum simplifies to

$$\mathbf{w} \stackrel{\text{(slow)}}{=} t_e \mathcal{K}_{\hat{\mathbf{p}}}^{(\text{ex})} \phi_{\mathbf{v},0}, \quad (4.55)$$

which means that the measurable angular distribution is the excitation operator acting on the Boltzmann distribution. Informally, Eq. (4.55) says that a slow diffusing dipole does not rotate before emission, so the point emission density is the point-wise product of the excitation efficiency function and the Boltzmann distribution. This situation is the angular analog to linear structured illumination microscopy [162], where spatial diffusion is assumed to be negligible and illumination patterns can be used to alias high-frequency spatial patterns into the passband of the imaging system.

4.2.6 Weak excitation of a free dipole

In the absence of a potential, the eigenvalues become $\lambda_{c,\ell m} = D\ell(\ell+1)$ and the eigenfunctions become $\phi_{c,\ell m} = \hat{\mathbf{E}}_{\ell m}/\sqrt{4\pi}$ (see section 4.2.3). Plugging these into Eq. (4.53) yields

$$\mathbf{w} \stackrel{\text{(free)}}{=} \sum_{\ell=0}^{\infty} \sum_{m=-\ell}^{\ell} \frac{t_e \kappa^{(\text{d})}}{D\ell(\ell+1) + \kappa^{(\text{d})}} \left(\hat{\mathbf{E}}_{\ell m}, \mathcal{K}_{\hat{\mathbf{p}}}^{(\text{ex})}/4\pi \right) \hat{\mathbf{E}}_{\ell m}. \quad (4.56)$$

For linearly polarized coherent illumination we can write Eq. (4.56) in the standard basis as

$$w(\theta) \stackrel{\text{(free)}}{=} \frac{t_e \kappa^{(\text{ex})}}{12\pi} \left[1 + \frac{3 \cos^2 \theta - 1}{1 + [6D/\kappa^{(\text{d})}]} \right], \quad (4.57)$$

where θ is the angle between $\hat{\mathbf{p}}$ and $\hat{\mathbf{s}}$. Figure 4.2 shows the behavior of Eq. (4.57) as θ and $6D/\kappa^{(\text{d})}$ are varied. For slow diffusion ($6D/\kappa^{(\text{d})} \ll 1$) the point emission density is identical to the excitation probability $|\hat{\mathbf{p}} \cdot \hat{\mathbf{s}}|^2$, and for fast diffusion ($6D/\kappa^{(\text{d})} \gg 1$) the point emission density is the constant Boltzmann distribution.

Notice that the infinite sum in Eq. (4.56) reduces to two non-zero terms in Eq. (4.57)

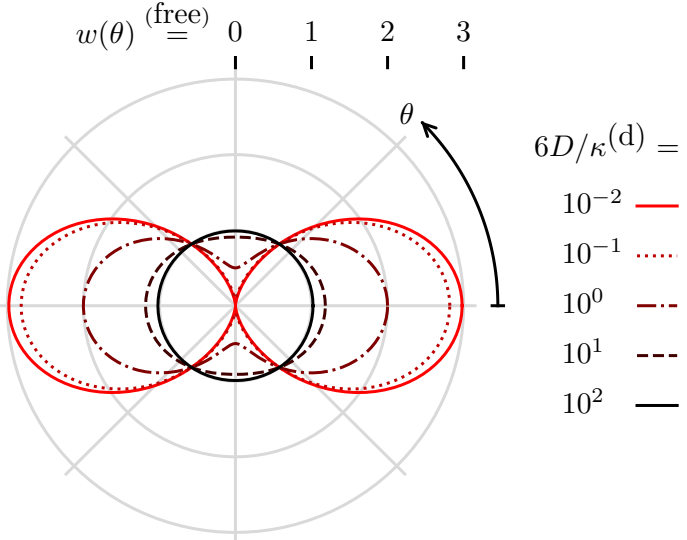


Figure 4.2: Weak-excitation emission density for a free dipole w (radius from center) as a function of the angle from the incident polarization θ (clockwise angle from positive x axis) and the diffusion rate to decay rate constant ratio $6D/\kappa^{(d)}$ (color). For slow diffusion $6D/\kappa^{(d)} \ll 1$ the emission density is the excitation probability, and for fast diffusion $6D/\kappa^{(d)} \gg 1$ the excited emission density is the constant Boltzmann distribution.

because coherent polarized illumination excites the (constant) Boltzmann distribution into a linear combination of six eigenfunctions that have only two distinct eigenvalues. For asymmetric potentials, coherent polarized illumination will excite the Boltzmann distribution into a linear combination of an infinite number of eigenfunctions, so the solution will contain an infinite number of terms.

4.2.7 Spatio-angular emission densities

So far we have been considering point emission densities $\mathbf{w} \in \mathbb{L}_2(\mathbb{S}^2)$ for single molecules at a single point in space. In this section we will extend our discussion to ensembles of molecules and three-dimensional angular emission densities represented by vectors $\mathbf{f} \in \mathbb{L}_2(\mathbb{R}^3 \times \mathbb{S}^2)$.

We start by defining a spatio-angular dynamics model similar to the angular dynamics model in section 4.2.4. First, we define a pair of functions $f^{(\text{gr})}(\mathbf{r}_o, \hat{\mathbf{s}}_o, t)$ and $f^{(\text{ex})}(\mathbf{r}_o, \hat{\mathbf{s}}_o, t)$ as the number of molecules in the ground and excited states, respectively, at position

$\mathbf{r}_o \in \mathbb{R}^3$, in orientation $\hat{\mathbf{s}} \in \mathbb{S}^2$, and at time t (per unit volume, solid angle, and time). These unnormalized functions are related to the normalized functions we considered earlier by

$$f^{(\text{gr})}(\mathbf{r}_o, \hat{\mathbf{s}}_o, t) = \rho(\mathbf{r}_o, t) w^{(\text{gr})}(\mathbf{r}_o, \hat{\mathbf{s}}_o, t), \quad (4.58)$$

$$f^{(\text{ex})}(\mathbf{r}_o, \hat{\mathbf{s}}_o, t) = \rho(\mathbf{r}_o, t) w^{(\text{ex})}(\mathbf{r}_o, \hat{\mathbf{s}}_o, t), \quad (4.59)$$

where $\rho(\mathbf{r}_o, t)$ is an orientation-independent *spatial density*—the number of fluorescent molecules per unit volume at point \mathbf{r}_o . We also define the associated Hilbert-space vectors $\mathbf{f}^{(\text{gr})}(t)$ and $\mathbf{f}^{(\text{ex})}(t)$. Next, we define a spatio-angular potential \mathbf{v} , a Smoluchowski operator $\mathcal{D}_{\mathbf{v}}$ that models how molecules diffuse in the spatio-angular potential \mathbf{v} , a spatio-angular excitation operator $\mathcal{K}_{\hat{\mathbf{p}}}^{(\text{ex})}$, and a decay rate constant $\kappa^{(\text{d})}$. With these definitions we can model the spatio-angular populations with

$$\frac{\partial}{\partial t} \begin{bmatrix} \mathbf{f}^{(\text{ex})}(t) \\ \mathbf{f}^{(\text{gr})}(t) \end{bmatrix} = \begin{bmatrix} \mathcal{D}_{\mathbf{v}} - \kappa^{(\text{d})} & \mathcal{K}_{\hat{\mathbf{p}}}^{(\text{ex})} \\ \kappa^{(\text{d})} & \mathcal{D}_{\mathbf{v}} - \mathcal{K}_{\hat{\mathbf{p}}}^{(\text{ex})} \end{bmatrix} \begin{bmatrix} \mathbf{f}^{(\text{ex})}(t) \\ \mathbf{f}^{(\text{gr})}(t) \end{bmatrix}. \quad (4.60)$$

We are interested in the spatio-angular emission density during an exposure from t_0 to t_1 given by

$$\mathbf{f} = \int_{t_0}^{t_1} dt \kappa^{(\text{d})} \mathbf{f}^{(\text{ex})}(t). \quad (4.61)$$

If spatial diffusion is negligible, then the spatio-angular model in Eq. (4.60) decouples into an angular model at each point weighted by a time-independent spatial density $\rho(\mathbf{r}_o)$, so we can write

$$f(\mathbf{r}_o, \hat{\mathbf{s}}_o) = \rho(\mathbf{r}_o) w(\mathbf{r}_o, \hat{\mathbf{s}}_o). \quad (4.62)$$

For each spatial point \mathbf{r}_o we can use the angular solutions developed in sections 4.2.4–4.2.6 to calculate $w(\mathbf{r}_o, \hat{\mathbf{s}}_o)$.

4.2.8 Spatio-angular imaging operator

In this section we complete our imaging model by finding the mapping between the spatio-angular emission density \mathbf{f} and the data we measure \mathbf{g} . It will be convenient to choose a basis for \mathbf{f} that splits the object-space spatial coordinates into a one-dimensional longitudinal coordinate r_o^{\parallel} aligned with the optical axis of the microscope, and a two-dimensional transverse coordinate \mathbf{r}_o^{\perp} . More specifically, we express \mathbf{f} in the following basis

$$f(\mathbf{r}_o^{\perp}, r_o^{\parallel}, \hat{\mathbf{s}}_o) = (\hat{\mathbf{e}}(\mathbf{r}_o^{\perp})\hat{\mathbf{e}}(r_o^{\parallel})\hat{\mathbf{e}}(\hat{\mathbf{s}}), \mathbf{f}). \quad (4.63)$$

Next, we model the irradiance measured at each point on a planar detector with the function $g(\mathbf{r}_d)$ with $\mathbf{r}_d \in \mathbb{R}^2$ or its associated Hilbert-space vector $\mathbf{g} \in \mathbb{L}_2(\mathbb{R}^2)$. Finally, we model the mapping between emission densities and data with a Hilbert-space operator $\mathcal{H} : \mathbb{L}_2(\mathbb{R}^3 \times \mathbb{S}^2) \rightarrow \mathbb{L}_2(\mathbb{R}^2)$ that acts on \mathbf{f}

$$\mathbf{g} = \mathcal{H}\mathbf{f}. \quad (4.64)$$

Several works [73, 76, 78, 80] have calculated the standard entries of \mathcal{H} for an aplanatic 4*f* optical system with a paraxial tube lens and unit magnification (or demagnified coordinates) as

$$h(\mathbf{r}_d, \mathbf{r}_o^{\perp}, r_o^{\parallel}, \hat{\mathbf{s}}_o) \equiv (\hat{\mathbf{e}}(\mathbf{r}_d), \mathcal{H}\hat{\mathbf{e}}(\mathbf{r}_o^{\perp})\hat{\mathbf{e}}(r_o^{\parallel})\hat{\mathbf{e}}(\hat{\mathbf{s}}_o)) = \sum_{i=0,1} |c_i(\mathbf{r}_d - \mathbf{r}_o^{\perp}, r_o^{\parallel}, \hat{\mathbf{s}}_o)|^2, \quad (4.65)$$

where

$$c_i(\mathbf{r}^\perp, r_o^{\parallel}, \hat{\mathbf{s}}_o) = \int_{\mathbb{R}^2} d\boldsymbol{\tau} C_i(\boldsymbol{\tau}, r_o^{\parallel}, \hat{\mathbf{s}}_o) \exp[i2\pi\boldsymbol{\tau} \cdot \mathbf{r}^\perp] \quad (4.66)$$

is the i th component of the dipole coherent spread function,

$$C_i(\boldsymbol{\tau}, r_o^{\parallel}, \hat{\mathbf{s}}_o) = A(\boldsymbol{\tau})\Phi(\boldsymbol{\tau}, r_o^{\parallel}) \sum_{j=0,1,2} g_{ij}(\boldsymbol{\tau}) s_j \quad (4.67)$$

is the i th component of the dipole coherent transfer function,

$$A(\boldsymbol{\tau}) = (1 - |\boldsymbol{\tau}|^2)^{-1/4} \Pi(|\boldsymbol{\tau}|/\nu_c) \quad (4.68)$$

is the aplanatic apodization function with full width $\nu_c = 2\text{NA}/\lambda$,

$$\Phi(\boldsymbol{\tau}, r_o^{\parallel}) = \exp \left[i2\pi r_o^{\parallel} \sqrt{\nu_m^2 - |\boldsymbol{\tau}|^2} \right] \quad (4.69)$$

is a phase-encoding function with $\nu_m = n_0/\lambda$, the functions $g_{ij}(\boldsymbol{\tau})$ model the i th field components in the pupil plane created by the j th component of a dipole

$$\begin{aligned} g_{00}(\boldsymbol{\tau}) &= \sin^2 \phi_\tau + \cos^2 \phi_\tau \sqrt{1 - |\boldsymbol{\tau}|^2}, & g_{10}(\boldsymbol{\tau}) &= \frac{1}{2} \sin(2\phi_\tau) \left(\sqrt{1 - |\boldsymbol{\tau}|^2} - 1 \right), \\ g_{01}(\boldsymbol{\tau}) &= \frac{1}{2} \sin(2\phi_\tau) \left(\sqrt{1 - |\boldsymbol{\tau}|^2} - 1 \right), & g_{11}(\boldsymbol{\tau}) &= \cos^2 \phi_\tau + \sin^2 \phi_\tau \sqrt{1 - |\boldsymbol{\tau}|^2}, \\ g_{02}(\boldsymbol{\tau}) &= |\boldsymbol{\tau}| \cos \phi_\tau, & g_{12}(\boldsymbol{\tau}) &= |\boldsymbol{\tau}| \sin \phi_\tau, \end{aligned} \quad (4.70)$$

and s_j is the j th component of the dipole unit vector $\hat{\mathbf{s}}_o$. This model is accurate for objectives with arbitrarily high numerical apertures (provided the objective is free from aberration and satisfies the aplanatic condition). Eqs. (4.68)–(4.70) model the apodization, phase shifts, and directional electric fields in high-NA optical systems, and in chapter 3 we constructed paraxial models by approximating these functions with low-order polynomials. Modeling a

mask in the back aperture of the objective can be accomplished by modifying the amplitude A or phase Φ functions. Following Stallinga [78], we can rewrite the standard entries in a form that is more efficient for computation

$$h(\mathbf{r}_d, \mathbf{r}_o^\perp, r_o^{\parallel}, \hat{\mathbf{s}}_o) = \sum_{j,j'=0,1,2} B_{jj'}(\mathbf{r}_d - \mathbf{r}_o^\perp, r_o^{\parallel}) s_j s_{j'}, \quad (4.71)$$

where

$$B_{jj'}(\mathbf{r}^\perp, r_o^{\parallel}) = \sum_{i=0,1} \beta_{ij}(\mathbf{r}^\perp, r_o^{\parallel}) \beta_{ij'}^*(\mathbf{r}^\perp, r_o^{\parallel}), \quad (4.72)$$

and

$$\beta_{ij}(\mathbf{r}^\perp, r_o^{\parallel}) = \int_{\mathbb{R}^2} d\boldsymbol{\tau} A(\boldsymbol{\tau}) \Phi(\boldsymbol{\tau}, r_o^{\parallel}) g_{ij}(\boldsymbol{\tau}) \exp[i2\pi\boldsymbol{\tau} \cdot \mathbf{r}^\perp]. \quad (4.73)$$

For general amplitude and phase masks, six Fourier transforms need to be computed for each defocus position. If the amplitude and phase masks are radial ($A(\boldsymbol{\tau})$ and $\Phi(\boldsymbol{\tau}, r_o^{\parallel})$ are independent of ϕ_τ), then we can exploit the following symmetries

$$\beta_{00}(\mathbf{r}^\perp, r_o^{\parallel}) = \beta_{11}(\mathcal{R}_{\pi/2}\mathbf{r}^\perp, r_o^{\parallel}), \quad (4.74)$$

$$\beta_{01}(\mathbf{r}^\perp, r_o^{\parallel}) = \beta_{10}(\mathbf{r}^\perp, r_o^{\parallel}), \quad (4.75)$$

$$\beta_{02}(\mathbf{r}^\perp, r_o^{\parallel}) = \beta_{12}(\mathcal{R}_{\pi/2}\mathbf{r}^\perp, r_o^{\parallel}), \quad (4.76)$$

where $\mathcal{R}_{\pi/2}$ is an operator that rotates transverse coordinates by $\pi/2$, and only compute three Fourier transforms per defocus position.

We can calculate the entries of \mathcal{H} in other bases by relating them to the standard entries. Choosing the spherical harmonics for the input basis is convenient because it allows us to exploit the angular bandlimit of the imaging system and work in an orthonormal basis.

Calculating the entries in this basis yields

$$\begin{aligned}
H_{\ell m}(\mathbf{r}_d, \mathbf{r}_o^\perp, r_o^{\parallel}) &\equiv \left(\hat{\mathbf{e}}(\mathbf{r}_d), \mathcal{H}\hat{\mathbf{e}}(\mathbf{r}_o^\perp)\hat{\mathbf{e}}(r_o^{\parallel}) \hat{\mathbf{E}}_{\ell m} \right) \\
&= \int_{\mathbb{S}^2} d\hat{\mathbf{s}}_o h(\mathbf{r}_d, \mathbf{r}_o^\perp, r_o^{\parallel}, \hat{\mathbf{s}}_o) Y_{\ell m}(\hat{\mathbf{s}}_o) \\
&= \sum_{j,j'=0,1,2} \left[\int_{\mathbb{S}^2} d\hat{\mathbf{s}}_o Y_{\ell m}(\hat{\mathbf{s}}_o) s_j s_{j'} \right] B_{jj'}(\mathbf{r}_d - \mathbf{r}_o^\perp, r_o^{\parallel}) \\
&= \frac{4\pi}{3} \sum_{j,j'=0,1,2} G_{\ell 11}^{m\epsilon_j \epsilon_{j'}} B_{jj'}(\mathbf{r}_d - \mathbf{r}_o^\perp, r_o^{\parallel}),
\end{aligned} \tag{4.77}$$

where $\epsilon_0 = 1$, $\epsilon_1 = -1$, $\epsilon_2 = 0$, and

$$G_{\ell\ell'\ell''}^{mm'm''} = \int_{\mathbb{S}^2} d\hat{\mathbf{s}} Y_{\ell m}(\hat{\mathbf{s}}) Y_{\ell' m'}(\hat{\mathbf{s}}) Y_{\ell'' m''}(\hat{\mathbf{s}}) \tag{4.78}$$

are the real Gaunt coefficients [163, 164]. The Gaunt coefficients $G_{\ell 11}^{mm'm''}$ are only nonzero for $\ell = 0, 2$, which means that \mathcal{H} only transmits six angular components.

4.3 Results

To demonstrate our model we will specify a geometric phantom under three different limits (fast angular diffusion, slow angular diffusion, and free dipoles), specify an imaging system, then simulate the irradiance patterns generated by the phantom under these three limits.

4.3.1 Phantom

We begin by choosing the following family of angular potentials

$$v_0(\hat{\mathbf{s}}_o; \theta) = -V_0(\hat{\mathbf{s}}_o \cdot [\hat{\mathbf{y}} \sin \theta + \hat{\mathbf{z}} \cos \theta])^2, \tag{4.79}$$

where $\hat{\mathbf{s}}_o$ is the object-space angular variable, θ is the angle between the symmetry axis and the $\hat{\mathbf{z}}$ axis in the $\hat{\mathbf{y}}\text{-}\hat{\mathbf{z}}$ plane, and V_0 is a positive constant. The corresponding Boltzmann

distributions are

$$\phi_0(\hat{\mathbf{s}}_o; \theta) = Z^{-1} \exp[V_0 \beta (\hat{\mathbf{s}}_o \cdot [\hat{\mathbf{y}} \sin \theta + \hat{\mathbf{z}} \cos \theta])^2], \quad (4.80)$$

which are Watson distributions with mean orientations $[\hat{\mathbf{y}} \sin \theta + \hat{\mathbf{z}} \cos \theta]$ and concentration parameter $V_0 \beta$ [165]. For our simulations we fix the concentration parameter to $V_0 \beta = 4$. This family of dipole distributions has its mean orientation in the $\hat{\mathbf{y}}\text{-}\hat{\mathbf{z}}$ plane, but the dipoles are not restricted to this plane. Next, we define a spatio-angular potential as

$$v(\mathbf{r}_o, \hat{\mathbf{s}}_o) = v_0(\hat{\mathbf{s}}_o; [\pi/4] \mathbf{r}_o \cdot \hat{\mathbf{y}}), \quad (4.81)$$

which consists of distributions with mean orientations that change with $\mathbf{r}_o \cdot \hat{\mathbf{y}}$. We assume that spatial diffusion is negligible, so we can write the spatio-angular equilibrium distribution as

$$\phi(\mathbf{r}_o, \hat{\mathbf{s}}_o) = \phi_0(\hat{\mathbf{s}}_o; [\pi/4] \mathbf{r}_o \cdot \hat{\mathbf{y}}), \quad (4.82)$$

and we can choose a time-independent spatial density

$$\rho(\mathbf{r}_o) = \sum_{i=0}^2 \sum_{j=0}^2 \delta(\mathbf{r}_o - i\hat{\mathbf{x}} - j\hat{\mathbf{y}} - [j/4]\hat{\mathbf{z}}). \quad (4.83)$$

The geometric phantom consists of nine labeled points in a three-dimensional grid measured in μm . The three rows of points are increasingly defocused (0, 0.25, and 0.5 μm of defocus), and the three columns of points have mean orientations that are increasingly tilted away from the $\hat{\mathbf{z}}$ axis towards the $\hat{\mathbf{y}}$ axis (0, $\pi/4$, and $\pi/2$ radians between the mean orientation and the $\hat{\mathbf{z}}$ axis). Finally, we illuminate the sample with coherent light linearly polarized

along the $\hat{\mathbf{p}}$ axis with standard entries

$$\left(\hat{\mathbf{e}}(\hat{\mathbf{s}}), \mathcal{K}_{\hat{\mathbf{p}}}^{(\text{ex})} \hat{\mathbf{e}}(\hat{\mathbf{s}}') \right) = \left(\hat{\mathbf{p}} \cdot \hat{\mathbf{s}}' \right)^2 \delta(\hat{\mathbf{s}} - \hat{\mathbf{s}}'). \quad (4.84)$$

Now that we have specified the geometry of our phantom, we will calculate the emission densities under three limits (fast angular diffusion, slow angular diffusion, and free dipoles). Plugging Eqs. (4.83) and (4.84) into Eqs. (4.54) and (4.62) yields the following emission density for weak excitation of dipoles undergoing fast angular diffusion

$$f_{(\text{fast})}^{\hat{\mathbf{p}}}(\mathbf{r}_o, \hat{\mathbf{s}}_o) = \rho(\mathbf{r}_o) \left[\int_{\mathbb{S}^2} d\hat{\mathbf{s}} (\hat{\mathbf{p}} \cdot \hat{\mathbf{s}})^2 \phi(\mathbf{r}_o, \hat{\mathbf{s}}) \right] \phi(\mathbf{r}_o, \hat{\mathbf{s}}_o). \quad (4.85)$$

Using Eq. (4.55) instead of Eq. (4.54) yields the following emission density for weak excitation of dipoles undergoing slow angular diffusion

$$f_{(\text{slow})}^{\hat{\mathbf{p}}}(\mathbf{r}_o, \hat{\mathbf{s}}_o) = \rho(\mathbf{r}_o) \left[(\hat{\mathbf{p}} \cdot \hat{\mathbf{s}}_o)^2 \phi(\mathbf{r}_o, \hat{\mathbf{s}}_o) \right]. \quad (4.86)$$

For our final phantom we consider free dipoles (no angular potential) with a spatially varying ratio $6D/\kappa^{(\text{d})}$. We modify Eq. (4.57) to create the emission density

$$f_{(\text{free})}^{\hat{\mathbf{p}}}(\mathbf{r}_o, \hat{\mathbf{s}}_o) = \rho(\mathbf{r}_o) \left[1 + \frac{3(\hat{\mathbf{s}}_o \cdot \hat{\mathbf{p}})^2 - 1}{1 + 10^{(\mathbf{r}_o \cdot \hat{\mathbf{y}})-1}} \right], \quad (4.87)$$

where the factor $10^{(\mathbf{r}_o \cdot \hat{\mathbf{y}})-1}$ models a position-dependent rotational mobility in the phantom.

4.3.2 Imaging system

To simulate our imaging system, we start with a phantom $f(\mathbf{r}_o, \hat{\mathbf{s}}_o)$, change to a basis of spherical harmonics using

$$F_{\ell m}(\mathbf{r}_o) = \int_{\mathbb{S}^2} d\hat{\mathbf{s}}_o f(\mathbf{r}_o, \hat{\mathbf{s}}_o) Y_{\ell m}(\hat{\mathbf{s}}_o), \quad (4.88)$$

then simulate the data using

$$g(\mathbf{r}_d) = \sum_{\ell=0}^{\infty} \sum_{m=-\ell}^{\ell} \int_{\mathbb{R}^2} d\mathbf{r}_o H_{\ell m}(\mathbf{r}_d, \mathbf{r}_o) F_{\ell m}(\mathbf{r}_o), \quad (4.89)$$

where the matrix elements $H_{\ell m}(\mathbf{r}_d, \mathbf{r}_o)$ can be calculated with Eq. (4.77). Note that $H_{\ell m}(\mathbf{r}_d, \mathbf{r}_o) = 0$ for $\ell > 2$, so we only need to calculate $F_{\ell m}(\mathbf{r}_o)$ for $\ell \leq 2$ —six total entries.

We choose NA = 1.4, $\lambda = 500$ nm, and $n_0 = 1.5$. We sample and plot the scaled irradiance at $20\times$ the Nyquist rate, $\Delta x = 1/[20(2\nu_c)]$, so the irradiance patterns are free of aliasing.

4.3.3 Simulated irradiance patterns

Figure 4.3 shows $f_{(\text{fast})}^{\hat{\mathbf{p}}}(\mathbf{r}_o, \hat{\mathbf{s}}_o)$ under two illumination polarizations ($\hat{\mathbf{p}} = \hat{\mathbf{x}} + \hat{\mathbf{y}}$ and $\hat{\mathbf{p}} = \hat{\mathbf{x}} - \hat{\mathbf{z}}$), their images, and profiles through each image. Fast-diffusing dipoles reach their Boltzmann distribution before decaying, so the emission densities in Fig. 4.3 are Watson-distributed and rotationally symmetric about a mean axis. The emission densities are weighted by constant excitation efficiencies (see Eqs. (4.54) and (4.85)), so each Watson distribution is scaled by a constant factor. Distributions that have more dipoles aligned parallel to the polarization direction are excited most efficiently, and the emission densities in Fig. 4.3 are scaled to represent this fact.

As expected, in-focus distributions (the bottom row of distributions in Figs. 4.3(a) and 4.3(b)) generate the brightest and most rotationally symmetric irradiance patterns, while defocused distributions spread the irradiance over a larger area on the detector and oblique defocused distributions display asymmetric irradiance patterns (the top row and center column is asymmetric in the $\hat{\mathbf{y}}$ direction). Notably, fast-diffusing dipoles under different polarized illuminations create irradiance patterns with different scales and the same shape.

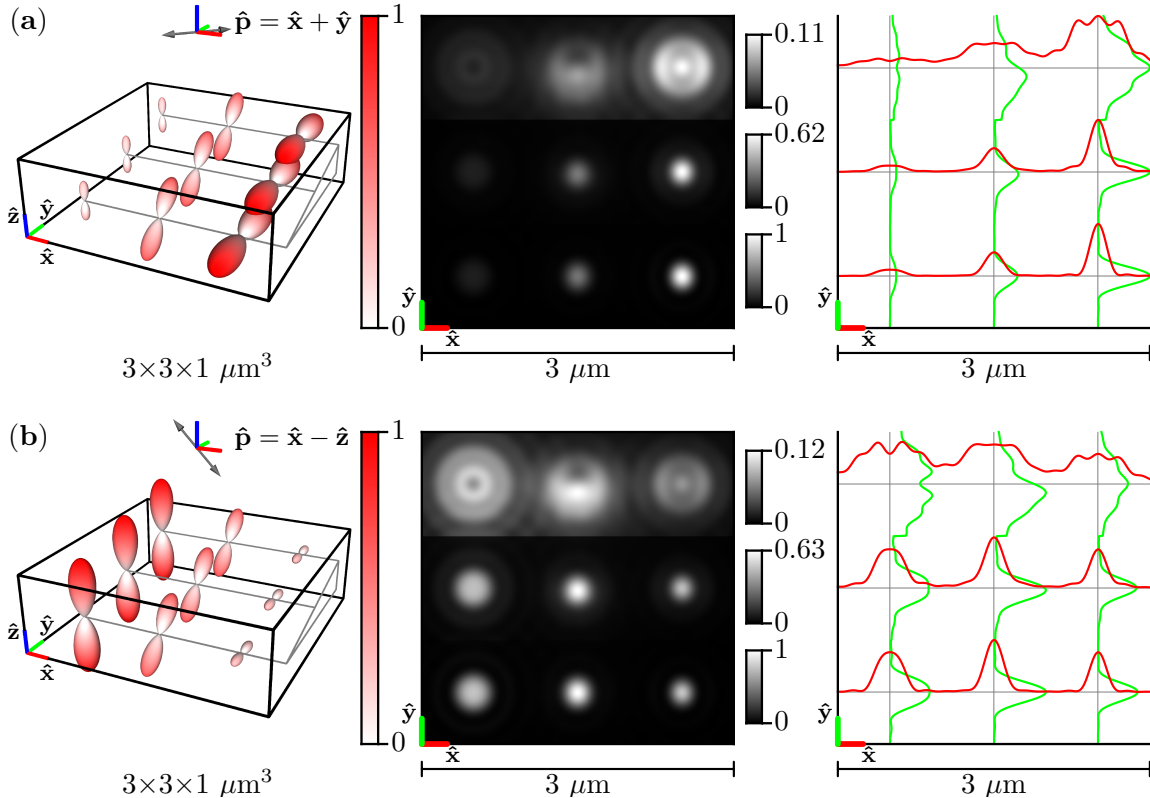


Figure 4.3: **Left:** A spatio-angular phantom undergoing fast angular diffusion—see Eq. (4.85)—under illumination by (a) $[\hat{x} + \hat{y}]$ polarized light and (b) $[\hat{x} - \hat{z}]$ polarized light. The phantom consists of nine point sources with varying defocus (rows) and mean orientation (columns). The radius and color of each glyph encode the value of the emission density $f_{(\text{fast})}^{\hat{P}}(\mathbf{r}_o, \hat{s}_o)$. **Center:** Irradiance patterns for an imaging system with $\text{NA} = 1.4$, $\lambda = 500 \text{ nm}$, and $n_0 = 1.5$ sampled at $20\times$ the Nyquist rate. Each row is individually normalized as indicated by the color bars. **Right:** Horizontal (red) and vertical (green) profiles through the irradiance pattern.

Figure 4.4 shows the same results as Fig. 4.3 but in the slow diffusion limit $f_{(\text{slow})}^{\hat{P}}(\mathbf{r}_o, \hat{s}_o)$.

Slow-diffusing dipoles do not rotate before emission, so the emission density is the point-wise product of the excitation efficiency function and the Boltzmann distribution (see Eqs. (4.55) and (4.86)). Importantly, this means that the emission densities are not rotationally symmetric (the point-wise product of two rotationally symmetric functions is not always rotationally symmetric). This asymmetry is especially apparent for Watson distributions with mean directions that are perpendicular to the polarization direction (the left column in

Fig. 4.4(a) and the right column in Fig. 4.4(b)). In addition to rotational asymmetry, slow-diffusing dipole emission density maxima are tilted towards the excitation polarized direction (see the right column in Fig. 4.4(a) and the left column in Fig. 4.4(b)), which is due to the point-wise product of the excitation efficiency function and the Boltzmann distribution.

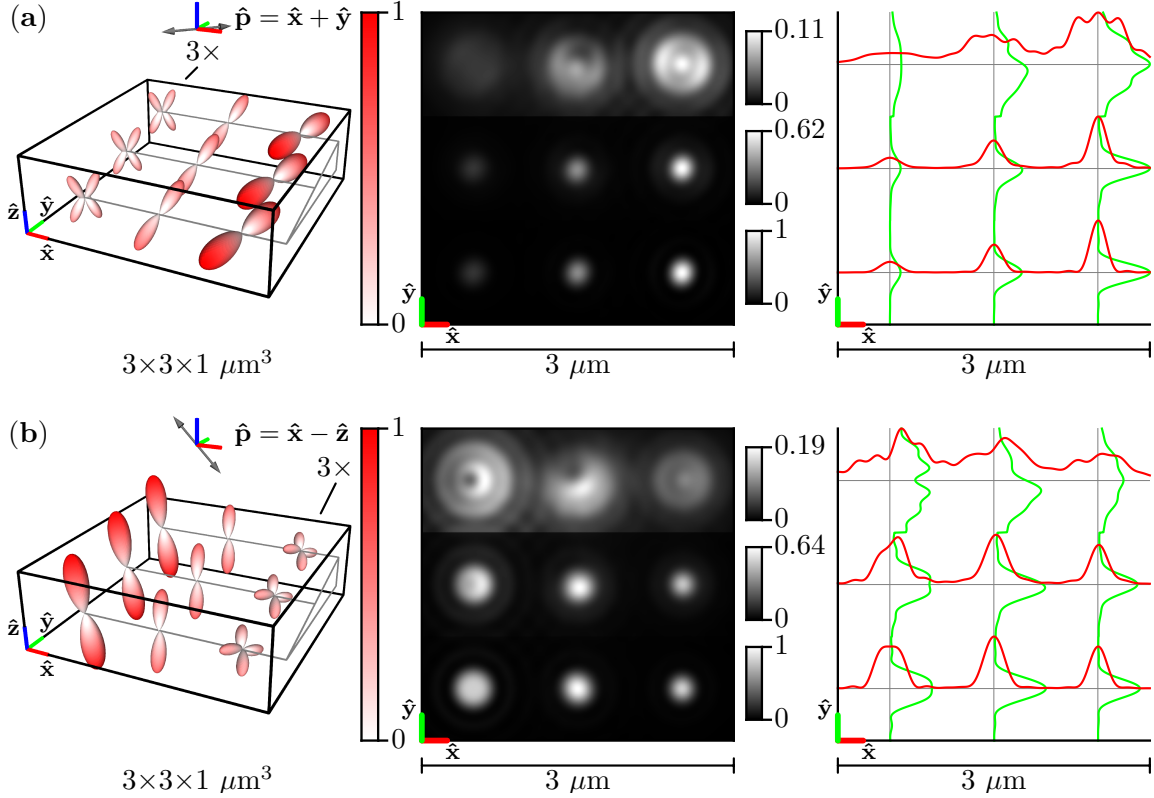


Figure 4.4: **Left:** A spatio-angular phantom undergoing slow angular diffusion—see Eq. (4.86)—under illumination by (a) $[\hat{x} + \hat{y}]$ polarized light and (b) $[\hat{x} - \hat{z}]$ polarized light. The phantom consists of nine point sources with varying defocus (rows) and mean orientation (columns). The radius and color of each glyph encode the value of the emission density $f_{(\text{slow})}^{\hat{p}}(\mathbf{r}_o, \hat{s}_o)$, and the left column (a) or right column (b) of glyphs are magnified by $3\times$ for visualization purposes. **Center:** Irradiance patterns for an imaging system with $\text{NA} = 1.4$, $\lambda = 500 \text{ nm}$, and $n_0 = 1.5$ sampled at $20\times$ the Nyquist rate. Each row is individually normalized as indicated by the color bars. **Right:** Horizontal (red) and vertical (green) profiles through the irradiance pattern.

The slow-diffusing dipoles in Fig. 4.4 display more asymmetric irradiance patterns than the fast-diffusing dipoles in Fig. 4.3. Perhaps surprisingly, defocused slow-diffusing dipoles

display irradiance asymmetry along both the $\hat{\mathbf{x}}$ and $\hat{\mathbf{y}}$ directions (see the top row and center column of Figs. 4.4(a) and 4.4(b)) despite the fact that the Watson distribution means are in the $\hat{\mathbf{y}}-\hat{\mathbf{z}}$ plane. This effect is a direct consequence of the excitation polarization—the emission density maxima are tilted towards the polarization axis, which gives the emission density maxima $\hat{\mathbf{x}}$, $\hat{\mathbf{y}}$, and $\hat{\mathbf{z}}$ components.

Figure 4.5 shows the results for the phantom of freely diffusing dipoles $f_{(\text{free})}^{\hat{\mathbf{P}}}(\mathbf{r}_o, \hat{\mathbf{s}}_o)$. For slow-diffusing free dipoles (left column), the emission density is identical to the excitation efficiency function, while for fast-diffusing free dipoles (right column), the emission density is nearly uniform. The irradiance patterns are similar for slow- and fast-diffusing free dipoles under different polarizations, but $[\hat{\mathbf{x}} - \hat{\mathbf{z}}]$ -polarized illumination of slow-diffusing defocused dipoles create asymmetric irradiance patterns (top row, left column of Fig. 4.5(b)).

4.4 Discussion and conclusions

4.4.1 When are diffusion decays multi-exponential, and when does it matter?

Existing works use monoexponential decays to model angular diffusion [76, 78, 82]—they assume that angular diffusion within a potential can be characterized by a single rotational relaxation time. We have shown that this assumption is only justified when the initial condition is a linear combination of eigenfunctions of the Smoluchowski operator that share a single non-zero eigenvalue. The monoexponential assumption is true for weak linearly polarized excitation of molecules in solution—the initial conditions and the eigenfunctions of the Smoluchowski operator are linear combinations of the $\ell = 0$ and $\ell = 2$ spherical harmonics that share a single non-zero eigenvalue. Perturbing the angular potential will change the eigenfunctions of the Smoluchowski operator and lead to multi-exponential decays.

In the limits of weak excitation and fast diffusion ($\lambda_{\mathbf{v},i} \gg \kappa^{(d)}$ for all $i > 0$) or slow dif-

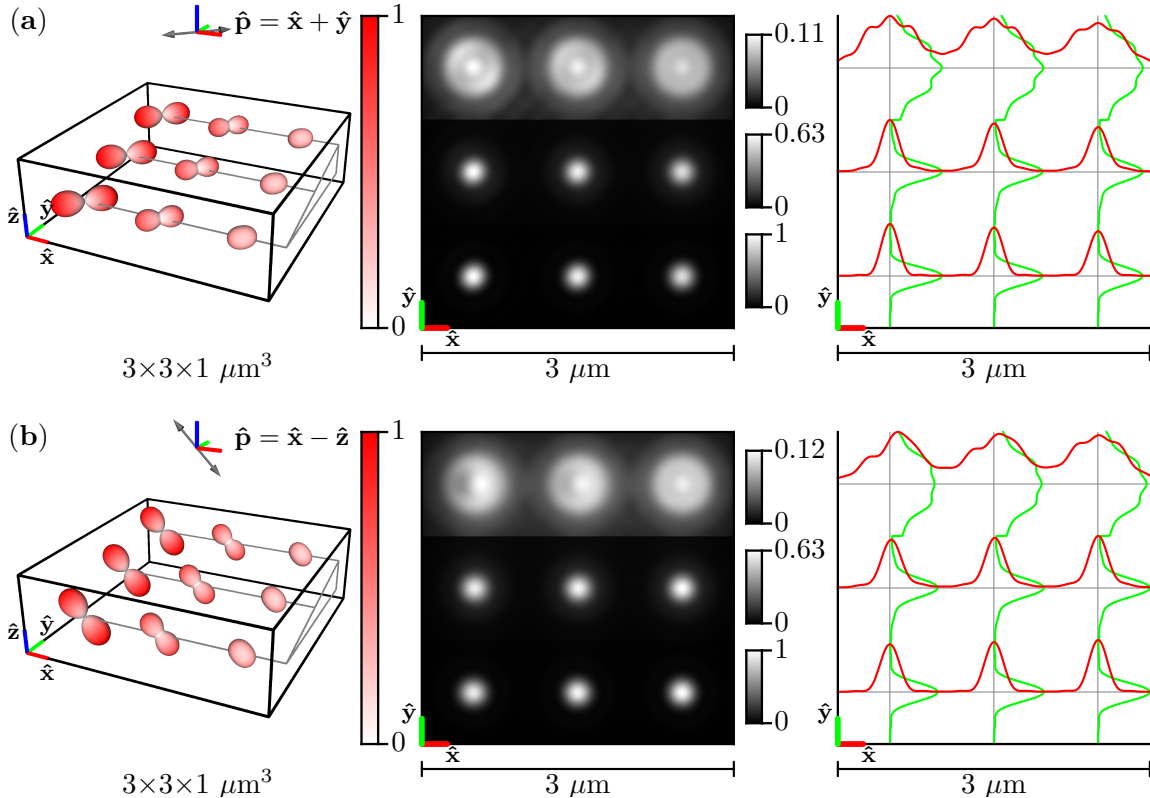


Figure 4.5: **Left:** A spatio-angular phantom consisting of free dipoles —see Eq. (4.87)— under illumination by **(a)** $[\hat{x} + \hat{y}]$ polarized light and **(b)** $[\hat{x} - \hat{z}]$ polarized light. The phantom consists of nine point sources with varying defocus (rows) and ratio of the diffusion coefficient to the decay rate $D/\kappa^{(d)}$ (columns). The radius and color of each glyph encode the value of the emission density $f_{(\text{free})}^{\hat{P}}(\tau_o, \hat{s}_o)$. **Center:** Irradiance patterns for an imaging system with $\text{NA} = 1.4$, $\lambda = 500 \text{ nm}$, and $n_0 = 1.5$ sampled at $20\times$ the Nyquist rate. Each row is individually normalized as indicated by the color bars. **Right:** Horizontal (red) and vertical (green) profiles through the irradiance pattern.

fusion ($\lambda_{\mathbf{v},i} \ll \kappa^{(d)}$), our results agree with the literature that makes the monoexponential assumption [76, 78, 82]. Weakly excited fast-diffusing dipoles reach their Boltzmann distribution before emission, so the emission density is the Boltzmann distribution multiplied by a constant excitation efficiency factor. Meanwhile, weakly excited slow-diffusing dipoles do not rotate before emission, so the emission density is the pointwise product of the excitation efficiency function and the Boltzmann distribution.

Our predictions diverge from the monoexponential literature [76, 78, 82] in the interme-

diate regime ($\lambda_{\mathbf{v},i} \approx \kappa^{(d)}$ for any $i > 0$), and the differences can be dramatic. To choose an adversarial example, consider an angular potential with two wells separated by a large but finite potential barrier. If molecules within one well are excited then they can diffuse quickly within that well, but they will take a long time to diffuse to the other well. Clearly, multiple diffusion times are needed to characterize the imaging process.

Multiple diffusion times are needed to characterize simpler angular potentials, too. Consider the widely used “wobble-in-a-cone” model with a single molecule that is initially oriented at the edge of the cone. In sections 4.2.2–4.2.3 we used differential equations and group theory to argue that the angular decay will be multi-exponential, but we can understand the argument qualitatively by approximating the diffusion as a discrete random walk of a single molecule. Initially, the dipole can move in three directions each with probability $\approx 1/3$ —clockwise, counterclockwise, and towards the center of the cone. Later, the molecule will be away from the edge of the cone, and the molecule can move in four directions with probability $\approx 1/4$. Therefore, molecules at the edge will move away from their initial condition faster on average than molecules away from the edge, so a single diffusion time is insufficient to characterize diffusion with a cone.

4.4.2 Is angular structured illumination different from polarized illumination?

We have used the term “angular structured illumination” instead of “polarized illumination” throughout this chapter for two reasons. First, unpolarized light can have angular structure—an unpolarized plane wave does not excite dipoles parallel to its propagation direction. Although we have focused on using polarized light to alias high angular frequency information into the passband, unpolarized light can be used to the same effect (albeit with less efficient aliasing than polarized light). Second, “angular structured illumination” highlights the deep similarity with spatial structured illumination. Readers familiar with spatial structured

illumination can apply their intuition to angular structured illumination techniques, and many existing spatial techniques have direct angular analogs.

4.4.3 How many angular components can we image?

The spatio-angular imaging operator \mathcal{H} only transmits six angular components, so \mathcal{H} can be decomposed into two operators: $\mathcal{H} = \mathcal{H}'\mathcal{P}$, where $\mathcal{P} : \mathbb{L}_2(\mathbb{R}^3 \times \mathbb{S}^2) \rightarrow [\mathbb{L}_2(\mathbb{R}^3)]^6$ is a projection operator onto the direct sum of six $\mathbb{L}_2(\mathbb{R}^3)$ spaces, and $\mathcal{H}' : [\mathbb{L}_2(\mathbb{R}^3)]^6 \rightarrow \mathbb{L}_2(\mathbb{R}^2)$. The fact that only six angular components are transmitted is a direct consequence of the angular band limit imposed by dipole radiation.

However, angular structured illumination allows us to alias a much larger number of angular components into the passband of the imaging system. For strong excitation of dipoles undergoing slow angular diffusion, a theoretically unlimited number of angular components can be aliased into the passband—see Eq. (4.47) and Fig. 4.1. Of course, the number of angular components is practically limited by diffusion, photobleaching, and noise—see Gustafsson [161] for an analogous discussion of how these factors affect spatial non-linear structured illumination. More practically, weak excitation of dipoles undergoing slow angular diffusion allows us to alias a total of fifteen angular components into the passband of the imaging system (corresponding to the $\ell = 0, 2, 4$ spherical harmonics). For fast-diffusing dipoles, aliasing does not occur and only six angular components (corresponding to the $\ell = 0, 2$ spherical harmonics) can be imaged.

Many other non-linear techniques can be used to alias high-frequency angular components into the passband. Two-photon excitation beams excite with a $\cos^4 \theta$ dependence, so a two-photon beam can alias higher angular frequencies than an equivalent single-photon beam [56]. A wide variety of other techniques that exploit three- or multi-state fluorescent molecules to alias high spatial frequencies can be adapted to alias high angular frequencies—see the supplement of [166] for a summary of non-linear spatial structured illumination techniques. For

a particular example, Hafi et al. adapted stimulated emission depletion microscopy (STED) to the angular case in a technique they called excitation polarization angle narrowing (ExPAN) [167]. Although they claimed their technique provided improved spatial resolution, this claim has been challenged [168] and we view ExPAN as a technique that provides improved angular resolution that can be used to infer higher spatial resolution if the coupling between spatial and angular information is known.

We have focused on cases where the exposure time is much longer than the diffusion and decay times—so-called *steady-state* experiments—but exposure times comparable to diffusion and decay times—so-called *time-resolved* experiments—are possible [60, 169, 170]. We can model these experiments within our framework by changing the limits of integration in Eqs. (4.42) or (4.61). Time-resolved experiments allow for the measurement of more angular components than steady-state experiments, and we view these techniques as important future directions.

4.4.4 How many angular components can we reconstruct?

Imaging an angular component is only the first step towards estimating an angular component. To estimate a parameter it must be a linear combination of eigenfunctions of $\mathcal{H}^\dagger \mathcal{H}$ with non-zero eigenvalues (equivalently, a linear combination of the right singular vectors of \mathcal{H} with non-zero singular values) [1, ch. 13.3]. We will explore these functions—the so-called *measurement space* of \mathcal{H} —in the next chapter.

For now we briefly mention two strategies for reconstructing multiple angular components. The first approach is to take N sequential measurements of the same object after changing the illumination or detection polarization, then use these measurements to reconstruct the angular components at each spatial position independently [37, 39, 48, 51, 55, 59, 115]. This approach amounts to approximating the complete imaging process $\mathcal{H}_{\text{multi}} : \mathbb{L}_2(\mathbb{R}^3 \times \mathbb{S}^2) \rightarrow [\mathbb{L}_2(\mathbb{R}^2)]^N$ with an imaging operator for each spatial point

$\mathcal{H}_{\text{point}} : \mathbb{L}_2(\mathbb{S}^2) \rightarrow \mathbb{R}^N$. Although this approach simplifies the reconstruction problem, it ignores valuable information that can be exploited. We advocate for joint spatio-angular reconstructions that use everything we know about the physics of the imaging process.

The second approach is to image single molecules and use their images to estimate angular components [68, 80, 82, 85]. In this case the imaging process can be modeled with a single imaging operator for each molecule $\mathcal{H}_{\text{single}} : \mathbb{L}_2(\mathbb{S}^2) \rightarrow \mathbb{L}_2(\mathbb{R}^2)$. This chapter’s potential contributions to single-molecule imaging are improved imaging operators $\mathcal{H}_{\text{single}}$ that can be used to access more parameters (multiple diffusion constants or high angular frequency components).

4.4.5 Stochastic spatio-angular imaging

A major limitation of this chapter is that we have only modeled the ensemble average behavior of dipole diffusion, emission, and imaging, when these processes are actually stochastic processes. More specifically, angular diffusion is a random walk on the sphere, emission is an exponential process, and photon imaging is a Poisson process. Existing works have modeled these stochastic processes and then extracted the ensemble averages [76, 78, 82], while here we have modeled the ensemble averages directly.

In this chapter we have focused on describing ensemble average features that have either been previously assumed absent (like the multi-exponential nature of diffusion) or not previously described (like non-linear angular structured illumination). Ultimately, optimal reconstructions will require complete stochastic descriptions of the imaging process so that correlations in the data can be exploited, and we consider stochastic descriptions of dipole imaging important future work.

CHAPTER 5

INVERSE PROBLEMS, SINGULAR-VALUE DECOMPOSITIONS, AND RECONSTRUCTION ALGORITHMS

Without any underlying symmetry properties,
the job of proving interesting results becomes extremely unpleasant.
The enjoyment of one's tools is an essential ingredient of successful work.
— DONALD E. KNUTH *The Art of Computer Programming Vol. II* (1969)

In chapters 2–4 we developed spatio-angular forward models for each step of the measurement process—polarized excitation, angular diffusion, and imaging. We used these models to develop an intuition for these imaging systems and to simulate the data generated by numerical phantoms. Although these models are valuable in their own right, their complete value emerges when they are combined with practical reconstruction algorithms that can estimate spatio-objects from measured data.

In this chapter we will pose several inverse problems and propose reconstruction algorithms for their solution. In chapter 4 we saw that the relationship between object parameters and the measured data can be extremely *nonlinear*—a scaled sum of inputs does not always result in a scaled sum of outputs. Solving nonlinear inverse problems can be extremely challenging and the algorithm developer can rarely make guarantees about the properties of the solutions. Oftentimes the most practical approach is to measure or simulate object-data pairs and use these pairs to train a nonlinear inverse model like a neural network [171]. Although these approaches are valid, we would prefer to avoid choosing which object-data pairs to measure or simulate, and we would like to guarantee as many properties about our reconstructions as we can. Fortunately, under weak restrictions on the object and measurements we can pose *linear* reconstruction problems that can be analyzed and solved efficiently using the *singular value decomposition* (SVD) [1, ch. 1].

The SVD provides deep insights into the behavior of a linear imaging system. If we have an infinite-dimensional Hilbert-space vector $\mathbf{f} \in \mathbb{U}$ that represents the object we would like to estimate, a J -dimensional vector of measurements $\mathbf{g} \in \mathbb{R}^J$, and an imaging operator $\mathcal{H} : \mathbb{U} \rightarrow \mathbb{V} = \mathbb{R}^J$ that acts linearly, i.e. if $\mathbf{g} = \mathcal{H}\mathbf{f}$ then $\alpha_1\mathbf{g}_1 + \alpha_2\mathbf{g}_2 = \mathcal{H}[\alpha_1\mathbf{f}_1 + \alpha_2\mathbf{f}_2]$ for scalar-valued α_1 and α_2 , then we can rewrite \mathcal{H} in terms of its SVD

$$\mathbf{g} = \mathcal{H}\mathbf{f} = \sum_{i=1}^R \sqrt{\mu_i} \mathbf{v}_i (\mathbf{u}_i, \mathbf{f}), \quad (5.1)$$

where R is the rank of \mathcal{H} , (\cdot, \cdot) denotes the inner product on \mathbb{U} , and $\{\mathbf{u}_i, \mathbf{v}_i, \mu_i\}$ is the *singular system* of \mathcal{H} that satisfies the eigenvalue equations

$$\mathcal{H}^\dagger \mathcal{H} \mathbf{u}_i = \mu_i \mathbf{u}_i, \quad (5.2)$$

$$\mathcal{H} \mathcal{H}^\dagger \mathbf{v}_i = \mu_i \mathbf{v}_i. \quad (5.3)$$

An arbitrary object \mathbf{f} can always be decomposed into the sum of two parts $\mathbf{f} = \mathbf{f}_{\text{meas}} + \mathbf{f}_{\text{null}}$ where $(\mathbf{u}_i, \mathbf{f}_{\text{meas}}) \neq 0$ and $(\mathbf{u}_i, \mathbf{f}_{\text{null}}) = 0$. With Eq. (5.1) in view, it is clear that \mathbf{f}_{null} will not contribute to the measured data, so \mathbf{f}_{null} will be impossible to reconstruct without using prior information about the object. Meanwhile, \mathbf{f}_{meas} does contribute to the data, and we can attempt to recover this component from the data. Equivalently, we can say that object space \mathbb{U} can be orthogonally decomposed into the direct sum of two subspaces $\mathbb{U} = \mathbb{U}_{\text{meas}} \oplus \mathbb{U}_{\text{null}}$. The object-space singular functions \mathbf{u}_i associated with non-zero eigenvalues $\mu_i \neq 0$ span the *measurement space* \mathbb{U}_{meas} , while the object-space singular functions associated with zero eigenvalues $\mu_i = 0$ span the *null space* \mathbb{U}_{null} .

The eigenvalues μ_i can provide further insights into the imaging process. The magnitude of an eigenvalue tells us how efficiently the imaging system can transmit its associated singular function \mathbf{u}_i to the data. Singular functions associated with the smallest eigenvalues are most easily corrupted by noise, so they are the most challenging components of the object

to recover. Second, degenerate eigenvalues indicate symmetries of the imaging system, and these symmetries can be exploited to reduce the number of eigenvalues and singular functions that need to be calculated and stored. Throughout this chapter we will formulate all of our algorithms in terms of μ_i , the eigenvalues of $\mathcal{H}^\dagger \mathcal{H}$, but we could equally formulate in terms of $\sigma_i = \sqrt{\mu_i}$, the singular values of \mathcal{H} .

The SVD also leads to a simple and efficient class of reconstruction algorithms. A reasonable starting place for estimating an object \mathbf{f} from data \mathbf{g} is to solve the least-squares optimization problem

$$\hat{\mathbf{f}}_{\text{LS}} = \underset{\mathbf{f}}{\operatorname{argmin}} \|\mathbf{g} - \mathcal{H}\mathbf{f}\|^2. \quad (5.4)$$

This optimization problem has a closed-form solution that is easily expressed in terms of the singular system of \mathcal{H}

$$\hat{\mathbf{f}}_{\text{LS}} = \sum_{i=1}^R \frac{1}{\sqrt{\mu_i}} \mathbf{u}_i (\mathbf{v}_i, \mathbf{g}). \quad (5.5)$$

This solution can be statistically justified as the maximum-likelihood estimator for data corrupted by uncorrelated Gaussian noise [1, ch. 13.3.4]. The solution in Eq. (5.5) carries a well-known problem—division by small eigenvalues μ_i can amplify noise to unacceptable levels. One approach to fixing this problem is to add a *Tikhonov regularization* term to the optimization problem

$$\hat{\mathbf{f}}_\eta = \underset{\mathbf{f}}{\operatorname{argmin}} \|\mathbf{g} - \mathcal{H}\mathbf{f}\|^2 + \eta \|\mathbf{f}\|^2, \quad (5.6)$$

where η is a positive constant. Once again, this optimization problem has a closed-form

solution in terms of the singular system of \mathcal{H}

$$\hat{\mathbf{f}}_\eta = \sum_{i=1}^R \frac{\sqrt{\mu_i}}{\mu_i + \eta} \mathbf{u}_i (\mathbf{v}_i, \mathbf{g}). \quad (5.7)$$

Statistically, adding a Tikhonov regularizer can be interpreted as applying a Bayesian prior that assumes the unknown parameters to be independent, zero-mean, Gaussian-distributed random variables with variance $1/(2\eta)$ [1, ch. 15.3.3]. Although this might be an unlikely assumption, adding a Tikhonov regularizer is a widely used and practical way to control noise amplification in linear reconstructions.

None of the mathematical techniques in this chapter are new—least-squares solutions were first used by Gauss in the 1790s (though Legendre published first in 1805) [172, 173], the theory of singular value decompositions of compact linear operators was developed by Schmidt in 1907 [174, 175], and Tikhonov regularizers were first applied in 1963 [176]. More recently, Barrett and colleagues at the University of Arizona have calculated singular value decompositions for a wide range of imaging systems [1, 177–183], and these techniques have started to gain wider use [184, 185]. Although we are applying well-established mathematical techniques, to our knowledge this is the first work to consider singular value decompositions when the object space is $\mathbb{U} = \mathbb{L}_2(\mathbb{R}^2 \times \mathbb{S}^2)$. This space is mathematically interesting because it consists of functions on the product space of a non-compact manifold \mathbb{R}^2 and a compact manifold \mathbb{S}^2 , which leads to a discrete set of continuous singular value spectra.

This chapter also contributes to the literature that considers the fundamental limits of polarized fluorescence microscopy [84, 117, 186, 187], and this work is the first to use singular-value decompositions to analyze which parameters of a fluorescent object can be reconstructed from measurements. Several works have used singular value decompositions to optimize measurements for reconstructing the polarization state of light [188–190], but here we focus on recovering parameters of fluorescent objects instead of the polarization state of light.

This chapter is organized as follows. We begin by posing a general nonlinear inverse problem, and we find the conditions under which the inverse problem is approximately linear. Next, we calculate singular value decompositions of three illustrative spatio-angular imaging systems. First, we consider angularly uniform excitation (for example, with unpolarized light and a high-NA condenser) of a thin sample under a high-NA detection arm. Second, we analyze a simple hypothetical instrument that uses polarized excitation to excite fluorophores in a cuvette with a surrounding hemispherical detector. We use this simple case to build our intuition and to calculate optimal polarization sampling schemes. Third, we consider the general case of a microscope that uses both polarized illumination and high-NA detection. We have chosen these three instruments to develop intuition about the illumination side alone, the detection side alone, and their combination. Finally, we describe a Tikhonov-regularized pseudoinverse reconstruction algorithm with an efficient implementation, and we conclude with a discussion.

5.1 Inverse problems

We start by posing a reasonably general class of spatio-angular inverse problems. First, consider an ensemble of two-state fluorescent molecules with aligned dipole absorption and emission moments. These molecules undergo spatial and angular diffusion while being excited with illumination light and decaying to emit photons that we can manipulate and detect. We have the freedom to make multiple measurements of the object by manipulating the excitation light or by manipulating the emitted photons and detector bins, but we can not control the position, diffusion, or decay dynamics of the molecules. Our goal is to choose measurements that can be used to recover as much as possible about the position, orientation, and dynamics of these fluorescent molecules. Ideally enough information can be recovered that the experimentalist can draw new conclusions about the molecules and their environment.

Mathematically, we can describe this ensemble using two functions $f^{(\text{gr})}(\mathbf{r}_o, \hat{\mathbf{s}}_o, t)$ and $f^{(\text{ex})}(\mathbf{r}_o, \hat{\mathbf{s}}_o, t)$ (or their associated Hilbert-space vectors $\mathbf{f}^{(\text{gr})}(t)$ and $\mathbf{f}^{(\text{ex})}(t)$) that describe the number of molecules per unit volume at position \mathbf{r}_o per unit solid angle oriented along $\hat{\mathbf{s}}_o$ per unit time at time t in the ground and excited states, respectively. We assume that these molecules are diffusing in a general potential $v(\mathbf{r}_o, \hat{\mathbf{s}}_o)$, that they are decaying with a general rate constant $\kappa^{(\text{d})}(\mathbf{r}_o, \hat{\mathbf{s}}_o)$, and that during the j th measurement they are being excited with a general rate constant $\kappa_j^{(\text{ex})}(\mathbf{r}_o, \hat{\mathbf{s}}_o)$. These dynamics can be captured by the following pair of coupled differential equations

$$\frac{\partial}{\partial t} \begin{bmatrix} \mathbf{f}^{(\text{ex})}(t) \\ \mathbf{f}^{(\text{gr})}(t) \end{bmatrix} = \begin{bmatrix} \mathcal{D}_{\mathbf{v}} - \mathcal{K}^{(\text{d})} & \mathcal{K}_j^{(\text{ex})} \\ \mathcal{K}^{(\text{d})} & \mathcal{D}_{\mathbf{v}} - \mathcal{K}_j^{(\text{ex})} \end{bmatrix} \begin{bmatrix} \mathbf{f}^{(\text{ex})}(t) \\ \mathbf{f}^{(\text{gr})}(t) \end{bmatrix}, \quad (5.8)$$

where $\mathcal{D}_{\mathbf{v}}$ is a Smoluchowski operator that models spatio-angular diffusion with entries

$$(\hat{\mathbf{e}}(\mathbf{r}_o, \hat{\mathbf{s}}_o), \mathcal{D}_{\mathbf{v}} \hat{\mathbf{e}}(\mathbf{r}'_o, \hat{\mathbf{s}}'_o)) = \nabla \cdot \exp[-\beta v(\mathbf{r}_o, \hat{\mathbf{s}}_o)] \mathbf{D} \exp[\beta v(\mathbf{r}'_o, \hat{\mathbf{s}}'_o)], \quad (5.9)$$

where ∇ is a gradient on $\mathbb{R}^3 \times \mathbb{S}^2$, \mathbf{D} is a generalized diffusion tensor, and $\beta = 1/k_B T$; $\mathcal{K}^{(\text{d})}$ models decay with entries

$$(\hat{\mathbf{e}}(\mathbf{r}_o, \hat{\mathbf{s}}_o), \mathcal{K}^{(\text{d})} \hat{\mathbf{e}}(\mathbf{r}'_o, \hat{\mathbf{s}}'_o)) = \kappa^{(\text{d})}(\mathbf{r}_o, \hat{\mathbf{s}}_o) \delta(\mathbf{r}_o - \mathbf{r}'_o) \delta(\hat{\mathbf{s}}_o - \hat{\mathbf{s}}'_o); \quad (5.10)$$

and $\mathcal{K}_j^{(\text{ex})}$ models the illumination pattern for the j th measurement with entries

$$(\hat{\mathbf{e}}(\mathbf{r}_o, \hat{\mathbf{s}}_o), \mathcal{K}_j^{(\text{ex})} \hat{\mathbf{e}}(\mathbf{r}'_o, \hat{\mathbf{s}}'_o)) = \kappa_j^{(\text{ex})}(\mathbf{r}_o, \hat{\mathbf{s}}_o) \delta(\mathbf{r}_o - \mathbf{r}'_o) \delta(\hat{\mathbf{s}}_o - \hat{\mathbf{s}}'_o). \quad (5.11)$$

If the molecules start in the ground state with spatial density $\rho(\mathbf{r}_o)$, then the initial condition is given by $f^{(\text{ex})}(\mathbf{r}_o, \hat{\mathbf{s}}_o, 0) = 0$ and $f^{(\text{gr})}(\mathbf{r}_o, \hat{\mathbf{s}}_o, 0) = \rho(\mathbf{r}_o)$. After solving Eq. (5.8) we can model the emission density during the j th measurement measured from time $t_{0,j}$ to time $t_{1,j}$

as

$$f_j(\mathbf{r}_o, \hat{\mathbf{s}}_o) = \int_{t_{0,j}}^{t_{1,j}} dt \kappa_j^{(d)}(\mathbf{r}_o, \hat{\mathbf{s}}_o) f^{(\text{ex})}(\mathbf{r}_o, \hat{\mathbf{s}}_o, t). \quad (5.12)$$

Finally, we can model the irradiance measured in the j th measurement by integrating the emission density $f_j(\mathbf{r}_o, \hat{\mathbf{s}}_o)$ multiplied by the point-response function $h_j^{(\text{det})}(\mathbf{r}_o, \hat{\mathbf{s}}_o)$

$$g_j = \int_{\mathbb{R}^3} d\mathbf{r}_o \int_{\mathbb{S}^2} d\hat{\mathbf{s}}_o h_j^{(\text{det})}(\mathbf{r}_o, \hat{\mathbf{s}}_o) f_j(\mathbf{r}_o, \hat{\mathbf{s}}_o). \quad (5.13)$$

We note that the experimentalist has freedom to choose excitation rate constants $\kappa_j^{(\text{ex})}(\mathbf{r}_o, \hat{\mathbf{s}}_o)$, detector responses $h_j^{(\text{det})}(\mathbf{r}_o, \hat{\mathbf{s}}_o)$, and measurement times $t_{0,j}$ and $t_{1,j}$. We also note that j can index many kinds of measurements—pixels on a detector, views of a multiview microscope, defocus settings, light-sheet scan positions, polarizer settings, etc.—so this framework is general enough to model a broad class of fluorescence microscopes.

Now that we have paid the notational overhead, we can propose a candidate for a *general fluorescence microscopy inverse problem*: given measurements g_j , a measurement scheme $\{\kappa_j^{(\text{ex})}(\mathbf{r}_o, \hat{\mathbf{s}}_o), h_j^{(\text{det})}(\mathbf{r}_o, \hat{\mathbf{s}}_o), t_{0,j}, t_{1,j}\}$, and the forward model in Eqs. (5.8)–(5.13), recover as much as possible about the labeling density $\rho(\mathbf{r}_o)$, the potential $v(\mathbf{r}_o, \hat{\mathbf{s}}_o)$, and the decay rates $\kappa_j^{(d)}(\mathbf{r}_o, \hat{\mathbf{s}}_o)$. This is an extremely nonlinear inverse problem that will be very challenging to solve.

One way to linearize the inverse problem is to lower our expectations for what we can hope to reconstruct. For example, Eq. (5.13) shows that there is a linear relationship between the data g_j and the emission density $f_j(\mathbf{r}_o, \hat{\mathbf{s}}_o)$. If we choose a fixed illumination pattern, then the emission density $f_j(\mathbf{r}_o, \hat{\mathbf{s}}_o)$ no longer depends on the illumination (mathematically, it loses its j dependence) and we can use linear reconstructions to recover it from the data. However, the emission density is not a particularly interesting object to reconstruct since it changes with the illumination pattern. We would prefer to recover illumination-invariant

properties of the sample if possible.

One way to find an illumination-invariant property of the sample is to linearize the problem by making assumptions (or by arranging experimental conditions that satisfy assumptions) about our object and measurements. In chapter 4 we showed that if (a) spatial diffusion is negligible, (b) angular diffusion is consistent with a spherical rotor model (c) excitation is weak to avoid saturation effects, (d) angular diffusion times are long compared to the fluorescence decay times, (e) exposure times are long compared to the diffusion and fluorescence decay times, (f) and the measurements are collected long after initial transient diffusion and fluorescence decay times (fluorescence dynamics have reached a steady state), then the following relationship holds

$$g_j = \int_{\mathbb{R}^3} d\mathbf{r}_o \int_{\mathbb{S}^2} d\hat{\mathbf{s}}_o h_j^{(\text{det})}(\mathbf{r}_o, \hat{\mathbf{s}}_o) h_j^{(\text{exc})}(\mathbf{r}_o, \hat{\mathbf{s}}_o) \bar{f}(\mathbf{r}_o, \hat{\mathbf{s}}_o), \quad (5.14)$$

where the excitation point response function is just a renamed version of the excitation rate constant

$$h_j^{(\text{exc})}(\mathbf{r}_o, \hat{\mathbf{s}}_o) = \kappa_j^{(\text{exc})}(\mathbf{r}_o, \hat{\mathbf{s}}_o), \quad (5.15)$$

and

$$\bar{f}(\mathbf{r}_o, \hat{\mathbf{s}}_o) = \rho(\mathbf{r}_o) \frac{\exp[-\beta v(\mathbf{r}_o, \hat{\mathbf{s}}_o)]}{\int_{\mathbb{S}^2} d\hat{\mathbf{s}} \exp[-\beta v(\mathbf{r}_o, \hat{\mathbf{s}}_o)]} \quad (5.16)$$

is the *spatio-angular Boltzmann density*—the product of the labeling density $\rho(\mathbf{r}_o)$ and the angular Boltzmann distribution at each spatial point. Notice that we distinguish the spatio-angular emission density f from the spatio-angular Boltzmann density \bar{f} with an overbar. The relationship between $\bar{f}(\mathbf{r}_o, \hat{\mathbf{s}}_o)$ and the data is linear, so the spatio-angular Boltzmann density is a reasonable candidate for us to try and reconstruct using the singular value decomposition. Therefore, Eq. (5.16) relates the sample properties $\rho(\mathbf{r}_o)$ and $v(\mathbf{r}_o, \hat{\mathbf{s}}_o)$ to our

reconstruction target $\bar{f}(\mathbf{r}_o, \hat{\mathbf{s}}_o)$. We emphasize that the spatio-angular Boltzmann density is only a reasonable target for reconstruction when conditions (a)–(f) are satisfied. If these conditions are not satisfied then we can either solve the modest problem of reconstructing the emission density $f(\mathbf{r}_o, \hat{\mathbf{s}}_o)$ or tackle the more general nonlinear problem. From this point forward we will assume that conditions (a)–(f) are satisfied unless we note otherwise.

5.2 SVD of uniform excitation with epi-detection

For our first SVD we make several simplifications to the general model in Eq. (5.14). First, we assume that the object is restricted to a single plane and let $\mathbf{r}_o \rightarrow \mathbf{r}_o^\perp$. Second, we assume that our measurements are made everywhere on a continuous two-dimensional plane and let $j \rightarrow \mathbf{r}_d \in \mathbb{R}^2$. This is an approximate model for a two-dimensional detector with small pixels. Third, we assume that the illumination pattern is constant $h^{(\text{ex})}(\mathbf{r}_o^\perp, \hat{\mathbf{s}}_o) = 1$, a condition that can be achieved by illuminating with unpolarized light, a high-NA condenser, and Köhler illumination. Finally, we assume that the imaging system is laterally shift-invariant. Under these conditions, the forward model takes the form

$$g(\mathbf{r}_d) = \int_{\mathbb{R}^2} d\mathbf{r}_o^\perp \int_{\mathbb{S}^2} d\hat{\mathbf{s}}_o h^{(\text{det})}(\mathbf{r}_d - \mathbf{r}_o^\perp, \hat{\mathbf{s}}_o) \bar{f}(\mathbf{r}_o^\perp, \hat{\mathbf{s}}_o). \quad (5.17)$$

We briefly note that this equation can be interpreted in two ways. The first interpretation is the one we just presented—angularly uniform excitation makes $h^{(\text{ex})}(\mathbf{r}_o^\perp, \hat{\mathbf{s}}_o) = 1$ and we are attempting to estimate $\bar{f}(\mathbf{r}_o^\perp, \hat{\mathbf{s}}_o)$. Alternatively, Eq. (5.17) takes a form similar to Eq. (5.13), which maps the emission density to the data. This leads to an interpretation where we are trying to recover the emission density $f(\mathbf{r}_o, \hat{\mathbf{s}}_o)$ from the data independent of the illumination pattern. By analyzing the kernel $h^{(\text{det})}(\mathbf{r}_d - \mathbf{r}_o^\perp, \hat{\mathbf{s}}_o)$, we can draw conclusions about both of these cases.

It will be convenient to define an associated linear Hilbert space operator $\mathcal{H}^{(\text{det})}$ with entries

$$(\hat{\mathbf{e}}(\mathbf{r}_d), \mathcal{H}^{(\text{det})}\hat{\mathbf{e}}(\mathbf{r}_o^\perp)\hat{\mathbf{e}}(\hat{\mathbf{s}}_o)) = h^{(\text{det})}(\mathbf{r}_d - \mathbf{r}_o^\perp, \hat{\mathbf{s}}_o). \quad (5.18)$$

If an aplanatic $4f$ optical system with a paraxial tube lens and unit magnification (or de-magnified coordinates) images a plane at a constant defocus position r_o^{\parallel} , the operator entries are given by [73, 76, 78, 80]

$$h^{(\text{det})}(\mathbf{r}_d - \mathbf{r}_o^\perp, \hat{\mathbf{s}}_o) = \sum_{j,j'=0,1,2} B_{jj'}(\mathbf{r}_d - \mathbf{r}_o^\perp, r_o^{\parallel}) s_j s_{j'}, \quad (5.19)$$

where

$$B_{jj'}(\mathbf{r}^\perp, r_o^{\parallel}) = \sum_{i=0,1} \beta_{ij}(\mathbf{r}^\perp, r_o^{\parallel}) \beta_{ij'}^*(\mathbf{r}^\perp, r_o^{\parallel}) \quad (5.20)$$

is the irradiance created at position \mathbf{r}^\perp on the detector when an $s_j s_{j'}$ angular distribution is placed at defocus position r_o^{\parallel} ,

$$\beta_{ij}(\mathbf{r}^\perp, r_o^{\parallel}) = \int_{\mathbb{R}^2} d\boldsymbol{\tau} A(\boldsymbol{\tau}) \Phi(\boldsymbol{\tau}, r_o^{\parallel}) g_{ij}(\boldsymbol{\tau}) \exp[i2\pi\boldsymbol{\tau} \cdot \mathbf{r}^\perp] \quad (5.21)$$

is the i th component of the electric field created at position \mathbf{r}^\perp on the detector by the j th component of a dipole,

$$A(\boldsymbol{\tau}) = (1 - |\boldsymbol{\tau}|^2)^{-1/4} \Pi(|\boldsymbol{\tau}|/\nu_c) \quad (5.22)$$

is the aplanatic apodization function with full width $\nu_c = 2\text{NA}/\lambda$,

$$\Phi(\boldsymbol{\tau}, r_o^{\parallel}) = \exp \left[i2\pi r_o^{\parallel} \sqrt{\nu_m^2 - |\boldsymbol{\tau}|^2} \right] \quad (5.23)$$

encodes the defocus phase with $\nu_m = n_0/\lambda$, the functions $g_{ij}(\boldsymbol{\tau})$ model the i th field components in the pupil plane created by the j th component of a dipole

$$\begin{aligned} g_{00}(\boldsymbol{\tau}) &= \sin^2 \phi_\tau + \cos^2 \phi_\tau \sqrt{1 - |\boldsymbol{\tau}|^2}, & g_{10}(\boldsymbol{\tau}) &= \frac{1}{2} \sin(2\phi_\tau) \left(\sqrt{1 - |\boldsymbol{\tau}|^2} - 1 \right), \\ g_{01}(\boldsymbol{\tau}) &= \frac{1}{2} \sin(2\phi_\tau) \left(\sqrt{1 - |\boldsymbol{\tau}|^2} - 1 \right), & g_{11}(\boldsymbol{\tau}) &= \cos^2 \phi_\tau + \sin^2 \phi_\tau \sqrt{1 - |\boldsymbol{\tau}|^2}, \\ g_{02}(\boldsymbol{\tau}) &= |\boldsymbol{\tau}| \cos \phi_\tau, & g_{12}(\boldsymbol{\tau}) &= |\boldsymbol{\tau}| \sin \phi_\tau, \end{aligned} \quad (5.24)$$

and s_j is the j th component of the dipole orientation coordinate $\hat{\mathbf{s}}_o$.

Expressing these entries in an object-space basis of spherical harmonics yields

$$(\hat{\mathbf{e}}(\mathbf{r}_d), \mathcal{H}^{(\text{det})} \hat{\mathbf{e}}(\mathbf{r}_o^\perp) \hat{\mathbf{E}}_{\ell m}) = H_{\ell m}^{(\text{det})}(\mathbf{r}_d - \mathbf{r}_o^\perp) = \frac{4\pi}{3} \sum_{j,j'=0,1,2} G_{\ell 11}^{m\epsilon_j \epsilon_{j'}} B_{jj'}(\mathbf{r}_d - \mathbf{r}_o^\perp, r_o^\parallel), \quad (5.25)$$

where $\epsilon_0 = 1$, $\epsilon_1 = -1$, $\epsilon_2 = 0$, and

$$G_{\ell\ell'\ell''}^{mm'm''} = \int_{\mathbb{S}^2} d\hat{\mathbf{s}} Y_{\ell m}(\hat{\mathbf{s}}) Y_{\ell' m'}(\hat{\mathbf{s}}) Y_{\ell'' m''}(\hat{\mathbf{s}}), \quad (5.26)$$

are the real Gaunt coefficients [163].

Expressing these entries in terms of object- and data-space complex exponentials and exploiting the shift-invariance of the imaging system yields

$$(\hat{\mathbf{E}}(\boldsymbol{\nu}_d), \mathcal{H}^{(\text{det})} \hat{\mathbf{E}}(\boldsymbol{\nu}_o) \hat{\mathbf{E}}_{\ell m}) = \mathsf{H}_{\ell m}^{(\text{det})}(\boldsymbol{\nu}_o) \delta(\boldsymbol{\nu}_d - \boldsymbol{\nu}_o), \quad (5.27)$$

where

$$\mathsf{H}_{\ell m}^{(\text{det})}(\boldsymbol{\nu}) = \int_{\mathbb{R}^2} d\mathbf{r} H_{\ell m}^{(\text{det})}(\mathbf{r}) \exp[-2\pi i \mathbf{r} \cdot \boldsymbol{\nu}] \quad (5.28)$$

is the spatio-angular transfer function which we calculate and plot in Fig. 5.1 for two defocus

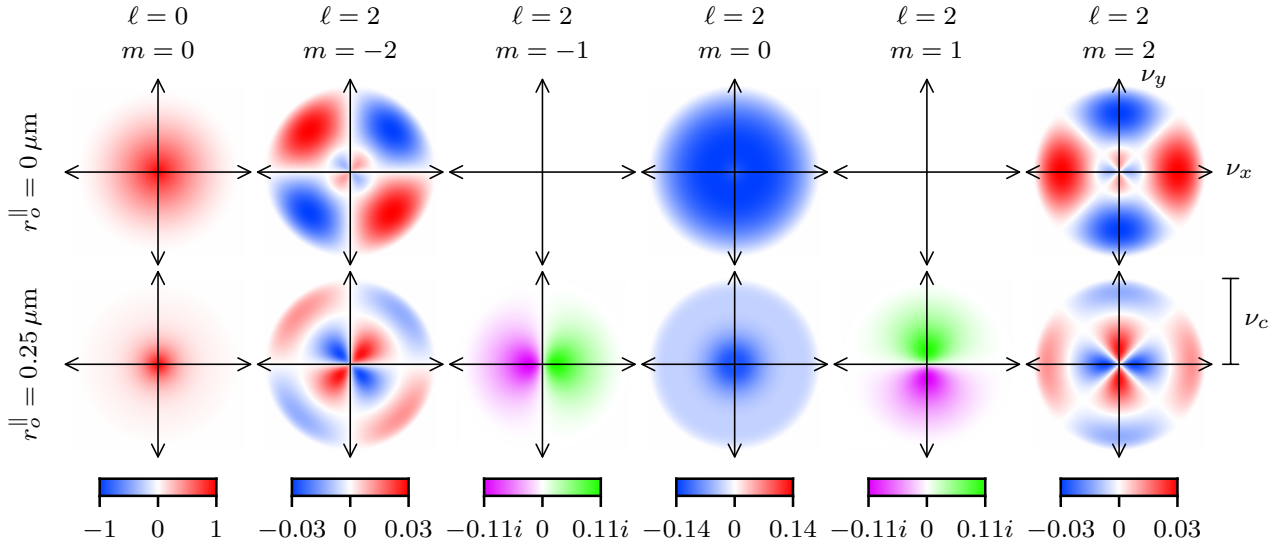


Figure 5.1: The spatio-angular transfer function $H_{\ell m}^{(\text{det})}(\boldsymbol{\nu})$ for two defocus positions (rows) with $\text{NA} = 1.4$, $n_0 = 1.5$, and $\lambda = 500 \text{ nm}$. Each column uses its own color scale (bottom color bars) and shows the transfer function for a different object-space spherical harmonic coefficient (ℓ, m) . Notice that real values are shown in a red-blue color scale while imaginary values are shown in a pink-green color scale. The position within each axis is the continuous spatial frequency $\boldsymbol{\nu}$. The transfer function is zero when $|\boldsymbol{\nu}| \geq \nu_c = 2\text{NA}/\lambda$, or when $\ell \neq 0, 2$, or when $|m| > \ell$.

positions. This basis choice gives a compact description of the detection process— $H_{\ell m}^{(\text{det})}(\boldsymbol{\nu})$ is only non-zero within six disks in the spatial-frequency domain, while $H_{\ell m}^{(\text{det})}(\mathbf{r})$ is only non-zero on six 2D planes in the spatial domain, and $h^{(\text{det})}(\mathbf{r}, \hat{\mathbf{s}}_o)$ is non-zero on an infinite number of planes (one plane for each point on sphere).

To interpret the spatio-angular transfer function $H_{\ell m}^{(\text{det})}(\boldsymbol{\nu})$ it is essential to have a clear understanding of the object- and data-space bases. For specific $(\ell, m, \boldsymbol{\nu})$ the value of $H_{\ell m}^{(\text{det})}(\boldsymbol{\nu})$ shows us how an object consisting of spherical harmonics $Y_{\ell m}(\hat{\mathbf{s}}_o)$ with spatial frequency $\exp[2\pi i \mathbf{r}_o^\perp \cdot \boldsymbol{\nu}]$ is modified by the imaging system as it is transmitted to the spatial frequency $\exp[2\pi i \mathbf{r}_d \cdot \boldsymbol{\nu}]$ on the detector. The magnitude (or complex modulus) of the transfer function indicates the attenuation (or amplification) of the object space component when it appears on the detector, while the phase (or complex argument) of the transfer function indicates the spatial phase shift of the object-space complex exponential component when it

appears on the detector. Equivalently, real positive values of the transfer function can be interpreted as transmission without a spatial phase shift, real negative values can be interpreted as transmission with a π spatial phase shift (maxima in the object become minima on the detector), and imaginary values can be interpreted as transmission with a $\pi/2$ spatial phase shift (maxima in the object become zeros on the detector).

When the object is in focus, the *zonal harmonics* (spherical harmonics with $m = 0$) are transmitted efficiently because the spatio-angular transfer function is large. Notably, the *sectoral harmonics* (spherical harmonics with $|m| = \ell$) are transmitted but relatively inefficiently (the transfer function is at most 3% of the maximum at $H_{00}^{(\text{det})}(\mathbf{0})$). In chapter 3 we made paraxial approximations that neglected the sectoral harmonic components, but here we can explicitly see their small contribution. Finally, the *tesseral harmonics* (spherical harmonics with $0 < |m| < \ell$) do not contribute to the image for in-focus objects, but defocused tesseral harmonic components have a purely imaginary spatio-angular transfer function. The imaginary transfer function for defocused tesseral objects leads to rotationally asymmetric point response functions. Therefore, centroid-based reconstruction algorithms that estimate the position of defocused tesseral objects will be biased. These biased estimates can be avoided by filtering the light emitted by defocused tesseral components [191] or by designing reconstruction schemes that use a complete model of the imaging process [80].

Before calculating the SVD of this operator, we point out a surprising property of the spatio-angular transfer function that we will use later. If we write the spatial frequency coordinates of the transfer function in polar coordinates $\nu \rightarrow (\nu, \phi_\nu)$ then

$$\sum_{\ell m} |\mathsf{H}_{\ell m}^{(\text{det})}(\nu, \phi_\nu)|^2 = \sum_{\ell m} |\mathsf{H}_{\ell m}^{(\text{det})}(\nu, \phi_\nu + \phi_0)|^2 \quad (5.29)$$

for any ϕ_0 . In words, the absolute square of the transfer function summed over the spherical harmonic components is rotationally symmetric. We will interpret this fact further after finding the SVD, but for now we simply show that it is true. The property in Eq. (5.29)

follows from the more strict property

$$|\mathbf{H}_{\ell m}^{(\text{det})}(\nu, \phi_\nu)|^2 + |\mathbf{H}_{\ell(-m)}^{(\text{det})}(\nu, \phi_\nu)|^2 = |\mathbf{H}_{\ell m}^{(\text{det})}(\nu, \phi_\nu + \phi_0)|^2 + |\mathbf{H}_{\ell(-m)}^{(\text{det})}(\nu, \phi_\nu + \phi_0)|^2, \quad (5.30)$$

which is plausible at a glance of Fig. 5.1, but showing this fact requires several steps. First, we realize that two-dimensional Fourier transforms preserve rotational invariance, so Eq. (5.30) follows from

$$|H_{\ell m}(r, \phi_r)|^2 + |H_{\ell(-m)}(r, \phi_r)|^2 = |H_{\ell m}(r, \phi_r + \phi_0)|^2 + |H_{\ell(-m)}(r, \phi_r + \phi_0)|^2. \quad (5.31)$$

Next, we examine the definition of $H_{\ell m}(\mathbf{r})$ in Eqs. (5.20)–(5.25) and realize that the only components of $H_{\ell m}(\mathbf{r})$ that are not rotationally symmetric are the $g_{ij}(\boldsymbol{\tau})$ functions. Therefore, Eq. (5.31) is true if the following functions are rotationally symmetric

$$a_{\ell m}(\boldsymbol{\tau}) = \left| \sum_{j,j'=0,1,2} \sum_{i=0,1} G_{\ell 11}^{m\epsilon_j \epsilon_{j'}} g_{ij}(\boldsymbol{\tau}) g_{ij'}(\boldsymbol{\tau}) \right|^2 + \left| \sum_{j,j'=0,1,2} \sum_{i=0,1} G_{\ell 11}^{-m\epsilon_j \epsilon_{j'}} g_{ij}(\boldsymbol{\tau}) g_{ij'}(\boldsymbol{\tau}) \right|^2. \quad (5.32)$$

After straightforward but tedious calculations we find that

$$a_{00}(\boldsymbol{\tau}) \propto 1, \quad a_{20}(\boldsymbol{\tau}) \propto (3|\boldsymbol{\tau}|^2 - 2)^2, \quad a_{21}(\boldsymbol{\tau}) \propto |\boldsymbol{\tau}|^2(1 - |\boldsymbol{\tau}|^2), \quad a_{22}(\boldsymbol{\tau}) \propto |\boldsymbol{\tau}|^4, \quad (5.33)$$

which are rotationally symmetric functions, so our claim in Eq. (5.29) is confirmed.

Now we are ready to calculate the SVD of $\mathcal{H}^{(\text{det})}$ by solving the eigenvalue problem

$$[\mathcal{H}^{(\text{det})}]^\dagger \mathcal{H}^{(\text{det})} \mathbf{u}_{\boldsymbol{\rho},k}^{(\text{det})} = \mu_{\boldsymbol{\rho},k}^{(\text{det})} \mathbf{u}_{\boldsymbol{\rho},k}^{(\text{det})}, \quad (5.34)$$

where $\boldsymbol{\rho} \in \mathbb{R}^2$ is a continuous index and k is a discrete index. We know that the singular functions will require both a continuous and a discrete index because the object space consists

of functions on the product space of a non-compact space \mathbb{R}^2 (continuous index) and a compact space \mathbb{S}^2 (discrete index).

First, we choose a basis for our object-space singular functions

$$\left(\hat{\mathbf{e}}(\mathbf{r}_o^\perp) \hat{\mathbf{E}}_{\ell m}, \mathbf{u}_{\boldsymbol{\rho}, k}^{(\text{det})} \right) = U_{\boldsymbol{\rho}, k; \ell m}^{(\text{det})}(\mathbf{r}_o^\perp). \quad (5.35)$$

Since the imaging system is laterally shift invariant, the lateral part of the singular functions are complex exponentials [1], and the object-space singular functions take the form

$$U_{\boldsymbol{\rho}, k; \ell m}^{(\text{det})}(\mathbf{r}_o^\perp) = \tilde{U}_{k; \ell m}^{(\text{det})}(\boldsymbol{\rho}) \exp[2\pi i \boldsymbol{\rho} \cdot \mathbf{r}_o^\perp]. \quad (5.36)$$

Next, we write the adjoint of the forward operator in terms of the transfer functions we have already calculated (see Eq. (5.25))

$$\left(\hat{\mathbf{e}}(\mathbf{r}_o^\perp) \hat{\mathbf{E}}_{\ell m}, [\mathcal{H}^{(\text{det})}]^\dagger \hat{\mathbf{e}}(\mathbf{r}_d) \right) = H_{\ell m}^{(\text{det})*}(\mathbf{r}_d - \mathbf{r}_o^\perp). \quad (5.37)$$

With the adjoint entries in hand, we can calculate the entries of $[\mathcal{H}^{(\text{det})}]^\dagger \mathcal{H}^{(\text{det})}$ and define its associated kernel $p_{\ell m, \ell' m'}^{(\text{det})}(\mathbf{r}_o^\perp - \mathbf{r}_o^{\perp'})$ as

$$\begin{aligned} \left(\hat{\mathbf{e}}(\mathbf{r}_o^\perp) \hat{\mathbf{E}}_{\ell m}, [\mathcal{H}^{(\text{det})}]^\dagger \mathcal{H}^{(\text{det})} \hat{\mathbf{e}}(\mathbf{r}_o^{\perp'}) \hat{\mathbf{E}}_{\ell' m'} \right) &\equiv p_{\ell m, \ell' m'}^{(\text{det})}(\mathbf{r}_o^\perp - \mathbf{r}_o^{\perp'}) \\ &= \int_{\mathbb{R}^2} d\mathbf{r}_d H_{\ell m}^{(\text{det})*}(\mathbf{r}_d - \mathbf{r}_o^\perp) H_{\ell' m'}^{(\text{det})}(\mathbf{r}_d - \mathbf{r}_o^{\perp'}). \end{aligned} \quad (5.38)$$

Now we are in a position to solve the eigenvalue problem in the following basis

$$\left(\hat{\mathbf{e}}(\mathbf{r}_o^\perp) \hat{\mathbf{E}}_{\ell m}, [\mathcal{H}^{(\text{det})}]^\dagger \mathcal{H}^{(\text{det})} \mathbf{u}_{\boldsymbol{\rho}, k}^{(\text{det})} \right) = \mu_{\boldsymbol{\rho}, k}^{(\text{det})} \tilde{U}_{k; \ell m}^{(\text{det})}(\boldsymbol{\rho}) \exp[2\pi i \boldsymbol{\rho} \cdot \mathbf{r}_o^\perp]. \quad (5.39)$$

The crux is to rewrite the left hand side in terms of known transfer functions:

$$\begin{aligned}
\left(\hat{\mathbf{e}}(\mathbf{r}_o^\perp) \hat{\mathbf{E}}_{\ell m}, [\mathcal{H}^{(\text{det})}]^\dagger \mathcal{H}^{(\text{det})} \mathbf{u}_{\boldsymbol{\rho}, k}^{(\text{det})} \right) &= \sum_{\ell' m'} \int_{\mathbb{R}^2} d\mathbf{r}_o^\perp p_{\ell m, \ell' m'}^{(\text{det})}(\mathbf{r}_o^\perp - \mathbf{r}_o^{\perp'}) \tilde{U}_{k; \ell' m'}^{(\text{det})}(\mathbf{r}_o^{\perp'}) \exp[2\pi i \boldsymbol{\rho} \cdot \mathbf{r}_o^{\perp'}] \\
&= \exp[2\pi i \boldsymbol{\rho} \cdot \mathbf{r}_o^\perp] \sum_{\ell' m'} P_{\ell m, \ell' m'}^{(\text{det})}(\boldsymbol{\rho}) \tilde{U}_{k; \ell' m'}^{(\text{det})}(\boldsymbol{\rho}) \\
&= \exp[2\pi i \boldsymbol{\rho} \cdot \mathbf{r}_o^\perp] \mathsf{H}_{\ell m}^{(\text{det})*}(\boldsymbol{\rho}) \sum_{\ell' m'} \mathsf{H}_{\ell' m'}^{(\text{det})}(\boldsymbol{\rho}) \tilde{U}_{k; \ell' m'}^{(\text{det})}(\boldsymbol{\rho}),
\end{aligned} \tag{5.40}$$

where we have used the following calculation

$$P_{\ell m}^{\ell' m'}(\boldsymbol{\rho}) = \int_{\mathbb{R}^2} d\mathbf{r} p_{\ell m, \ell' m'}^{(\text{det})}(\mathbf{r}) \exp[-2\pi \boldsymbol{\rho} \cdot \mathbf{r}] = \mathsf{H}_{\ell m}^{(\text{det})*}(\boldsymbol{\rho}) \mathsf{H}_{\ell' m'}^{(\text{det})}(\boldsymbol{\rho}). \tag{5.41}$$

Equating the right-hand sides of Eqs. (5.39) and (5.41) yields

$$\left[\sum_{\ell' m'} \mathsf{H}_{\ell' m'}(\boldsymbol{\rho}) \tilde{U}_{k; \ell' m'}^{(\text{det})}(\boldsymbol{\rho}) \right] \mathsf{H}_{\ell m}^{(\text{det})*}(\boldsymbol{\rho}) = \mu_{\boldsymbol{\rho}, k}^{(\text{det})} \tilde{U}_{k; \ell m}^{(\text{det})}(\boldsymbol{\rho}). \tag{5.42}$$

For a given $\boldsymbol{\rho}$ the term in square brackets is a constant, so the left-hand side is a rank-one operator and we can read off the eigenvalues and eigenfunctions directly from Eq. (5.42).

After normalizing, we find the eigenfunctions are

$$\tilde{U}_{k; \ell m}^{(\text{det})}(\boldsymbol{\rho}) = \delta_{k0} \frac{\mathsf{H}_{\ell m}^{(\text{det})*}(\boldsymbol{\rho})}{\sqrt{\sum_{\ell m} |\mathsf{H}_{\ell m}^{(\text{det})}(\boldsymbol{\rho})|^2}}, \tag{5.43}$$

and the eigenvalues are

$$\mu_{\boldsymbol{\rho}, k}^{(\text{det})} = \delta_{k0} \sum_{\ell m} |\mathsf{H}_{\ell m}^{(\text{det})}(\boldsymbol{\rho})|^2. \tag{5.44}$$

The object-space singular functions in the standard basis are

$$(\hat{\mathbf{e}}(\mathbf{r}_o^\perp) \hat{\mathbf{e}}(\hat{\mathbf{s}}_o), \mathbf{u}_{\boldsymbol{\rho},k}) = u_{\boldsymbol{\rho},k}^{(\text{det})}(\mathbf{r}_o^\perp, \hat{\mathbf{s}}_o) = \delta_{k0} \exp[2\pi i \boldsymbol{\rho} \cdot \mathbf{r}_o^\perp] \frac{\sum_{\ell m} \mathsf{H}_{\ell m}^{(\text{det})*}(\boldsymbol{\rho}) Y_{\ell m}(\hat{\mathbf{s}}_o)}{\sqrt{\sum_{\ell m} |\mathsf{H}^{(\text{det})}(\boldsymbol{\rho})|^2}}, \quad (5.45)$$

and the data-space singular functions are

$$\left(\hat{\mathbf{e}}(\mathbf{r}_d), \mathbf{v}_{\boldsymbol{\rho},k}^{(\text{det})} \right) = v_{\boldsymbol{\rho},k}^{(\text{det})}(\mathbf{r}_d) = \delta_{k0} \exp[2\pi i \boldsymbol{\rho} \cdot \mathbf{r}_d]. \quad (5.46)$$

To simplify our depiction of the object-space singular functions it will be useful to define the following function that drops the spatial part of the singular function:

$$\tilde{u}_k^{(\text{det})}(\boldsymbol{\rho}, \hat{\mathbf{s}}_o) = \delta_{k0} \frac{\sum_{\ell m} \mathsf{H}_{\ell m}^{(\text{det})*}(\boldsymbol{\rho}) Y_{\ell m}(\hat{\mathbf{s}}_o)}{\sqrt{\sum_{\ell m} |\mathsf{H}^{(\text{det})}(\boldsymbol{\rho})|^2}}. \quad (5.47)$$

With the mathematical form of the SVD complete, we can move on to its interpretation. The data-space singular functions are complex exponentials $\exp[2\pi i \boldsymbol{\rho} \cdot \mathbf{r}_d]$ as we would expect for any two-dimensional shift-invariant imaging system. More interestingly, the object-space singular functions are the product of complex exponentials $\exp[2\pi i \boldsymbol{\rho} \cdot \mathbf{r}_o^\perp]$ and a sum of spherical harmonics $Y_{\ell m}(\hat{\mathbf{s}}_o)$ weighted by the conjugate spatio-angular transfer function $\mathsf{H}_{\ell m}^{(\text{det})*}(\boldsymbol{\rho})$. The weights are different for each spatial frequency $\boldsymbol{\rho}$, so the angular part of the singular function changes for different spatial frequencies.

This result leads to perhaps the most wide-reaching conclusion of this dissertation—fluorescence microscopes transmit angular components that vary with spatial frequency. A typical way to interpret the data measured by an unmodified fluorescence microscope is to consider the data as a spatially blurred (convolved) version of the true fluorophore distribution. In reality, every fluorescence microscope (we know of no exceptions) images spatial frequency-dependent angular distributions from the object, so the orientation of the fluorescent emitters plays a large role in the interpretation of the data. Although users of

fluorescent microscopes often interpret deconvolved data as the orientation-independent fluorophore concentration, the fluorophore concentration is not in the measurement space so it is not an estimable parameter. At best, unmodified fluorescence microscopes can estimate the fluorophore concentration weighted by a nonuniform angular distribution. Estimates of fluorophore concentration from spatially deconvolved data can be extremely biased, especially when the object contains high spatial frequency components.

The singular values of the imaging system can be calculated directly from the spatio-angular transfer function using Eq. (5.44). Earlier, we established Eq. (5.29), which now shows that the singular value spectrum is degenerate on any circle with fixed $|\rho|$ —a fact that has deep significance for this imaging system. This degeneracy of singular values indicates rotational and mirror symmetry of the imaging system that we can exploit to reduce the number of singular values and singular functions we need to compute, display, and store [1, ch. 7.2.9]. More specifically, instead of calculating the singular system for each ρ in a plane \mathbb{R}^2 , we only need to calculate the singular system for each $|\rho|$ on the positive real line \mathbb{R}_+ then exploit the symmetry to efficiently find the singular system at the remaining ρ .

It might seem like we are making two contradictory claims. We are claiming that the imaging system is rotationally symmetric, while earlier we claimed that defocused tesserel harmonic components give rise to rotationally asymmetric point response functions. These claims are consistent, and to understand them we need to clarify our definition of rotational symmetry. The degeneracy of singular values shows that the complete imaging system is rotationally symmetric in the sense that functional rotation operators \mathcal{T}_ϕ commute with $[\mathcal{H}^{(\text{det})}]^\dagger \mathcal{H}^{(\text{det})}$. Explicitly, this means that imaging, back projecting, then rotating the object gives the same result as rotating, imaging, then back projecting. Meanwhile, the point response functions are not rotationally symmetric since $h^{(\text{det})}(r, \phi_r, \hat{\mathbf{s}}_o)$ depends on ϕ_r . See Barrett and Myers for a discussion of this peculiarity [1, ch. 7.2.9].

Now that we understand the symmetry of the imaging system, we can plot the singular

system for each $|\rho|$ on the positive real line \mathbb{R}_+ without loss of generality—the singular systems for general ρ can be found by symmetry. Figure 5.2 shows the complete singular value spectrum and the object-space singular functions for five specific choices of ρ at two defocus positions. The object-space singular functions associated with low spatial frequencies are relatively uniform, but as the spatial frequency increases the associated singular functions become less rotationally symmetric. The rotational asymmetry of the singular functions means that the fluorophore concentration is not estimable—only the specific singular function at each spatial frequency can be estimated. As the object is defocused, the singular spectrum drops off faster with spatial frequency. This fact is familiar to all microscopists who observe that defocusing the object results in a smoother image. Finally, we note that in-focus objects have real-valued singular functions while defocused objects have complex-valued singular functions. This follows directly from the transfer function $H_{\ell m}^{(\text{det})}(\nu)$, which is real-valued for in-focus objects and complex-valued for defocused objects. Therefore, the complex-valued singular functions are directly related to the rotationally asymmetric point response functions of tesseral spherical harmonic components.

5.3 SVD of polarized excitation with uniform detection

Now, inscribe in the earth an icosahedron, the sphere inscribed in it will be Venus.
— JOHANNES KEPLER *Mysterium Cosmographicum* (1596)

Similar to the previous section, we start by simplifying the general model in Eq. (5.14) into a specific model that we can analyze. Here we restrict our sample to a small cuvette of fluorophores with uniformly distributed orientations so that we can drop the spatial dependence \mathbf{r}_o . We place a single hemispherical detector around the cuvette that collects exactly half of the light emitted by the sample and model the situation by setting $h_j^{(\text{exc})}(\mathbf{r}_o, \hat{\mathbf{s}}_o) = 1$. Finally, we illuminate the cuvette with a plane wave of linearly polarized light where we can choose the polarization to be any point on the sphere $\hat{\mathbf{p}} \in \mathbb{S}^2$. If we measure the irradiance

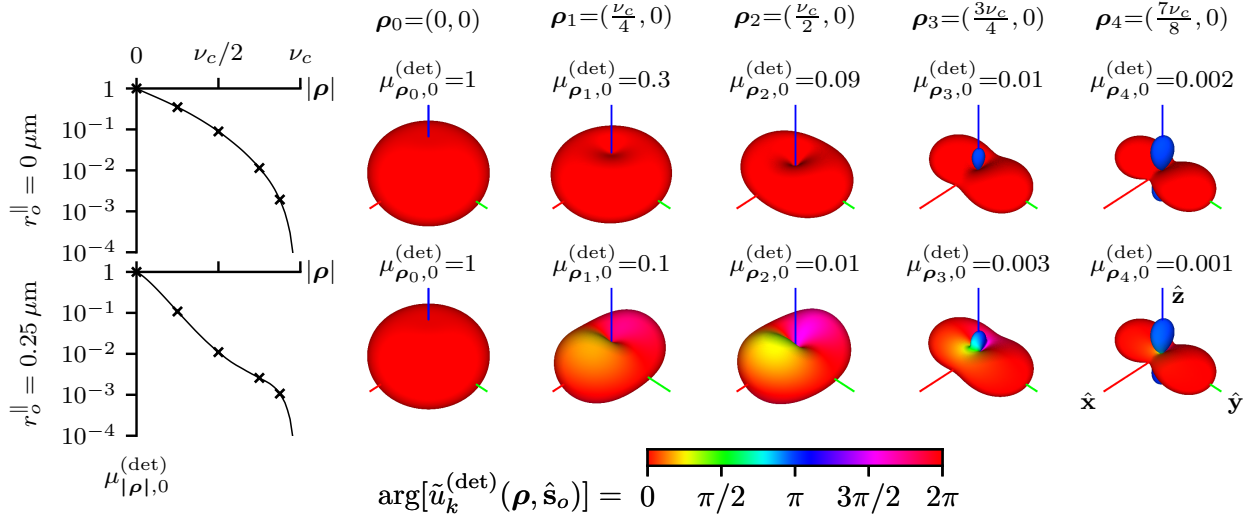


Figure 5.2: The singular system of $\mathcal{H}^{(\text{det})}$ for two defocus positions (rows). The left column shows the eigenvalues of $[\mathcal{H}^{(\text{det})}]^\dagger \mathcal{H}^{(\text{det})}$ as a function of $|\rho|$, while the right columns show the angular part of five object-space singular functions $\tilde{u}_k^{(\text{det})}(\rho, \hat{s}_o)$ —see Eq. (5.47). The five choices of ρ are labeled at the top of each column and are marked with crosses in the eigenvalue spectrum. The radius of each glyph along direction \hat{s}_o indicates the magnitude $|\tilde{u}_k^{(\text{det})}(\rho, \hat{s}_o)|$ while the color indicates the phase $\arg[\tilde{u}_k^{(\text{det})}(\rho, \hat{s}_o)]$.

on the detector for every incident polarization then we set $j \rightarrow \hat{\mathbf{p}}$, and we can model the complete instrument with

$$g(\hat{\mathbf{p}}) = \int_{\mathbb{S}^2} d\hat{s}_o h^{(\text{exc})}(\hat{\mathbf{p}}, \hat{s}_o) \bar{f}(\hat{s}_o), \quad (5.48)$$

where

$$h^{(\text{exc})}(\hat{\mathbf{p}}, \hat{s}_o) = \frac{3}{\sqrt{4\pi}} |\hat{\mathbf{p}} \cdot \hat{s}_o|^2 \quad (5.49)$$

is the point response function, $|\hat{\mathbf{p}} \cdot \hat{s}_o|^2$ models the angular dependence of polarized excitation, and $3/\sqrt{4\pi}$ is a normalization factor so that $\int_{\mathbb{S}^2} d\hat{s}_o h^{(\text{exc})}(\hat{\mathbf{p}}, \hat{s}_o) Y_{00}(\hat{s}_o) = 1$. For this setup we ask and answer two questions: (1) How much information about the object can we recover if we make measurements using every polarization setting? (2) How many discrete samples should we make and where should we place them?

5.3.1 Transfer functions

We begin our analysis by defining an associated linear Hilbert space operator $\mathcal{H}^{(\text{exc})}$ with entries

$$(\hat{\mathbf{e}}(\hat{\mathbf{p}}), \mathcal{H}^{(\text{exc})}\hat{\mathbf{e}}(\hat{\mathbf{s}}_o)) = h^{(\text{exc})}(\hat{\mathbf{p}}, \hat{\mathbf{s}}_o). \quad (5.50)$$

Expressing these entries in terms of an object-space spherical harmonic basis yields

$$(\hat{\mathbf{e}}(\hat{\mathbf{p}}), \mathcal{H}^{(\text{exc})}\hat{\mathbf{E}}_{\ell m}) = H_{\ell m}^{(\text{exc})}(\hat{\mathbf{p}}) = \int_{\mathbb{S}^2} d\hat{\mathbf{s}}_o h^{(\text{exc})}(\hat{\mathbf{p}}, \hat{\mathbf{s}}_o) Y_{\ell m}(\hat{\mathbf{s}}_o). \quad (5.51)$$

We normalized so that $H_{00}^{(\text{exc})}(\hat{\mathbf{p}}) = 1$, but calculating $H_{2m}^{(\text{exc})}(\hat{\mathbf{p}})$ requires some manipulation

$$\begin{aligned} H_{2m}^{(\text{exc})}(\hat{\mathbf{p}}) &= \frac{3}{\sqrt{4\pi}} \int_{\mathbb{S}^2} d\hat{\mathbf{s}}_o |\hat{\mathbf{p}} \cdot \hat{\mathbf{s}}_o|^2 Y_{2m}(\hat{\mathbf{s}}_o) \\ &= \frac{1}{\sqrt{4\pi}} \int_{\mathbb{S}^2} d\hat{\mathbf{s}}_o [1 + 2P_2(\hat{\mathbf{p}} \cdot \hat{\mathbf{s}}_o)] Y_{2m}(\hat{\mathbf{s}}_o) \\ &= \frac{1}{\sqrt{4\pi}} \int_{\mathbb{S}^2} d\hat{\mathbf{s}}_o \left[1 + \frac{8\pi}{5} \sum_{m'=-2}^2 Y_{2m'}(\hat{\mathbf{p}}) Y_{2m'}(\hat{\mathbf{s}}_o) \right] Y_{2m}(\hat{\mathbf{s}}_o) \\ &= \frac{1}{\sqrt{4\pi}} \frac{8\pi}{5} \sum_{m'=-2}^2 Y_{2m'}(\hat{\mathbf{p}}) \delta_{mm'} \\ &= \frac{4\sqrt{\pi}}{5} Y_{2m}(\hat{\mathbf{p}}), \end{aligned} \quad (5.52)$$

where we have expanded in terms of Legendre polynomials, applied the spherical harmonic addition theorem, exploited the orthonormality of the spherical harmonics, then used the discrete sifting theorem. Bringing these results together yields the complete transfer function

$$H_{\ell m}^{(\text{exc})}(\hat{\mathbf{p}}) = \sqrt{4\pi} Y_{\ell m}(\hat{\mathbf{p}}) \left(\delta_{0\ell} + \frac{2}{5} \delta_{2\ell} \right). \quad (5.53)$$

This transfer function implies that only $\ell = 0$ and $\ell = 2$ components are transmitted to the data. Since $|m| \leq \ell$ there are $1 + 5 = 6$ components transmitted, so $\mathcal{H}^{(\text{exc})}$ is at most a rank-six operator.

5.3.2 Singular-value decomposition

To establish the actual rank we need to calculate the SVD by solving the eigenvalue equation

$$[\mathcal{H}^{(\text{exc})}]^\dagger \mathcal{H}^{(\text{exc})} \mathbf{u}_{kn}^{(\text{exc})} = \mu_{kn}^{(\text{exc})} \mathbf{u}_{kn}^{(\text{exc})}, \quad (5.54)$$

where k and n are discrete indices. For now we proceed on faith that using two discrete indices is an appropriate choice, and we will interpret this choice after we find the singular system. Expanding Eq. (5.54) in a basis of spherical harmonics yields

$$\int_{\mathbb{S}^2} d\hat{\mathbf{p}} H_{\ell m}^{(\text{exc})*}(\hat{\mathbf{p}}) \sum_{\ell' m'} H_{\ell' m'}^{(\text{exc})}(\hat{\mathbf{p}}) U_{kn; \ell' m'}^{(\text{exc})} = \mu_{kn}^{(\text{exc})} U_{kn; \ell m}^{(\text{exc})}. \quad (5.55)$$

After rearranging

$$\sum_{\ell' m'} \left[\int_{\mathbb{S}^2} d\hat{\mathbf{p}} H_{\ell m}^{(\text{exc})*}(\hat{\mathbf{p}}) H_{\ell' m'}^{(\text{exc})}(\hat{\mathbf{p}}) \right] U_{kn; \ell' m'}^{(\text{exc})} = \mu_{kn}^{(\text{exc})} U_{kn; \ell m}^{(\text{exc})}, \quad (5.56)$$

then evaluating the integral in square brackets we find that

$$\sum_{\ell' m'} \delta_{\ell \ell'} \delta_{mm'} \left(\delta_{0\ell'} + \frac{4}{25} \delta_{2\ell'} \right) U_{kn; \ell' m'}^{(\text{exc})} = \mu_{kn}^{(\text{exc})} U_{kn; \ell m}^{(\text{exc})}. \quad (5.57)$$

By inspection, we can choose the normalized eigenfunctions to be

$$U_{kn; \ell m}^{(\text{exc})} = \left(\hat{\mathbf{E}}_{\ell m}, \mathbf{u}_{kn}^{(\text{exc})} \right) = \delta_{k\ell} \delta_{nm}, \quad (5.58)$$

which are the spherical harmonics in a standard basis

$$u_{kn}^{(\text{exc})}(\hat{\mathbf{s}}_o) = \left(\hat{\mathbf{e}}(\hat{\mathbf{s}}), \mathbf{u}_{kn}^{(\text{exc})} \right) = Y_{kn}(\hat{\mathbf{s}}_o), \quad (5.59)$$

and the eigenvalues are

$$\mu_{kn}^{(\text{exc})} = \delta_{0k} + \frac{4}{25} \delta_{2k} \quad \text{for } -k \leq n \leq k. \quad (5.60)$$

There are six non-zero eigenvalues, so we conclude that $\mathcal{H}^{(\text{exc})}$ is a rank-six operator.

This fact may come as a surprise since we are modeling the mapping between a continuous object and continuous data— $\mathcal{H}^{(\text{exc})}$ is a CC operator in the language of Barrett and Myers [1]. If the object and the data are both continuous, we might intuitively expect the operator to have a continuous spectrum, an infinite number of singular functions, and an infinite (or undefined) rank. This intuition is incorrect—the continuity of the object and data geometries has no bearing on the continuity of the spectrum. Instead, testing the *compactness* of the operator allows us to determine if the operator has a discrete spectra [1, ch. 1.4]. Operators that satisfy the Hilbert–Schmidt condition are compact, so we plug our kernel into the Hilbert–Schmidt test and find that

$$\int_{\mathbb{S}^2} d\hat{\mathbf{p}} \int_{\mathbb{S}^2} d\hat{\mathbf{s}}_o |h^{(\text{exc})}(\hat{\mathbf{p}}, \hat{\mathbf{s}}_o)|^2 < \infty \quad (5.61)$$

because the kernel is bounded and the regions of integration are finite. Therefore, $\mathcal{H}^{(\text{exc})}$ is a compact operator with a discrete spectrum.

Although we have established that $\mathcal{H}^{(\text{exc})}$ has a discrete spectrum, it is still not obvious that it should be a rank-six operator. To establish this fact, we can laboriously calculate the singular value decomposition as we have done above. Alternatively, we can recognize that the kernel $|\hat{\mathbf{p}} \cdot \hat{\mathbf{s}}_o|^2$ is a homogeneous polynomial of degree two in three

variables. Homogeneous polynomials of degree d in n variables form “ n multichoose d ” $= \binom{n}{d} = \binom{n+d-1}{d}$ -dimensional vector spaces [192, ch. 1.2], so the $d = 2$ and $n = 3$ kernels form a $\binom{\binom{3}{2}}{2} = \binom{4}{2} = 6$ -dimensional vector space.

When we started the singular-value decomposition calculation we made the surprising choice to use two discrete indices for the eigenvalues and eigenfunctions. Now it is clear that we needed two indices to index the spherical harmonic eigenfunctions. Additionally, our use of two discrete indices combined with the structure of the singular values tells us about the symmetries of the imaging system. The singular spectrum consists of a singlet and a 5-plet and this multiplet structure indicates this imaging system’s complete rotational $\mathbb{SO}(3)$ symmetry. An N -plet can only appear if the symmetry group of the imaging system has an irreducible representation of dimension N , and $\mathbb{SO}(3)$ has irreducible representations of every integer dimension (including five as expected). Our eigenfunction indices k and n specify the irreducible representation and the different eigenfunctions within each irreducible representation, respectively.

The degeneracy of the 5-plet implies that the singular functions are not unique. We have chosen the spherical harmonics for convenience, but any linear combination of the $\ell = 2$ spherical harmonics that form an orthonormal set can be chosen as the $k = 2$ singular functions. This observation reflects the fact that the ℓ th band of spherical harmonics spans a $(2\ell + 1)$ -dimensional rotationally invariant subspace of $\mathbb{L}_2(\mathbb{S}^2)$. Any function that is a linear combination of $\ell = 2$ spherical harmonics can be rotated and it will remain a linear combination of $\ell = 2$ spherical harmonics.

Given that this imaging system is a rank-6 operator, it is natural to ask if six measurements are sufficient to recover as much as possible about the object. We can answer this question analytically by choosing six sampling points, calculating the spectrum of the continuous-to-discrete operator, then comparing the spectrum to the ideal spectrum we found when we sampled continuously.

To start we need to choose six sample points, and intuition guides us towards choosing six equally spaced points on the sphere. The six vertices of an octahedron are equally spaced, but these vertices are split into three pairs of antipodal points and antipodal samples are identical since $|\hat{\mathbf{p}} \cdot \hat{\mathbf{s}}_o|^2 = |(-\hat{\mathbf{p}}) \cdot \hat{\mathbf{s}}_o|^2$. Instead, we need to choose six equally spaced *axes* on the sphere, and the six inscribed axes of an icosahedron provide exactly the samples we need. If we place the first sample point along the $\hat{\mathbf{z}}$ axis $\hat{\mathbf{p}}_0 = [0, 0, 1]$ then the remaining five sample points are

$$\hat{\mathbf{p}}_j = \left[\frac{2}{\sqrt{5}} \cos\left(\frac{2\pi j}{5}\right), \frac{2}{\sqrt{5}} \sin\left(\frac{2\pi j}{5}\right), \frac{1}{\sqrt{5}} \right], \quad j \in \{1, 2, 3, 4, 5\}. \quad (5.62)$$

Now that we have a finite number of samples we can express the complete forward model in matrix notation as

$$\begin{bmatrix} g_0 \\ g_1 \\ g_2 \\ g_3 \\ g_4 \\ g_5 \end{bmatrix} = \sqrt{\frac{4\pi}{6}} \begin{bmatrix} Y_{00}(\hat{\mathbf{p}}_0) & \frac{2}{5}Y_{2-2}(\hat{\mathbf{p}}_0) & \frac{2}{5}Y_{2-1}(\hat{\mathbf{p}}_0) & \frac{2}{5}Y_{20}(\hat{\mathbf{p}}_0) & \frac{2}{5}Y_{21}(\hat{\mathbf{p}}_0) & \frac{2}{5}Y_{22}(\hat{\mathbf{p}}_0) \\ Y_{00}(\hat{\mathbf{p}}_1) & \frac{2}{5}Y_{2-2}(\hat{\mathbf{p}}_1) & \frac{2}{5}Y_{2-1}(\hat{\mathbf{p}}_1) & \frac{2}{5}Y_{20}(\hat{\mathbf{p}}_1) & \frac{2}{5}Y_{21}(\hat{\mathbf{p}}_1) & \frac{2}{5}Y_{22}(\hat{\mathbf{p}}_1) \\ Y_{00}(\hat{\mathbf{p}}_2) & \frac{2}{5}Y_{2-2}(\hat{\mathbf{p}}_2) & \frac{2}{5}Y_{2-1}(\hat{\mathbf{p}}_2) & \frac{2}{5}Y_{20}(\hat{\mathbf{p}}_2) & \frac{2}{5}Y_{21}(\hat{\mathbf{p}}_2) & \frac{2}{5}Y_{22}(\hat{\mathbf{p}}_2) \\ Y_{00}(\hat{\mathbf{p}}_3) & \frac{2}{5}Y_{2-2}(\hat{\mathbf{p}}_3) & \frac{2}{5}Y_{2-1}(\hat{\mathbf{p}}_3) & \frac{2}{5}Y_{20}(\hat{\mathbf{p}}_3) & \frac{2}{5}Y_{21}(\hat{\mathbf{p}}_3) & \frac{2}{5}Y_{22}(\hat{\mathbf{p}}_3) \\ Y_{00}(\hat{\mathbf{p}}_4) & \frac{2}{5}Y_{2-2}(\hat{\mathbf{p}}_4) & \frac{2}{5}Y_{2-1}(\hat{\mathbf{p}}_4) & \frac{2}{5}Y_{20}(\hat{\mathbf{p}}_4) & \frac{2}{5}Y_{21}(\hat{\mathbf{p}}_4) & \frac{2}{5}Y_{22}(\hat{\mathbf{p}}_4) \\ Y_{00}(\hat{\mathbf{p}}_5) & \frac{2}{5}Y_{2-2}(\hat{\mathbf{p}}_5) & \frac{2}{5}Y_{2-1}(\hat{\mathbf{p}}_5) & \frac{2}{5}Y_{20}(\hat{\mathbf{p}}_5) & \frac{2}{5}Y_{21}(\hat{\mathbf{p}}_5) & \frac{2}{5}Y_{22}(\hat{\mathbf{p}}_5) \end{bmatrix} \begin{bmatrix} F_{00} \\ F_{2-2} \\ F_{2-1} \\ F_{20} \\ F_{21} \\ F_{22} \end{bmatrix}, \quad (5.63)$$

where we have used the transfer function in Eq. (5.53) and multiplied by $1/\sqrt{6}$ to normalize.

Calculating these entries and refactoring yields

$$\begin{bmatrix} g_0 \\ g_1 \\ g_2 \\ g_3 \\ g_4 \\ g_5 \end{bmatrix} = \begin{bmatrix} 0.41 & 0 & 0 & 0.91 & 0 & 0 \\ 0.41 & 0 & 0 & -0.18 & 0.63 & 0.63 \\ 0.41 & 0.37 & 0.60 & -0.18 & 0.20 & -0.51 \\ 0.41 & -0.60 & 0.37 & -0.18 & -0.51 & 0.20 \\ 0.41 & 0.60 & -0.37 & -0.18 & -0.51 & 0.20 \\ 0.41 & -0.37 & -0.60 & -0.18 & 0.20 & -0.51 \end{bmatrix} \begin{bmatrix} F_{00} \\ \frac{2}{5}F_{2-2} \\ \frac{2}{5}F_{2-1} \\ \frac{2}{5}F_{20} \\ \frac{2}{5}F_{21} \\ \frac{2}{5}F_{22} \end{bmatrix}, \quad (5.64)$$

where we have rounded the matrix entries to two figures. The columns of the matrix in Eq. (5.64) are orthonormal, so by inspection the data-space singular functions are the columns of the matrix in Eq. (5.64), the object-space singular functions are the spherical harmonic functions, and the singular values are identical to the continuous case: a singlet with unit magnitude and a 5-plet with magnitude 2/5 (equivalently, eigenvalues with magnitude 4/25). This means that we can make six icosahedral measurements and recover the same amount of information as if we took measurements at every possible point.

In the continuous case the multiplet structure arose from the $\mathbb{SO}(3)$ symmetry of the imaging system. With discrete samples the imaging system can no longer have a continuous (Lie) symmetry group, so the imaging system must have a discrete symmetry with at least one five-dimensional irreducible representation. Unsurprisingly, this imaging system is symmetric under the order-60 icosahedral group (usually denoted \mathbf{A}_5 since it is isomorphic to the alternating group of degree 5), and this group has a five-dimensional irreducible representation as expected [193, ch. 3.1].

Since the underlying continuous imaging system has $\mathbb{SO}(3)$ symmetry, we can place our discrete samples in any icosahedral sampling position and maintain the same singular values and singular functions. In other words, when we chose our sampling scheme in Eq. (5.62) we only aligned our icosahedral samples with the $\hat{\mathbf{z}}$ axis for convenience. We could align

our icosahedral samples with any axis and achieve the same result. Figure 5.3 shows two possible sampling schemes that have the same singular values and singular functions.

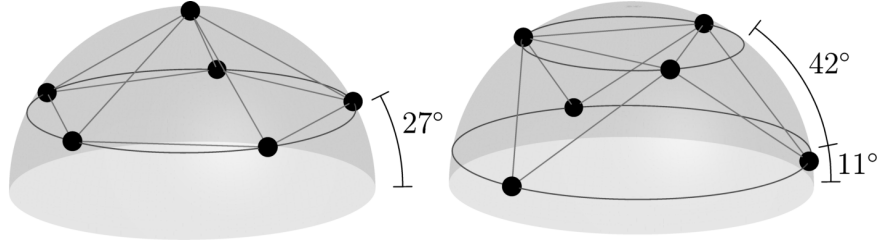


Figure 5.3: Two optimal icosahedral sampling schemes—each dot indicates a placement of the illumination polarization $\hat{\mathbf{p}}$. All icosahedral sampling schemes are optimal, and new icosahedral schemes can be found by rigidly rotating the illustrated points to other positions.

Since the icosahedral sampling scheme has the same spectrum and singular values as continuous sampling, we naturally expect that the icosahedral sampling scheme is optimal in some sense. Foreman et al. [190] have studied a related problem of finding optimal sampling schemes for polarimeters that attempt to reconstruct the polarization of light (not parameters of fluorescent objects like we're considering here). Although their parameters and measurement system are different from ours, their formulation of an optimization problem applies to our problem directly. They show or provide references for the equivalence of the following definitions of an optimal sampling scheme: (1) the condition number of \mathcal{H} is minimized, (2) the equally weighted variance (a scalar measure of noise amplification) [188] of \mathcal{H} is minimized, (3) the determinant of $\mathcal{H}^\dagger \mathcal{H}$ is maximized, (4) the product of the eigenvalues of $\mathcal{H}^\dagger \mathcal{H}$ is maximized. We use their definition of an optimal sampling scheme and show that icosahedral sampling is optimal.

For an arbitrary six-measurement imaging operator $\mathcal{H}^{(6,\text{exc})}$ (not necessarily with icosahedral sampling) with entries

$$(\hat{\mathbf{e}}_j, \mathcal{H}^{(6,\text{exc})} \hat{\mathbf{e}}(\hat{\mathbf{s}}_o)) = \frac{3}{\sqrt{6 \cdot 4\pi}} (\hat{\mathbf{p}}_j \cdot \hat{\mathbf{s}}_o)^2, \quad (5.65)$$

we can calculate the trace of $\mathcal{H}^{(6,\text{exc})}[\mathcal{H}^{(6,\text{exc})}]^\dagger$ as

$$\text{tr}(\mathcal{H}^{(6,\text{exc})}[\mathcal{H}^{(6,\text{exc})}]^\dagger) = \sum_{j=0}^5 \int_{\mathbb{S}^2} d\hat{\mathbf{s}}_o \frac{9}{6 \cdot 4\pi} (\hat{\mathbf{p}}_j \cdot \hat{\mathbf{s}}_o)^4 = \frac{9}{2} \int_0^\pi d\theta \sin \theta \cos^4 \theta = \frac{9}{5}. \quad (5.66)$$

Therefore, the sum of the eigenvalues of $\mathcal{H}^{(6,\text{exc})}[\mathcal{H}^{(6,\text{exc})}]^\dagger$ is $9/5$ independent of where we place the sample points $\{\hat{\mathbf{p}}_j\}$. The maximum determinant is obtained when $\mathcal{H}^{(6,\text{exc})}[\mathcal{H}^{(6,\text{exc})}]^\dagger$ is diagonal, and we know that the first diagonal entry of $[\mathcal{H}^{(6,\text{exc})}]^\dagger \mathcal{H}^{(6,\text{exc})}$ is independent of the sample points

$$(\hat{\mathbf{E}}_{00}, [\mathcal{H}^{(6,\text{exc})}]^\dagger \mathcal{H}^{(6,\text{exc})} \hat{\mathbf{E}}_{00}) = 1. \quad (5.67)$$

Therefore, the optimal first eigenvalue is one. To find the five remaining optimal eigenvalues we need to maximize the product of all six eigenvalues while fixing their sum to $9/5$, and we can use the method of Lagrange multipliers to show that this is achieved when the five remaining eigenvalues are $4/25$ (equivalently, the singular values are $2/5$). These optimal eigenvalues are identical to the eigenvalues we found for icosahedral sampling, so icosahedral sampling scheme is optimal.

As usual, mathematicians have studied a broader class of the types of sampling problems discussed here. Foreman et al. [190] identified their sampling schemes as examples of spherical 2-designs in \mathbb{R}^3 [194]. More generally, N -point spherical t -designs specify a set of N points that can be sampled and averaged to exactly integrate a degree t polynomial on the sphere, and tables of spherical t -designs are available from Neil Sloane's website [195].

Here we are attempting to find sampling points that we can average to exactly integrate functions of the form $|\hat{\mathbf{p}} \cdot \hat{\mathbf{s}}_o|^2 f(\hat{\mathbf{s}}_o)$. Our singular value decomposition showed that we can only hope to reconstruct object functions $f(\hat{\mathbf{s}}_o)$ that are homogeneous polynomials of degree 2, and the function $|\hat{\mathbf{p}} \cdot \hat{\mathbf{s}}_o|^2$ is also a homogeneous polynomial of degree 2. Therefore, $|\hat{\mathbf{p}} \cdot \hat{\mathbf{s}}_o|^2 f(\hat{\mathbf{s}}_o)$ is a homogeneous polynomial of degree 4. Exact sampling rules for homogeneous polynomials

of degree $2t$ on the sphere are called *spherical (t, t) -designs* or *spherical half-designs of order $2t$* . As expected, the minimal spherical $(2, 2)$ -design in \mathbb{R}^3 consists of six equiangular lines that go through the vertices of an icosahedron [196].

5.3.3 Optimal illumination polarizations under geometric constraints

Many experimental situations have geometric constraints that make icosahedral sampling infeasible. In these cases it is valuable to know how to find and optimize sampling schemes that are full rank under the constraint. Suppose that we make polarization measurements everywhere on a great circle of the sphere so that the data are given by

$$g(\hat{\mathbf{p}}) = \int_{\mathbb{S}^2} d\hat{\mathbf{s}}_o \delta(\hat{\mathbf{p}} \cdot \hat{\mathbf{n}})(\hat{\mathbf{p}} \cdot \hat{\mathbf{s}}_o)^2 \bar{f}(\hat{\mathbf{s}}_o), \quad (5.68)$$

where $\hat{\mathbf{n}} \in \mathbb{S}^2$ is an arbitrary axis. In this case the kernel of the operator is a homogeneous polynomial of degree 2 in 2 variables (the delta function collapses one variable), so the rank of the operator is $\binom{2}{2} = \binom{3}{2} = 3$. This means that if polarization sampling is restricted to a single great circle, then three measurements are sufficient to make the operator full rank.

Now consider a geometry where we make polarization measurements everywhere on two great circles so that our data are given by

$$g_i(\hat{\mathbf{p}}) = \int_{\mathbb{S}^2} d\hat{\mathbf{s}}_o \delta(\hat{\mathbf{p}} \cdot \hat{\mathbf{n}}_i)(\hat{\mathbf{p}} \cdot \hat{\mathbf{s}}_o)^2 f(\hat{\mathbf{s}}_o), \quad \text{for } i = 0, 1, \quad (5.69)$$

where $\hat{\mathbf{n}}_0$ and $\hat{\mathbf{n}}_1$ are distinct axes $\hat{\mathbf{n}}_0 \cdot \hat{\mathbf{n}}_1 \neq 1$. We can no longer make a combinatoric argument for the rank of this operator, but we can give an upper bound by constructing a degree-two null function. Without loss of generality, choose $\hat{\mathbf{n}}_0 = \hat{\mathbf{y}}$ and $\hat{\mathbf{n}}_1 = \sin \varphi \hat{\mathbf{x}} + \cos \varphi \hat{\mathbf{y}}$. In spherical coordinates, $\hat{\mathbf{s}}_o = \cos \phi \sin \theta \hat{\mathbf{x}} + \sin \phi \sin \theta \hat{\mathbf{y}} + \cos \theta \hat{\mathbf{z}}$, and the kernel becomes $\delta(\hat{\mathbf{p}} \cdot \hat{\mathbf{n}}_i)(\hat{\mathbf{p}} \cdot \hat{\mathbf{s}}_o)^2 = \cos^2(\phi - \phi_i)$, where $\phi_0 = 0$ and $\phi_1 = \varphi$. For this sampling scheme we can

construct a null function

$$f^{(\text{null})}(\hat{\mathbf{s}}_o) = \begin{cases} \sin^2 \theta \left(\cos 2\phi - \frac{1}{2} \right), & \text{if } \varphi = \frac{\pi}{2}, \\ \sin^2 \theta \left(\cos 2\phi + \left[\frac{1-\cos 2\varphi}{\sin 2\varphi} \right] \sin 2\phi - \frac{1}{2} \right), & \text{otherwise,} \end{cases} \quad (5.70)$$

which we can confirm is a null function with the calculation

$$\int_{\mathbb{S}^2} d\hat{\mathbf{s}}_o \cos^2(\phi - \phi_i) f^{(\text{null})}(\hat{\mathbf{s}}_o) = 0, \quad \text{for } i = 0, 1. \quad (5.71)$$

The maximum rank is six, and we have constructed one null function. Therefore, the rank of an imaging system that samples everywhere on two unique great circles is at most five. It follows that any rank-six sampling configuration must not be constrained to two great circles.

We conjecture that sampling everywhere on any three unique great circles will give rise to a rank-six operator. Although we have been unable to show this conclusively, we have been unable to find any exceptions. When we place six samples on the sphere that cannot be connected by two great circles, calculate their corresponding matrix elements, then calculate the matrix rank, the rank has been six for every configuration of the 10,000 random configurations we have tried. In summary, to find a rank-six sampling operator it is necessary for the six samples to live on three unique great circles, and we suspect that this condition is sufficient.

Once a set of candidate full-rank sampling operators has been identified, we need to choose between them. We suggest choosing the sampling operator that optimizes the condition number of the measurement matrix. A different metric could be optimized if the experimentalist is interested in estimating a particular parameter.

5.4 SVD of polarized illumination and epi-detection

For our final SVD we analyze an imaging system that combines icosahedral polarized illumination with a high-NA detection system. We model this imaging system with

$$g_j(\mathbf{r}_d) = \int_{\mathbb{S}^2} d\hat{\mathbf{s}}_o \int_{\mathbb{R}^2} d\mathbf{r}_o^\perp h^{(\text{det})}(\mathbf{r}_d - \mathbf{r}_o^\perp, \hat{\mathbf{s}}_o) h^{(\text{exc})}(\hat{\mathbf{p}}_j, \hat{\mathbf{s}}_o) \bar{f}(\mathbf{r}_o^\perp, \hat{\mathbf{s}}_o), \quad (5.72)$$

where $h^{(\text{det})}(\mathbf{r}_d - \mathbf{r}_o^\perp, \hat{\mathbf{s}}_o)$ is defined in Eq. (5.19), $h^{(\text{exc})}(\hat{\mathbf{p}}_j, \hat{\mathbf{s}}_o)$ is defined in Eq. (5.49), and $\hat{\mathbf{p}}_j$ are the icosahedral sampling points in Eq. (5.62) together with $\hat{\mathbf{p}}_0 = [0, 0, 1]$. To simplify our notation we define a Hilbert-space operator $\mathcal{H}^{(\text{epi})}$ with entries

$$\left(\hat{\mathbf{e}}(\mathbf{r}_d) \hat{\mathbf{e}}_j, \mathcal{H}^{(\text{epi})} \hat{\mathbf{e}}(\mathbf{r}_o^\perp) \hat{\mathbf{e}}(\hat{\mathbf{s}}_o) \right) \equiv h_j^{(\text{epi})}(\mathbf{r}_d - \mathbf{r}_o^\perp, \hat{\mathbf{s}}_o) = h^{(\text{det})}(\mathbf{r}_d - \mathbf{r}_o^\perp, \hat{\mathbf{s}}_o) h^{(\text{exc})}(\hat{\mathbf{p}}_j, \hat{\mathbf{s}}_o). \quad (5.73)$$

Similar to the previous two sections, we calculate the entries of $\mathcal{H}^{(\text{epi})}$ in several different bases before calculating its SVD. Expressing the entries in a basis of object-space spherical harmonics yields

$$\begin{aligned} H_{j,\ell m}^{(\text{epi})}(\mathbf{r}_d - \mathbf{r}_o^\perp) &\equiv \left(\hat{\mathbf{e}}(\mathbf{r}_d) \hat{\mathbf{e}}_j, \mathcal{H}^{(\text{epi})} \hat{\mathbf{e}}(\mathbf{r}_o^\perp) \hat{\mathbf{E}}_{\ell m} \right) \\ &= \int_{\mathbb{S}^2} d\hat{\mathbf{s}}_o h^{(\text{det})}(\mathbf{r}_d - \mathbf{r}_o^\perp, \hat{\mathbf{s}}_o) h^{(\text{exc})}(\hat{\mathbf{p}}_j, \hat{\mathbf{s}}_o) Y_{\ell m}(\hat{\mathbf{s}}_o) \\ &= \int_{\mathbb{S}^2} d\hat{\mathbf{s}}_o \left[\sum_{\ell' m'} H_{\ell' m'}^{(\text{det})}(\mathbf{r}_d - \mathbf{r}_o^\perp) Y_{\ell' m'}(\hat{\mathbf{s}}_o) \right] \left[\sum_{\ell'' m''} H_{\ell'' m''}^{(\text{exc})}(\hat{\mathbf{p}}_j) Y_{\ell'' m''}(\hat{\mathbf{s}}_o) \right] Y_{\ell m}(\hat{\mathbf{s}}_o) \\ &= \sum_{\ell' m'} \sum_{\ell'' m''} G_{\ell \ell' \ell''}^{m m' m''} H_{\ell' m'}^{(\text{det})}(\mathbf{r}_d - \mathbf{r}_o^\perp) H_{\ell'' m''}^{(\text{exc})}(\hat{\mathbf{p}}_j). \end{aligned} \quad (5.74)$$

Both $H_{\ell m}^{(\text{det})}(\mathbf{r}_d - \mathbf{r}_o^\perp)$ and $H_{\ell m}^{(\text{exc})}(\hat{\mathbf{p}}_j)$ are only non-zero for $\ell = 0, 2$, so $H_{j,\ell m}^{(\text{epi})}(\mathbf{r}_d - \mathbf{r}_o^\perp)$ is only non-zero for $\ell = 0, 2, 4$. Therefore, we need to calculate $H_{j,\ell m}^{(\text{epi})}(\mathbf{r}_d - \mathbf{r}_o^\perp)$ for $1 + 5 + 9 = 15$ spherical harmonic coefficients, six illumination polarizations j , and every point on a 2D plane $\mathbf{r}_d - \mathbf{r}_o^\perp$.

Next, we calculate the entries of $\mathcal{H}^{(\text{epi})}$ in an object-space basis of spherical harmonics and complex exponentials and a data-space basis of complex exponentials

$$(\hat{\mathbf{e}}(\boldsymbol{\nu}_d)\hat{\mathbf{e}}_j, \mathcal{H}^{(\text{epi})}\hat{\mathbf{e}}(\boldsymbol{\nu}_o)\hat{\mathbf{E}}_{\ell m}) \equiv \mathsf{H}_{j,\ell m}^{(\text{epi})}(\boldsymbol{\nu}_o)\delta(\boldsymbol{\nu}_d - \boldsymbol{\nu}_o), \quad (5.75)$$

where

$$\mathsf{H}_{j,\ell m}^{(\text{epi})}(\boldsymbol{\nu}) = \int_{\mathbb{R}^2} d\mathbf{r} H_{j,\ell m}^{(\text{epi})}(\mathbf{r}) \exp[-2\pi i \mathbf{r} \cdot \boldsymbol{\nu}] = \sum_{\ell' m'} \sum_{\ell'' m''} G_{\ell' \ell'' \ell'' m''}^{m m' m''} \mathsf{H}_{\ell' m'}^{(\text{det})}(\boldsymbol{\nu}) H_{\ell'' m''}^{(\text{exc})}(\hat{\mathbf{p}}_j). \quad (5.76)$$

We have already calculated $\mathsf{H}_{\ell m}^{(\text{det})}(\boldsymbol{\nu})$ and $H_{\ell m}^{(\text{exc})}(\hat{\mathbf{p}}_j)$, so we have a clear path for calculating $\mathsf{H}_{j,\ell m}^{(\text{epi})}(\boldsymbol{\nu})$. The spatio-angular transfer function $\mathsf{H}_{j,\ell m}^{(\text{epi})}(\boldsymbol{\nu})$ is only non-zero for fifteen spherical harmonic coefficients, six illumination polarizations j , and every point within a disk of radius ν_c , which we plot in Fig. 5.4 for an in-focus object.

Now we can proceed towards the SVD by solving the eigenvalue problem

$$[\mathcal{H}^{(\text{epi})}]^\dagger \mathcal{H}^{(\text{epi})} \mathbf{u}_{\boldsymbol{\rho},k}^{(\text{epi})} = \mu_{\boldsymbol{\rho},k}^{(\text{epi})} \mathbf{u}_{\boldsymbol{\rho},k}^{(\text{epi})}. \quad (5.77)$$

Following our earlier work, we choose a basis for our object-space singular functions and use shift-invariance to fix the spatial component of the singular function

$$(\hat{\mathbf{e}}(\mathbf{r}_o^\perp)\hat{\mathbf{E}}_{\ell m}, \mathbf{u}_{\boldsymbol{\rho},k}^{(\text{epi})}) = \tilde{U}_{k;\ell m}^{(\text{epi})}(\boldsymbol{\rho}) \exp[2\pi i \boldsymbol{\rho} \cdot \mathbf{r}_o^\perp]. \quad (5.78)$$

Next, we write the entries of the adjoint operator as

$$(\hat{\mathbf{e}}(\mathbf{r}_o^\perp)\hat{\mathbf{E}}_{\ell m}, [\mathcal{H}^{(\text{epi})}]^\dagger \hat{\mathbf{e}}(\mathbf{r}_d)\hat{\mathbf{e}}_j) = H_{j,\ell m}^{(\text{epi})*}(\mathbf{r}_d - \mathbf{r}_o^\perp). \quad (5.79)$$

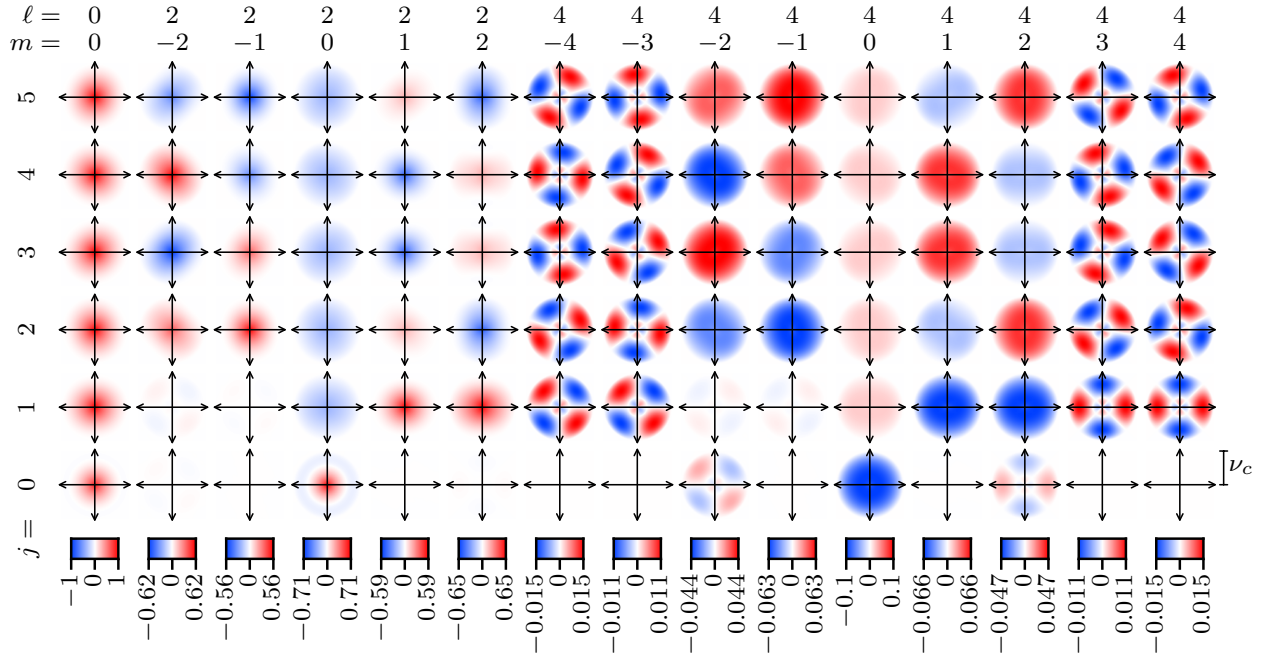


Figure 5.4: The in-focus transfer function $H_{j,\ell m}^{(epi)}(\nu)$ for six icosahedral illuminations (rows) and fifteen spherical harmonic components (columns) with $NA = 1.4$, $n_0 = 1.5$, and $\lambda = 500 \text{ nm}$. Each column uses its own color scale (bottom color bars). The position within each axis is the continuous spatial frequency ν . The transfer function is zero when $|\nu| \geq \nu_c = 2NA/\lambda$, when $j < 0$ or $j > 6$, when $\ell \neq 0, 2, 4$, or when $|m| > \ell$.

Now we can calculate the entries of $[\mathcal{H}^{(epi)}]^\dagger \mathcal{H}^{(epi)}$ as

$$\begin{aligned} \left(\hat{\mathbf{e}}(\mathbf{r}_o^\perp) \hat{\mathbf{E}}_{\ell m}, [\mathcal{H}^{(epi)}]^\dagger \mathcal{H}^{(epi)} \hat{\mathbf{e}}(\mathbf{r}_o^{\perp'}) \hat{\mathbf{E}}_{\ell' m'} \right) &\equiv p_{\ell m, \ell' m'}^{(epi)}(\mathbf{r}_o^\perp - \mathbf{r}_o^{\perp'}) \\ &= \sum_j \int_{\mathbb{R}^2} d\mathbf{r}_d H_{j, \ell m}^{(epi)*}(\mathbf{r}_d - \mathbf{r}_o^\perp) H_{j, \ell' m'}^{(epi)}(\mathbf{r}_d - \mathbf{r}_o^{\perp'}). \end{aligned} \quad (5.80)$$

Writing the eigenvalue problem explicitly yields

$$\left(\hat{\mathbf{e}}(\mathbf{r}_o^\perp) \hat{\mathbf{E}}_{\ell m}, [\mathcal{H}^{(epi)}]^\dagger \mathcal{H}^{(epi)} \mathbf{u}_{\rho, k}^{(epi)} \right) = \mu_{\rho, k}^{(epi)} \tilde{U}_{k; \ell m}^{(epi)}(\rho) \exp[2\pi i \rho \cdot \mathbf{r}_o^\perp]. \quad (5.81)$$

Rewriting the left-hand side in terms of known transfer functions yields

$$\left(\hat{\mathbf{e}}(\mathbf{r}_o^\perp) \hat{\mathbf{E}}_{\ell m}, [\mathcal{H}^{(epi)}]^\dagger \mathcal{H}^{(epi)} \mathbf{u}_{\rho, k}^{(epi)} \right) = \sum_{\ell' m'} \int_{\mathbb{R}^2} d\mathbf{r}_o^{\perp'} p_{\ell m, \ell' m'}^{(epi)}(\mathbf{r}_o^\perp - \mathbf{r}_o^{\perp'}) \tilde{U}_{k; \ell' m'}^{(epi)}(\mathbf{r}_o^{\perp'}) \exp[2\pi i \rho \cdot \mathbf{r}_o^{\perp'}]$$

$$\begin{aligned}
&= \exp[2\pi i \boldsymbol{\rho} \cdot \mathbf{r}_o^\perp] \sum_{\ell' m'} P_{\ell m, \ell' m'}^{(\text{epi})}(\boldsymbol{\rho}) \tilde{U}_{k; \ell' m'}^{(\text{epi})}(\boldsymbol{\rho}) \\
&= \exp[2\pi i \boldsymbol{\rho} \cdot \mathbf{r}_o^\perp] \sum_{\ell' m'} \sum_j \mathsf{H}_{j, \ell m}^{(\text{epi})*}(\boldsymbol{\rho}) \mathsf{H}_{j, \ell' m'}^{(\text{epi})}(\boldsymbol{\rho}) \tilde{U}_{k; \ell' m'}^{(\text{epi})}(\boldsymbol{\rho}),
\end{aligned} \tag{5.82}$$

where we have used the following calculation

$$P_{\ell m, \ell' m'}^{(\text{epi})}(\boldsymbol{\rho}) = \int_{\mathbb{R}^2} d\mathbf{r} p_{\ell m, \ell' m'}^{(\text{epi})}(\mathbf{r}) \exp[-2\pi \boldsymbol{\rho} \cdot \mathbf{r}] = \sum_j \mathsf{H}_{j, \ell m}^{(\text{epi})*}(\boldsymbol{\rho}) \mathsf{H}_{j, \ell' m'}^{(\text{epi})}(\boldsymbol{\rho}). \tag{5.83}$$

Equating the right-hand sides of Eqs. (5.81) and (5.82) yields

$$\sum_{\ell' m'} \left[\sum_j \mathsf{H}_{j, \ell m}^{(\text{epi})*}(\boldsymbol{\rho}) \mathsf{H}_{j, \ell' m'}^{(\text{epi})}(\boldsymbol{\rho}) \right] \tilde{U}_{k; \ell' m'}^{(\text{epi})}(\boldsymbol{\rho}) = \mu_{\boldsymbol{\rho}, k}^{(\text{epi})} \tilde{U}_{k; \ell m}^{(\text{epi})}(\boldsymbol{\rho}), \tag{5.84}$$

where the brackets enclose the entries of a 15×15 matrix for each $\boldsymbol{\rho}$. Each matrix is the sum of six outer products, so the matrix will be at most rank six. We refer to the rank of each 15×15 matrix as the *angular rank* R_a of the operator $\mathcal{H}^{(\text{epi})}$.

Although we cannot calculate the eigenfunctions and eigenvalues of a 15×15 matrix in closed form, we can easily find a numerical approximation. Once the eigenvalues $\mu_{\boldsymbol{\rho}, k}$ and the 15×1 eigenvectors $\tilde{U}_{k; \ell m}^{(\text{epi})}(\boldsymbol{\rho})$ have been approximated and normalized, it is straightforward to calculate the complete object-space singular functions in the standard basis

$$u_{\boldsymbol{\rho}, k}^{(\text{epi})}(\mathbf{r}_o^\perp, \hat{\mathbf{s}}_o) = \exp[2\pi i \boldsymbol{\rho} \cdot \mathbf{r}_o^\perp] \sum_{\ell m} \tilde{U}_{k; \ell m}^{(\text{epi})}(\boldsymbol{\rho}) Y_{\ell m}(\hat{\mathbf{s}}_o). \tag{5.85}$$

For visualizing the singular functions, the following definition is useful

$$\tilde{u}_{\boldsymbol{\rho}, k}^{(\text{epi})}(\hat{\mathbf{s}}_o) = \sum_{\ell m} \tilde{U}_{k; \ell m}^{(\text{epi})}(\boldsymbol{\rho}) Y_{\ell m}(\hat{\mathbf{s}}_o). \tag{5.86}$$

Finally, the data-space singular functions can be found by calculating 6×1 vectors

$$\tilde{V}_{k;j}^{(\text{epi})}(\boldsymbol{\rho}) = \sqrt{\mu_{\boldsymbol{\rho},k}^{(\text{epi})}} \sum_{\ell m} \mathsf{H}_{j,\ell m}^{(\text{epi})}(\boldsymbol{\rho}) \tilde{U}_{k;\ell m}^{(\text{epi})}(\boldsymbol{\rho}), \quad (5.87)$$

then multiplying by complex exponentials

$$v_{\boldsymbol{\rho},k;j}^{(\text{epi})}(\mathbf{r}_d) = \tilde{V}_{k;j}^{(\text{epi})}(\boldsymbol{\rho}) \exp[2\pi i \boldsymbol{\rho} \cdot \mathbf{r}_d]. \quad (5.88)$$

Figure 5.5 shows the angular part of the object-space singular functions $\tilde{u}_{\boldsymbol{\rho},k}^{(\text{epi})}(\hat{\mathbf{s}}_o)$ and the eigenvalues $\mu_{\boldsymbol{\rho},k}^{(\text{epi})}$ that we approximated numerically. When we calculated the singular system of $\mathcal{H}^{(\text{det})}$ we established the rotational symmetry of the eigenvalues analytically by studying properties of the operator entries—see Eq. (5.29). Although we know of no similar relationship for the singular system of $\mathcal{H}^{(\text{epi})}$, we have numerical evidence for the same rotational symmetry. More specifically, the eigenvalues $\mu_{\boldsymbol{\rho},k}^{(\text{epi})}$ only depend on $|\boldsymbol{\rho}|$, so we only need to calculate the singular system for each $|\boldsymbol{\rho}|$ on the positive real line \mathbb{R}_+ . This degeneracy reflects that fact that rigid rotations of the whole object (each position and orientation at the same time) commute with $[\mathcal{H}^{(\text{epi})}]^\dagger \mathcal{H}^{(\text{epi})}$.

There is at least one more easily interpreted degeneracy in the eigenvalue spectrum $\mu_{\boldsymbol{\rho},k}^{(\text{epi})}$. For $\boldsymbol{\rho} = 0$ the eigenvalue spectrum consists of two singlets and two doublets. When we studied the eigenvalues of $[\mathcal{H}^{(\text{exc})}]^\dagger \mathcal{H}^{(\text{exc})}$ we found that the eigenvalue spectrum consisted of a singlet and a 5-plet, which reflected the $\mathbb{SO}(3)$ symmetry of the imaging operator. Now that we have combined the excitation and detection operators into a single operator we have lost the complete $\mathbb{SO}(3)$ symmetry because the collection solid angle on the detection side is less than 2π (equivalently, $\text{NA} < n_o$). This fact breaks the $\mathbb{SO}(3)$ symmetry, but the imaging system still retains an $\mathbb{O}(2)$ symmetry with its characteristic one- and two-dimensional irreducible representations [159]. This degeneracy reflects the fact that rotations of the fluorophore distributions at each spatial position commute with $[\mathcal{H}^{(\text{epi})}]^\dagger \mathcal{H}^{(\text{epi})}$ when

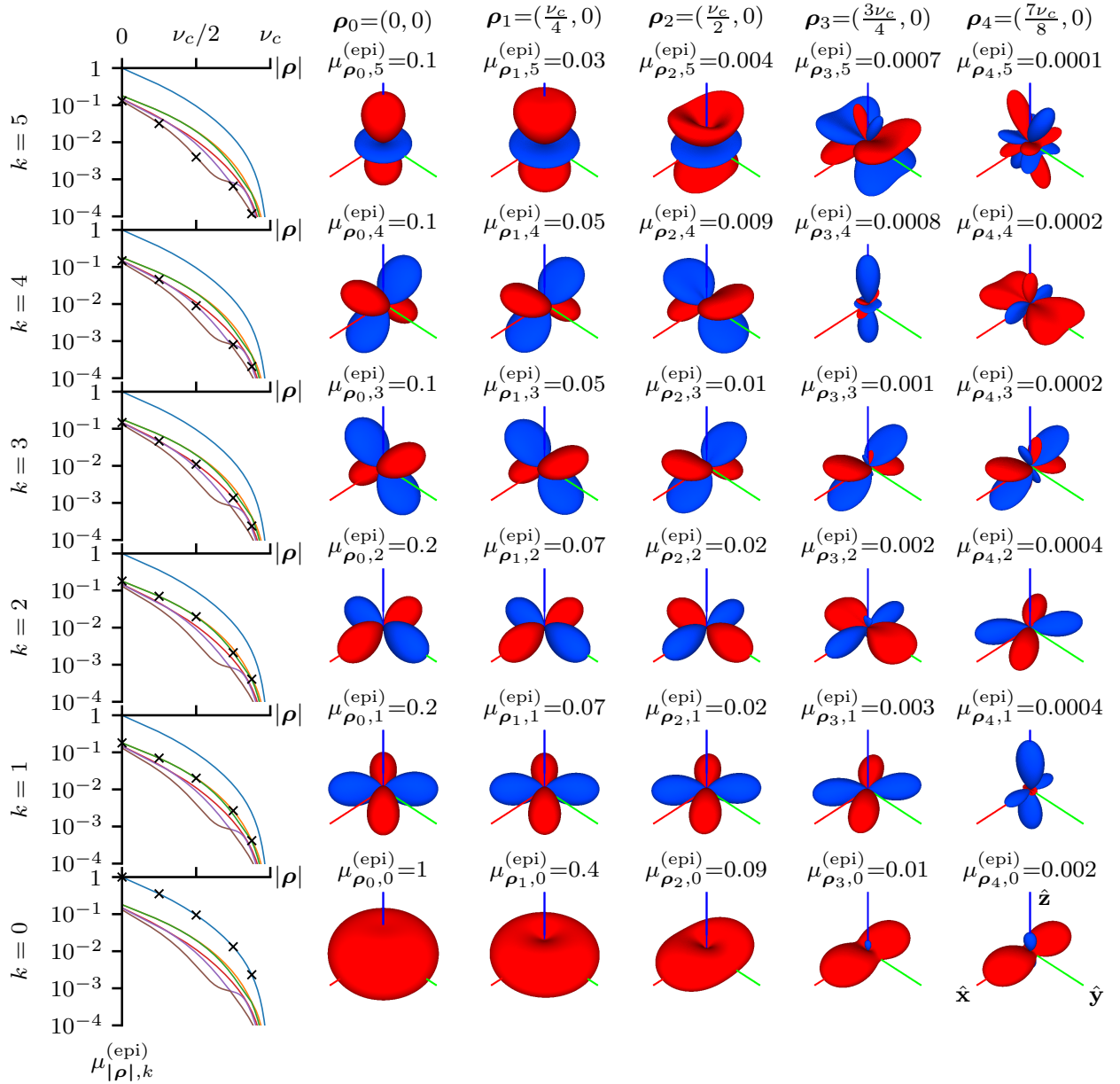


Figure 5.5: The singular system of $\mathcal{H}^{(\text{epi})}$ for in-focus objects measured with six icosahedral illumination polarizations. The left column shows the eigenvalues of $[\mathcal{H}^{(\text{epi})}]^\dagger \mathcal{H}^{(\text{epi})}$ as a function of $|\boldsymbol{\rho}|$, while the right columns show the angular part of five object-space singular functions $\tilde{u}_k^{(\text{epi})}(\boldsymbol{\rho}, \hat{\mathbf{s}}_o)$ —see Eq. (5.86). The five choices of $\boldsymbol{\rho}$ are labeled at the top of each column and are marked with crosses in the eigenvalue spectrum. All six eigenvalue spectra are shown in each row so they can be readily compared. The radius of each glyph along direction $\hat{\mathbf{s}}_o$ indicates the magnitude $|\tilde{u}_k^{(\text{det})}(\boldsymbol{\rho}, \hat{\mathbf{s}}_o)|$ while the color indicates the sign—red is positive and blue is negative.

the fluorophore distribution is spatially uniform (i.e. $\rho = 0$).

For $\rho \neq 0$ the doublets split into singlets except at specific spatial frequencies (for example, see $|\rho| \approx 3\nu_c/4$ for $k = 4$ and $k = 5$). These points indicate symmetry operators that rotate individual fluorophore distributions at a fixed non-zero spatial frequency. These points are called “accidental” degeneracies, and they indicate extra members of the symmetry group of $\mathcal{H}^{(\text{epi})}$ that are difficult to predict. In addition to the points where two branches of the spectrum meet, there are accidental degeneracies between branches at branch-dependent spatial frequencies. To spot these degeneracies, draw horizontal lines through the spectra in the left column of Fig. 5.5 and find lines that intersect multiple branches. These degeneracies indicate symmetry operators that rotate and scale objects simultaneously. We have not studied these accidental degeneracies in detail, and we do not know what underlying symmetry groups they indicate. Although accidental degeneracies are of theoretical interest, it is not clear to us if studying them further will lead to benefits beyond marginally faster singular value decompositions.

5.5 Reconstruction algorithms

In this section we develop an efficient reconstruction algorithm for the microscope we modeled in the previous section: we illuminate with polarized light, image with a high-NA objective, then repeat the imaging under several illumination polarization settings. This class of imaging system can be modeled by

$$g_j(\mathbf{r}_d) = \int_{\mathbb{R}^2} d\mathbf{r}_o^\perp \int_{\mathbb{S}^2} d\hat{\mathbf{s}}_o h_j^{(\text{epi})}(\mathbf{r}_d - \mathbf{r}_o^\perp, \hat{\mathbf{s}}_o) \bar{f}(\mathbf{r}_o^\perp, \hat{\mathbf{s}}_o), \quad (5.89)$$

where the kernel factors into

$$h_j^{(\text{epi})}(\mathbf{r}, \hat{\mathbf{s}}_o) = h^{(\text{det})}(\mathbf{r}, \hat{\mathbf{s}}_o) h^{(\text{exc})}(\hat{\mathbf{p}}_j, \hat{\mathbf{s}}_o). \quad (5.90)$$

Our goal is to estimate as much as we can about the object $\bar{f}(\mathbf{r}_o^\perp, \hat{\mathbf{s}}_o)$ from our measurements $g_j(\mathbf{r}_d)$ and our knowledge of the function $h_j^{(\text{epi})}(\mathbf{r}, \hat{\mathbf{s}}_o)$.

Throughout this section we will use continuous coordinates to model positions in the object \mathbf{r}_o^\perp and on the detector \mathbf{r}_d . Real data will have discrete detector coordinates, but for now we treat continuous coordinates as a good approximation for discrete coordinates. The reconstruction algorithms in this section can be applied to discrete data by approximating the continuous Fourier transforms by discrete Fourier transforms (with suitable scaling and padding).

5.5.1 Step 1: Modeling and calibration

Before beginning the reconstruction we need a model for the imaging system. The easiest way to obtain a model $h_j^{(\text{epi})}(\mathbf{r}, \hat{\mathbf{s}}_o)$ is to adapt the models presented earlier in this chapter. Measuring this function directly is a potential option, but this would require precise control over the orientation of a single emitter, which is not currently feasible.

However, we can make experimentally feasible measurements of components of $h^{(\text{epi})}(\mathbf{r}, \hat{\mathbf{s}}_o)$ if we change to a different basis. For example, if we change to a basis of object-space spherical harmonics using

$$H_{j,\ell m}^{(\text{epi})}(\mathbf{r}) = \int_{\mathbb{S}^2} d\hat{\mathbf{s}}_o h^{(\text{epi})}(\mathbf{r}, \hat{\mathbf{s}}_o) Y_{\ell m}(\hat{\mathbf{s}}_o), \quad (5.91)$$

then we can measure $H_{j,00}^{(\text{epi})}(\mathbf{r})$ by placing beads with uniformly oriented dipoles in the imaging system and measuring their images. Additionally, if we change to a basis of object- and data-space spatial harmonics using

$$\mathsf{H}_{j,\ell m}^{(\text{epi})}(\boldsymbol{\nu}) = \int_{\mathbb{R}^2} d\mathbf{r} H_{j,\ell m}^{(\text{epi})}(\mathbf{r}) \exp[-2\pi i \mathbf{r} \cdot \boldsymbol{\nu}], \quad (5.92)$$

then we can measure $\mathsf{H}_{j,00}^{(\text{epi})}(\mathbf{0})$ by placing a spatially and angularly uniform fluorescent lake in

the imaging system and measuring its image. Although neither of these approaches provide complete measurements of $h_j^{(\text{epi})}(\mathbf{r}, \hat{\mathbf{s}}_o)$, these simple objects can be used to help calibrate the imaging system and test theoretical models.

5.5.2 Step 2: Precalculating the SVD

With a model of the imaging system $h_j^{(\text{epi})}(\mathbf{r}_d - \mathbf{r}_o^\perp, \hat{\mathbf{s}}_o)$ in hand, we can precalculate the SVD. It is tempting to discretize object space and data space, calculate a finite-dimensional matrix representation of $h_j^{(\text{epi})}(\mathbf{r}_d - \mathbf{r}_o, \hat{\mathbf{s}}_o)$, then numerically approximate its SVD, but a back-of-the-envelope calculation reveals that this approach does not scale well. If we discretize the spatial components into N^2 voxels, discretize the sphere into S points, and make J measurements, then a discrete version of $h_j^{(\text{epi})}(\mathbf{r}_d - \mathbf{r}_o^\perp, \hat{\mathbf{s}}_o)$ will require $N^2S \times N^2J$ entries and calculating its SVD will require $\mathcal{O}(N^6 J^2 S)$ operations when $S > J$ [197]. In real experiments $N \approx 10^3$, $S \approx 10^2$ and $J \approx 6$, so storing $h_j^{(\text{epi})}(\mathbf{r}_d - \mathbf{r}_o^\perp, \hat{\mathbf{s}}_o)$ in double-precision floating-point format will require ≈ 50 TB of memory and taking its SVD will require $\approx 10^{22}$ floating-point operations.

Fortunately, we can exploit symmetry to reduce the memory and computation requirements. The first step is to choose a basis that provides a compact description of the imaging system. In object-space spherical harmonics and object- and data-space complex exponentials, $h_j^{(\text{epi})}(\mathbf{r}_d - \mathbf{r}_o^\perp, \hat{\mathbf{s}}_o)$ becomes

$$\mathsf{H}_{j,\ell m}^{(\text{epi})}(\boldsymbol{\nu}) = \int_{\mathbb{R}^2} d\mathbf{r} \int_{\mathbb{S}^2} d\hat{\mathbf{s}}_o h^{(\text{epi})}(\mathbf{r}, \hat{\mathbf{s}}_o) \exp[-2\pi i \mathbf{r} \cdot \boldsymbol{\nu}] Y_{\ell m}(\hat{\mathbf{s}}_o), \quad (5.93)$$

which can be computed most efficiently using

$$\mathsf{H}_{j,\ell m}^{(\text{epi})}(\boldsymbol{\nu}) = \sum_{\ell' m'} \sum_{\ell'' m''} G_{\ell \ell' \ell''}^{mm'm''} \mathsf{H}_{\ell' m'}^{(\text{det})}(\boldsymbol{\nu}) H_{\ell'' m''}^{(\text{exc})}(\hat{\mathbf{p}}_j), \quad (5.94)$$

where

$$\mathsf{H}_{\ell m}^{(\det)}(\boldsymbol{\nu}) = \int_{\mathbb{R}^2} d\mathbf{r} H_{\ell m}^{(\det)}(\mathbf{r}) \exp[-2\pi i \mathbf{r} \cdot \boldsymbol{\nu}], \quad (5.95)$$

$$H_{\ell m}^{(\det)}(\mathbf{r}) = \int_{\mathbb{S}^2} d\hat{\mathbf{s}}_o h^{(\det)}(\mathbf{r}, \hat{\mathbf{s}}_o) Y_{\ell m}(\hat{\mathbf{s}}_o) \propto \sum_{j,j'=0,1,2} G_{\ell 11}^{m \epsilon_j \epsilon_{j'}} B_{jj'}(\mathbf{r}, r_o^{\parallel}), \quad (5.96)$$

$$H_{\ell m}^{(\text{exc})}(\hat{\mathbf{p}}_j) = \int_{\mathbb{S}^2} d\hat{\mathbf{s}}_o h^{(\text{exc})}(\hat{\mathbf{p}}_j, \hat{\mathbf{s}}_o) Y_{\ell m}(\hat{\mathbf{s}}_o), \quad (5.97)$$

and more detail on calculating $H_{\ell m}^{(\det)}(\mathbf{r})$ from $B_{jj'}(\mathbf{r}, r_o^{\parallel})$ can be found in section 5.2. Because $\mathsf{H}_{j,\ell m}^{(\text{epi})}(\boldsymbol{\nu})$ is only non-zero for 15 spherical harmonic components, we can discretize it using only $15N^2J$ entries ≈ 10 MB.

Next, we calculate and store the singular value decomposition of a $15 \times J$ matrix at each of the N^2 spatial frequencies. Most numerical packages can approximate SVDs from the matrices $\mathsf{H}_{j,\ell m}^{(\text{epi})}(\boldsymbol{\nu})$ directly, but if an SVD routine is unavailable the eigendecomposition of

$$P_{\ell m, \ell' m'}^{(\text{epi})}(\boldsymbol{\rho}) = \sum_j \mathsf{H}_{j,\ell m}^{(\text{epi})*}(\boldsymbol{\rho}) \mathsf{H}_{j,\ell' m'}^{(\text{epi})}(\boldsymbol{\rho}), \quad (5.98)$$

can be computed instead. In either case, the result will be a set of $R = N^2J$ (if the rank of each $15 \times J$ matrix is J) eigenvalues $\mu_{\boldsymbol{\rho},k}^{(\text{epi})}$, object-space singular functions $\tilde{U}_{k;\ell m}^{(\text{epi})}(\boldsymbol{\rho})$, and data-space singular functions $\tilde{V}_{k;j}^{(\text{epi})}(\boldsymbol{\rho})$. In this basis storing the SVD only requires ≈ 20 MB, and computing the SVD of N^2 matrices of size $15 \times J$ only requires $\approx 10^{10}$ floating point operations.

5.5.3 Step 3: Calculate the regularized pseudoinverse

Earlier in this chapter we introduced a Tikhonov-regularized pseudoinverse that could be expressed in terms of the forward operator's SVD as

$$\hat{\mathbf{f}}_{\eta} = \sum_{i=0}^R \frac{\sqrt{\mu_i}}{\mu_i + \eta} \mathbf{u}_i (\mathbf{v}_i, \mathbf{g}). \quad (5.99)$$

This solution is basis-independent, but we would like our final result to be in the easily interpreted standard basis. Storing the SVD in a standard basis is infeasible, so we need to apply the Tikhonov-regularized pseudoinverse in the spatial frequency basis. To put our data in the correct basis we take our raw data $g_j(\mathbf{r}_d)$ and take its spatial Fourier transform

$$G_j(\boldsymbol{\nu}) = \int_{\mathbb{R}^2} d\mathbf{r}_d g_j(\mathbf{r}_d) \exp[-2\pi i \mathbf{r}_d \cdot \boldsymbol{\nu}]. \quad (5.100)$$

Now we can apply a Tikhonov-regularized pseudoinverse using our stored SVD

$$\hat{F}_{\eta;\ell m}(\boldsymbol{\nu}) = \sum_{k=1}^{R_a} \frac{\sqrt{\mu_{\boldsymbol{\nu},k}}}{\mu_{\boldsymbol{\nu},k} + \eta} \tilde{U}_{k;\ell m}^{(\text{epi})}(\boldsymbol{\nu}) \sum_j \tilde{V}_{k;j}^{(\text{epi})}(\boldsymbol{\nu}) G_j(\boldsymbol{\nu}), \quad (5.101)$$

where R_a is the angular rank. The result $\hat{F}_{\eta;\ell m}(\boldsymbol{\nu})$ contains estimates of all of the parameters we can hope to reconstruct, but these estimates are in a basis that is difficult to interpret. We would like to store our parameters in a standard basis, but this would require much more storage than necessary. If we discretize the sphere into S points then we would need to store $(S/R_a) \times$ more information than necessary. Smooth visualizations require $S \approx 500$, so storing in a standard basis will require $\approx 75 \times$ more information than necessary.

We can move one step closer to the standard basis while minimizing storage inflation. If we take the inverse Fourier transform of $\hat{F}_{\eta;\ell m}(\boldsymbol{\nu})$ we find the estimates of the spherical harmonic coefficients at each spatial position

$$\hat{F}_{\eta;\ell m}(\mathbf{r}_o^\perp) = \int_{\mathbb{R}^2} d\boldsymbol{\nu} \hat{F}_{\eta;\ell m}(\boldsymbol{\nu}) \exp[2\pi i \mathbf{r}_o^\perp \cdot \boldsymbol{\nu}]. \quad (5.102)$$

Prescribing firm guidelines for choosing a regularization parameter η is impossible without full knowledge of the stochastic properties of the objects and imaging process. We recommend performing reconstructions over a wide range of η values (including $\eta = 0$) then choosing the

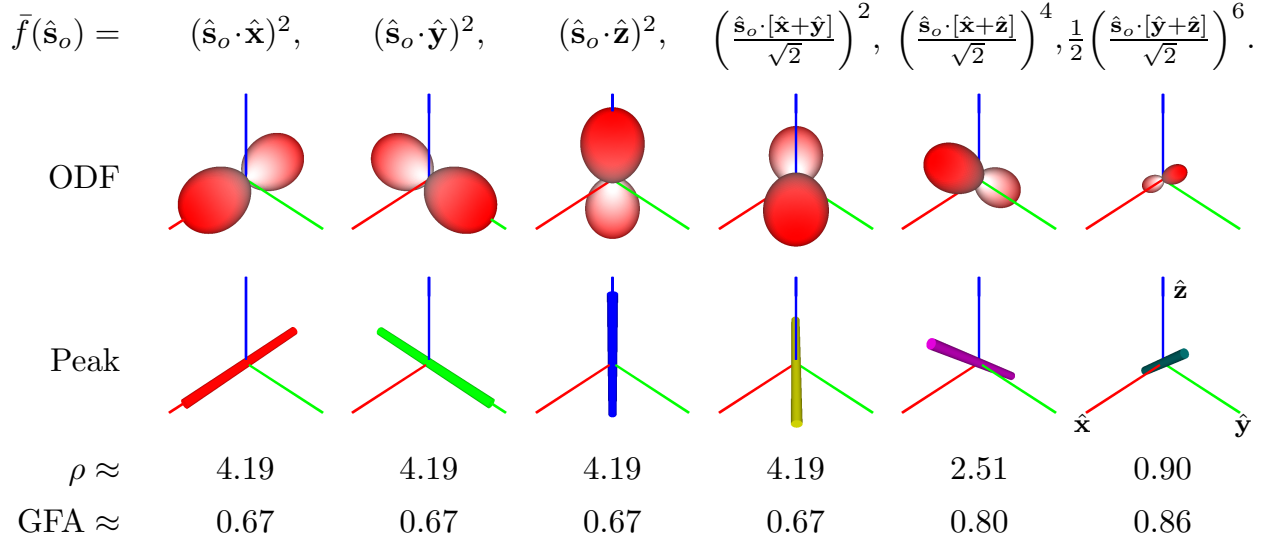


Figure 5.6: Demonstration of angular visualization schemes. Each column shows a different angular function for a single spatial point $\bar{f}(\hat{\mathbf{s}}_o)$ specified by the upper label. The first row shows an orientation distribution function (ODF) visualization that doubly encodes the magnitude of $\bar{f}(\hat{\mathbf{s}}_o)$ into the glyph radius and glyph color. Notice that red encodes the maximum for each glyph instead of a fixed value. The second row shows the peak directions visualized with an oriented cylinder colored using the absolute value method. Once again, the peak orientation is doubly encoded into the orientation and color of the cylinder. Finally, we calculate the density ρ and the generalized fractional anisotropy (GFA). These scalar values can be visualized using any color map.

smallest value of η that suppresses noise without washing out features of interest. Although the choice of η is qualitative, we find empirically that high-quality data can yield high-quality reconstructions for a wide range of η —see the reconstructions in chapter 6.

5.5.4 Step 4: Visualize and interpret

Figure 5.6 demonstrates four ways to visualize individual spatial points from a spatio-angular reconstruction. We have found these visuals to be the most useful for understanding and interpreting reconstructions. In this section we describe how to calculate these visuals in detail.

Starting with the stored reconstruction $\hat{F}_{\eta; \ell m}(\mathbf{r}_o^\perp)$, our goal is to calculate and plot useful

visuals. To avoid storage inflation we have postponed our conversion to a standard basis until visualization time. Our first step is to choose a set of N points on the sphere $\{\hat{\mathbf{s}}_{o,n}\}$ that we would like to visualize. The Fibonacci lattice is an attractive choice because it leads to well-spaced points that are inexpensive to compute for arbitrary N . The polar angles $\{\theta_n\}$ and azimuthal angles $\{\phi_n\}$ of the Fibonacci lattice with N points are given by [198, 199]

$$\theta_n = \cos^{-1}(1 - (2n + 1)/N), \quad (5.103)$$

$$\phi_n = \pi(3 - \sqrt{5})n. \quad (5.104)$$

Choosing a larger N will make the final visuals appear smoother at additional computational expense. Empirically we have found that $N = 500$ is an appropriate starting point for most visualizations.

Next, we choose a set of spatial points $\{\mathbf{r}_{o,i}^\perp\}$ where we would like to visualize the object. We recommend starting with a modest number of spatial points by downsampling or thresholding the reconstruction because visualizing every spatial point is visually overwhelming and computationally expensive. Empirically we have found that visualizing more than 10^4 spatial points overwhelms most users who are trying to interpret the results and most computers that are trying to render them without a dedicated graphics card.

With our spherical points $\{\hat{\mathbf{s}}_{o,n}\}$ and spatial points $\{\mathbf{r}_{o,i}^\perp\}$ we can calculate the *orientation distribution functions (ODFs)* at each point

$$\hat{f}_\eta(\mathbf{r}_{o,i}^\perp, \mathbf{s}_{o,n}) = \sum_{\ell m} \hat{F}_{\eta; \ell m}(\mathbf{r}_{o,i}^\perp) Y_{\ell m}(\mathbf{s}_{o,n}). \quad (5.105)$$

Notice that the spherical harmonics $Y_{\ell m}(\mathbf{s}_{o,n})$ can be computed once then reused. The ODFs can be visualized by drawing a glyph at each point $\{\mathbf{r}_{o,i}^\perp\}$ with a radius along each direction $\{\hat{\mathbf{s}}_{o,n}\}$ given by $\hat{f}_\eta(\mathbf{r}_{o,i}^\perp, \mathbf{s}_{o,n})$. We have used red and blue to indicate positive and negative values or a blue-white-red color map to doubly encode the value of $\hat{f}_\eta(\mathbf{r}_{o,i}^\perp, \mathbf{s}_{o,n})$ into the

radius and the color of the glyph.

In addition to drawing a complete glyph at each point $\{\mathbf{r}_{o,i}^\perp\}$, we have found that drawing a cylinder or thin line at each point $\{\mathbf{r}_{o,i}^\perp\}$ along the direction where the function is largest $\hat{\mathbf{s}}_\eta^{(pk)}(\mathbf{r}_{o,i}^\perp) = \text{argmax}_{\hat{\mathbf{s}}_o} \hat{f}_\eta(\mathbf{r}_{o,i}^\perp, \hat{\mathbf{s}}_o)$ is a good way to summarize and understand the reconstruction. In many cases the viewing direction obscures the direction of the cylinder or line, so encoding the direction of the line in color can reduce visual degeneracy. In all of our reconstructions we have colored the $\hat{\mathbf{x}}$, $\hat{\mathbf{y}}$, and $\hat{\mathbf{z}}$ components of $\hat{\mathbf{s}}_\eta^{(pk)}(\mathbf{r}_{o,i}^\perp)$ with weighted red, green, and blue color channels, respectively. In the computer graphics and magnetic resonance imaging (MRI) literature this color mapping is usually called the *absolute value method* [200]. Although the absolute value method is widely used and easy to understand, it suffers from ambiguities that can be avoided by using more sophisticated color maps [201].

We can also calculate and plot scalar summary statistics for each spatial point. The estimated number of fluorophores at each point or *fluorophore density* is given directly by

$$\hat{\rho}_\eta(\mathbf{r}_o^\perp) = \hat{F}_{\eta;00}(\mathbf{r}_o^\perp), \quad (5.106)$$

which is a subset of the stored reconstruction in Eq. (5.102). Another useful scalar summary statistic is the *generalized fractional anisotropy* [202, 203], which is

$$\hat{\text{GFA}}_\eta(\mathbf{r}_o^\perp) = \sqrt{1 - \frac{\left[\hat{F}_{\eta;00}(\mathbf{r}_o^\perp)\right]^2}{\sum_{\ell m} \left[\hat{F}_{\eta;\ell m}(\mathbf{r}_o^\perp)\right]^2}}. \quad (5.107)$$

Although both of these parameters are useful for summarizing the data, strictly speaking neither is estimable since they do not live in the measurement space of the imaging system. We know that estimates of ρ and GFA can be biased, so we need to be skeptical of any conclusions drawn from them. Averaging over larger spatial regions can reduce (but not eliminate) these biases.

5.5.5 Summary and practical tips

Table 5.1 summarizes the steps of the reconstruction algorithm with `numpy` pseudocode to aid implementation. In no particular order, we give a few practical tips for implementing this reconstruction algorithm.

Although the spherical harmonic indices ℓ and m are convenient for pen-and-paper calculations, a single collapsed index allows us to use simple rectangular arrays to store values. We only need the even spherical harmonics, so an appropriate collapsed index is given by $s = [\ell(\ell + 1) + m]/2$.

The `numpy` function `einsum` (inspired by Krister Åhlander's C++ library [204]) is an extremely efficient way to program the multidimensional array multiplications required for these reconstructions. The effort required to learn `einsum` is small compared to the dividends paid during the implementation of a single complicated multidimensional array multiplication. See the examples in Table 5.1 and `numpy`'s excellent documentation [205] to get started.

We recommend thoroughly understanding the behavior of the forward model before attempting to implement a reconstruction. Starting with a known numerical phantom $\bar{f}(\mathbf{r}_o^\perp, \hat{\mathbf{s}}_o)$, calculate its spatio-angular spectrum using

$$\bar{\mathcal{F}}_{\ell m}(\boldsymbol{\nu}) = \int_{\mathbb{R}^2} d\mathbf{r}_o^\perp \int_{\mathbb{S}^2} d\hat{\mathbf{s}}_o \bar{f}(\mathbf{r}_o^\perp, \hat{\mathbf{s}}_o) \exp[-2\pi i \mathbf{r}_o^\perp \cdot \boldsymbol{\nu}] Y_{\ell m}(\hat{\mathbf{s}}_o). \quad (5.108)$$

Next, simulate the data spectrum using

$$G_j(\boldsymbol{\nu}) = \sum_{\ell m} \mathcal{H}_{j,\ell m}^{(\text{epi})}(\boldsymbol{\nu}) \bar{\mathcal{F}}_{\ell m}(\boldsymbol{\nu}). \quad (5.109)$$

Finally, calculate the data in a standard basis

$$g_j(\mathbf{r}_d) = \int_{\mathbb{R}^2} d\mathbf{r}_d G_j(\boldsymbol{\nu}) \exp[2\pi i \mathbf{r}_d \cdot \boldsymbol{\nu}]. \quad (5.110)$$

Models can be debugged or improved by comparing the results with the microscope developer's expectations and adjusting the model accordingly.

Steps	Symbols	numpy pseudocode
<i>Precalculations</i>		
Define and/or measure a model	$h^{(\text{epi})}(\mathbf{r}_d - \mathbf{r}_o^\perp, \hat{\mathbf{s}}_o)$	def $h(\mathbf{rd}, \mathbf{ro}, \mathbf{so}, \text{*params})$: ...
Calculate the model in a compact basis	$\mathbf{H}_{j;\ell m}^{(\text{epi})}(\boldsymbol{\nu})$	$\mathbf{H}.\text{shape} \rightarrow (1000, 1000, 15, 6)$
Calculate the SVD		$\mathbf{u}, \mathbf{s}, \mathbf{v} = \text{np.linalg.svd}(\mathbf{H}, \text{full_matrices=False})$
... object space singular functions	$\tilde{U}_{k;\ell m}^{(\text{epi})}(\boldsymbol{\nu})$	$\mathbf{u}.\text{shape} \rightarrow (1000, 1000, 15, 6)$
... singular values	$\sqrt{\mu_{\boldsymbol{\nu};k}}$	$\mathbf{s}.\text{shape} \rightarrow (1000, 1000, 6)$
... data space singular functions	$\tilde{V}_{k;j}^{(\text{epi})}(\boldsymbol{\nu})$	$\mathbf{v}.\text{shape} \rightarrow (1000, 1000, 6, 6)$
<i>Reconstruction</i>		
Collect data	$g_j(\mathbf{r}_d)$	$\mathbf{g}.\text{shape} \rightarrow (1000, 1000, 6)$
DFT	$G_j(\boldsymbol{\nu})$	$\mathbf{G} = \text{np.fft.fft2}(\mathbf{g}, \text{axes=(0,1)})$
Choose η and regularize singular values	$\sigma_{\eta,\boldsymbol{\nu},k} = \frac{\sqrt{\mu_{\boldsymbol{\nu};k}}}{\mu_{\boldsymbol{\nu};k} + \eta}$	$\mathbf{sr} = \text{np.sqrt}(\mathbf{s}) / (\mathbf{s} + \mathbf{eta})$
Estimate $\hat{\mathbf{F}}_{\eta;\ell m}(\boldsymbol{\nu})$	$\sum_k \sigma_{\eta,\boldsymbol{\nu},k} \tilde{U}_{k;\ell m}^{(\text{epi})}(\boldsymbol{\nu}) \dots$	$\mathbf{F} = \text{np.einsum}('xyk, xysk, xyjk, xyj->xyz',$
	$\sum_j \tilde{V}_{k;j}^{(\text{epi})}(\boldsymbol{\nu}) G_j(\boldsymbol{\nu})$	$\mathbf{sr}, \mathbf{u}, \mathbf{v}, \mathbf{G})$
Inverse DFT then save	$\hat{F}_{\eta;\ell m}(\mathbf{r}_o^\perp)$	$\mathbf{Fr} = \text{np.fft.ifft2}(\mathbf{F}, \text{axes=(0,1)})$
<i>Visualization</i>		
Choose spherical points	$\{\hat{\mathbf{s}}_{o,n}\}$	$\text{sp}. \text{shape} \rightarrow (500, 3)$
Calculate SH to ODF coefficients	$Y_{\ell m}(\hat{\mathbf{s}}_{o,n})$	$\mathbf{Y}[\mathbf{n}, \mathbf{s}] = \text{sphharm}(\mathbf{s21}(\mathbf{s}), \mathbf{s2m}(\mathbf{s}), \text{sp}[\mathbf{n}, :])$
Choose mask (e.g. density > 0.5)	$\{\mathbf{r}_{o,i}\}$	$\mathbf{mask} = \mathbf{Fr}[:, :, 0] > 0.5$
Orientation distribution functions (ODFs)	$\hat{f}_\eta(\mathbf{r}_{o,i})$	$\text{ODF} = \text{np.einsum}('ns, is->ni', \mathbf{Y}, \text{Fr}[\text{mask}])$
Peak directions	$\hat{\mathbf{s}}_\eta^{(\text{pk})}(\mathbf{r}_{o,i}^\perp)$	$\text{np.amax}(\text{ODF}, \text{axis=0})$
Density	$\hat{\rho}_\eta(\mathbf{r}_o^\perp)$	$\mathbf{Fr}[:, :, 0]$
Generalized fractional anisotropy	$\text{GFA}_\eta(\mathbf{r}_o^\perp)$	$\text{np.sqrt}(1 - (\mathbf{Fr}[:, :, 0]**2 / \text{np.sum}(\mathbf{Fr}**2, \text{axis=-1})))$

Table 5.1: Summary of the reconstruction algorithm for a polarized illumination spatio-angular microscope.

5.6 Discussion and conclusions

5.6.1 Are icosahedral polarization samples always optimal?

In this chapter we showed that icosahedral polarization samples are optimal for polarized illumination with uniform detection, but we have made no claims about optimal sampling schemes for polarized illumination with high-NA detection. We suspect that icosahedral sampling schemes are nearly optimal for high-NA detection, but truly optimal sampling schemes will likely depend on the detection NA.

Our earlier definition of an optimal sampling scheme was the scheme that minimized the condition number of the operator, but the condition number is not defined for non-compact operators like the ones we are considering here. Instead, the Schatten 2-norm could be optimized. If $\mu_{\rho,k}(\mathcal{H})$ are the eigenvalues of $\mathcal{H}^\dagger \mathcal{H}$ with continuous index $\rho \in \mathbb{R}^2$ and discrete index k , then the Schatten 2-norm is

$$\|\mathcal{H}\|_2 = \left(\sum_k \int_{\mathbb{R}^2} d\rho \mu_{\rho,k}(\mathcal{H}) \right)^{\frac{1}{2}}, \quad (5.111)$$

which is large when \mathcal{H} has large and uniform singular value spectra [206].

5.6.2 Does the reconstruction algorithm exploit every symmetry?

Our reconstruction algorithm exploited the shift-invariance of the imaging system to minimize the computation and storage requirements for our algorithm. Several other symmetries are present (various rotational symmetries, symmetries related to accidental degeneracies), so it is natural to ask if we can further reduce the computation and storage requirements.

In short, every symmetry can be exploited to reduce computation and storage requirements, but some symmetries are more challenging to exploit than others. Shift-invariance is easy to exploit because the symmetry group is *abelian* (elements of the group commute) and

it acts on the plane \mathbb{R}^2 *transitively* (any point can be shifted to any other point by the action of a group element). We have demonstrated how to exploit these types of symmetries using Fourier transforms (and their associated abelian FFT algorithms) to solve the SVDs and reconstruction problems in a basis of spatial frequencies.

In contrast, the one-dimensional rotation group (or the rotation group in two dimensions $\mathbb{SO}(2)$) is an abelian group that acts *non-transitively* on the plane \mathbb{R}^2 , so it partitions the object and data geometries into *orbits*. Some orbits are *free*, which means that every group action moves every point in the orbit (like $\mathbb{SO}(2)$ acting on any circle about the origin), while other orbits are *stable* under some group elements (like $\mathbb{SO}(2)$ acting on the origin). The situation is further complicated by *non-abelian* symmetry groups with multi-dimensional irreducible representations (like $\mathbb{O}(2)$ and its two-dimensional irreducible representations).

Åhlander and Munthe-Kaas have shown how to exploit every symmetry to reduce storage and computation requirements when finding the eigendecomposition of finite-dimensional matrices [207]. This work is extremely relevant to our problem of finding the SVD of continuous-to-discrete operators since these SVDs require eigendecompositions of finite-dimensional matrices. Additionally, there are non-abelian FFT algorithms that can be used to improve the speed of the basis changes [208]. Non-abelian symmetries have not been completely exploited in image science (though they have been identified, see [1, ch. 7.2.9] and [181, sec. 6]), and we view these techniques as important future that work may lessen the burden of many SVD algorithms.

5.6.3 Can we use alternative priors or reconstruction algorithms?

Reconstructing with a Tikhonov-regularized pseudoinverse requires us to assume that we are estimating independent, zero-mean, Gaussian-distributed random variables with variance $1/(2\eta)$, where η is the regularization parameter. Although this might be a reasonable approximation to the true distribution of the parameters, a broader class of reconstruction

algorithms would clearly be desirable. Additionally, pseudoinverse algorithms like the one described here can result in negative estimates for $\bar{f}(\mathbf{r}_o, \hat{\mathbf{s}}_o)$, which is clearly undesirable.

There is a large literature of reconstruction algorithms for linear imaging systems—see Barrett and Myers for a review [1, ch. 15]. Among these algorithms are techniques for incorporating statistical priors, constraining solutions to be positive, and guaranteeing convergence, among other attractive properties. However, a large majority of these algorithms require the reconstruction to be performed in the standard basis, which imposes extremely large storage and computation constraints on this specific problem. These considerations have led us to avoid several common reconstruction algorithms like Richardson–Lucy iteration (or maximum-likelihood expectation maximization (MLEM)) because the computational requirements are excessive. We view Tikhonov-regularized pseudoinverse reconstructions as an imperfect starting place, and we think that finding or developing reconstruction algorithms that incorporate statistical priors and positivity constraints while remaining efficient in any basis is important future work.

CHAPTER 6

DUAL-VIEW SPATIO-ANGULAR MICROSCOPY

So much of our human resourcefulness comes from having multiple ways to describe the same situations—so that each one of those different perspectives may help us to get around the deficiencies of the other ones.
— MARVIN MINSKY *The Emotion Machine* (2006)

IN this chapter we build on our work in chapters 2–5 to develop a model and reconstruction scheme for a polarized-illumination dual-view light-sheet microscope. Notably, we apply our sampling results from chapter 5 to design a rank-6 polarization sampling scheme that is optimal under practical geometric constraints. We verify our methods by imaging giant unilamellar vesicles (GUVs)—a physical phantom with an approximately known spatio-angular density—and confirming that our experimental results match our expectations. We conclude by demonstrating our methods on a biological specimen—actin-labeled U2OS cells.

6.1 Forward model and transfer functions

We start by calculating the transfer function for a dual-view inverted selective plane illumination microscope (diSPIM) [101] with asymmetric detection objectives (1.1 and 0.71 NA) [102], computer-controlled illumination-side liquid crystal polarizers, and tiltable light sheets—see Fig. 6.1. We were motivated to pursue spatio-angular microscopy with this dual view design because of its potential to image with nearly isotropic spatial and angular resolution.

We start by considering an arbitrary three-dimensional angular Boltzmann density $\bar{f}(\mathbf{r}_o, \hat{\mathbf{s}}_o) \in \mathbb{L}_2(\mathbb{R}^3 \times \mathbb{S}^2)$. Notice that we are explicitly considering thick objects by using a three-dimensional coordinate \mathbf{r}_o instead of restricting ourselves to thin objects by using a two-dimensional coordinate \mathbf{r}_o^\perp . Light-sheet imaging systems illuminate the object with a sheet of light, collect a two-dimensional image, then scan the sheet or the object to build a three-dimensional dataset that we can index with a three-dimensional coordinate \mathbf{r}_d . Similar to

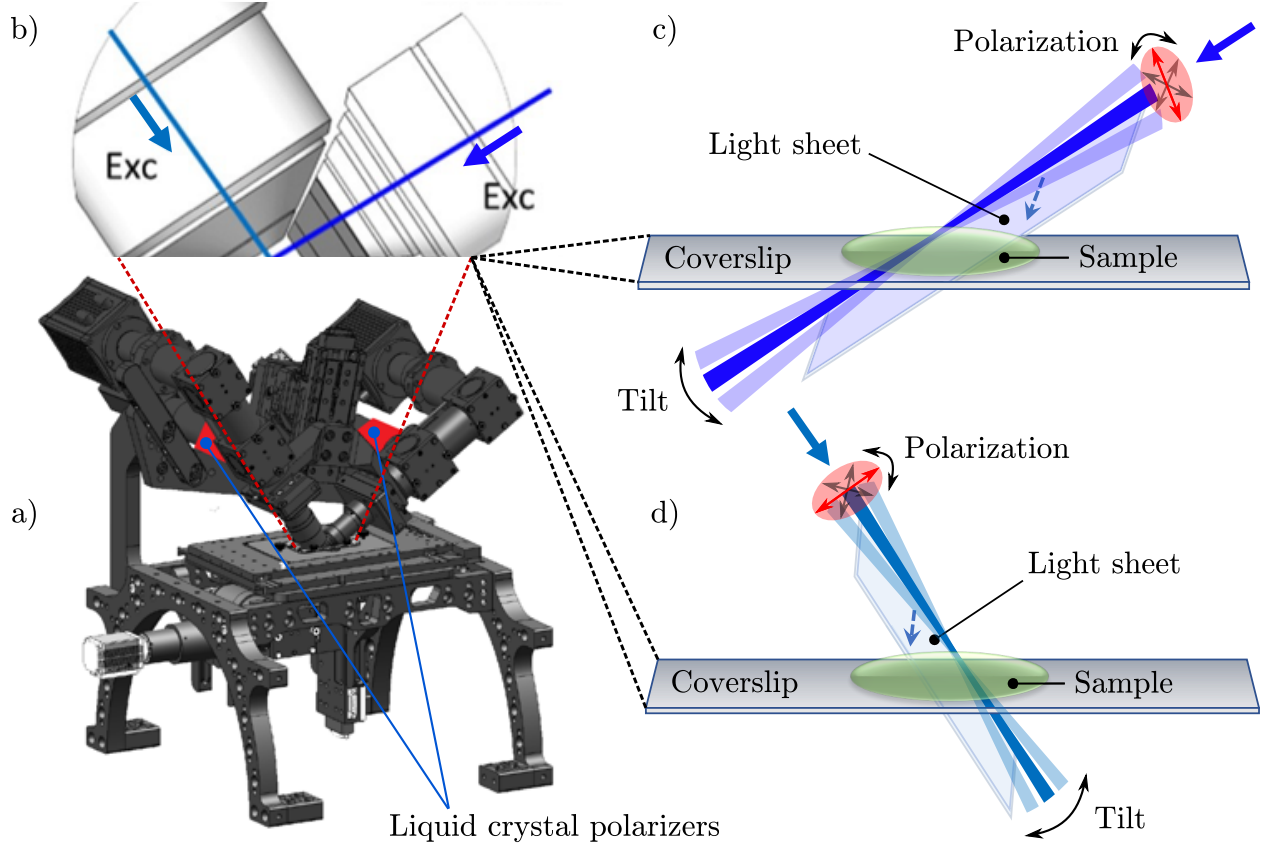


Figure 6.1: A dual-view light sheet microscope with asymmetric detection objectives (1.1 and 0.71 NA), computer-controlled illumination-side liquid crystal polarizers, and tiltable light sheets. a) Overview of the microscope with liquid crystal polarizers highlighted in red. b) A zoomed region near the sample highlights the asymmetric NA objectives. c) Excitation from the low-NA objective along the dark-blue axis—a polarized Gaussian beam is scanned through the sample to create a light sheet. The polarization and tilt angle of the light sheet are computer controlled. d) Excitation from the high-NA objective is controlled with the same degrees of freedom as the low-NA objective.

our work in chapter 5, we index sequential measurements of the object under different illumination polarizations with a discrete index j . Finally, we measure the same object under two orthogonal illumination/viewing directions, which we index with a new discrete index v . Therefore, our complete dataset takes the form $g_{jv}(\mathbf{r}_d) \in \mathbb{L}_2(\mathbb{R}^3)^P$ where P is the total number of illumination polarizations.

Notice that we have written the discrete indices j and v side by side instead of separated by a comma to indicate that they are paired in the same way that the spherical harmonic

indices ℓ and m are paired. For example, consider the case where we illuminate with three polarizations for the first view and two polarizations for the second view. Symbolically it is most convenient to keep track of both the polarization and view indices, but in a computer program it is most convenient to collapse these indices into a single index that ranges from one to five.

In section 5.1 we showed that the angular Boltzmann density is linearly related to the measured data under a specific set of conditions. We assume that these conditions hold so that the relationship between the object and the data takes the form

$$g_{jv}(\mathbf{r}_d) = \int_{\mathbb{S}^2} d\hat{\mathbf{s}}_o \int_{\mathbb{R}^3} d\mathbf{r}_o h_{jv}^{(di)}(\mathbf{r}_d, \mathbf{r}_o, \hat{\mathbf{s}}_o) \bar{f}(\mathbf{r}_o, \hat{\mathbf{s}}_o), \quad (6.1)$$

where $h_{jv}^{(di)}(\mathbf{r}_d, \mathbf{r}_o, \hat{\mathbf{s}}_o)$ is the generalized point-response function for the polarized diSPIM. This point-response function can be factored into the product of excitation and detection point-response functions

$$h_{jv}^{(di)}(\mathbf{r}_d, \mathbf{r}_o, \hat{\mathbf{s}}_o) = h_{jv}^{(di,exc)}(\mathbf{r}_d, \mathbf{r}_o, \hat{\mathbf{s}}_o) h_v^{(di,det)}(\mathbf{r}_d - \mathbf{r}_o, \hat{\mathbf{s}}_o), \quad (6.2)$$

where we have assumed (1) that the detection point-response function is independent of the excitation polarization by dropping the j -dependence of $h^{(di,det)}$ (polarized detection can be modeled by retaining the j -dependence), and (2) that the detection point-response function is shift invariant in three dimensions.

At this stage is it useful to choose a coordinate system and introduce a pair of rotation matrices that describe the relative orientations of each view. We choose the $+ \hat{\mathbf{z}}$ and $+ \hat{\mathbf{x}}$ directions to be aligned with detection optical axes for view 0 and view 1, respectively, in the direction of light travel for detected light. With this choice we can relate the two views

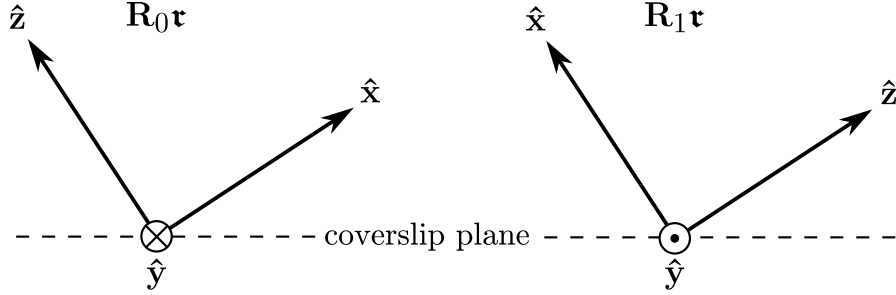


Figure 6.2: Dual-view light sheet microscope coordinates.

with the rotation matrices

$$\mathbf{R}_0 = \begin{bmatrix} 1 & 0 & 0 \\ 0 & 1 & 0 \\ 0 & 0 & 1 \end{bmatrix}, \quad \mathbf{R}_1 = \begin{bmatrix} 0 & 0 & 1 \\ 0 & -1 & 0 \\ 1 & 0 & 0 \end{bmatrix}, \quad (6.3)$$

as shown in Fig. 6.2. We choose \mathbf{R}_0 to be the identity matrix so that all of our coordinates are aligned with view 0. The rotation matrix for \mathbf{R}_1 swaps the \hat{x} and \hat{z} axes and inverts the \hat{y} axis (equivalently, \mathbf{R}_1 rotates by π about the $\hat{x} + \hat{z}$ axis). Notice that the rotation matrices \mathbf{R}_v have positive determinant $\det \mathbf{R}_v = +1$, so they are members of $\mathbb{SO}(3)$. Additionally, we have made a special choice for our coordinate system so that the rotation matrices are *involutory*—they are their own inverse $\mathbf{R}_v^{-1} = \mathbf{R}_v$. This choice is convenient because implementations do not have to keep track of both \mathbf{R}_v and \mathbf{R}_v^{-1} , but other coordinate choices without this property are possible. We will keep track of both \mathbf{R}_v and \mathbf{R}_v^{-1} in this chapter for clarity.

Now we can calculate the polarized diSPIM excitation point-response function explicitly. If the illumination light sheet is created by focusing a collimated Gaussian beam either (a) in one dimension (e.g. with a cylindrical lens) or (b) in two dimensions and scanning the beam rapidly compared to the exposure time, then the excitation point-response function

can be modeled as

$$h_{jv}^{(\text{di,exc})}(\mathbf{r}_d, \mathbf{r}_o, \hat{\mathbf{s}}_o) = \left[\frac{w_0}{w(\mathbf{R}_v^{-1}\mathbf{r}_d \cdot \hat{\mathbf{x}})} \right]^2 \exp \left[\frac{-2(\mathbf{R}_v^{-1}(\mathbf{r}_d - \mathbf{r}_o) \cdot \hat{\mathbf{z}})^2}{w(\mathbf{R}_v^{-1}\mathbf{r}_d \cdot \hat{\mathbf{x}})^2} \right] h^{(\text{exc})}(\hat{\mathbf{p}}_{jv}, \hat{\mathbf{s}}_o), \quad (6.4)$$

where w_0 is the beam waist radius, $w(x) = w_0\sqrt{1 + (x/x_R)^2}$ is the depth-dependent beam radius, $x_R = \pi w_0^2 n_0 / \lambda$ is the Rayleigh range, and $h^{(\text{exc})}(\hat{\mathbf{p}}_{jv}, \hat{\mathbf{s}}_o)$ is the excitation point-response function we analyzed in chapter 5 given by

$$h^{(\text{exc})}(\hat{\mathbf{p}}_{jv}, \hat{\mathbf{s}}_o) = \frac{3}{\sqrt{4\pi}} (\hat{\mathbf{p}}_{jv} \cdot \hat{\mathbf{s}}_o)^2. \quad (6.5)$$

The numerator in the exponential in Eq. (6.4) models the Gaussian profile of the light sheet along the detection optical axis, while the denominator in the exponential models the varying beam radius along the illumination optical axis. Gaussian beams are paraxial, so it is appropriate to model the light-sheet with a constant polarization.

To model the diSPIM detection point-response function we can reuse the models we developed in earlier chapters. Let $h^{(\text{det})}(\mathbf{r}_d - \mathbf{r}_o^\perp, r_o^\parallel, \hat{\mathbf{s}}_o; \text{NA})$ be the irradiance measured at point \mathbf{r}_d on a two-dimensional detector from a point source at position $(\mathbf{r}_o^\perp, r_o^\parallel)$ with orientation $\hat{\mathbf{s}}_o$ and detection numerical aperture NA (see Eq. (5.19), but here we carry the axial position r_o^\parallel and the numerical aperture NA as parameters). In the diSPIM we collect a two-dimensional image for each focal position as we scan the focus through the sample (or scan the sample through the focus) to build up a three-dimensional image. Therefore, the diSPIM detection point-response function $h^{(\text{di,det})}$ can be written in terms of $h^{(\text{det})}$ as

$$h_v^{(\text{di,det})}(\mathbf{r}, \hat{\mathbf{s}}_o) = h^{(\text{det})}\left(\mathbf{R}_v^{-1}\mathbf{r} - [\mathbf{R}_v^{-1}\mathbf{r} \cdot \hat{\mathbf{z}}]\hat{\mathbf{z}}, \mathbf{R}_v^{-1}\mathbf{r} \cdot \hat{\mathbf{z}}, \mathbf{R}_v^{-1}\hat{\mathbf{s}}_o; \text{NA}_v\right), \quad (6.6)$$

where the first argument on the right-hand side $\mathbf{R}_v^{-1}\mathbf{r} - [\mathbf{R}_v^{-1}\mathbf{r} \cdot \hat{\mathbf{z}}]\hat{\mathbf{z}}$ is a view-independent transverse coordinate, the second argument on the right-hand side $\mathbf{R}_v^{-1}\mathbf{r} \cdot \hat{\mathbf{z}}$ is a view-

independent axial coordinate, the third argument $\mathbf{R}_v^{-1}\hat{\mathbf{s}}_o$ is a view-independent angular coordinate, and

$$\text{NA}_v = \begin{cases} 1.1 & \text{for } v = 0, \\ 0.71 & \text{for } v = 1. \end{cases} \quad (6.7)$$

Comparing Eqs. (6.4) and (6.6) shows that we do not rotate the argument $\hat{\mathbf{s}}_o$ in Eq. (6.4) while we do rotate the argument $\mathbf{R}_v^{-1}\hat{\mathbf{s}}_o$ in Eq. (6.6). Our choice to omit the rotation in Eq. (6.4) is only for convenience—we could choose to rotate both arguments $\hat{\mathbf{p}}_{jv}$ and $\hat{\mathbf{s}}_o$ and get the same results since the dot product in Eq. (6.5) is unchanged by rotations. This choice will be most convenient when we compare different polarization sampling schemes $\{\hat{\mathbf{p}}_{jv}\}$ in the next section. Notice that we cannot drop the rotations in Eq. (6.6) because $h^{(\text{det})}$ is not rotation invariant.

We have assembled a complete model of the polarized diSPIM in Eqs. (6.2), (6.4), and (6.6), but this model is computationally expensive because it is only laterally shift invariant for each view. Fortunately, we can make reasonable approximations and find a three-dimensionally shift-invariant model that captures the most important features of the imaging system.

First, we assume that the illumination light sheet does not broaden appreciably along its propagation direction so that $w(z) \approx w_0$. Under this assumption we can approximate Eq. (6.4) with a shift-invariant version where $\mathbf{r} = \mathbf{r}_d - \mathbf{r}_o$

$$h_{jv}^{(\text{di,exc})}(\mathbf{r}, \hat{\mathbf{s}}_o) \stackrel{(\text{unif})}{=} \exp\left[-2\left(\mathbf{R}_v^{-1}\mathbf{r} \cdot \hat{\mathbf{z}}/w_0\right)^2\right] h^{(\text{exc})}(\hat{\mathbf{p}}_{jv}, \hat{\mathbf{s}}_o). \quad (6.8)$$

This assumption is always valid within a Rayleigh range of the beam focus, so we restrict our attention to this region. Now we can write the complete transfer function under the

uniform-sheet approximation as

$$h_{jv}^{(di)}(\mathbf{r}, \hat{\mathbf{s}}_o) \stackrel{(unif)}{=} \exp\left[-2\left(\mathbf{R}_v^{-1}\mathbf{r} \cdot \hat{\mathbf{z}}/w_0\right)^2\right] h^{(exc)}(\hat{\mathbf{p}}_{jv}, \hat{\mathbf{s}}_o) \\ h^{(det)}\left(\mathbf{R}_v^{-1}\mathbf{r} - [\mathbf{R}_v^{-1}\mathbf{r} \cdot \hat{\mathbf{z}}]\hat{\mathbf{z}}, \mathbf{R}_v^{-1}\mathbf{r} \cdot \hat{\mathbf{z}}, \mathbf{R}_v^{-1}\hat{\mathbf{s}}_o; \text{NA}_v\right). \quad (6.9)$$

Next, we assume that the detection point-response function does not vary appreciably across the thickness of the light sheet. To estimate the validity of this assumption, we can compare the depth of focus of the detection arm $D = \lambda n_0 / \text{NA}^2$ to the light-sheet thickness w_0 . In our asymmetric NA instrument, the depth of focus will be smallest for the high-NA view—for $\text{NA} = 1.1$, $\lambda = 500 \text{ nm}$, $n_0 = 1.3$ we have a $0.54 \mu\text{m}$ depth of focus. Therefore, we choose illumination beam waists w_0 that are on the order of $0.54 \mu\text{m}$ so that the detection point response function can be evaluated at $\mathbf{R}_v^{-1}\mathbf{r} \cdot \hat{\mathbf{z}} = 0$, which gives the approximate model

$$h_{jv}^{(di)}(\mathbf{r}, \hat{\mathbf{s}}_o) \stackrel{(thin)}{=} \exp\left[-2\left(\mathbf{R}_v^{-1}\mathbf{r} \cdot \hat{\mathbf{z}}/w_0\right)^2\right] h^{(exc)}(\hat{\mathbf{p}}_{jv}, \hat{\mathbf{s}}_o) \times \\ h^{(det)}\left(\mathbf{R}_v^{-1}\mathbf{r} - [\mathbf{R}_v^{-1}\mathbf{r} \cdot \hat{\mathbf{z}}]\hat{\mathbf{z}}, 0, \mathbf{R}_v^{-1}\hat{\mathbf{s}}_o; \text{NA}_v\right). \quad (6.10)$$

We have already computed the single-view excitation and detection transfer functions, so calculating the transfer functions for the polarized diSPIM is relatively straightforward. We define a diSPIM Hilbert-space operator $\mathcal{H}^{(di)}$ with entries

$$\left(\hat{\mathbf{e}}(\mathbf{r}_d)\hat{\mathbf{e}}_{jv}, \mathcal{H}^{(di)}\hat{\mathbf{e}}(\mathbf{r}_o)\hat{\mathbf{e}}(\hat{\mathbf{s}}_o)\right) = h_{jv}^{(di)}(\mathbf{r}_d - \mathbf{r}_o, \hat{\mathbf{s}}_o), \quad (6.11)$$

then we change to an object-space basis of spherical harmonics with a spherical Fourier transform (see Eq. (5.74) for a detailed calculation)

$$\left(\hat{\mathbf{e}}(\mathbf{r}_d)\hat{\mathbf{e}}_{jv}, \mathcal{H}^{(di)}\hat{\mathbf{e}}(\mathbf{r}_o)\hat{\mathbf{E}}_{\ell m}\right) = H_{jv,\ell m}^{(di)}(\mathbf{r}_d - \mathbf{r}_o), \quad (6.12)$$

where

$$H_{jv,\ell m}^{(\text{di})}(\mathbf{r}) \stackrel{\text{(thin)}}{=} \exp\left[-2\left(\mathbf{R}_v^{-1}\mathbf{r} \cdot \hat{\mathbf{z}}/w_0\right)^2\right] \sum_{\ell' m' \ell'' m''} G_{\ell' m' \ell'' m''}^{mm'm''} H_{\ell' m'}^{(\text{exc})}(\hat{\mathbf{p}}_{jv}) \times \\ \int_{\mathbb{S}^2} d\hat{\mathbf{s}}_o h^{(\text{det})}\left(\mathbf{R}_v^{-1}\mathbf{r} - [\mathbf{R}_v^{-1}\mathbf{r} \cdot \hat{\mathbf{z}}]\hat{\mathbf{z}}, 0, \mathbf{R}_v^{-1}\hat{\mathbf{s}}_o; \text{NA}_v\right) Y_{\ell'' m''}(\hat{\mathbf{s}}_o). \quad (6.13)$$

Earlier we evaluated the spherical Fourier transform of $h^{(\text{det})}$, but the second line of Eq. (6.13) requires us to calculate the same transform in rotated angular coordinates. We briefly digress to show how this calculation can be completed efficiently using the Wigner D-matrices. Suppose we have a spherical function $f(\hat{\mathbf{s}})$ and its spherical Fourier transform

$$F_{\ell m} = \int_{\mathbb{S}^2} d\hat{\mathbf{s}} f(\hat{\mathbf{s}}) Y_{\ell m}(\hat{\mathbf{s}}). \quad (6.14)$$

The spherical Fourier transform of same function in rotated coordinates is given by

$$F'_{\ell' m'} = \int_{\mathbb{S}^2} d\hat{\mathbf{s}} f(\mathbf{R}^{-1}\hat{\mathbf{s}}) Y_{\ell' m'}(\hat{\mathbf{s}}), \quad (6.15)$$

where $\mathbf{R} \in \mathbb{SO}(3)$ is a rotation matrix. After making a change of coordinates $\mathbf{R}^{-1}\hat{\mathbf{s}} \rightarrow \hat{\mathbf{s}}$

$$F'_{\ell' m'} = \int_{\mathbb{S}^2} d\hat{\mathbf{s}} f(\hat{\mathbf{s}}) Y_{\ell' m'}(\mathbf{R}\hat{\mathbf{s}}), \quad (6.16)$$

we expand $f(\hat{\mathbf{s}})$ into a spherical-harmonic series

$$F'_{\ell' m'} = \int_{\mathbb{S}^2} d\hat{\mathbf{s}} \left[\sum_{\ell=0}^{\infty} \sum_{m=-\ell}^{\ell} F_{\ell m} Y_{\ell m}(\hat{\mathbf{s}}) \right] Y_{\ell' m'}(\mathbf{R}\hat{\mathbf{s}}), \quad (6.17)$$

then rearrange to find

$$F'_{\ell' m'} = \sum_{\ell=0}^{\infty} \sum_{m=-\ell}^{\ell} \left[\int_{\mathbb{S}^2} d\hat{\mathbf{s}} Y_{\ell m}(\hat{\mathbf{s}}) Y_{\ell' m'}(\mathbf{R}\hat{\mathbf{s}}) \right] F_{\ell m}. \quad (6.18)$$

The integral in square brackets is only non-zero when $\ell = \ell'$, so we perform the sum over ℓ and give the integral its own symbol

$$F'_{\ell m'} = \sum_{m=-\ell}^{\ell} \Delta_{mm'}^{\ell}(\mathbf{R}) F_{\ell m}, \quad (6.19)$$

where

$$\Delta_{mm'}^{\ell}(\mathbf{R}) = \int_{\mathbb{S}^2} d\hat{\mathbf{s}} Y_{\ell m}(\hat{\mathbf{s}}) Y_{\ell m'}(\mathbf{R}\hat{\mathbf{s}}) \quad (6.20)$$

are the *real Wigner D-matrices*—see the appendix in Kautz et al. for a similar result [209]. The Wigner D-matrices are square $(2\ell + 1) \times (2\ell + 1)$ matrices for each rotation \mathbf{R} and band ℓ , and these matrices can be used to calculate the spherical harmonic coefficients of a rotated function. Notice that rotations only change the spherical harmonic coefficients within each band since each band of spherical harmonics spans an $(2\ell + 1)$ -dimensional rotationally invariant subspace of $\mathbb{L}_2(\mathbb{S}^2)$.

We can use Eq. (6.19) to simplify the result in Eq. (6.13) to

$$H_{j_{\mathbf{v}}, \ell m}^{(\text{di})}(\mathbf{r}) \underset{(\text{thin})}{=} \exp \left[-2 \left(\mathbf{R}_{\mathbf{v}}^{-1} \mathbf{r} \cdot \hat{\mathbf{z}} / w_0 \right)^2 \right] \sum_{\ell' m' \ell'' m''} \sum_{\ell''' m''' m'''} G_{\ell \ell' \ell''}^{m m' m''} H_{\ell' m'}^{(\text{exc})}(\hat{\mathbf{p}}_{j_{\mathbf{v}}}) \times \\ \sum_{m'''=\ell''}^{\ell''} \Delta_{m''' m''}^{\ell''}(\mathbf{R}_{\mathbf{v}}) H_{\ell'' m''}^{(\text{det})} \left(\mathbf{R}_{\mathbf{v}}^{-1} \mathbf{r} - [\mathbf{R}_{\mathbf{v}}^{-1} \mathbf{r} \cdot \hat{\mathbf{z}}] \hat{\mathbf{z}}, 0; \text{NA}_{\mathbf{v}} \right). \quad (6.21)$$

Calculating $\Delta_{mm'}^{\ell}(\mathbf{R})$ efficiently for arbitrary \mathbf{R} , ℓ , m , and m' is challenging—see Pinchon and Hoggan for one approach [210]. Fortunately, we only have two rotation matrices $\mathbf{R}_{\mathbf{v}}$, and $H^{(\text{det})}$ is only non-zero for $\ell = 0$ and $\ell = 2$ terms. This means we only need to calculate $2(1^2 + 5^2) = 52$ integrals, which is feasible symbolically. Most of these integrals are trivial and can be calculated by hand

$$\Delta_{00}^0(\mathbf{R}_{\mathbf{v}}) = 1, \quad \Delta_{mm'}^2(\mathbf{R}_0) = \delta_{mm'}. \quad (6.22)$$

The remaining integrals can be evaluated with a computer algebra package, and we write the values $\Delta_{mm'}^2(\mathbf{R}_1)$ in matrix notation as

$$\Delta^2(\mathbf{R}_1) = \begin{bmatrix} 0 & -1 & 0 & 0 & 0 \\ -1 & 0 & 0 & 0 & 0 \\ 0 & 0 & -1/2 & 0 & \sqrt{3}/2 \\ 0 & 0 & 0 & 1 & 0 \\ 0 & 0 & \sqrt{3}/2 & 0 & 1/2 \end{bmatrix}. \quad (6.23)$$

As expected this matrix is involuntary $[\Delta^2(\mathbf{R}_1)]^{-1} = \Delta^2(\mathbf{R}_1)$.

Finally, we change to an object- and data-space basis of complex exponentials with a three-dimensional Fourier transform

$$(\hat{\mathbf{E}}(\mathbf{v}_d)\hat{\mathbf{e}}_{j\mathbf{v}}, \mathcal{H}^{(\text{di})}\hat{\mathbf{E}}(\mathbf{v}_o)\hat{\mathbf{E}}_{\ell m}) = \mathsf{H}_{j\mathbf{v},\ell m}^{(\text{di})}(\mathbf{v}_d)\delta(\mathbf{v}_d - \mathbf{v}_o), \quad (6.24)$$

where

$$\begin{aligned} \mathsf{H}_{j\mathbf{v},\ell m}^{(\text{di})}(\mathbf{v}) &\stackrel{\text{(unif)}}{=} \frac{\exp\left[-(w_0 \mathbf{R}_\mathbf{v}^{-1} \mathbf{v} \cdot \hat{\mathbf{z}})^2/2\right]}{\sqrt{\pi/2}/w_0} \sum_{\ell' m' \ell'' m''} G_{\ell\ell' \ell'' m''}^{m m' m''} H_{\ell' m'}^{(\text{exc})}(\hat{\mathbf{p}}_{j\mathbf{v}}) \times \\ &\quad \sum_{m'''=\ell''}^{\ell''} \Delta_{m''' m''}^{\ell''}(\mathbf{R}_\mathbf{v}) \mathsf{H}_{\ell'' m''}^{(\text{det})} \left(\mathbf{R}_\mathbf{v}^{-1} \mathbf{v} - [\mathbf{R}_\mathbf{v}^{-1} \mathbf{v} \cdot \hat{\mathbf{z}}] \hat{\mathbf{z}}, 0; \text{NA}_\mathbf{v} \right), \end{aligned} \quad (6.25)$$

where $\mathbf{v} \in \mathbb{R}^3$ indexes three-dimensional spatial frequencies. Equation (6.25) is the key result of this section—it gives us an efficient way to calculate the spatio-angular transfer function of the polarized diSPIM in terms of the transfer functions we calculated in chapter 5. From our previous work we know that the excitation and detection transfer functions are only non-zero for $\ell = 0, 2$, so the complete transfer function is only non-zero for $\ell = 0, 2, 4$, which is at most 15 non-zero angular terms.

6.2 Singular value decomposition

Next, we find the SVD of $\mathcal{H}^{(\text{di})}$ by building on our work in section 5.3 and solving the eigenvalue problem

$$[\mathcal{H}^{(\text{di})}]^\dagger \mathcal{H}^{(\text{di})} \mathbf{u}_{\mathbf{p},k}^{(\text{di})} = \mu_{\mathbf{p},k}^{(\text{di})} \mathbf{u}_{\mathbf{p},k}^{(\text{di})}, \quad (6.26)$$

where $\mathbf{p} \in \mathbb{R}^3$ is a continuous index and k is a discrete index. Choosing a basis for the object-space singular functions and exploiting the three-dimensional shift invariance yields

$$\left(\hat{\mathbf{e}}(\mathbf{r}_o) \hat{\mathbf{E}}_{\ell m}, \mathbf{u}_{\mathbf{p},k}^{(\text{di})} \right) = \tilde{U}_{k;\ell m}(\mathbf{p}) \exp[2\pi i \mathbf{p} \cdot \mathbf{r}_o]. \quad (6.27)$$

Next, we write the entries of the adjoint operator as

$$\left(\hat{\mathbf{e}}(\mathbf{r}_o) \hat{\mathbf{E}}_{\ell m}, [\mathcal{H}^{(\text{di})}]^\dagger \hat{\mathbf{e}}(\mathbf{r}_d) \hat{\mathbf{e}}_{jv} \right) = H_{jv,\ell m}^{(\text{di})*}(\mathbf{r}_d - \mathbf{r}_o). \quad (6.28)$$

Now we can calculate the entries of $[\mathcal{H}^{(\text{di})}]^\dagger \mathcal{H}^{(\text{di})}$ as

$$\begin{aligned} \left(\hat{\mathbf{e}}(\mathbf{r}_o) \hat{\mathbf{E}}_{\ell m}, [\mathcal{H}^{(\text{di})}]^\dagger \mathcal{H}^{(\text{di})} \hat{\mathbf{e}}(\mathbf{r}'_o) \hat{\mathbf{E}}_{\ell' m'} \right) &\equiv p_{\ell m, \ell' m'}^{(\text{di})}(\mathbf{r}_o - \mathbf{r}'_o) \\ &= \sum_{jv} \int_{\mathbb{R}^3} d\mathbf{r}_d H_{jv,\ell m}^{(\text{di})*}(\mathbf{r}_d - \mathbf{r}_o) H_{jv,\ell' m'}^{(\text{di})}(\mathbf{r}_d - \mathbf{r}'_o). \end{aligned} \quad (6.29)$$

Writing the eigenvalue problem in a specific basis yields

$$\left(\hat{\mathbf{e}}(\mathbf{r}_o) \hat{\mathbf{E}}_{\ell m}, [\mathcal{H}^{(\text{di})}]^\dagger \mathcal{H}^{(\text{di})} \mathbf{u}_{\mathbf{p},k}^{(\text{di})} \right) = \mu_{\mathbf{p},k}^{(\text{di})} \tilde{U}_{k;\ell m}^{(\text{di})}(\mathbf{p}) \exp[2\pi i \mathbf{p} \cdot \mathbf{r}_o], \quad (6.30)$$

and rewriting the left-hand side in terms of known transfer functions yields

$$\left(\hat{\mathbf{e}}(\mathbf{r}_o) \hat{\mathbf{E}}_{\ell m}, [\mathcal{H}^{(\text{di})}]^\dagger \mathcal{H}^{(\text{di})} \mathbf{u}_{\mathbf{p},k}^{(\text{di})} \right) = \sum_{\ell' m'} \int_{\mathbb{R}^3} d\mathbf{r}'_o p_{\ell m, \ell' m'}^{(\text{di})}(\mathbf{r}_o - \mathbf{r}'_o) \tilde{U}_{k;\ell' m'}^{(\text{di})}(\mathbf{r}'_o) \exp[2\pi i \mathbf{p} \cdot \mathbf{r}'_o]$$

$$\begin{aligned}
&= \exp[2\pi i \mathbf{p} \cdot \mathbf{r}_o] \sum_{\ell' m'} P_{\ell m, \ell' m'}^{(\text{di})}(\mathbf{p}) \tilde{U}_{k; \ell' m'}^{(\text{di})}(\mathbf{p}) \\
&= \exp[2\pi i \mathbf{p} \cdot \mathbf{r}_o] \sum_{\ell' m'} \sum_j \mathsf{H}_{j \mathbf{v}, \ell m}^{(\text{di})*}(\mathbf{p}) \mathsf{H}_{j \mathbf{v}, \ell' m'}^{(\text{di})}(\mathbf{p}) \tilde{U}_{k; \ell' m'}^{(\text{di})}(\mathbf{p}),
\end{aligned} \tag{6.31}$$

where we have used the following calculation

$$P_{\ell m, \ell' m'}^{(\text{di})}(\mathbf{p}) = \int_{\mathbb{R}^3} d\mathbf{r} p_{\ell m, \ell' m'}^{(\text{di})}(\mathbf{r}) \exp[-2\pi \mathbf{p} \cdot \mathbf{r}] = \sum_{j \mathbf{v}} \mathsf{H}_{j \mathbf{v}, \ell m}^{(\text{di})*}(\mathbf{p}) \mathsf{H}_{j \mathbf{v}, \ell' m'}^{(\text{di})}(\mathbf{p}). \tag{6.32}$$

Equating the right-hand sides of Eqs. (6.30) and (6.31) yields

$$\sum_{\ell' m'} \left[\sum_{j \mathbf{v}} \mathsf{H}_{j \mathbf{v}, \ell m}^{(\text{di})*}(\mathbf{p}) \mathsf{H}_{j \mathbf{v}, \ell' m'}^{(\text{di})}(\mathbf{p}) \right] \tilde{U}_{k; \ell' m'}^{(\text{di})}(\mathbf{p}) = \mu_{\mathbf{p}, k}^{(\text{di})} \tilde{U}_{k; \ell m}^{(\text{di})}(\mathbf{p}), \tag{6.33}$$

where the brackets enclose the entries of a 15×15 matrix for each \mathbf{p} . We can numerically calculate the 15 eigenvalues $\mu_{\mathbf{p}, k}^{(\text{di})}$ and 15×1 eigenvectors $\tilde{U}_{k; \ell m}^{(\text{di})}(\mathbf{p})$ of each 15×15 matrix then use the results to calculate the complete object-space singular functions in the standard basis

$$u_{\mathbf{p}, k}^{(\text{di})}(\mathbf{r}_o, \hat{\mathbf{s}}_o) = \exp[2\pi i \mathbf{p} \cdot \mathbf{r}_o] \sum_{\ell m} \tilde{U}_{k; \ell m}^{(\text{di})}(\mathbf{p}) Y_{\ell m}(\hat{\mathbf{s}}_o). \tag{6.34}$$

Finally, the data-space singular functions can be found by calculating $P \times 1$ vectors

$$\tilde{V}_{k; j \mathbf{v}}^{(\text{di})}(\mathbf{p}) = \sqrt{\mu_{\mathbf{p}, k}^{(\text{di})}} \sum_{\ell m} \mathsf{H}_{j \mathbf{v}, \ell m}^{(\text{di})}(\mathbf{p}) \tilde{U}_{k; \ell m}^{(\text{di})}(\mathbf{p}), \tag{6.35}$$

then multiplying these vectors by complex exponentials

$$v_{\mathbf{p}, k; j \mathbf{v}}^{(\text{di})}(\mathbf{r}_d) = \tilde{V}_{k; j \mathbf{v}}^{(\text{di})}(\mathbf{p}) \exp[2\pi i \mathbf{p} \cdot \mathbf{r}_d]. \tag{6.36}$$

Now that we have calculated the mathematical form of the SVD of $\mathcal{H}^{(\text{di})}$ we can use

the results to compare designs, develop our intuition for the limits of the imaging system, and perform reconstructions. In the next section we compare polarization samples using a simplified version of the complete SVD, then we use the complete SVD to develop a reconstruction algorithm that is similar to our earlier two-dimensional reconstruction algorithm. Finally, we apply the reconstruction algorithm to real data collected with the instrument.

6.3 Optimal polarization sampling

Our goal is to choose a set of illumination polarizations $\{\hat{\mathbf{p}}_{jv}\} \in (\mathbb{S}^2)^P$ — P points on the sphere—that allow us to estimate a useful and easily interpreted set of object parameters. One set of parameters we would like to estimate is the spherical harmonic coefficients for the $\ell = 0$ and $\ell = 2$ bands. In section 5.3.3 we showed that these parameters are estimable from six polarization measurements. Furthermore, these functions span a rotationally invariant subspace of $\mathbb{L}_2(\mathbb{S}^2)$, so the reconstructions will be much easier to interpret than rotationally variant subsets of these functions.

If we were free to place our polarization samples anywhere on the sphere we would place them at the vertices of an icosahedron. Unfortunately, the nominal diSPIM illumination geometry constrains us to placing the polarizations on two great circles perpendicular to the illumination optical axes. Mathematically, we are limited to choosing polarizations that satisfy

$$\hat{\mathbf{p}}_{jv} \cdot \mathbf{R}_v \hat{\mathbf{x}} = 0. \quad (6.37)$$

In Section 5.3.3 we found that instruments with polarization samples on two great circles will be at most rank five, which means that the nominal diSPIM instrument cannot estimate the coefficients of angular fluorophore distributions in the six-dimensional $\ell = 0$ and $\ell = 2$ rotationally invariant subspaces.

To overcome this limitation we augmented the instrument with computer-controlled mirrors so that the propagation direction of the illumination light sheet was no longer constrained to a single axis. In principle we could tilt the illumination light sheet in any orientation, but most tilting orientations would move parts of light sheet out of the focal plane of the detection objective. Therefore, we tilted the illumination light sheet about the light sheet plane's normal axis. For example, we tilted the $[\hat{\mathbf{x}}\text{-}\hat{\mathbf{y}}]$ plane light-sheet about the $\hat{\mathbf{z}}$ axis so that the $[\hat{\mathbf{x}}\text{-}\hat{\mathbf{y}}]$ plane is still illuminated and new polarization orientations are accessible. After implementing light-sheet tilting, the polarization samples need to satisfy the looser constraint

$$\hat{\mathbf{p}}_{jv} \cdot \mathbf{R}_v \mathbf{R}_{\hat{\mathbf{z}}}(\phi) \hat{\mathbf{x}} = 0, \quad (6.38)$$

where $\mathbf{R}_{\hat{\mathbf{z}}}(\phi)$ denotes a rotation about the $\hat{\mathbf{z}}$ axis by angle ϕ with entries

$$\mathbf{R}_{\hat{\mathbf{z}}}(\phi) = \begin{bmatrix} \cos \phi & -\sin \phi & 0 \\ \sin \phi & \cos \phi & 0 \\ 0 & 0 & 1 \end{bmatrix}. \quad (6.39)$$

We implemented practical tilt angles that satisfied $|\phi| \lesssim 15^\circ$, a limit set by aberrations, which is more than enough to access illumination polarizations that will make the operator rank six. Notice that our tilting scheme does not change the spatial illumination pattern when light-sheet broadening is negligible, so all of the models we have developed still apply to the augmented instrument.

Next, we need to choose a reasonable definition for an optimal polarization scheme. One possible approach is to choose polarization samples $\{\hat{\mathbf{p}}_{jv}\}$ that optimize the Schatten 2-norm

of the imaging operator

$$\left\| \mathcal{H}_{\{\hat{\mathbf{p}}_{jv}\}}^{(di)} \right\|_2 = \left(\sum_k \int_{\mathbb{R}^3} d\mathbf{p} \mu_{\mathbf{p},k} \left(\mathcal{H}_{\{\hat{\mathbf{p}}_{jv}\}}^{(di)} \right) \right)^{\frac{1}{2}}, \quad (6.40)$$

where $\mathcal{H}_{\{\hat{\mathbf{p}}_{jv}\}}^{(di)}$ denotes the diSPIM imaging operator with illumination polarizations $\{\hat{\mathbf{p}}_{jv}\}$, and $\mu_{\mathbf{p},k} \left(\mathcal{H}_{\{\hat{\mathbf{p}}_{jv}\}}^{(di)} \right)$ denotes the eigenvalues of $\left[\mathcal{H}_{\{\hat{\mathbf{p}}_{jv}\}}^{(di)} \right]^\dagger \mathcal{H}_{\{\hat{\mathbf{p}}_{jv}\}}^{(di)}$. Unfortunately, this is not a computationally feasible approach because evaluating the Schatten 2-norm requires us to calculate the singular spectrum for each sampling scheme. To calculate the singular spectrum for an ROI with $1000 \times 1000 \times 1000$ spatial points, we would need to compute the singular values of 10^9 matrices with 15×15 entries each, which requires ~ 1 minute of computation time on a four-core machine. Performing a reasonably dense search over the sampling scheme space (placing P points on the sphere) would require a parallel implementation and patience.

To reduce the computational burden we restrict our attention to flat-field objects (objects with zero spatial frequency $\mathbf{v} = 0$). We define a flat-field operator $\mathcal{H}_{\{\hat{\mathbf{p}}_{jv}\}}^{(di,flat)} : \mathbb{L}_2(\mathbb{S}^2) \rightarrow \mathbb{R}^P$ that maps flat-field objects to flat-field data, then we optimize its spectrum. With Eq. (6.25) in view, the entries of this new operator are given by

$$\begin{aligned} \left(\hat{\mathbf{e}}_{jv}, \mathcal{H}_{\{\hat{\mathbf{p}}_{jv}\}}^{(di,flat)} \hat{\mathbf{E}}_{\ell m} \right) &= \mathsf{H}_{jv,\ell m}^{(di)}(\mathbf{0}) \\ &= \sum_{\ell' m' \ell'' m''} \sum G_{\ell' \ell'' \ell''' m''}^{m m' m''} H_{\ell' m'}^{(exc)}(\hat{\mathbf{p}}_{jv}) \sum_{m'''=\ell''}^{\ell''} \Delta_{m''' m''}^{\ell''}(\mathbf{R}_v) \mathsf{H}_{\ell'' m''}^{(det)}(\mathbf{0}, 0; \text{NA}_v). \end{aligned} \quad (6.41)$$

Although the spatio-angular detection transfer function $\mathsf{H}_{\ell m}^{(det)}(\mathbf{v}, 0; \text{NA}_v)$ cannot be evaluated in closed form for arbitrary transverse spatial frequencies \mathbf{v} , we can calculate its value at $\mathbf{v} = 0$ by calculating the integral

$$\mathsf{H}_{\ell m}^{(det)}(\mathbf{0}, 0; \text{NA}_v) = \int_{\mathbb{S}^2} d\hat{\mathbf{s}} \Pi \left(\frac{\hat{\mathbf{s}} \cdot \hat{\mathbf{z}}}{\cos \alpha_v} \right) (\hat{\mathbf{s}} \cdot \hat{\mathbf{z}})^{-1/2} \left[\int_{\mathbb{S}^2} d\hat{\mathbf{s}}_o [1 - (\hat{\mathbf{s}} \cdot \hat{\mathbf{s}}_o)^2] Y_{\ell m}(\hat{\mathbf{s}}_o) \right], \quad (6.42)$$

where $\text{NA}_v = n_0 \sin \alpha_v$. Equation (6.42) follows directly from our earlier work by setting $\nu = 0$ in Eq. (5.28), but a quick reinterpretation is useful. The value of $H_{\ell m}^{(\text{det})}(\mathbf{0}, 0; \text{NA})$ can be interpreted as the power collected from a flat-field distribution of fluorophores with angular distribution $Y_{\ell m}(\hat{\mathbf{s}}_o)$ by an objective with its optical axis aligned with $\hat{\mathbf{z}}$ and numerical aperture NA. On the right-hand side, we recognize the bracketed integrand term $[1 - (\hat{\mathbf{s}} \cdot \hat{\mathbf{s}}_o)^2]$ as the $\sin^2 \theta$ dipole radiation pattern of a dipole oriented parallel to $\hat{\mathbf{s}}_o$, and the bracketed integral as its spherical Fourier transform. The middle term $(\hat{\mathbf{s}} \cdot \hat{\mathbf{z}})^{-1/2}$ is the apodization factor for an aplanatic objective, and the left term $\Pi\left(\frac{\hat{\mathbf{s}} \cdot \hat{\mathbf{z}}}{\cos \alpha_v}\right)$ is the collection cone of the objective. We integrate the product of these three terms over the sphere to calculate the total power collected by the objective. In appendix 6.6 we evaluate this integral in closed form as

$$H_{\ell m}^{(\text{det})}(\mathbf{0}, 0; \text{NA}_v) = \frac{16}{3} \pi^{3/2} \left[(1 - \sqrt{\cos \alpha_v}) \delta_{0\ell} - \frac{1}{20\sqrt{5}} (4 + \sqrt{\cos \alpha_v} [7 - 3 \cos(2\alpha_v)]) \delta_{\ell 2} \delta_{m0} \right]. \quad (6.43)$$

Now we can use Eqs. (6.43) and (6.41) to efficiently calculate the 15×6 entries of the diSPIM flat-field operator $\mathcal{H}_{\{\hat{\mathbf{p}}_{jv}\}}^{(\text{di,flat})}$.

By inspection of Eq. (6.41), we expect the object-space singular functions of the flat-field operator to be linear combinations of the $\ell = 0, 2$ and 4 spherical harmonics. We are only interested in ensuring that our polarization sampling scheme can reconstruct the $\ell = 0$ and $\ell = 2$ spherical harmonics, so we introduce an operator that projects general spherical functions onto this subspace $\mathcal{P}_{\ell=2} : \mathbb{L}_2(\mathbb{S}^2) \rightarrow \mathbb{L}_2(\mathbb{S}^2)$ with entries

$$(\hat{\mathbf{E}}_{\ell m}, \mathcal{P}_{\ell=2} \hat{\mathbf{E}}_{\ell' m'}) = \delta_{\ell\ell'} \delta_{mm'} \quad \text{for } \ell \leq 2. \quad (6.44)$$

Now we can optimize the combined operator $\mathcal{H}_{\{\hat{\mathbf{p}}_{jv}\}}^{(\text{di,flat})} \mathcal{P}_{\ell=2}$ that has 6×6 non-zero entries.

We can say that our sampling scheme can estimate the $\ell = 0$ and $\ell = 2$ spherical harmonics

if this combined operator is rank six.

We have found two constraints, \mathbb{A} and \mathbb{B} , on our sampling schemes $\{\hat{\mathbf{p}}_{jv}\}$: the sampling scheme must give rise to a rank-six operator $\mathbb{A} = \left\{ \text{rank}(\mathcal{H}_{\{\hat{\mathbf{p}}_{jv}\}}^{(\text{di,flat})} \mathcal{P}_{\ell=2}) = 6 \right\}$ and it must be achievable in the tilting diSPIM instrument $\mathbb{B} = \left\{ \hat{\mathbf{p}}_{jv} \cdot \mathbf{R}_v \mathbf{R}_{\hat{\mathbf{z}}}(\phi) \hat{\mathbf{x}} = 0 \right\}$. Our only remaining choice is a function to optimize. The Schatten 2-norm is a natural choice—we find the sampling scheme that maximizes the root sum of squares of the singular values of $\mathcal{H}_{\{\hat{\mathbf{p}}_{jv}\}}^{(\text{di,flat})} \mathcal{P}_{\ell=2}$ subject to the constraints \mathbb{A} and \mathbb{B}

$$\underset{\{\hat{\mathbf{p}}_{jv}\} \in \mathbb{A} \cap \mathbb{B}}{\text{argmax}} \left\| \mathcal{H}_{\{\hat{\mathbf{p}}_{jv}\}}^{(\text{di,flat})} \mathcal{P}_{\ell=2} \right\|_2. \quad (6.45)$$

Qualitatively, this optimization problem leads to designs that “recover as much as possible about all six parameters”. Unfortunately, this optimization problem can lead to solutions that barely meet the rank-six condition—the smallest singular values can be extremely small. Our goal is to choose a design that measures the six parameters well with none measured poorly, so the Schatten norm is not a good choice.

To combat this issue we optimized the condition number of the matrix

$$\underset{\{\hat{\mathbf{p}}_{jv}\} \in \mathbb{A} \cap \mathbb{B}}{\text{argmax}} \kappa \left(\mathcal{H}_{\{\hat{\mathbf{p}}_{jv}\}}^{(\text{di,flat})} \mathcal{P}_{\ell=2} \right), \quad (6.46)$$

where $\kappa(\mathcal{A}) = \max(\mu(\mathcal{A}))/\min(\mu(\mathcal{A}))$ is the ratio of the maximum and minimum non-zero singular values of \mathcal{A} . Qualitatively, this optimization problem leads to designs that “leave no parameter behind”. Notice that the condition number is only well-defined for operators with a discrete spectrum (compact operators) since an operator with a continuous spectrum does not have a minimum non-zero singular value.

The parameter space in Eq. (6.46) is challenging to search because it is continuous in some parameters and discrete in others. We cannot take derivatives and find analytic solutions, so we use a heuristic approach and discretize the continuous parameters. Discretizing the

search space has the advantage of providing solutions that will be simple to implement experimentally, but of course discretizing removes any guarantees that our sampling schemes will be globally optimal. We discretize the tilt angle into three choices $\phi \in \{-\pi/12, 0, \pi/12\}$ and the polarizer angle into six choices $\theta \in \{0, \pi/6, \pi/3, \pi/2, 2\pi/3, 5\pi/6\}$. This discretization means that a brute-force search will need to place six sampling points among $2 \times 3 \times 6 = 36$ possible sampling positions. Each objective function evaluation requires us to calculate a 6×6 matrix and calculate its singular values which requires ~ 2 ms on a single-core machine. With these choices, a brute-force search is feasible since $\binom{36}{6} \approx 2 \times 10^6$ objective function evaluations will take about 2 hours.

Figure 6.3 shows the optimized polarization sampling schemes for diSPIM instruments with and without light-sheet tilting. Without tilting, the optimal samples use equally spaced polarization samples with three samples from each illumination direction, and this sampling scheme is rank 5. With tilting, the optimal samples are asymmetric samples from each illumination direction, and this sampling scheme is rank 6.

6.4 Reconstruction algorithm

We can adapt the reconstruction algorithm presented in section 5.5 to reconstruct the spatio-angular Boltzmann distribution from measurements collected with the polarized diSPIM. First, we calculate the diSPIM spatio-angular transfer function $H_{jv,\ell m}^{(\text{di})}(\mathbf{v})$ using Eq. (6.25), and we treat this transfer function as a 6×15 matrix at each three-dimensional spatial frequency. Next, we calculate and store the singular system of each 6×15 matrix, which results in a set of object-space singular functions $\tilde{U}_{k;\ell m}^{(\text{di})}(\mathbf{p})$, data-space singular functions $\tilde{U}_{k;\ell m}^{(\text{di})}(\mathbf{p})$, and singular values $\mu_{\mathbf{p},k}^{(\text{di})}$. If the complete singular system can be stored in memory, then that is the most efficient option. However, in practical datasets the number of spatial frequencies can approach 10^9 , which means that we would need to precompute $[6(15) + 6(6) + 6] \times 10^9 \approx 500$ GB of data then load this data into memory to perform reconstructions.

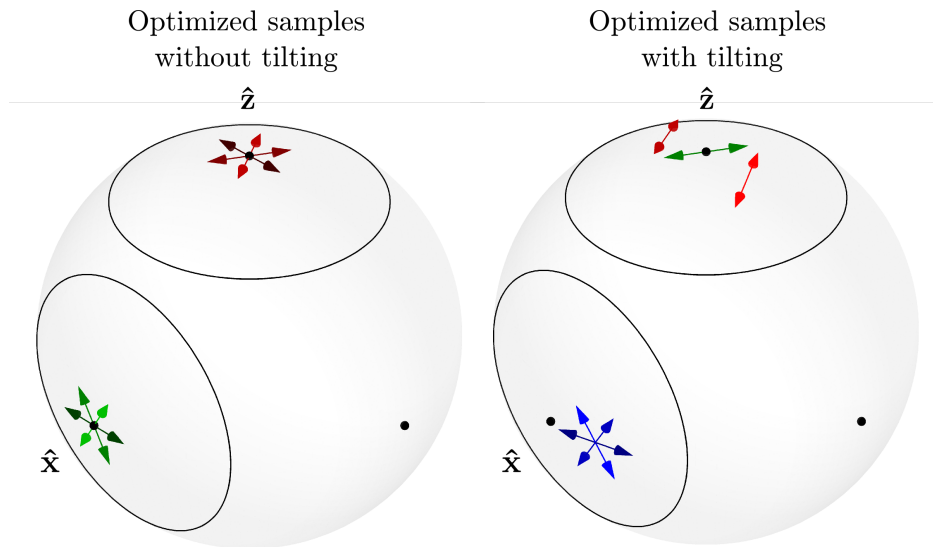


Figure 6.3: Optimized polarization samples for the diSPIM instrument with and without illumination tilting. Each point on the sphere represents a possible illumination optical axis, and the pair of circles enclose the detection numerical apertures (with two detection arms centered on the \hat{x} and \hat{z} axes). One polarization sample is specified by its illumination optical axis (represented by a point on the sphere) and its polarization orientation (represented by an arrow perpendicular to the illumination optical axis). The arrow colors do not encode any necessary information—they serve as an easy referencing scheme. **Left:** The optimal polarization samples for the diSPIM without tilting are three equally spaced polarization orientations for each illumination axis (three red arrows for one view and three green arrows for the other view). **Right:** When we allow illumination axis tilting about the detection optical axis, we reoptimize the polarization samples and find an asymmetric sampling scheme. From the first view we tilt the illumination axis and collect three equally spaced polarization samples (blue arrows). From the other view, we orient the polarizer in the direction of the first illumination axis then collect two samples under both illumination tilting orientations (red arrows). Finally, we rotate the polarizer by $\pi/3$, illuminate from the nominal axis, and collect the sixth sample (green arrow).

To ease this burden we can exploit the properties of the transfer function to compute and store a small number of values that can be combined to generate all of the entries $H_{jv,\ell m}^{(\text{di})}(\mathbf{v})$. Equation (6.25) shows a natural way to decompose the complete transfer function into three parts—an spatial excitation part, an angular excitation part, and a detection part—and each of these can be precalculated, stored, and combined efficiently using the real Gaunt coefficients and real Wigner D-matrices. At reconstruction time we can compute the complete transfer function at a given spatial frequency, compute its singular value decomposition, perform the reconstruction for that spatial frequency, then move on to the next spatial frequency. This approach delays a large fraction of the computations until reconstruction time, but it relieves the burden of having to store and manipulate 500 GB datasets.

With the singular system of the imaging system in hand, we can proceed directly to the reconstruction. We start by taking the three-dimensional Fourier transform of the data

$$G_{jv}(\mathbf{v}) = \int_{\mathbb{R}^3} d\mathbf{r}_d g_{jv}(\mathbf{r}_d) \exp[-2\pi i \mathbf{r}_d \cdot \mathbf{v}]. \quad (6.47)$$

Next, we apply a Tikhonov-regularized pseudoinverse using our stored singular system

$$\hat{\mathsf{F}}_{\eta;\ell m}(\mathbf{v}) = \sum_{k=1}^6 \frac{\sqrt{\mu_{\mathbf{v},k}}}{\mu_{\mathbf{v}} + \eta} \tilde{U}_{k;\ell m}^{(\text{di})}(\mathbf{v}) \sum_{jv} \tilde{V}_{k;jv}^{(\text{di})}(\mathbf{v}) G_{jv}(\mathbf{v}). \quad (6.48)$$

Finally, we take an inverse three-dimensional Fourier transform

$$\hat{F}_{\eta;\ell m}(\mathbf{r}_o) = \int_{\mathbb{R}^3} d\mathbf{v} \hat{\mathsf{F}}_{\eta;\ell m}(\mathbf{v}) \exp[2\pi i \mathbf{r}_o \cdot \mathbf{v}], \quad (6.49)$$

and store the result until we are ready to visualize with the algorithms we developed in section 5.5.

6.5 Reconstructions and discussion

To test our instrument, reconstruction algorithm, and polarization sampling schemes, we imaged two samples with known relationships between the position and the orientation of the fluorescent molecules.

First, we prepared giant unilamellar vesicles (GUVs) via electroformation [211, 212], labeled the vesicles with di-8-ANEPPS (a membrane-crossing dye with a dipole transition moment oriented normal to the membrane [213]), then fixed the vesicles to a coverslip coated with cationic BSA. We imaged the GUVs with the polarized diSPIM under 42 illumination polarizations that included illumination tilting, then we used the reconstruction algorithm described in section 6.4 to recover the spherical harmonics coefficients at each spatial position. We performed reconstructions using two subsets of the 42-polarization dataset that correspond to sampling schemes described in Fig. 6.3—optimized samples with and without illumination tilting.

Figure 6.4 visualizes our reconstruction from six optimal tilting polarization samples. We expect a perfect imaging system to reconstruct a sphere with tightly peaked ODFs on the sphere’s surface, peak orientation cylinders oriented normal to the sphere, and a uniform density on the sphere’s surface. Our reconstruction matches most of these expectations: we reconstruct ODFs that cover the sphere’s surface with peak orientations that are normal to the sphere everywhere except near the two detection optical axes. We also observe that the fluorescence density is uniform on the surface of the sphere within $\approx 50\%$ —we observe the highest reconstructed fluorescence densities on the regions of the sphere perpendicular to the detection optical axes. Both of these artefacts can be attributed to the null space of the imaging system. The poor angular reconstructions near the viewing directions can be directly attributed to the relatively small tilting angles available in the diSPIM—we would not expect these kinds of artefacts from an ideal icosahedral sampling scheme. The nonuniform density can also be attributed to the relatively small tilting angles—we collect

the largest signals from dipoles oriented perpendicular to the viewing axes, so other directions are more susceptible to corruption by noise.

Figure 6.5 shows a sliced visualization of peak orientations from the same GUV sample that compares reconstructions with and without illumination tilting. We see clear evidence that illumination polarization tilting improves the reconstructions in the regions that bisect the detection optical axes. We also observe that all orientations are reconstructed accurately except for orientations near the detection optical axes.

We investigated the limitations of our imaging system and reconstruction scheme by comparing our experimental GUV results with simulations. Figure 6.6 shows (A) a numerical GUV phantom alongside (B) the experimental data and its reconstruction. We generated a numerical phantom that matched our expectation for the object that we imaged—a $6 \mu\text{m}$ diameter spherical shell with dipole moments oriented normal to the surface of the sphere. We simulated the numerical phantom using a continuous mathematical phantom

$$f^{(\text{guv})}(\mathbf{r}_o, \hat{\mathbf{s}}_o) = \Pi \left(\frac{|\mathbf{r}_o| - r_c}{t} \right) \left| \frac{\hat{\mathbf{s}}_o \cdot \mathbf{r}_o}{|\mathbf{r}_o|} \right|^4, \quad (6.50)$$

where $r_c = 3 \mu\text{m}$ is the radius of the spherical shell and $t = 500 \text{ nm}$ is the thickness of the spherical shell. We discretized the continuous phantom onto a 130 nm^3 cubic voxel grid and plotted the result in subfigure (A, a). Notice that the density is uniform along all three circumference profiles shown in subfigure (A, a, iv). Next, we simulated noise-free data with a light-sheet tilting sampling scheme (A, b), reconstructed the object using a small regularization parameter (A, c), then simulated the data generated by the reconstructed phantom (A, d). Comparing the first simulated dataset (A, b) to the second simulated dataset (A, d) voxelwise showed a maximum 2% difference, which can be attributed to the regularization applied during the reconstruction. Performing an identical comparison with an unregularized reconstruction (not shown in the figure) resulted in a maximum difference of $10^{-5}\%$, which can be attributed to floating point error. The reconstructed density profiles

(A, c, iv) are even along all three directions, which indicates the antipodal symmetry (or centrosymmetry) of the phantom and the reconstructions. The reconstructed density profiles fall as low as 60% of the maximum density.

In Fig. 6.6 (B) we show the data we collected, the regularized reconstruction, and the resimulated data for direct comparison with the phantom in Fig. 6.6 (A). The data in subfigures (b, i–iv) show strong qualitative agreement between simulation and experiment, while the data in subfigures (b, v–vi) do not agree as clearly—we hypothesize a calibration or model mismatch error. The reconstructions in subfigures (c) match qualitatively (orientations match, tilting fixes angular degeneracy) and show reasonable numerical agreement between the density profiles. Specifically, the red and green profiles in subfigures (c, iv) corresponding to the profiles perpendicular to the viewing directions match well including a density drop down to 50% of the maximum. The blue profiles in subfigures (c, iv) match poorly—we hypothesize that this mismatch is due to a combination of the coverslip (which we did not simulate) and increased sample motion for points on the GUV far from the coverslip.

We also investigated the limitations of our sampling schemes by simulating data and reconstructions from experimental sampling schemes and potential future sampling schemes. The first and second rows of Fig. 6.7 show data and reconstructions from sampling schemes that we used to collect experimental data—a no-tilt sampling scheme and the optimal tilting sampling scheme detailed in Fig. 6.3—while the third and fourth rows show two potential future schemes—a six-illumination icosahedral scheme and a 16-sample scheme at Fibonacci lattice points (see Eq. (5.104)).

The first and second rows of Fig. 6.7 share many features with our experimental reconstruction in Figs. 6.4 and 6.5. First, we can clearly see that dipoles in the plane of the optical axes are not reconstructed accurately—this can be seen most clearly in the red peaks in subfigure (A, ii) of Fig. 6.7. Second, we see that using light-sheet tilting fixes the issue—

subfigure (B, ii) of Fig. 6.7 no longer shows a red band of peaks in the plane of the optical axes. Third, our simulation shares several limitations with our real reconstructions—the fluorophore density is underestimated near the optical axes and overestimated in the direction perpendicular to these axes. Additionally, the orientation of dipoles near the optical axes are estimated imperfectly.

We numerically tested two additional sampling schemes—a six-illumination icosahedral sampling scheme (see Fig. 5.3) where each view sampled three illumination polarizations, and a sixteen-illumination Fibonacci sampling scheme. Both sampling schemes resulted in good orientation reconstructions along all orientations including near the optical axes, and both sampling schemes reduced the density bias (70% and 85% minimum density for icosahedral and Fibonacci samples, respectively). We consider improved multiview designs that can estimate the density of fluorescent molecules without bias at the same time as their orientation as important future work.

We also investigated the effect of regularization in our reconstruction by plotting numerical reconstructions from the GUV phantom using sampling with light-sheet tilting. Figure 6.8 shows how increasing the regularization parameter smooths the reconstruction both spatially and angularly. There are two useful ways to interpret these plots. First, they can be used to spot overregularization artefacts—choosing a regularization parameter that is too large will result in a reconstruction with orientations along the \hat{y} axis (plotted with green peaks). Second, these plots can be used to understand the effect of noise on the reconstruction. Low SNR data will require larger regularization parameters, which will result in orientation estimates that are biased towards the \hat{y} axis. These results show that if noise is eliminated, then the tilting sampling scheme is sufficient to recover a uniform density on the sphere. Therefore, the fact that the dual-view imaging system cannot estimate densities for all orientations is due to both noise and instrumental limitations. We can summarize these findings in a mathematical way by saying that the singular value spectrum is non-uniform,

so we lose some spatio-angular components to noise before others.

Next, we prepared U2OS cells labeled with Alexa Fluor 488 phalloidin—an actin-binding fluorophore with transition dipole moments that align parallel to the long axis of actin fibers [67]. Figure 6.9 shows a visualization of our reconstruction that shows evidence that we can reconstruct the three-dimensional orientation of fluorescent molecules in three-dimensional biological structures.

Taken together, these data and simulations show that a dual-view polarized light-sheet microscope with tilting illumination can recover the three-dimensional position and orientation of fluorescent molecules. We have clear evidence that our models, reconstruction schemes, and visualization tools yield results that match our expectations. Furthermore, comparing our reconstructions with and without light-sheet tilting supports the validity of our models and their ability to make useful predictions that can improve the design of spatio-angular instruments.

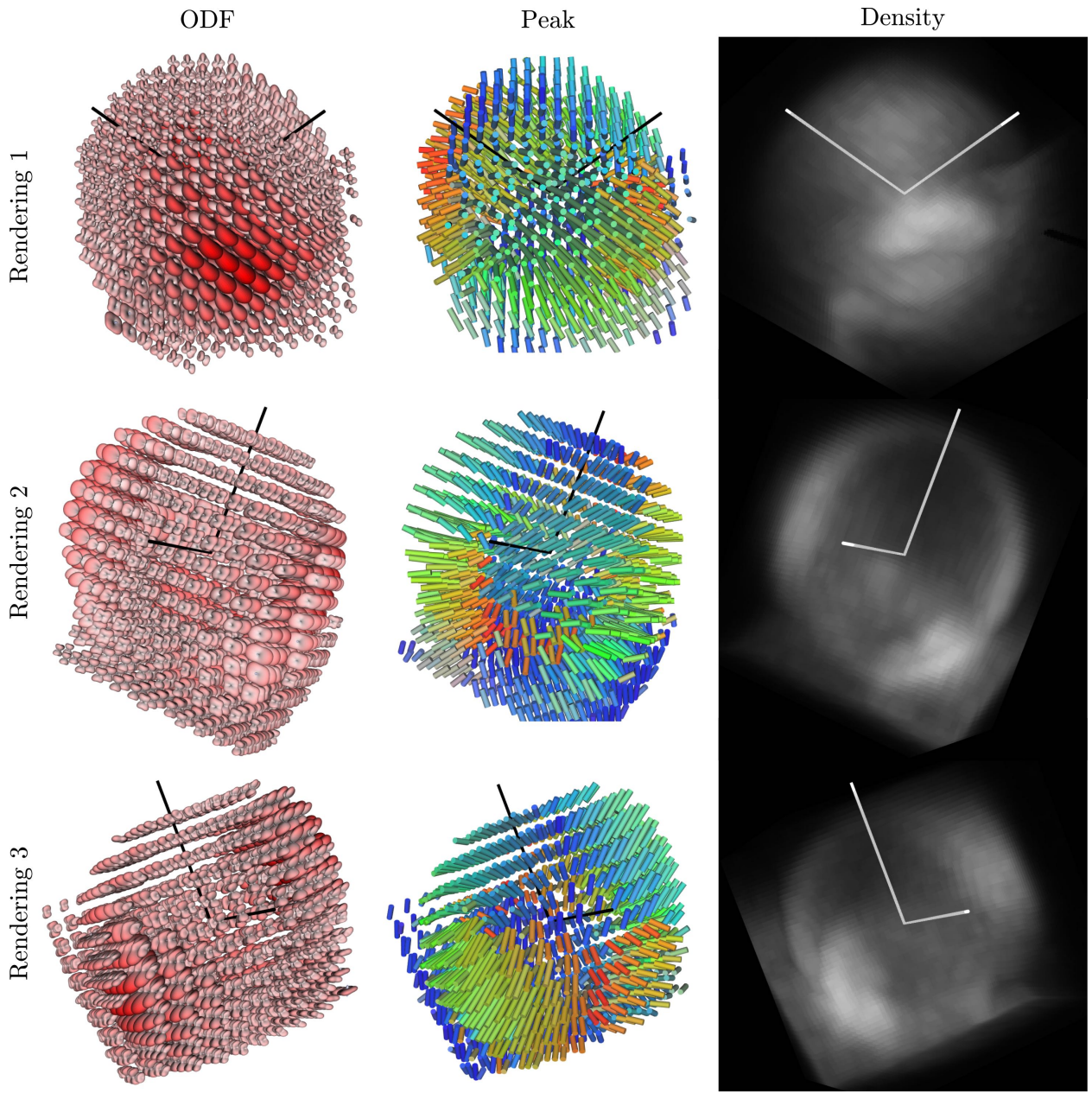


Figure 6.4: A three-dimensional spatio-angular reconstruction of a GUV measured with six optimal tilting polarization samples. Each row shows a rendering from a different viewing direction of the same reconstruction, and each column shows a different way to visualize the reconstruction. The left column visualizes the orientation distribution functions (ODFs), the center column visualizes the peak orientations (where most fluorophores are oriented at each position), and the right column shows a maximum intensity projection of the spatial density of fluorophores. See Fig. 5.6 for more details about these visualizations. The pair of black (white) lines in the first and second (third) columns indicate the detection optical axes of the instrument, and the interior bisector of these lines is normal to the coverslip (a visible plane at the bottom of each viewing direction). The diameter of the GUV is $6.1 \mu\text{m}$.

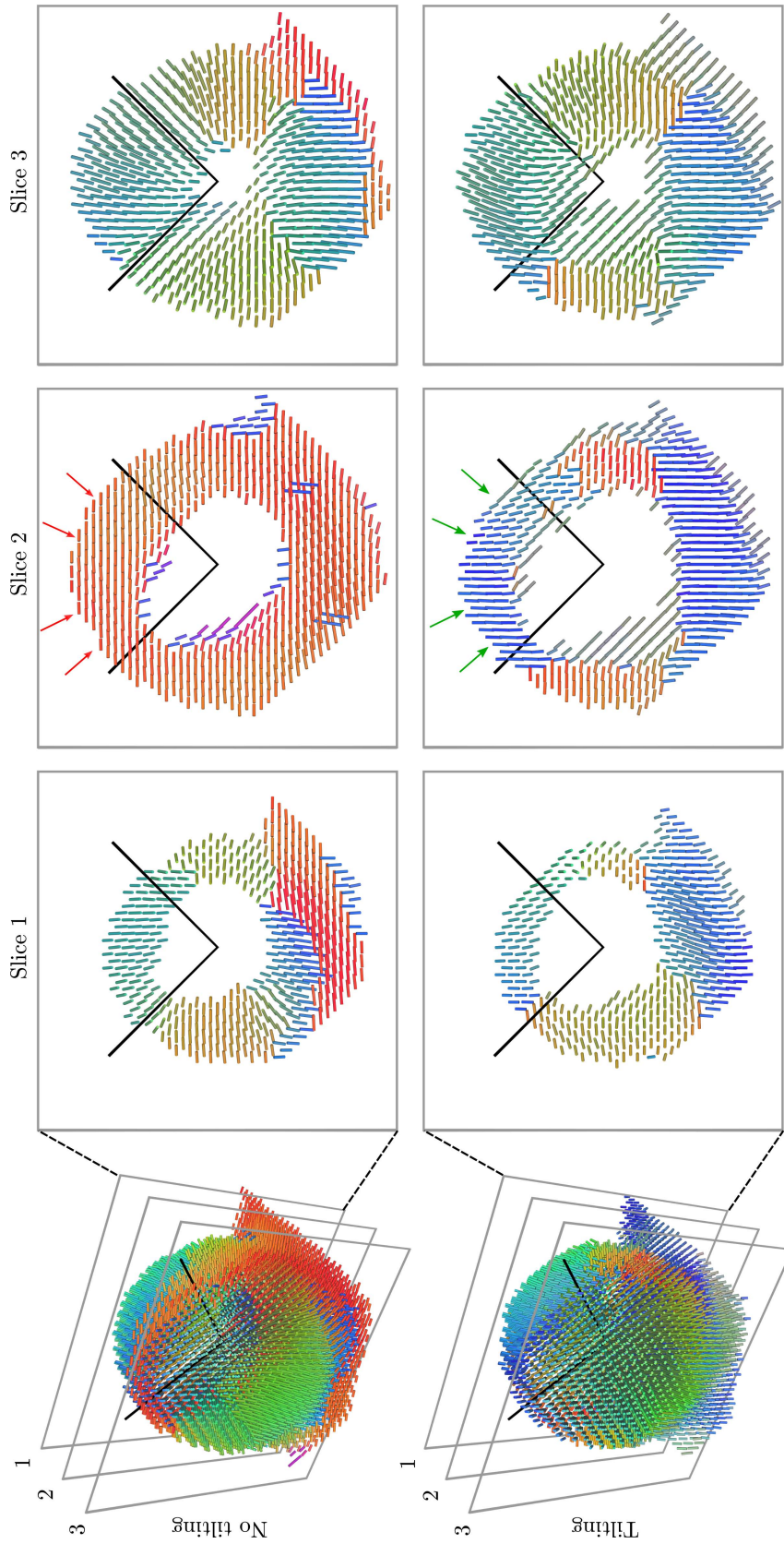
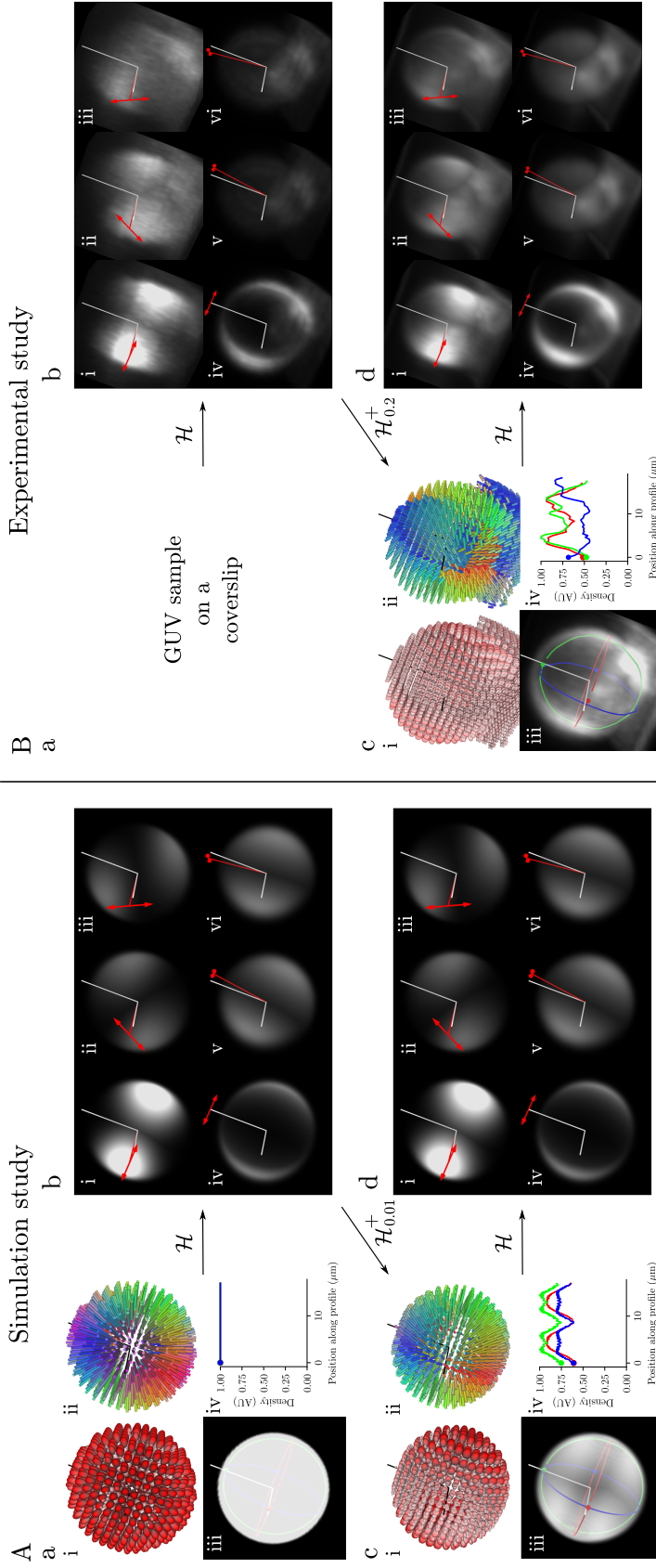


Figure 6.5: Sliced spatio-angular reconstructions of GUV peaks with and without tilting polarization samples. The left column shows the complete three-dimensional peak reconstruction, and the right column shows slices through these reconstructions. The bottom and top rows show the reconstruction with and without illumination tilting, respectively. The reconstructions show good agreement everywhere except in a central slice of the GUV (slice 2). The reconstruction that does not use illumination tilting displays incorrect orientations for positions that are near the interior bisector of the detection optical axes (see red arrows in the top row of slice 2). Tilting corrects these artefacts and allows us to reconstruct the correct orientation everywhere (see green arrows in the bottom row of slice 2). These visuals also show that the largest orientation errors occur near the detection optical axes (black lines).



199

Figure 6.6: A simulation study (A) and an experimental study (B) of a GUV imaged with a light-sheet tilting sampling scheme. In the simulation study we generated a uniformly labeled spherical shell with normally oriented dipoles (a), simulated the data we would expect to collect after imaging this phantom (b), applied a regularized reconstruction operator to simulate what we would expect to recover (c), then resimulated the data we would expect to collect after imaging the reconstructed phantom. We applied an identical procedure to the experimental data without the benefit of a known object. Comparing subfigures (b) and (d) lends support to the correctness of the reconstruction algorithm—we expect these results to be identical modulo the effects of regularization. Comparing subfigures (A) and (B) lends support to the quality of our models for reconstructing the position and orientation of three dimensional fluorescent ensembles. Two mismatches between (A) and (B) are notable—the blue profile in subfigures (c, iv) do not match possibly due to sample motion and coverslip effects, and the data in subfigures (b, v-vi) do not match possibly due to miscalibration or model mismatch.

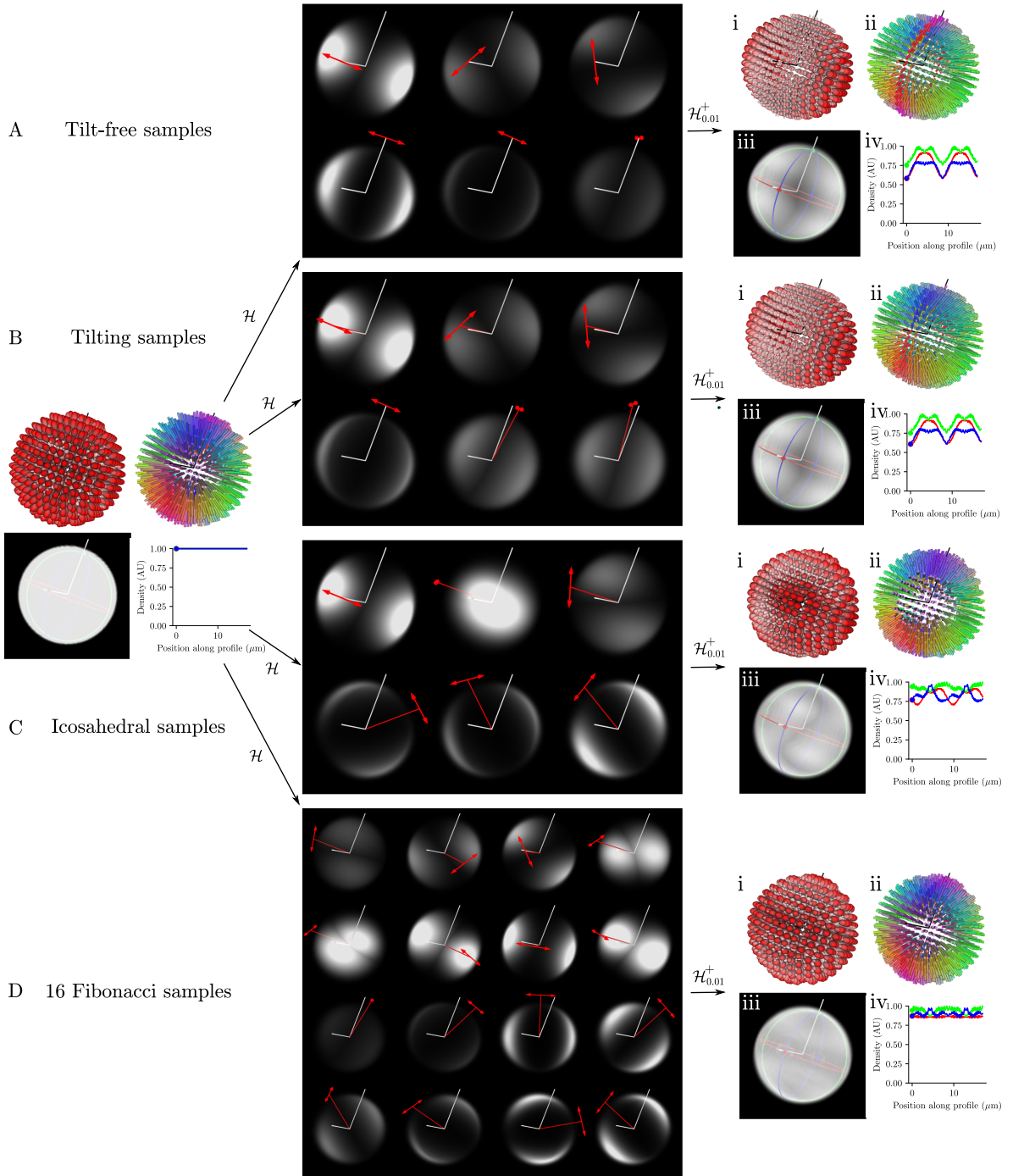


Figure 6.7: A simulated GUV with four simulated reconstructions under different sampling conditions—(A) six tilt-free samples, (B) six tilting samples, (C) six icosahedral samples, and (D) 16 Fibonacci samples. Each reconstruction was performed with regularization $\eta = 0.01$. Adding tilting fixes angular degeneracy (see incorrect red peaks in (A, ii)), increasing the tilting angle to access icosahedral sampling improves the density uniformity (see 70% minimum density in (C, iv)), and increasing the number of samples further improves the density uniformity (see 85% minimum density in (D, iv)).

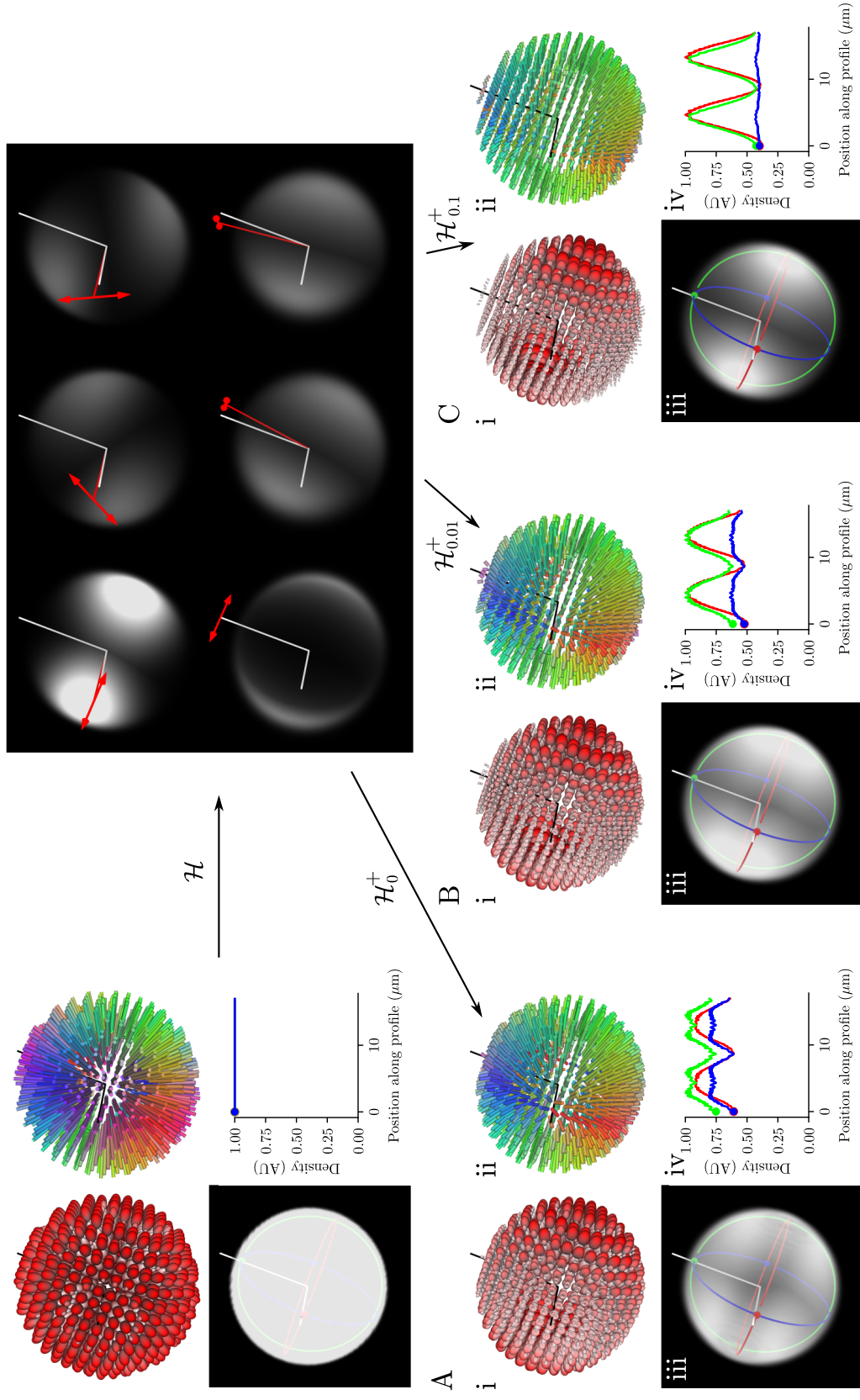


Figure 6.8: Regularization study of GUV reconstructions with tilted light-sheet sampling. Each row shows a reconstruction from a numerical phantom with increasing regularization from left to right (A) $\eta = 0$, (B) $\eta = 0.01$, and (C) $\eta = 0.1$. Increasing the regularization results in spatially and angularly smoothed reconstructions. The high-frequency spatial components in the unregularized density image are an aliasing artefact of reconstructing onto a voxel grid with sharp edges.

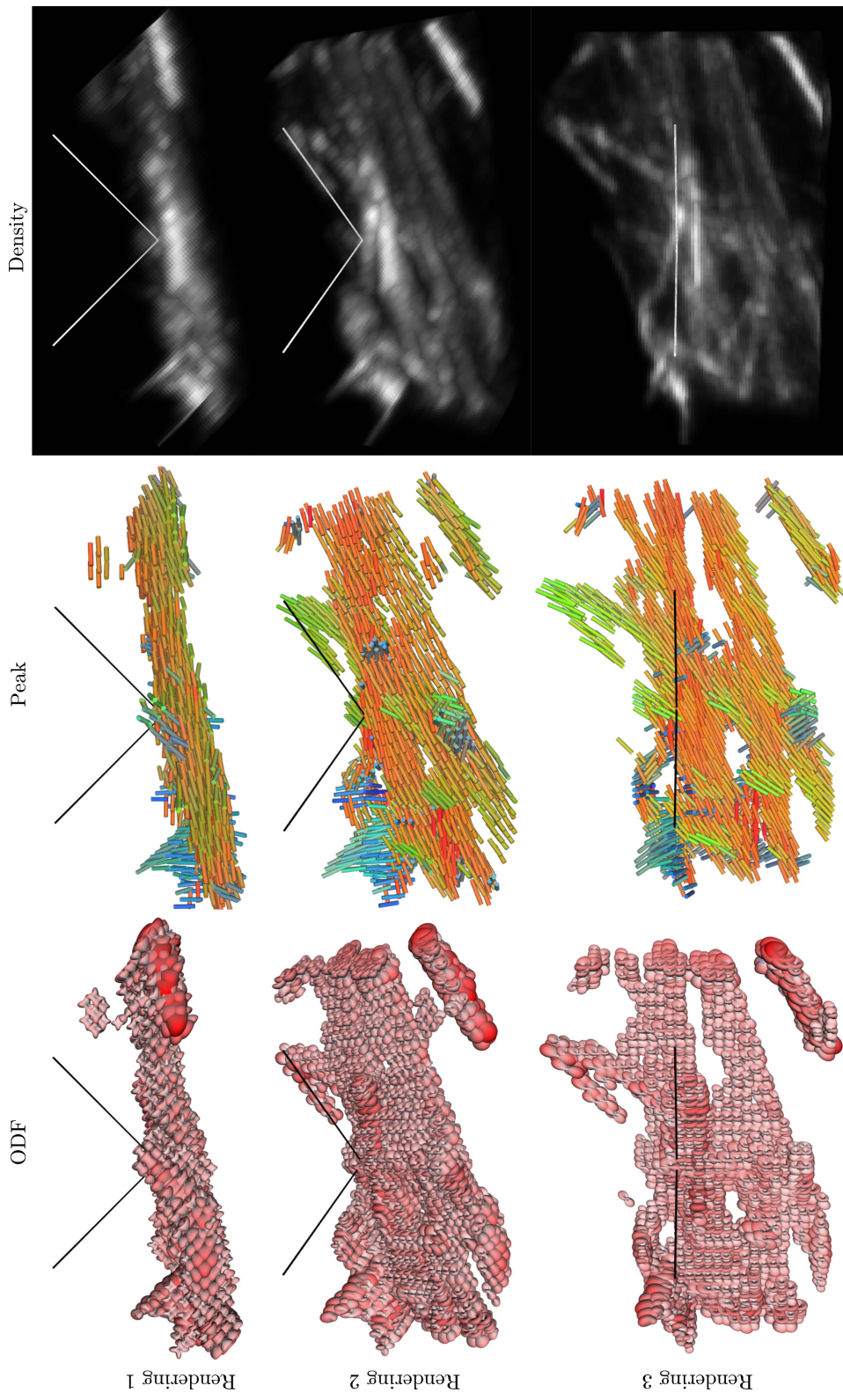


Figure 6.9: A three-dimensional spatio-angular reconstruction of U2OS cells labeled with Alexa Fluor 488 phalloidin. Each row shows a rendering from a different viewing direction of the same reconstruction: the top row viewing direction is in the plane of the coverslip with the coverslip normal pointing up, the bottom row viewing direction is pointing parallel to the coverslip normal, and the middle row is at 45° angle between these viewing directions. Each column shows a different visualization of the reconstruction. The reconstruction shows three-dimensional orientations of actin fibers in the plane of the coverslip (orange and yellow peaks) and out of the plane of the coverslip (blue peaks). The maximum dimension of the field of view is $12.2 \mu\text{m}$.

6.6 Appendix: Flat-field detection transfer function

In this appendix we evaluate the following nested integral which appears in Eq. (6.42)

$$H_{\ell m}^{(\text{det})}(\mathbf{0}, 0; \text{NA}) = \int_{\mathbb{S}^2} d\hat{\mathbf{s}} \Pi \left(\frac{\hat{\mathbf{s}} \cdot \hat{\mathbf{z}}}{\cos \alpha} \right) (\hat{\mathbf{s}} \cdot \hat{\mathbf{z}})^{-1/2} \left[\int_{\mathbb{S}^2} d\hat{\mathbf{s}}_o [1 - (\hat{\mathbf{s}} \cdot \hat{\mathbf{s}}_o)^2] Y_{\ell m}(\hat{\mathbf{s}}_o) \right]. \quad (6.51)$$

Before attacking this calculation, we establish a few useful tools and identities. First, we consider functions on the unit symmetric interval $f(x) \in \mathbb{L}_2([-1, 1])$. These functions can be expanded into a Fourier–Legendre series

$$f(x) = \sum_{\ell=0}^{\infty} F_{\ell} P_{\ell}(x), \quad (6.52)$$

where $P_{\ell}(x)$ are Legendre polynomials, which span $\mathbb{L}_2([-1, 1])$. The Legendre polynomials satisfy

$$\int_{-1}^1 dx P_{\ell}(x) P_{\ell'}(x) = \frac{2}{2\ell + 1} \delta_{\ell\ell'}, \quad (6.53)$$

so they are orthogonal but not orthonormal. We can calculate the Fourier–Legendre coefficients using Fourier’s trick—multiply both sides of Eq. (6.52) by $P_{\ell}(x)$, integrate over the interval $[-1, 1]$, then apply the orthogonality relation to find that

$$F_{\ell} = \frac{2\ell + 1}{2} \int_{-1}^1 dx f(x) P_{\ell}(x). \quad (6.54)$$

We will refer to the coefficients F_{ℓ} as the *Fourier–Legendre transform* of $f(x)$.

We can use the Fourier–Legendre transform to help calculate the spherical Fourier transform of rotationally symmetric functions that take the form $f(\hat{\mathbf{s}} \cdot \hat{\mathbf{s}}')$ where $\hat{\mathbf{s}}'$ is a parameter.

If the spherical Fourier transform takes the form

$$F_{\ell m}(\hat{\mathbf{s}}') = \int_{\mathbb{S}^2} d\hat{\mathbf{s}} f(\hat{\mathbf{s}} \cdot \hat{\mathbf{s}}') Y_{\ell m}(\hat{\mathbf{s}}), \quad (6.55)$$

then we can expand $f(\hat{\mathbf{s}} \cdot \hat{\mathbf{s}}')$ into its Fourier–Legendre series and proceed step by step

$$\begin{aligned} F_{\ell m}(\hat{\mathbf{s}}') &= \int_{\mathbb{S}^2} d\hat{\mathbf{s}} \left[\sum_{\ell'} F_{\ell'} P_{\ell'}(\hat{\mathbf{s}} \cdot \hat{\mathbf{s}}') \right] Y_{\ell m}(\hat{\mathbf{s}}) \\ &= \sum_{\ell'} F_{\ell'} \int_{\mathbb{S}^2} d\hat{\mathbf{s}} P_{\ell'}(\hat{\mathbf{s}} \cdot \hat{\mathbf{s}}') Y_{\ell m}(\hat{\mathbf{s}}), \\ &= \sum_{\ell' m'} \frac{4\pi}{2\ell' + 1} F_{\ell'} Y_{\ell' m'}(\hat{\mathbf{s}}') \int_{\mathbb{S}^2} d\hat{\mathbf{s}} Y_{\ell' m'}(\hat{\mathbf{s}}) Y_{\ell m}(\hat{\mathbf{s}}) \\ &= \sum_{\ell' m'} \frac{4\pi}{2\ell' + 1} F_{\ell'} Y_{\ell' m'}(\hat{\mathbf{s}}') \delta_{\ell' \ell} \delta_{m' m} \\ &= \frac{4\pi}{2\ell + 1} Y_{\ell m}(\hat{\mathbf{s}}') F_{\ell} \\ &= 2\pi Y_{\ell m}(\hat{\mathbf{s}}') \int_{-1}^1 dx f(x) P_{\ell}(x), \end{aligned} \quad (6.56)$$

where we have rearranged the equation, applied the spherical harmonic addition theorem, used the orthogonality of spherical harmonics, used the discrete sifting theorem, then used the definition of the Fourier–Legendre transform. Equation (6.56) shows that we can reduce an infinite set of integrals over the sphere to a single integral over the interval $[-1, 1]$.

We can use Eq. (6.56) to evaluate Eq. (6.51). The inner integral evaluates to

$$\begin{aligned} \int_{\mathbb{S}^2} d\hat{\mathbf{s}}_o [1 - (\hat{\mathbf{s}} \cdot \hat{\mathbf{s}}_o)^2] Y_{\ell m}(\hat{\mathbf{s}}_o) &= 2\pi Y_{\ell m}(\hat{\mathbf{s}}) \int_{-1}^1 dx (1 - x^2) P_{\ell}(x) \\ &= 2\pi Y_{\ell m}(\hat{\mathbf{s}}) \left[\frac{4}{3} \delta_{0\ell} - \frac{4}{15} \delta_{\ell 2} \right]. \end{aligned} \quad (6.57)$$

Finally, we apply Eq. (6.56) to the outer integral and complete the calculation

$$\begin{aligned}
H_{\ell m}^{(\text{det})}(\mathbf{0}, 0; \text{NA}) &= \int_{\mathbb{S}^2} d\hat{\mathbf{s}} \Pi\left(\frac{\hat{\mathbf{s}} \cdot \hat{\mathbf{z}}}{\cos \alpha}\right) (\hat{\mathbf{s}} \cdot \hat{\mathbf{z}})^{-1/2} \left[2\pi Y_{\ell m}(\hat{\mathbf{s}}) \left[\frac{4}{3} \delta_{0\ell} - \frac{4}{15} \delta_{\ell 2} \right] \right] \\
&= 2\pi \left[\frac{4}{3} \delta_{0\ell} - \frac{4}{15} \delta_{\ell 2} \right] \int_{\mathbb{S}^2} d\hat{\mathbf{s}} \Pi\left(\frac{\hat{\mathbf{s}} \cdot \hat{\mathbf{z}}}{\cos \alpha}\right) (\hat{\mathbf{s}} \cdot \hat{\mathbf{z}})^{-1/2} Y_{\ell m}(\hat{\mathbf{s}}) \\
&= 4\pi^2 \left[\frac{4}{3} \delta_{0\ell} - \frac{4}{15} \delta_{\ell 2} \right] Y_{\ell m}(\hat{\mathbf{z}}) \int_{\cos \alpha}^1 dx x^{-1/2} P_\ell(x) \\
&= 4\pi^2 \left[\frac{4}{3} \delta_{0\ell} - \frac{4}{15} \delta_{\ell 2} \right] \frac{1}{2\sqrt{\pi}} [\delta_{\ell 0} + \sqrt{5} \delta_{\ell 2} \delta_{m 0}] \times \\
&\quad \left[(2 - 2\sqrt{\cos \alpha}) \delta_{0\ell} + \left(\frac{2}{5} + \frac{1}{10} \sqrt{\cos \alpha} (7 - 3 \cos(2\alpha)) \right) \delta_{2\ell} \right] \\
&= \frac{16}{3} \pi^{3/2} \left[(1 - \sqrt{\cos \alpha}) \delta_{0\ell} - \frac{1}{20\sqrt{5}} (4 + \sqrt{\cos \alpha} [7 - 3 \cos(2\alpha)]) \delta_{\ell 2} \delta_{m 0} \right].
\end{aligned} \tag{6.58}$$

CHAPTER 7

MODELING EMERGING SPATIO-ANGULAR MICROSCOPES

In the study of wisdom, many views and few judgments.

— JOSEPH JOUBERT (1815)

Chapters 5 and 6 presented models for a reasonably broad class of spatio-angular fluorescence microscopes—single- and dual-view microscopes with arbitrary numerical apertures and arbitrary excitation polarization orientations. In chapter 6 we found that a dual-view microscope could be modeled directly in terms of a model for a single-view microscope by employing rotation matrices \mathbf{R}_v and generalized convolution-multiplication theorems (the Gaunt coefficients and the Wigner D-matrices). This work gives us hope that we have completed all of our physical modeling—that arbitrary fluorescence microscopes can be modeled by simply linearly combining our existing models.

In some cases this hope is warranted. If we add a third (or n th) view to our dual-view design, we can reuse all of the models in chapters 5 and 6 with suitable redefinitions of the rotation matrices \mathbf{R}_v . However, not all possible designs can be modeled with linear combinations of existing models. For example, it is not clear how we should modify or combine our existing point-response functions to account for spatially structured illumination, a detection-side polarization or pupil splitter, or a detection-side micro-lens array.

The key difference between these cases is *coherence*. If we make new *incoherent* measurements of the object (for example, by adding an extra view), then we can linearly combine the models we have developed to create a new model. However, if we make new *coherent* measurements of the object (i.e. we modify electric fields in the instrument), then we need to develop new models. Recall that we always measure the irradiance (the absolute square of the electric field), so our linear point-response functions map fluorophore distributions to irradiance patterns. To model the effects of electric-field modifiers (gratings, polarizers, phase masks, microlenses), we need to modify the coherent point-response functions, model

interference effects, then take the absolute square to find the new point-response functions.

In this chapter we will develop forward models for three emerging classes of spatio-angular microscopes—microscopes with spatio-angular structured illumination; microscopes with polarization splitters, pupil splitters, or phase masks; and light-field microscopes with a microlens array in the nominal detector plane. The first two microscopes have the same symmetries as the microscopes we considered in chapter 6, so their singular systems and reconstruction schemes have a familiar form. On the other hand, the light-field microscope has less symmetry than the microscopes we have considered so far, so we calculate the explicit form of the singular value decomposition and reconstruction scheme. Although we cannot model every possible microscope design, we have chosen a set of representative microscopes with models that can be combined or modified to model an extremely large set of possibilities. We conclude by discussing these possibilities and speculating on optimal designs.

7.1 Spatio-angular structured illumination

First, we consider a model for a microscope with spatially and angularly structured illumination. We have already modeled microscopes with angularly structured illumination using polarizers and variable illumination orientations, so we focus on how to extend our models to include spatially structured illumination in two or three dimensions.

We consider our object to be a three-dimensional angular Boltzmann distribution $\bar{f}(\mathbf{r}_o, \hat{\mathbf{s}}_o) \in \mathbb{L}_2(\mathbb{R}^3 \times \mathbb{S}^2)$, our data to be a set of J images with each image collected under a different illumination pattern $g_j(\mathbf{r}_d) \in \mathbb{L}_2(\mathbb{R}^2)^J$, and the linear relationship between the object and data to be

$$g_j(\mathbf{r}_d) = \int_{\mathbb{R}^3} d\mathbf{r}_o \int_{\mathbb{S}^2} d\hat{\mathbf{s}}_o h_j^{(\text{si})}(\mathbf{r}_d, \mathbf{r}_o, \hat{\mathbf{s}}_o) \bar{f}(\mathbf{r}_o, \hat{\mathbf{s}}_o), \quad (7.1)$$

where $h_j^{(\text{si})}(\mathbf{r}_d, \mathbf{r}_o, \hat{\mathbf{s}}_o)$ is a generalized point-response function, and (si) indicates that this is

the model for structured illumination. We can decompose this point-response function into excitation and detection point-response functions

$$h_j^{(\text{si})}(\mathbf{r}_d, \mathbf{r}_o, \hat{\mathbf{s}}_o) = h_j^{(\text{si,exc})}(\mathbf{r}_o, \hat{\mathbf{s}}_o) h^{(\text{det})}(\mathbf{r}_d - \mathbf{r}_o^\perp, r_o^\parallel, \hat{\mathbf{s}}_o), \quad (7.2)$$

where $h^{(\text{det})}(\mathbf{r}_d - \mathbf{r}_o^\perp, r_o^\parallel, \hat{\mathbf{s}}_o)$ is the usual detection point-response function we considered in chapters 5 and 6, and $h_j^{(\text{si,exc})}(\mathbf{r}_o, \hat{\mathbf{s}}_o)$ is the excitation point-response function. Compared to our earlier work, the excitation point response function is now dependent on \mathbf{r}_o to model the spatial dependence of excitation.

The typical approach for creating a structured illumination pattern is to interfere several plane waves in the sample. If we illuminate the sample with N plane waves and the n th plane wave can be described by its wave vector \mathbf{k}_n , phase ϕ_n , and linear polarization $\hat{\mathbf{p}}_n$ (subject to the constraint $\hat{\mathbf{p}}_n \cdot \mathbf{k}_n = 0$), then the electric field pattern in the sample is given by

$$\mathbf{E}(\mathbf{r}_o) = \sum_{n=0}^{N-1} \hat{\mathbf{p}}_n \exp[i(\mathbf{k}_n \cdot \mathbf{r}_o + \phi_n)]. \quad (7.3)$$

If we illuminate the sample with J different patterns, then we can add an index j to the illumination electric field and find that the excitation point-response function takes the form

$$h_j^{(\text{si,exc})}(\mathbf{r}_o, \hat{\mathbf{s}}_o) = |\mathbf{E}_j(\mathbf{r}_o) \cdot \hat{\mathbf{s}}_o|^2, \quad (7.4)$$

which means that the electric fields interfere *before* exciting the dipoles oriented along direction $\hat{\mathbf{s}}_o$.

We can build our intuition for spatio-angular structured illumination by adding an index j to the wave vector, phase, and polarization, then writing the excitation transfer function as

$$h_j^{(\text{si,exc})}(\mathbf{r}_o, \hat{\mathbf{s}}_o) = \left| \left(\sum_{n=0}^{N-1} \hat{\mathbf{p}}_{jn} \exp[i(\mathbf{k}_{jn} \cdot \mathbf{r}_o + \phi_{jn})] \right) \cdot \hat{\mathbf{s}}_o \right|^2. \quad (7.5)$$

In this form it is clear that if we illuminate with a single plane wave $N = 1$, then the excitation transfer function reduces to the form $|\hat{\mathbf{p}}_j \cdot \hat{\mathbf{s}}_o|^2$, which we studied in chapters 5 and 6. Expanding the vectors $\hat{\mathbf{p}}$ and $\hat{\mathbf{s}}_o$ into their three components (denoted by adding an index i) yields the form

$$\begin{aligned} h_j^{(\text{si,exc})}(\mathbf{r}_o, \hat{\mathbf{s}}_o) &= \left| \sum_{i=0}^2 \sum_{n=0}^{N-1} p_{ijn} s_i \exp[i(\mathbf{k}_{jn} \cdot \mathbf{r}_o + \phi_{jn})] \right|^2 \\ &= \sum_{i=0}^2 \sum_{i'=0}^2 \sum_{n=0}^{N-1} \sum_{n'=0}^{N-1} p_{ijn} p_{i'jn'} s_i s_{i'} \exp[i([\mathbf{k}_{jn'} - \mathbf{k}_{jn}] \cdot \mathbf{r}_o + \phi_{jn'} - \phi_{jn})]. \end{aligned} \quad (7.6)$$

The second row of Eq. (7.6) shows that the differences of wave vectors $[\mathbf{k}_{jn'} - \mathbf{k}_{jn}]$ appears in the excitation transfer function, which means that high spatial frequency information can be aliased into the passband of the detection system. Gustafsson and coworkers have shown that making careful choices of the wave vectors \mathbf{k}_{jn} and phases ϕ_{jn} can lead to an invertible system of equations that can yield reconstructions with twice the spatial resolution of a diffraction-limited image [162, 214]. Our work in chapter 6 parallels Gustafsson's work—we made careful choices of $\hat{\mathbf{p}}$ to find an invertible system of equations that yielded reconstructions with rotationally invariant angular resolution.

A microscopist interested in building a spatio-angular structured illumination microscope is faced with the problem of choosing appropriate wave vectors, phases, and polarizations. Although we cannot give a solution to this problem at this time, we can make a few comments.

First, only six unique illumination polarization orientations are necessary—more than six

polarizations might improve robustness to noise but will not make higher angular frequencies accessible. We expect icosahedral polarization sampling to be optimal, but this remains unconfirmed.

Second, interfering plane waves with user-controlled polarizations allows for several opportunities not afforded to typical spatial structured illumination designs. For example, illuminating the sample with two coherent plane waves that have different \mathbf{k} vectors, orthogonal polarizations, and a relative phase of π will result in a spatially structured polarization pattern with a spatially uniform irradiance, which allows fewer illumination patterns to be used. Ströhl and Kaminski have proposed these types of illumination patterns for fast volumetric imaging [215], and we speculate that these types of illumination patterns will also appear in optimal spatio-angular sampling schemes.

Finally, we speculate that formulating the optimization problem in terms of $\mathbf{k} \in \mathbb{S}^2$, $\phi \in \mathbb{S}^1$, and $\hat{\mathbf{p}} \in \mathbb{S}^2$ may lead to a more challenging optimization problem than a more abstract formulation. Two-dimensional Jones vectors $\mathbf{J} \in \mathbb{C}^2$ are a useful way to model the polarization and phase of a plane wave traveling along a single axis [216, 217], and recent work has shown that three-dimensional Jones vectors $\mathbf{J} \in \mathbb{C}^3$ (so-called generalized Jones vectors) can be useful for modeling polarized light propagation in all three dimensions [218, 219]. Reformulating the sampling problem in terms of three-dimensional Jones vectors may lead to additional insight.

7.2 Detection-side polarization splitters, pupil splitters, and phase masks

Next, we model microscopes with polarization splitters, pupil splitters, or phase masks placed in the back focal plane of the detection objective. As usual, we consider our object to be a three-dimensional angular Boltzmann distribution $\bar{f}(\mathbf{r}_o, \hat{\mathbf{s}}_o) \in \mathbb{L}_2(\mathbb{R}^3 \times \mathbb{S}^2)$. On the detection side, we collect J' images (by imaging with multiple cameras or by subdividing a single cam-

era) for each of the J illumination patterns, so our data takes the form $g_{jj'}(\mathbf{r}_d) \in \mathbb{L}_2(\mathbb{R}^2)^{JJ'}$.

Most splitting schemes will collect the same number of images for each illumination pattern, but if this is not the case then the pair of indices (j,j') can be replaced with a single collapsed index.

The linear relationship between the object and data takes the form

$$g_{jj'}(\mathbf{r}_d) = \int_{\mathbb{R}^3} d\mathbf{r}_o \int_{\mathbb{S}^2} d\hat{\mathbf{s}}_o h_{jj'}^{(\text{spl})}(\mathbf{r}_d, \mathbf{r}_o, \hat{\mathbf{s}}_o) \bar{f}(\mathbf{r}_o, \hat{\mathbf{s}}_o), \quad (7.7)$$

where $h_{jj'}^{(\text{spl})}(\mathbf{r}_d, \mathbf{r}_o, \hat{\mathbf{s}}_o)$ is the generalized point-response function, and (spl) indicates that this is the model for split apertures. We can decompose the generalized point-response function into excitation and detection point-response functions

$$h_{jj'}^{(\text{spl})}(\mathbf{r}_d, \mathbf{r}_o, \hat{\mathbf{s}}_o) = h_j^{(\text{exc})}(\mathbf{r}_o, \hat{\mathbf{s}}_o) h_{j'}^{(\text{spl,det})}(\mathbf{r}_d - \mathbf{r}_o^\perp, r_o^\parallel, \hat{\mathbf{s}}_o). \quad (7.8)$$

We have already studied several forms of the excitation point-response function—linearly polarized plane waves in chapter 5, multiview polarized light sheets in chapter 6, and spatio-angular structured illumination in the previous section—and these models can be reused directly. In the rest of this section we will study several possible forms of the split detection point-response function.

In general, the split detection point-response function can be decomposed as

$$h_{j'}^{(\text{spl,det})}(\mathbf{r}_d - \mathbf{r}_o^\perp, r_o^\parallel, \hat{\mathbf{s}}_o) = \sum_{i,i'=0,1,2} B_{ii'j'}(\mathbf{r}_d - \mathbf{r}_o^\perp, r_o^\parallel) s_i s_{i'} \quad (7.9)$$

where

$$B_{ii'j'}(\mathbf{r}^\perp, r_o^\parallel) = \sum_{n=0,1} \beta_{nij}(\mathbf{r}^\perp, r_o^\parallel) \beta_{ni'j}^*(\mathbf{r}^\perp, r_o^\parallel), \quad (7.10)$$

is the irradiance created on the j' th split of the detector at position \mathbf{r}^\perp when an $s_i s_{i'}$ angular distribution is placed at defocus position r_o^\parallel ,

$$\beta_{nij'}(\mathbf{r}^\perp, r_o^\parallel) = \int_{\mathbb{R}^2} d\boldsymbol{\tau} M_{nj'}(\boldsymbol{\tau}) A(\boldsymbol{\tau}) \Phi(\boldsymbol{\tau}, r_o^\parallel) g_{ni}(\boldsymbol{\tau}) \exp[i2\pi\boldsymbol{\tau} \cdot \mathbf{r}^\perp], \quad (7.11)$$

is the n th component of the electric field created at position \mathbf{r}^\perp on the detector by the i th component of a dipole, $M_{nj'}(\boldsymbol{\tau})$ is a mask function that we will discuss in the remainder of this section, and $A(\boldsymbol{\tau})$, $\Phi(\boldsymbol{\tau}, r_o^\parallel)$, and $g_{ni}(\boldsymbol{\tau})$ are the amplitude, phase, and Green's tensor functions we defined earlier in section 5.2.

The mask function $M_{nj'}(\boldsymbol{\tau})$ is the key tool for modeling splits in the back aperture of the detection objective. The value of $M_{nj'}(\boldsymbol{\tau})$ is the transmission coefficient (a complex value with magnitude less than one) of the n th component of the electric field at position $\boldsymbol{\tau}$ in the back aperture plane for the j' th split of the detector. A wide range of polarization and amplitude splitters can be modeled with real-valued mask functions, and phase masks can be modeled with complex-valued mask functions. We briefly show how these mask functions can be used to model existing splitters before we speculate on future designs.

The four-way polarization splitter used in Mehta et al. [67] can be modeled with the mask function

$$M_{nj'}^{(4\text{pol})}(\boldsymbol{\tau}) = \delta_{n0} \cos(j'\pi/4) + \delta_{n1} \sin(j'\pi/4), \quad \text{for } j' = 0, 1, 2, 3. \quad (7.12)$$

For example, during the $j' = 0$ measurement Eq. (7.12) takes the value 1 when $n = 0$ (for $\hat{\mathbf{x}}$ -oriented fields) and 0 when $n = 1$ (for $\hat{\mathbf{y}}$ -oriented fields). Notice that $\boldsymbol{\tau}$ does not appear on the right-hand side of Eq. (7.12) because the aperture is clear (we are only splitting polarizations, not amplitudes).

Pupil splitters are easiest to model when the pupil position vector $\boldsymbol{\tau}$ is written in polar coordinates (τ, ϕ_τ) . For example, if the circular pupil is split in half (into two 'D's) then

each of these paths is further split into two orthogonal polarizations [personal communication, Tomomi Tani], then this mask can be modeled with the function

$$M_{nj'}^{(2\text{pol}/2\text{amp})}(\tau, \phi_\tau) = [\delta_{n0}\delta_{\lfloor j'/2 \rfloor, 0} + \delta_{n1}\delta_{\lfloor j'/2 \rfloor, 1}] \Pi\left(\frac{\phi_\tau - j'\pi/2}{\pi/2}\right), \quad \text{for } j' = 0, 1, 2, 3, \quad (7.13)$$

where $\lfloor \cdot \rfloor$ denotes the floor function (the largest integer smaller than the argument), and Π denotes the rectangle function.

Phase masks combined with splitters can be modeled using complex-valued mask functions. For example, Backer et al. used a quadrated phase mask (a tetrahedral phase pyramid) and an orthogonal polarization splitter [80, 147, 220], which can be modeled with the mask function

$$M_{nj'}^{(2\text{pol}/\text{quad})}(\tau_x, \tau_y) = [\delta_{n0}\delta_{j'0} + \delta_{n1}\delta_{j'1}] \exp[iC(|\tau_x| + |\tau_y|)], \quad \text{for } j' = 0, 1, \quad (7.14)$$

where C is a real constant.

The space of possible mask functions is extremely large. The angular rank of an arbitrary detection path is at most six, so a six-way splitter ($J' = 6$) is an appropriate choice. Under this constraint the set of possible mask functions lives in the space $M_{ij'}(\boldsymbol{\tau}) \in \mathbb{L}_2(\mathbb{R}^2)^{12}$. Choosing an optimal mask from these possibilities is not trivial, but we can make a few intuitive speculations about an optimal mask's features. First, we speculate that an optimal mask for general spatio-angular microscopy will be real-valued—i.e. it will not modify the emitted light's phase. Introducing a phase mask (sometimes called point-spread function engineering) can be a valuable approach if the designer has a prior about the sample, but in general a phase mask will broaden the point-spread function and make the reconstruction more susceptible to corruption by noise. Second, we speculate that an optimal mask function will display a six-fold symmetry. This hypothesis is based on the intuition we built when

we found that the optimal illumination scheme was extremely symmetric (icosahedral). One example of a splitter that displays six-fold symmetry is an orthogonal polarization splitter combined with a trisected pupil modeled by the mask function

$$M_{nj'}^{(2p/3a)}(\tau, \phi_\tau) = \left[\delta_{n0} \cos\left(\frac{j'\pi}{3} - \frac{\pi}{2} \left\lfloor \frac{j'}{3} \right\rfloor\right) + \delta_{n1} \sin\left(\frac{j'\pi}{3} - \frac{\pi}{2} \left\lfloor \frac{j'}{3} \right\rfloor\right) \right] \Pi\left(\frac{\phi_\tau - j'\pi/3}{\pi/3}\right),$$

for $j' = 0, 1, 2, 3, 4, 5.$

(7.15)

We hypothesize that this mask optimizes the Schatten 2-norm for general spatio-angular imaging.

Many mask functions have been designed to optimize the imaging of single molecules. Phase masks are widely used in single-molecule imaging because they allow the microscope designer to encode information about the molecule into the shape of point-spread function. The Lew group has developed a tri-spot phase mask with an orthogonal polarization splitter [84, 85, 221], which can be modeled by modifying the phase component of Eq. (7.14). They identified their design by (1) showing that existing designs were rank 5, (2) modifying their design to measure the missing parameter, then (3) confirming that the new design was rank 6. This approach led to the first full-rank phase mask, but the mask is asymmetric, nonintuitive, and potentially suboptimal. Based on our intuition about symmetric sampling schemes, we hypothesize that an orthogonal polarization splitter with a trisected phase mask modeled with the mask function

$$M_{nj'}^{(2p/3ph)}(\tau, \phi_\tau) = [\delta_{n0}\delta_{j'0} + \delta_{n1}\delta_{j'1}] \exp\left[iC\Pi\left(\frac{\phi_\tau - j'\pi/3}{\pi/3}\right)\right], \quad \text{for } j' = 0, 1, \quad (7.16)$$

is full rank and optimizes the Schatten 2-norm of the imaging operator for single molecules.

Clearly there are still many open design problems in spatio-angular imaging. Our discussion in this section has focused on choosing an optimal 6-way split for the detection side, but

in general we can design both the illumination and detection sampling schemes. With both polarized illumination and split detection, the maximum rank is 15, so we need to design 15 measurements. The detection rank cannot be larger than 6, so we hypothesize that an optimal design will use 3 serial illumination polarizations and a 5-way detection-side splitter. Even more challenging design problems arise when considering the choices for spatially structured illumination combined with detection splitters.

We conclude this section by mentioning another important use of the mask function—modeling aberrations. Most biological samples suffer from depth-dependent, sample-induced aberrations that degrade image quality, and adaptive optics can be used to estimate and correct these aberrations. The mask function can be used to model these aberrations and their potentially polarization-dependent components. We view the application of adaptive optics to spatio-angular microscopy as important future work.

7.3 Light-field detection

In this section we model a microscope that uses polarized illumination and light-field detection. A light-field detector consists of a microlens array in the nominal detector plane with the detector moved to the focal plane of the microlenses. We begin by discussing the imaging system, its symmetries, and its point-response function. Afterwards, we calculate the imaging system’s transfer function, singular system, and reconstruction scheme.

This section extends Broxton et al. [222] and related work [223] from a wave-optics model that estimates spatial fluorophore distributions to a vectorial-optics model that estimates spatio-angular fluorophore distributions. More recently, Quicke has developed a vectorial-optics model for light-field microscopy, but his work focuses on estimating angularly isotropic fluorophore densities [224].

As usual, we consider our object to be a three-dimensional angular Boltzmann density $\bar{f}(\mathbf{r}_o, \hat{\mathbf{s}}_o) \in \mathbb{L}_2(\mathbb{R}^3 \times \mathbb{S}^2)$. A polarized light-field microscope measures the irradiance on a

two-dimensional plane for each illumination polarization, so the data takes the familiar form $g_j(\mathbf{r}_d) \in \mathbb{L}_2(\mathbb{R}^2)^J$ and the linear relationship between the object and the data takes the form

$$g_j(\mathbf{r}_d) = \int_{\mathbb{R}^3} d\mathbf{r}_o \int_{\mathbb{S}^2} d\hat{\mathbf{s}}_o h_j^{(\text{lf})}(\mathbf{r}_d, \mathbf{r}_o, \hat{\mathbf{s}}_o) \bar{f}(\mathbf{r}_o, \hat{\mathbf{s}}_o). \quad (7.17)$$

where $h_j^{(\text{lf})}(\mathbf{r}_d, \mathbf{r}_o, \hat{\mathbf{s}}_o)$ is the light-field point-response function, and (lf) indicates that this is the model for light-field detection.

The model in Eq. (7.17) takes the same form as any polarized illumination single-view microscope model, except we have not assumed that the point-response function is shift invariant. To understand the lack of shift invariance, consider an in-focus isotropic emitter imaged by a light-field detector with the center of a microlens on the optical axis. When the emitter is positioned on the optical axis, the irradiance will be approximately uniform behind the central microlens and approximately zero elsewhere. As the emitter is translated in the focal plane, the image changes its functional form (the shifted emitter's image is not just a shifted version of the on-axis emitter's image). For example, if the emitter is translated to a position between two microlenses, then the image will be approximately uniform within the two adjacent microlenses and approximately zero elsewhere. Clearly, a light-field detector is not shift invariant.

However, if we shift the emitter by an integer number of microlens diameters (in de-magnified coordinates), then the image will be a shifted version of the original. Although a light-field detector is not *continuously shift invariant*, it is *discretely shift invariant*. Broxton et al. mention discrete shift invariance as a tool for reducing computations [222, section 3.4], but they give few details about how they exploit this symmetry. Here we explicitly show how to exploit the discrete shift invariance of the light-field microscope to reduce the storage and computation requirements for simulating and reconstructing from polarized light-field microscope data.

To rewrite Eq. (7.17) in a way that exploits the imaging system's discrete shift invariance,

we need to make a change of coordinates. The key insight is that we can parameterize the real line with a pair of numbers: an integer and a real number with a bounded magnitude. Mathematically, we can decompose the real line into continuous segments indexed by the integers $\mathbb{R} = \mathbb{Z} \times [-r_\mu, r_\mu]$, where r_μ is the microlens radius. Similarly, we can decompose the plane into continuous squares indexed by pairs of integers $\mathbb{R}^2 = \mathbb{Z}^2 \times [-r_\mu, r_\mu]^2$.

We can use this trick to replace our two-dimensional data coordinate $\mathbf{r}_d \in \mathbb{R}^2$ with a pair of two-dimensional coordinates $(\mathbf{r}_d, \mathbf{r}_d^\square)$, where $\mathbf{r}_d \in \mathbb{Z}^2$ indexes the microlens and $\mathbf{r}_d^\square \in [-r_\mu, r_\mu]^2$ parameterizes the position behind the microlens. Similarly, we can replace our three-dimensional object-space coordinate $\mathbf{r}_o \in \mathbb{R}^3$ with a pair of two-dimensional transverse coordinates and an axial coordinate $(\mathbf{r}_o, \mathbf{r}_o^\square, r_o^\parallel)$, where $\mathbf{r}_o \in \mathbb{Z}^2$ indexes the microlens (projected into object space), $\mathbf{r}_o^\square \in [-r_\mu, r_\mu]^2$ parameterizes the position behind the microlens (projected into object space), and $r_o^\parallel \in \mathbb{R}$ parameterizes the axial position.

We can use these new coordinates to rewrite the object, data, point-response function, and their relationship in Eq. (7.17) as

$$g_{j,\mathbf{r}_d}(\mathbf{r}_d^\square) = \sum_{\mathbf{r}_o} \int_{\square} d\mathbf{r}_o^\square \int_{\mathbb{R}} dr_o^\parallel \int_{\mathbb{S}^2} d\hat{\mathbf{s}}_o h_{j,\mathbf{r}_d-\mathbf{r}_o}^{(\text{lf})}(\mathbf{r}_d^\square, \mathbf{r}_o^\square, r_o^\parallel, \hat{\mathbf{s}}_o) \bar{f}_{\mathbf{r}_o}(\mathbf{r}_o^\square, r_o^\parallel, \hat{\mathbf{s}}_o), \quad (7.18)$$

where the argument $\mathbf{r}_d - \mathbf{r}_o$ reflects the discrete shift-invariance of the imaging system and $\square = [-r_\mu, r_\mu]^2$ is the domain of integration. We can decompose the point-response function into a product of two functions

$$h_{j,\mathbf{r}}^{(\text{lf})}(\mathbf{r}_d^\square, \mathbf{r}_o^\square, r_o^\parallel, \hat{\mathbf{s}}_o) = h_j^{(\text{exc})}(\hat{\mathbf{s}}_o) h_{\mathbf{r}}^{(\text{det,lf})}(\mathbf{r}_d^\square, \mathbf{r}_o^\square, r_o^\parallel, \hat{\mathbf{s}}_o), \quad (7.19)$$

where $h^{(\text{exc})}$ is the spatially uniform excitation point-response function we considered in chapter 5, and $h^{(\text{det,lf})}$ is the detection point-response function that we need to calculate.

In chapter 5 we calculated the function $\beta_{ni}(\mathbf{r}, r_o^\parallel)$ as the n th component of the field created at position \mathbf{r} in the nominal detector plane by the i th component of an on-axis dipole emitter

at defocus position r_o^{\parallel} . In the light-field detector the fields in the nominal detector plane need to be modified by the microlens array then propagated to the new detector position. Each square microlens imparts a phase given by

$$\phi(\mathbf{r}) = \exp\left[\frac{-i\pi|\mathbf{r}|^2}{\lambda f_\mu}\right] \Pi\left(\frac{r_x}{r_\mu}\right) \Pi\left(\frac{r_y}{r_\mu}\right), \quad (7.20)$$

and the complete microlens array imparts the phase

$$\Phi(\mathbf{r}) = \sum_{\mathbf{r}} \phi(\mathbf{r} - r_\mu \mathbf{r}). \quad (7.21)$$

Immediately after the microlenses, the fields are given by $\beta_{ni}(\mathbf{r}, r_o^{\parallel})\Phi(\mathbf{r})$. Additionally, the input fields $\beta_{ni}(\mathbf{r}, r_o^{\parallel})$ are continuously shift-invariant, so shifting the input emitter to position \mathbf{r}_o^{\square} will give rise to the fields $\beta_{ni}(\mathbf{r} - \mathbf{r}_o^{\square}, r_o^{\parallel})\Phi(\mathbf{r})$ immediately after the microlenses.

The next step is propagate the fields to the detector with a Fresnel propagator [222]

$$\beta_{ni}^{(lf)}(\mathbf{r}_d, \mathbf{r}_o^{\square}, r_o^{\parallel}) = \int_{\mathbb{R}^2} d\mathbf{r} \beta_{ni}(\mathbf{r} - \mathbf{r}_o^{\square}, r_o^{\parallel})\Phi(\mathbf{r}) \exp\left[\frac{-\pi|\mathbf{r} - \mathbf{r}_d|^2}{\lambda f_\mu}\right], \quad (7.22)$$

which can be evaluated efficiently by filtering in the spatial Fourier domain [134, 225]. Explicitly, the function $\beta_{ni}^{(lf)}(\mathbf{r}_d, \mathbf{r}_o^{\square}, r_o^{\parallel})$ is the n th component of the field created at position \mathbf{r}_d in the light-field detector plane by the i th component of a dipole at position $(\mathbf{r}_o^{\square}, r_o^{\parallel})$. It will be useful to rewrite this function in terms of our new coordinate system as

$$\beta_{ni}^{(lf)}(\mathbf{r}_d, \mathbf{r}_o^{\square}, r_o^{\parallel}) \rightarrow \beta_{ni,\mathbf{r}}^{(lf)}(\mathbf{r}_d, \mathbf{r}_o^{\square}, r_o^{\parallel}). \quad (7.23)$$

Now that we know the fields on the detector, we can calculate the irradiance created by

a $s_i s_{i'}$ angular distribution as

$$B_{ii',\mathbf{r}}^{(\text{lf})}(\mathbf{r}_d^\square, \mathbf{r}_o^\square, r_o^\parallel) = \sum_{n=0,1} \beta_{ni,\mathbf{r}}^{(\text{lf})}(\mathbf{r}_d^\square, \mathbf{r}_o^\square, r_o^\parallel) \beta_{ni',\mathbf{r}}^{(\text{lf})*}(\mathbf{r}_d^\square, \mathbf{r}_o^\square, r_o^\parallel). \quad (7.24)$$

Finally, we sum over all possible angular distributions to find the detection point-response function

$$h_{\mathbf{r}}^{(\text{det,lf})}(\mathbf{r}_d^\square, \mathbf{r}_o^\square, r_o^\parallel, \hat{\mathbf{s}}_o) = \sum_{i,i'=0,1,2} B_{ii',\mathbf{r}}^{(\text{lf})}(\mathbf{r}_d^\square, \mathbf{r}_o^\square, r_o^\parallel) s_i s_{i'}. \quad (7.25)$$

In chapters 5 and 6 we formulated all of our models and reconstructions schemes as continuous-to-continuous algorithms. For real reconstructions we recommended that each continuous coordinate be replaced by discretely sampled coordinates at each detector pixel position, and that each Fourier transform should be approximated by a discrete Fourier transform. These recommendations ignore the effects of pixel-sized sampling apertures, but they are reasonable approximations when the reconstructions are computationally constrained.

In light-field reconstructions we no longer have the luxury of an obvious discretization scheme because of the lack of continuous shift-invariance—we need to explicitly choose a discretization scheme for both data and object space. The data-space discretization is obvious—choose sampling apertures that match the real pixels:

$$w_{\mathbf{r}_d^\square}^{(\text{det})}(\mathbf{r}_d^\square) = \Pi \left(\frac{\mathbf{r}_d^\square - r_{\text{px}} \mathbf{r}_d^\square}{r_{\text{px}}} \right), \quad (7.26)$$

where r_{px} is half the pixel side length. In typical designs the number of pixels along each side of a microlens is $r_\mu/r_{\text{px}} \approx 10\text{--}20$. Choosing a discretization scheme for the object is less obvious. Broxton used the object-space discretization

$$w_{\mathbf{r}_o^\square, \mathbf{r}_o^\parallel}^{(\text{obj})}(\mathbf{r}_o^\square, r_o^\parallel) = \Pi \left(\frac{\mathbf{r}_o^\square - r_{\text{vx}}^\perp \mathbf{r}_o^\square}{r_{\text{vx}}^\perp} \right) \Pi \left(\frac{r_o^\parallel - r_{\text{vx}}^\parallel \mathbf{r}_o^\parallel}{r_{\text{vx}}^\parallel} \right), \quad (7.27)$$

where r_{vx}^\perp is the transverse extent of the object-space voxels and r_{vx}^\parallel is the axial extent of the object-space voxels. Typical choices for are $r_{\text{vx}}^\perp \approx r_\mu/3$ and $r_{\text{vx}}^\parallel \approx r_\mu$, but these are only guidelines. Light-field microscopes have depth-dependent transverse resolution, so depth-dependent grid sizes may be worth investigating.

Now we can discretize the detection point-response function with

$$h_{\mathbf{r}, \mathbf{r}_d^\square, \mathbf{r}_o^\square, \mathbf{r}_o^\parallel}^{(\text{det,lf,dd})}(\hat{\mathbf{s}}_o) = \int_{\square} d\mathbf{r}_d^\square w_{\mathbf{r}_d^\square}^{(\text{det})}(\mathbf{r}_d^\square) \int_{\square} d\mathbf{r}_o^\square \int_{\mathbb{R}} dr_o^\parallel w_{\mathbf{r}_o^\square, \mathbf{r}_o^\parallel}^{(\text{obj})}(\mathbf{r}_o^\square, r_o^\parallel) h_{\mathbf{r}}^{(\text{det,lf})}(\mathbf{r}_d^\square, \mathbf{r}_o^\square, r_o^\parallel, \hat{\mathbf{s}}_o). \quad (7.28)$$

Multiplying this point-response function with the excitation point-response function yields the complete discrete-to-discrete model of the light-field microscope

$$h_{j, \mathbf{r}, \mathbf{r}_d^\square, \mathbf{r}_o^\square, \mathbf{r}_o^\parallel}^{(\text{lf,dd})}(\hat{\mathbf{s}}_o) = h_j^{(\text{exc})}(\hat{\mathbf{s}}_o) h_{\mathbf{r}, \mathbf{r}_d^\square, \mathbf{r}_o^\square, \mathbf{r}_o^\parallel}^{(\text{det,lf,dd})}(\hat{\mathbf{s}}_o), \quad (7.29)$$

and the relationship between the discretized object and data is given by

$$g_{j, \mathbf{r}_d, \mathbf{r}_d^\square} = \sum_{\mathbf{r}_o} \sum_{\mathbf{r}_o^\square} \sum_{\mathbf{r}_o^\parallel} \int_{\mathbb{S}^2} d\hat{\mathbf{s}}_o h_{j, \mathbf{r}_d - \mathbf{r}_o, \mathbf{r}_d^\square, \mathbf{r}_o^\square, \mathbf{r}_o^\parallel}^{(\text{lf,dd})}(\hat{\mathbf{s}}_o) \bar{f}_{\mathbf{r}_o, \mathbf{r}_o^\square, \mathbf{r}_o^\parallel}(\hat{\mathbf{s}}_o). \quad (7.30)$$

Although we have not discretized the angular coordinate $\hat{\mathbf{s}}_o$, we still consider this a discrete-to-discrete model because the imaging system transfers only fifteen angular components.

Instead of discretizing the detection point-response function directly, we can discretize the irradiance created by an $s_i s_{i'}$ angular distribution

$$B_{ii', \mathbf{r}, \mathbf{r}_d^\square, \mathbf{r}_o^\square, \mathbf{r}_o^\parallel}^{(\text{lf,dd})} = \int_{\square} d\mathbf{r}_d^\square w_{\mathbf{r}_d^\square}^{(\text{det})}(\mathbf{r}_d^\square) \int_{\square} d\mathbf{r}_o^\square \int_{\mathbb{R}} dr_o^\parallel w_{\mathbf{r}_o^\square, \mathbf{r}_o^\parallel}^{(\text{obj})}(\mathbf{r}_o^\square, r_o^\parallel) B_{ii', \mathbf{r}}^{(\text{lf})}(\mathbf{r}_d^\square, \mathbf{r}_o^\square, r_o^\parallel), \quad (7.31)$$

and calculate the detection point-response function as

$$h_{\mathbf{r}, \mathbf{r}_d^\square, \mathbf{r}_o^\square, \mathbf{r}_o^\parallel}^{(\text{det,lf,dd})}(\hat{\mathbf{s}}_o) = \sum_{i, i'=0, 1, 2} B_{ii', \mathbf{r}, \mathbf{r}_d^\square, \mathbf{r}_o^\square, \mathbf{r}_o^\parallel}^{(\text{lf,dd})} s_i s_{i'}. \quad (7.32)$$

We will use the function $B_{ii',\mathbf{r},\mathbf{r}_d^\square,\mathbf{r}_o^\square,\mathbf{r}^\parallel}^{(\text{lf,dd})}$ to simplify our next calculation.

Now we are ready to calculate the transfer functions for the polarized illumination light-field microscope. We start by defining an imaging operator $\mathcal{H}^{(\text{lf,dd})}$ with entries

$$(\hat{\mathbf{e}}_j \hat{\mathbf{e}}_{\mathbf{r}_d} \hat{\mathbf{e}}_{\mathbf{r}_d^\square}, \mathcal{H}^{(\text{lf,dd})} \hat{\mathbf{e}}_{\mathbf{r}_o} \hat{\mathbf{e}}_{\mathbf{r}_o^\square} \hat{\mathbf{e}}_{\mathbf{r}_o^\parallel} \hat{\mathbf{e}}(\hat{\mathbf{s}}_o)) = h_j^{(\text{exc})}(\hat{\mathbf{s}}_o) h_{\mathbf{r}_d - \mathbf{r}_o, \mathbf{r}_d^\square, \mathbf{r}_o^\square, \mathbf{r}_o^\parallel}^{(\text{det,lf,dd})}(\hat{\mathbf{s}}_o). \quad (7.33)$$

Changing to a basis of object-space spherical harmonics yields

$$(\hat{\mathbf{e}}_j \hat{\mathbf{e}}_{\mathbf{r}_d} \hat{\mathbf{e}}_{\mathbf{r}_d^\square}, \mathcal{H}^{(\text{lf,dd})} \hat{\mathbf{e}}_{\mathbf{r}_o} \hat{\mathbf{e}}_{\mathbf{r}_o^\square} \hat{\mathbf{e}}_{\mathbf{r}_o^\parallel} \hat{\mathbf{E}}_{\ell m}) = \sum_{\ell' m'} \sum_{\ell'' m''} G_{\ell \ell' \ell''}^{m m' m''} H_{j, \ell' m'}^{(\text{exc})} H_{\mathbf{r}_d - \mathbf{r}_o, \mathbf{r}_d^\square, \mathbf{r}_o^\square, \mathbf{r}_o^\parallel, \ell'' m''}^{(\text{det,lf,dd})}, \quad (7.34)$$

where the expression for $H_{j, \ell' m'}^{(\text{exc})}$ can be found in Eq. (5.53), and $H_{\mathbf{r}, \mathbf{r}_d^\square, \mathbf{r}_o^\square, \mathbf{r}_o^\parallel, \ell m}^{(\text{det,lf,dd})}$ is given by

$$H_{\mathbf{r}, \mathbf{r}_d^\square, \mathbf{r}_o^\square, \mathbf{r}_o^\parallel, \ell m}^{(\text{det,lf,dd})} = \sum_{i, i'=0,1,2} G_{\ell 11}^{m \epsilon_i \epsilon_{i'}} B_{ii', \mathbf{r}, \mathbf{r}_d^\square, \mathbf{r}_o^\square, \mathbf{r}^\parallel}^{(\text{lf,dd})}, \quad (7.35)$$

and $\epsilon_0 = 1$, $\epsilon_1 = -1$, and $\epsilon_2 = 0$. Finally, changing to a basis of complex exponentials yields

$$(\hat{\mathbf{e}}_j \hat{\mathbf{E}}_{\mathbf{v}_d} \hat{\mathbf{e}}_{\mathbf{r}_d^\square}, \mathcal{H}^{(\text{lf,dd})} \hat{\mathbf{E}}_{\mathbf{v}_o} \hat{\mathbf{e}}_{\mathbf{r}_o^\square} \hat{\mathbf{e}}_{\mathbf{r}_o^\parallel} \hat{\mathbf{E}}_{\ell m}) = \mathsf{H}_{j, \mathbf{v}_d, \mathbf{r}_d^\square, \mathbf{r}_o^\square, \mathbf{r}_o^\parallel, \ell m}^{(\text{lf,dd})} \delta_{\mathbf{v}_d, \mathbf{v}_o}, \quad (7.36)$$

where

$$\mathsf{H}_{j, \mathbf{v}, \mathbf{r}_d^\square, \mathbf{r}_o^\square, \mathbf{r}_o^\parallel, \ell m}^{(\text{lf,dd})} = \sum_{\ell' m'} \sum_{\ell'' m''} G_{\ell \ell' \ell''}^{m m' m''} H_{j, \ell' m'}^{(\text{exc})} \mathsf{H}_{\mathbf{v}, \mathbf{r}_d^\square, \mathbf{r}_o^\square, \mathbf{r}_o^\parallel, \ell'' m''}^{(\text{det,lf,dd})}, \quad (7.37)$$

and

$$\mathsf{H}_{\mathbf{v}, \mathbf{r}_d^\square, \mathbf{r}_o^\square, \mathbf{r}_o^\parallel, \ell'' m''}^{(\text{det,lf,dd})} = \sum_{\mathbf{r}} H_{\mathbf{r}, \mathbf{r}_d^\square, \mathbf{r}_o^\square, \mathbf{r}_o^\parallel, \ell m}^{(\text{det,lf,dd})} \exp[-i 2\pi \mathbf{r} \cdot \mathbf{v}] \quad (7.38)$$

is the two-dimensional discrete-space Fourier transform.

Now we are ready to solve the eigenvalue problem

$$[\mathcal{H}^{(\text{lf})}]^\dagger \mathcal{H}^{(\text{lf})} \mathbf{u}_{\mathbf{p}, \mathbf{p}^\square, k}^{(\text{lf})} = \mu_{\mathbf{p}, \mathbf{p}^\square, k}^{(\text{lf})} \mathbf{u}_{\mathbf{p}, \mathbf{p}^\square, k}^{(\text{lf})}, \quad (7.39)$$

where $(\mathbf{p}, \mathbf{p}^\square, k) \in \mathbb{Z}^2 \times \mathbb{Z}^2 \times \mathbb{Z}$ are discrete indices for the eigenfunctions. Notice that we have purposefully excluded an axial index \mathbf{p}^\parallel because we are only taking a single image of the three-dimensional object.

Choosing a basis for the object-space singular functions and exploiting the discrete two-dimensional shift invariance yields functions of the form

$$\left(\hat{\mathbf{e}}_{\mathbf{r}} \hat{\mathbf{e}}_{\mathbf{r}_o^\square} \hat{\mathbf{e}}_{\mathbf{r}_o^\parallel} \hat{\mathbf{E}}_{\ell m}, \mathbf{u}_{\mathbf{p}, \mathbf{p}^\square, k}^{(\text{lf})} \right) = \tilde{U}_{\mathbf{p}^\square, k; \mathbf{r}_o^\square, \mathbf{r}_o^\parallel, \ell m}^{(\text{lf})}(\mathbf{p}) \exp[2\pi i \mathbf{p} \cdot \mathbf{r}]. \quad (7.40)$$

After a long calculation that mimics section 6.2, we find that the eigenvalue problem can be expressed in this basis as

$$\begin{aligned} \sum_{\mathbf{r}_o^\square, \mathbf{r}_o^\parallel, \ell' m'} \left[\sum_{\mathbf{r}_d^\square, j} \mathsf{H}_{j, \mathbf{p}, \mathbf{r}_d^\square, \mathbf{r}_o^\square, \mathbf{r}_o^\parallel, \ell m}^{(\text{lf}, \text{dd})*} \mathsf{H}_{j, \mathbf{p}, \mathbf{r}_d^\square, \mathbf{r}_o^\square, \mathbf{r}_o^\parallel, \ell' m'}^{(\text{lf}, \text{dd})} \right] \tilde{U}_{\mathbf{p}^\square, k; \mathbf{r}_o^\square, \mathbf{r}_o^\parallel, \ell' m'}^{(\text{lf})}(\mathbf{p}) \\ = \mu_{\mathbf{p}, \mathbf{p}^\square, k}^{(\text{lf})} \tilde{U}_{\mathbf{p}^\square, k; \mathbf{r}_o^\square, \mathbf{r}_o^\parallel, \ell m}^{(\text{lf})}(\mathbf{p}). \end{aligned} \quad (7.41)$$

If we let N denote the number of elements in the set $\{\mathbf{r}_o^\square, \mathbf{r}_o^\parallel, \ell m\}$ (typically $\approx 3^2 \times 50 \times 15 = 6750$), then the square brackets in Eq. (7.41) enclose an $N \times N$ matrix for each discrete spatial frequency \mathbf{p} . The rank of this matrix is at most the size of the set $\{\mathbf{r}_d^\square, j\}$ (typically $\approx 20^2 \times 6 = 2400$). Calculating the eigenvalues and eigenvectors of this matrix yield $\mu_{\mathbf{p}, \mathbf{p}^\square, k}^{(\text{lf})}$ and $\tilde{U}_{\mathbf{p}^\square, k; \mathbf{r}_o^\square, \mathbf{r}_o^\parallel, \ell m}^{(\text{lf})}(\mathbf{p})$, respectively.

Now we can calculate the complete object-space singular functions with

$$u_{\mathbf{p}, \mathbf{p}^\square, k; \mathbf{r}_o, \mathbf{r}_o^\square, \mathbf{r}_o^\parallel}^{(\text{lf})}(\hat{\mathbf{s}}_o) = \exp[2\pi i \mathbf{p} \cdot \mathbf{r}_o] \sum_{\ell m} \tilde{U}_{\mathbf{p}^\square, k; \mathbf{r}_o^\square, \mathbf{r}_o^\parallel, \ell m}^{(\text{lf})}(\mathbf{p}) Y_{\ell m}(\hat{\mathbf{s}}_o). \quad (7.42)$$

We can compute the data-space singular functions by calculating

$$\tilde{V}_{\mathbf{p}^\square, k; j, btr_d^\square}^{(\text{lf})}(\mathbf{p}) = \sqrt{\mu_{\mathbf{p}, \mathbf{p}^\square, k}^{(\text{lf})}} \sum_{\mathbf{r}_o^\square, \mathbf{r}_o^\parallel, \ell m} \mathsf{H}_{j, \mathbf{p}, \mathbf{r}_d^\square, \mathbf{r}_o^\square, \mathbf{r}_o^\parallel, \ell m}^{(\text{lf}, \text{dd})} \tilde{U}_{\mathbf{p}^\square, k; \mathbf{r}_o^\square, \mathbf{r}_o^\parallel, \ell m}^{(\text{lf})}(\mathbf{p}), \quad (7.43)$$

then multiplying the result by discrete complex exponentials

$$v_{\mathbf{p}, \mathbf{p}^\square, k; j, \mathbf{r}_d, \mathbf{r}_d^\square}^{(\text{lf})} = \tilde{V}_{\mathbf{p}^\square, k; j, \mathbf{r}_d^\square}^{(\text{lf})}(\mathbf{p}) \exp[2\pi i \mathbf{p} \cdot \mathbf{r}_d]. \quad (7.44)$$

A Tikhonov-regularized reconstruction of light-field data takes a similar form to our previous reconstruction schemes. Starting with data $g_{j, \mathbf{r}_d, \mathbf{r}_d^\square}$, we take the discrete Fourier transform along the microlens index dimension

$$G_{j, \mathbf{v}, \mathbf{r}_d^\square} = \sum_{\mathbf{r}_d} g_{j, \mathbf{r}_d, \mathbf{r}_d^\square} \exp[2\pi i \mathbf{r}_d \cdot \mathbf{v}]. \quad (7.45)$$

Next, we compute our object-space estimates with a Tikhonov-regularized pseudoinverse

$$\hat{\mathsf{F}}_{\eta; \mathbf{v}, \mathbf{r}_o^\square, \mathbf{r}_o^\parallel, \ell m} = \sum_{\mathbf{p}^\square, k} \frac{\sqrt{\mu_{\mathbf{v}, \mathbf{p}^\square, k}^{(\text{lf})}}}{\mu_{\mathbf{v}, \mathbf{p}^\square, k}^{(\text{lf})} + \eta} \tilde{U}_{\mathbf{p}^\square, k; \mathbf{r}_o^\square, \mathbf{r}_o^\parallel, \ell m}^{(\text{lf})}(\mathbf{v}) \sum_{j, \mathbf{r}_d^\square} \tilde{V}_{\mathbf{p}^\square, k; j, \mathbf{r}_d^\square}^{(\text{lf})}(\mathbf{v}) G_{j, \mathbf{v}, \mathbf{r}_d^\square}. \quad (7.46)$$

Finally, we take the inverse discrete Fourier transform

$$\hat{F}_{\eta; \mathbf{r}, \mathbf{r}_o^\square, \mathbf{r}_o^\parallel, \ell m} = \sum_{\mathbf{v}} \hat{\mathsf{F}}_{\eta; \mathbf{v}, \mathbf{r}_o^\square, \mathbf{r}_o^\parallel, \ell m} \exp[2\pi i \mathbf{v} \cdot \mathbf{r}], \quad (7.47)$$

and store the result. As usual, we can visualize the reconstruction using the methods discussed in chapter 5.

7.4 Discussion

All of the emerging instruments discussed in this chapter have a potentially useful niche. Spatially structured illumination will be essential for maximizing the spatial resolution of spatio-angular imaging, and early designs are already beginning to appear [115, 226]. The light-sheet illumination scheme we considered in chapter 6 is another form of structured illumination that we exploited for optical sectioning [101], and point-scanning structured illumination techniques show additional promise for fast high-resolution spatio-angular imaging [93, 94]. We anticipate that the highest resolution spatio-angular microscopes that image densely labeled objects will employ some form of spatially structured illumination.

Detection-side polarization splitters and pupil splitters will be essential for pushing the angular resolution of spatio-angular imaging systems into the $\ell = 4$ band. Additionally, detection-side polarizers and splitters are much faster than the angularly structured illumination schemes that we considered in chapters 5 and 6—it is much faster to take parallel detection-side polarization measurements than serial illumination-side polarization measurements. We anticipate that the fastest spatio-angular microscopes with rotationally invariant angular resolution will employ a six-way detection-side polarization and pupil splitter.

Finally, light-field detection designs show promise for fast detection of thick three-dimensional angular distributions, but challenges still lie ahead. First, light-field detection schemes are known to display depth-dependent transverse resolution. This is not an issue for reconstructing sparse samples, but it can make the interpretation of dense samples challenging. Second, early analysis of the singular systems of light-field detection systems has shown that these imaging systems display depth-dependent *angular* resolution. This makes the interpretation of the reconstructions even more challenging. Finally, efficient implementations of the models and reconstructions schemes described in this chapter are not trivial to develop and debug. Any comparison of computational microscopes needs to consider both the computation required to reconstruct from data and the expertise and time

required to develop the reconstruction scheme. On these metrics, light-field detection designs are at a disadvantage compared to any three dimensionally shift-invariant imaging system. However, we believe that these challenges can be overcome, and we anticipate that light-field spatio-angular imaging systems will outperform other designs for reasonably thin samples (a few depths of field thick) with fast dynamics when diffraction-limited spatial resolution is not necessary.

CHAPTER 8

CONCLUSIONS AND OUTLOOK

This dissertation has demonstrated that spatio-angular fluorescence microscopy is possible, practical, and useful. By unifying polarized fluorescence spectroscopy, microscopy, and image science into a mathematical framework then studying the physical limits that this class of instruments face, we have been able to design novel imaging systems that can measure new information from densely labeled fluorescent samples.

We began in chapter 2 by describing ensembles of fluorescent dipole emitters as members of the Hilbert space $\mathbb{L}_2(\mathbb{R}^3 \times \mathbb{S}^2)$ —square-integrable functions that take a value at each point on a sphere and at each point in space—and images as members of the Hilbert space $\mathbb{L}_2(\mathbb{R}^2)$ —square-integrable functions that take a value at each point on a plane. We described the mapping between these spaces with a linear Hilbert-space operator \mathcal{H} and described how this operator can be usefully expressed in four different bases.

In chapter 3 we calculated the specific form of the entries of \mathcal{H} for a paraxial $4f$ imaging system and demonstrated how these entries can be used. Studying the specific form of the transfer functions led us to conclude that the fields emitted by dipole emitters create angularly bandlimited signals that carry six times as much information as monopole emitters.

In chapter 4 we analyzed a complete spatio-angular fluorescence experiment: polarized illumination followed by angular diffusion, emission, and detection by a high-NA imaging system. We found that angular diffusion in a potential cannot be described by a single rotational time scale—the full spectrum of the angular diffusion operator must be considered. To avoid this complexity and allow for reconstructions, we studied cases where the complete imaging process is approximately linear.

In chapter 5 we posed general spatio-angular inverse problems and found the parameter regimes where they are linear. In these specific cases, we calculated singular value decompositions of the relevant operators and found that icosahedral polarization sampling schemes

are optimal.

In chapter 6 we used all of the work in chapters 2–5 to develop a model for a polarized illumination dual-view light-sheet imaging system. We found the limits of this imaging system, proposed an augmented system that could measure the orientation of all fluorescent molecules, then demonstrated that our models made useful predictions. In this chapter we demonstrated the first imaging system that can measure the three-dimensional position and orientation of densely labeled fluorescent molecules.

In chapter 7 we extended our imaging models to a wider range of microscopes including systems with spatially structured illumination, detection-side polarization and aperture splitters, and light field detectors. We concluded that there is still room for development in spatio-angular fluorescence microscopy, and we speculated on the form that future optimal designs might take.

A critic of this dissertation may point to a lack of specific scientific application or broader societal impact. Are we solving problems that do not need to be solved? The author values these concerns and offers three defenses for the value of this work.

First, **existing biological applications can benefit**. In chapter 1 we reviewed a varied set of biological applications that use polarized fluorescence spectroscopy or polarized fluorescence microscopy. This work has shown that these efforts have not yet exploited the full potential of the signals emitted by dipole emitters. The author feels confident that instruments and reconstruction techniques that achieve physical limits will lead to new discoveries in biology.

Second, **elegant theory is valuable**. Reasoning about physical systems, instrument designs, and reconstructions is extremely difficult without solid theoretical tools. This work has introduced many theoretical tools with the goal of streamlining thinking, not impeding it. Although the notation and details can be intimidating, the high-level ideas—geometry

first, symmetry second, basis third—are simple, and they can aid the reasoning of any practitioner. The author feels confident that this dissertation has introduced tools to the fields of polarized fluorescence spectroscopy and fluorescence microscopy that will make their work easier, not harder. Please note that the claim “elegant theory is valuable” does not contradict any claim for the value of experiment. Science and engineering cannot proceed without experiment, and this author celebrates the exciting back-and-forth relationship between theory and experiment.

Third, synthesis is enabling. Perrin’s work synthesized several disparate observations into a consistent model that enabled later applications that he did not envision, and similar examples abound in the history of science. This author is hopeful that this work has synthesized polarized fluorescence spectroscopy, fluorescence microscopy, and image science in a way that will enable future applications.

What kinds of applications might spatio-angular fluorescence microscopy enable? One potential area is *fluorescent force sensors*. By encoding the force across a protein into the orientation and rotational mobility of a dipole emitter (see Fig. 8.1), biologists may be able to exploit spatio-angular fluorescence microscopy to read out pico-newton scale directional forces in three dimensions. Existing methods are limited to measuring force magnitudes ($|F|$) with a single channel at SNRs typical of fluorescent proteins, while the proposed approach would allow measurements of three-dimensional force vectors (F) in multiple channels at SNRs typical of synthetic fluorophores.

Another potential area is *fluorescent voltage sensing*. Many existing sensors encode membrane potentials (V) into the brightness of a fluorescent molecule so that neural activity can be monitored in living organisms. The scalar potential is sufficient to determine the complete electric field (E) when charges are static, but charges are not static in neurons. To determine the electric field when charges are moving, the vector potential (A) must be measured at the same time as the scalar potential. Do vector potentials play any role in neural func-

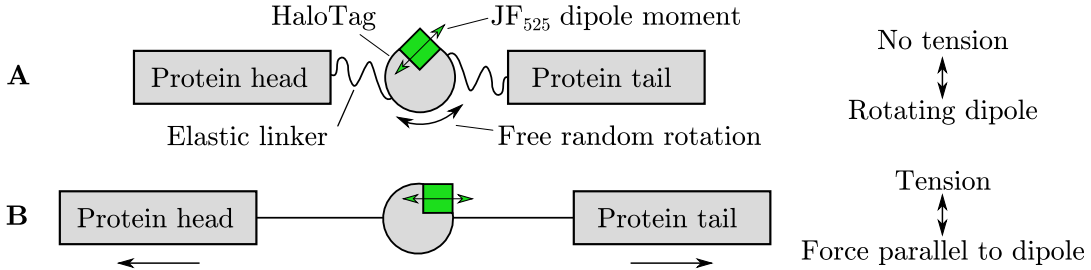


Figure 8.1: The proposed molecular force sensor consists of a HaloTag conjugated to a synthetic fluorescent ligand sandwiched between a pair of elastic linkers. **(A)** Without tension the dipole moment of the fluorescent molecule is free to rotate randomly. **(B)** Under tension the dipole moment is parallel to the tension force. Therefore, the force orientation and magnitude are encoded into the orientation and rotational mobility of the fluorophore which can be decoded using spatio-angular microscopy.

tion? Can both scalar and vector potentials be encoded into the orientation and rotational mobility of fluorescent molecules?

Some of the mathematical models developed in this work may have broader applications as well. Ensembles of dipole emitters can be usefully modeled as functions from each point in space and each point on the sphere to real numbers $\mathbf{f} : \mathbb{R}^3 \times \mathbb{S}^2 \rightarrow \mathbb{R}$ and similar functions arise in diffusion MRI. Inspiration for new imaging systems may flow in both directions. Modeling transmission polarized microscopes will require the more formidable object space of unitary matrix-valued functions $\mathbf{f} : \mathbb{R}^3 \rightarrow \mathbb{SU}(3)$, where $\mathbb{SU}(3)$ is the space of 3×3 unitary matrices with determinant +1. Members of $\mathbb{SU}(3)$ can be used to describe birefringent and diattenuating objects that modify the polarization state of the light passing through them [219]. We expect that Fourier analysis of operators acting on $L_2(\mathbb{R}^3; \mathbb{SU}(3))$ will lead to extensions of the insights collected in this dissertation. An additional challenge is that transmission microscopy is *bilinear* instead of linear, so generalizations of bilinear transfer functions (often called transmission cross coefficients in microscopy [227]) will be required.

The results in this dissertation and the potential applications make the author very optimistic for the future of spatio-angular fluorescence microscopy. *Onwards!*

Bibliography

- [1] H. H. Barrett and K. J. Myers. *Foundations of image science*. Wiley-Interscience, 2004. (cited on pp. xi, 15, 23, 27, 37, 56, 81, 95, 98, 99, 121, 123, 125, 126, 137, 140, 145, 170, and 171)
- [2] J. Jackson. *Classical electrodynamics*. Wiley, 1975. (cited on p. 5)
- [3] N. B. Monardes. *Historia medicinal de las cosas que se traen de nuestras Indias Occidentales*. Seville, 1565. (cited on p. 6)
- [4] W. E. Safford. Lignum nephriticum—its history and an account of the remarkable fluorescence of its infusion. In *Annual report of the Board of Regents of the Smithsonian Institution. Washington*, pages 271–298. Government Printing Office, 1916. (cited on p. 7)
- [5] F. H. Garrison. *An introduction to the history of medicine*. Philadelphia: W.B. Saunders Company, 1917. (cited on p. 7)
- [6] F. M. Grimaldi. *Physicomathesis de lumine, coloribus, et iride, aliisque annexis*. Bologna, 1665. (cited on p. 7)
- [7] R. Boyle. *Experiments and considerations touching colours*. London, 1664. (cited on p. 7)
- [8] I. Newton. *Of colours*. Cambridge University Library, 1665. (cited on p. 7)
- [9] I. Newton. *Opticks: or, a treatise of the reflections, refractions, inflections and colours of light*. London, 1704. (cited on p. 7)
- [10] I. Newton. New theory about light and colors. *Philos. Trans. R. Soc.*, pages 3075–3087, 1671. (cited on p. 7)
- [11] A. U. Acuña, F. Amat-Guerri, P. Morcillo, M. Liras, and B. Rodríguez. Structure and formation of the fluorescent compound of lignum nephriticum. *Org. Lett.*, 11(14):3020–3023, 2009. (cited on p. 7)
- [12] A. U. Acuña and F. Amat-Guerri. Early history of solution fluorescence: The lignum nephriticum of Nicolás Monardes. *SpringerLink*, pages 3–20, 2007. (cited on p. 7)
- [13] G. G. Stokes. On the change of refrangibility of light. *Philos. Trans. R. Soc. Lond.*, 1852. (cited on pp. 8 and 87)
- [14] J. F. W. Herschel. On a case of superficial colour presented by a homogeneous liquid internally colourless. *Proc. R. Soc. Lond.*, 5:547, 1851. (cited on p. 8)
- [15] B. Valeur and M. N. Berberan-Santos. A brief history of fluorescence and phosphorescence before the emergence of quantum theory. *J. Chem. Educ.*, 88(6):731–738, 2011. (cited on p. 8)

- [16] F. Göppelsröder. Über eine fluorescirende substanz aus dem Kuba-holze (fortsetzung) and über fluorescenzanalyse [On a fluorescent substance extracted from Cuba wood and on fluorescence analysis]. *J. Prakt. Chem.*, 104:10–27, 1868. (cited on p. 8)
- [17] W. Kass. *Tracing technique in geohydrology*. CRC Press, 2018. (cited on p. 8)
- [18] F. Weigert. Über polarisiertes fluoreszenzlicht. *Verh. d. Deutsch. Physik. Ges.*, 3(1):100–102, 1920. (cited on pp. 8 and 88)
- [19] S. J. Wawilow and W. L. Lewschin. Beiträge zur frage über polarisiertes fluoreszenzlicht von farbstofflösungen. II. *Z. Phys.*, 16:135–154, 1923. (cited on pp. 8 and 88)
- [20] F. Perrin. Polarisation de la lumière de fluorescence. vie moyenne des molécules dans l'état excité. *J. de Physique et Le Radium*, 7(12):390–401, 1926. (cited on pp. 8 and 88)
- [21] A. Jabłoński. On the notion of emission anisotropy. *Bull. de L'Academie Polonaise des Sci.*, 8(4):259–264, 1960. (cited on p. 9)
- [22] G. Weber. Polarization of the fluorescence of macromolecules. 1. Theory and experimental method. *Biochem. J.*, 51(2):145–155, 1952. (cited on pp. 10 and 88)
- [23] G. Weber. Polarization of the fluorescence of macromolecules. 2. Fluorescent conjugates of ovalbumin and bovine serum albumin. *Biochem. J.*, 51(2):155–167, 1952. (cited on pp. 10 and 88)
- [24] A. C. Albrecht. Polarizations and assignments of transitions: The method of photoselection. *J. Mol. Spectrosc.*, 6:84–108, 1961. (cited on p. 10)
- [25] J. R. Lakowicz. *Principles of fluorescence spectroscopy*. Springer, New York, 3rd edition, 2006. (cited on pp. 10, 88, and 93)
- [26] E. Abbe. On the estimation of aperture in the microscope. *J. R. Microsc. Soc.*, 1(3):388–423, 1881. (cited on p. 11)
- [27] M. Mansuripur. *Classical optics and its applications*. Cambridge University Press, 2009. (cited on pp. 11 and 26)
- [28] O. Heimstädt. Das fluoreszenzmikroskop. *Z. Wiss. Mikrosk.*, 28:330–337, 1911. (cited on p. 11)
- [29] M. Haitinger. *Fluoreszenzmikroskopie*. Leipzig, 1938. (cited on p. 11)
- [30] J. S. Ploem. The use of a vertical illuminator with interchangeable dichroic mirrors for fluorescence microscopy with incidental light. *Z. Wiss. Mikrosk.*, 68(3):129–142, 1967. (cited on p. 11)
- [31] A. H. Coons, R. N. Jones, and H. J. Creech. Immunological properties of an antibody containing a fluorescent group. *Proc. Soc. Expt. Biol. Med.*, 1941. (cited on p. 11)

- [32] H. F. Talbot. Experiments on light. *London, Edinburgh, Dublin Philos. Mag. J. Sci.*, 5(29):321–334, 1834. (cited on p. 11)
- [33] P. F. J. Cheshire. The early history of the polariscope, and the polarizing microscope. *J. R. Microsc. Soc.*, 43(1):1–18, 1923. (cited on p. 11)
- [34] W. J. Schmidt. Doppelbrechung der kernspindel und zugfasertheorie der chromosomenbewegung. *Zeitschrift fur Zellforschung und Mikroskopische Anat. Abt B Chromosom.*, 1(1):253–264, 1939. (cited on p. 11)
- [35] S. Inoué. Polarization optical studies of the mitotic spindle. *Chromosoma*, 5(1):487–500, 1953. (cited on p. 11)
- [36] P. R. Dragsten and W. W. Webb. Mechanism of the membrane potential sensitivity of the fluorescent membrane probe merocyanine 540. *Biochemistry*, 17(24):5228–5240, 1978. (cited on p. 12)
- [37] D. Axelrod. Carbocyanine dye orientation in red cell membrane studied by microscopic fluorescence polarization. *Biophys. J.*, 26(3):557–573, 1979. (cited on pp. 12, 88, and 121)
- [38] T. P. Burghardt and N. L. Thompson. Motion of myosin cross-bridges in skeletal muscle fibers studied by time-resolved fluorescence anisotropy decay. *Biochemistry*, 24(14):3731–3735, 1985. (cited on p. 12)
- [39] R. E. Dale, S. C. Hopkins, U. A. van der Heide, T. Marszałek, M. Irving, and Y. E. Goldman. Model-independent analysis of the orientation of fluorescent probes with restricted mobility in muscle fibers. *Biophys. J.*, 76(3):1606–1618, 1999. (cited on pp. 12, 78, 88, and 121)
- [40] N. L. Thompson and T. P. Burghardt. Total internal reflection fluorescence: Measurement of spatial and orientational distributions of fluorophores near planar dielectric interfaces. *Biophys. Chem.*, 25(1):91–97, 1986. (cited on p. 12)
- [41] M. Chalfie, Y. Tu, G. Euskirchen, W. W. Ward, and D. C. Prasher. Green fluorescent protein as a marker for gene expression. *Science*, 263:802–806, 1994. (cited on p. 12)
- [42] S. Inoué, O. Shimomura, M. Goda, M. Shribak, and P. T. Tran. Fluorescence polarization of green fluorescence protein. *Proc. Natl. Acad. Sci.*, 99(7):4272–4277, 2002. (cited on p. 12)
- [43] F. I. Rosell and S. G. Boxer. Polarized absorption spectra of green fluorescent protein single crystals: transition dipole moment directions. *Biochemistry*, 42(1):177–183, 2003. (cited on p. 12)
- [44] R. Varma and S. Mayor. GPI-anchored proteins are organized in submicron domains at the cell surface. *Nature*, 394(6695):798–801, 1998. (cited on p. 12)

- [45] P. Sharma, R. Varma, R. C. Sarasij, Ira, K. Gousset, G. Krishnamoorthy, M. Rao, and S. Mayor. Nanoscale organization of multiple GPI-anchored proteins in living cell membranes. *Cell*, 116(4):577–589, 2004. (cited on p. 12)
- [46] A. M. Vrabioiu and T. J. Mitchison. Structural insights into yeast septin organization from polarized fluorescence microscopy. *Nature*, 443:466–469, 2006. (cited on pp. 12, 19, and 22)
- [47] A. M. Vrabioiu and T. J. Mitchison. Symmetry of septin hourglass and ring structures. *J. Mol. Biol.*, 372(1):37–49, 2007. (cited on p. 12)
- [48] B. S. DeMay, N. Noda, A. S. Gladfelter, and R. Oldenbourg. Rapid and quantitative imaging of excitation polarized fluorescence reveals ordered septin dynamics in live yeast. *Biophys. J.*, 101(4):985–994, 2011. (cited on pp. 12, 88, and 121)
- [49] B. S. DeMay, X. Bai, L. Howard, P. Occhipinti, R. A. Miseroll, E. T. Spiliotis, R. Oldenbourg, and A. S. Gladfelter. Septin filaments exhibit a dynamic, paired organization that is conserved from yeast to mammals. *The J. Cell Biol.*, 193(6):1065–1081, 2011. (cited on p. 12)
- [50] V. Swaminathan, J. M. Kalappurakkal, S. B. Mehta, P. Nordenfelt, T. I. Moore, N. Koga, D. A. Baker, R. Oldenbourg, T. Tani, S. Mayor, T. A. Springer, and C. M. Waterman. Actin retrograde flow actively aligns and orients ligand-engaged integrins in focal adhesions. *Proc. Natl. Acad. Sci.*, 114(40):10648–10653, 2017. (cited on p. 12)
- [51] A. L. Mattheyses, M. Kampmann, C. E. Atkinson, and S. M. Simon. Fluorescence anisotropy reveals order and disorder of protein domains in the nuclear pore complex. *Biophys. J.*, 99(6):1706–1717, 2010. (cited on pp. 12, 19, 22, 88, and 121)
- [52] M. Kampmann, C. E. Atkinson, A. L. Mattheyses, and S. M. Simon. Mapping the orientation of nuclear pore proteins in living cells with polarized fluorescence microscopy. *Nat. Struct. Mol. Biol.*, 18(6):643–649, 2011. (cited on p. 12)
- [53] N. Nakai, K. Sato, T. Tani, K. Saito, F. Sato, and S. Terada. Genetically encoded orientation probes for F-actin for fluorescence polarization microscopy. *Microscopy*, 2019. (cited on p. 12)
- [54] A. Gasecka, T.-J. Han, C. Favard, B. R. Cho, and S. Brasselet. Quantitative imaging of molecular order in lipid membranes using two-photon fluorescence polarimetry. *Biophys. J.*, 97(10):2854–2862, 2009. (cited on p. 12)
- [55] S. Brasselet. Polarization-resolved nonlinear microscopy: Application to structural molecular and biological imaging. *Adv. Opt. Photonics*, 3(3):205, 2011. (cited on pp. 12, 42, 78, 88, and 121)
- [56] P. Ferrand, P. Gasecka, A. Kress, X. Wang, F.-Z. Bioud, J. Duboisset, and S. Brasselet. Ultimate use of two-photon fluorescence microscopy to map orientational behavior of fluorophores. *Biophys. J.*, 106(11):2330–2339, 2014. (cited on pp. 12 and 120)

- [57] A. L. Mattheyses, A. D. Hoppe, and D. Axelrod. Polarized fluorescence resonance energy transfer microscopy. *Biophys. J.*, 87(4):2787–2797, 2004. (cited on p. 12)
- [58] A. H. Clayton, Q. S. Hanley, D. J. Arndt-Jovin, V. Subramaniam, and T. M. Jovin. Dynamic fluorescence anisotropy imaging microscopy in the frequency domain (rFLIM). *Biophys. J.*, 83(3):1631–1649, 2002. (cited on p. 12)
- [59] J. Siegel, K. Suhling, S. Lévéque-Fort, S. E. D. Webb, D. M. Davis, D. Phillips, Y. Sabharwal, and P. M. W. French. Wide-field time-resolved fluorescence anisotropy imaging (TR-FAIM): Imaging the rotational mobility of a fluorophore. *Rev. Sci. Instruments*, 74(1):182–192, 2003. (cited on pp. 12, 88, and 121)
- [60] K. Suhling, J. Siegel, P. M. P. Lanigan, S. Lévéque-Fort, S. E. D. Webb, D. Phillips, D. M. Davis, and P. M. W. French. Time-resolved fluorescence anisotropy imaging applied to live cells. *Opt. Lett.*, 29(6):584–586, 2004. (cited on pp. 12 and 121)
- [61] T. Ha, T. Enderle, D. S. Chemla, P. R. Selvin, and S. Weiss. Single molecule dynamics studied by polarization modulation. *Phys. Rev. Lett.*, 77(19):3979–3982, 1996. (cited on pp. 13 and 88)
- [62] S. Weiss. Fluorescence spectroscopy of single biomolecules. *Science*, 283(5408):1676–1683, 1999. (cited on p. 13)
- [63] J. T. Fourkas. Rapid determination of the three-dimensional orientation of single molecules. *Opt. Lett.*, 26(4):211–213, 2001. (cited on pp. 13, 22, and 64)
- [64] J. Hohlbein and C. G. Hübner. Simple scheme for rapid three-dimensional orientation determination of the emission dipole of single molecules. *Appl. Phys. Lett.*, 86(12):121104, 2005. (cited on p. 13)
- [65] C.-Y. Lu and D. A. Vanden Bout. Analysis of orientational dynamics of single fluorophore trajectories from three-angle polarization experiments. *J. Chem. Phys.*, 128(24):244501, 2008. (cited on p. 13)
- [66] J. N. Forkey, M. E. Quinlan, M. A. Shaw, J. E. T. Corrie, and Y. E. Goldman. Three-dimensional structural dynamics of myosin V by single-molecule fluorescence polarization. *Nature*, 422(6930):399–404, 2003. (cited on pp. 13, 22, and 88)
- [67] S. B. Mehta, M. McQuilken, P. J. La Rivière, P. Occhipinti, A. Verma, R. Oldenbourg, A. S. Gladfelter, and T. Tani. Dissection of molecular assembly dynamics by tracking orientation and position of single molecules in live cells. *Proc. Natl. Acad. Sci.*, 113(42):E6352–E6361, 2016. (cited on pp. 13, 19, 22, 88, 93, 196, and 212)
- [68] A. S. Backer, A. S. Biebricher, G. A. King, G. J. L. Wuite, I. Heller, and E. J. G. Peterman. Single-molecule polarization microscopy of DNA intercalators sheds light on the structure of S-DNA. *Sci. Adv.*, 5(3), 2019. (cited on pp. 13, 88, and 122)

- [69] J. H. Lewis and Z. Lu. Resolution of ångström-scale protein conformational changes by analyzing fluorescence anisotropy. *Nat. Struct. Mol. Biol.*, 26(9):802–807, 2019. (cited on p. 13)
- [70] B. Sick, B. Hecht, and L. Novotny. Orientational imaging of single molecules by annular illumination. *Phys. Rev. Lett.*, 85:4482–4485, 2000. (cited on pp. 13 and 79)
- [71] M. Böhmer and J. Enderlein. Orientation imaging of single molecules by wide-field epifluorescence microscopy. *J. Opt. Soc. Am. B*, 20(3):554–559, 2003. (cited on pp. 13, 20, and 62)
- [72] A. Lieb, J. M. Zavislan, and L. Novotny. Single-molecule orientations determined by direct emission pattern imaging. *J. Opt. Soc. Am. B*, 21(6):1210–1215, 2004. (cited on pp. 13, 20, and 62)
- [73] L. Novotny and B. Hecht. *Principles of nano-optics*. Cambridge University Press, 2006. (cited on pp. 13, 41, 65, 108, and 132)
- [74] E. Toprak, J. Enderlein, S. Syed, S. A. McKinney, R. G. Petschek, T. Ha, Y. E. Goldman, and P. R. Selvin. Defocused orientation and position imaging (DOPI) of myosin V. *Proc. Natl. Acad. Sci.*, 103(17):6495–6499, 2006. (cited on pp. 13, 20, 79, and 88)
- [75] S. Stallinga and B. Rieger. Position and orientation estimation of fixed dipole emitters using an effective Hermite point spread function model. *Opt. Express*, 20(6):5896–5921, 2012. (cited on p. 13)
- [76] M. D. Lew, M. P. Backlund, and W. E. Moerner. Rotational mobility of single molecules affects localization accuracy in super-resolution fluorescence microscopy. *Nano Lett.*, 13(9):3967–3972, 2013. (cited on pp. 13, 19, 79, 80, 88, 93, 108, 117, 118, 122, and 132)
- [77] M. P. Backlund, M. D. Lew, A. S. Backer, S. J. Sahl, and W. E. Moerner. The role of molecular dipole orientation in single-molecule fluorescence microscopy and implications for super-resolution imaging. *ChemPhysChem*, 15(4):587–599, 2014. (cited on pp. 13 and 19)
- [78] S. Stallinga. Effect of rotational diffusion in an orientational potential well on the point spread function of electric dipole emitters. *J. Opt. Soc. Am. A*, 32(2):213–223, 2015. (cited on pp. 13, 20, 48, 51, 88, 93, 99, 108, 110, 117, 118, 122, and 132)
- [79] M. P. Backlund, M. D. Lew, A. S. Backer, S. J. Sahl, G. Grover, A. Agrawal, R. Piestun, and W. E. Moerner. Simultaneous, accurate measurement of the 3D position and orientation of single molecules. *Proc. Natl. Acad. Sci.*, 109(47):19087–19092, 2012. (cited on p. 13)

- [80] A. S. Backer and W. E. Moerner. Extending single-molecule microscopy using optical Fourier processing. *J. Phys. Chem. B*, 118(28):8313–8329, 2014. (cited on pp. 13, 20, 42, 57, 62, 79, 108, 122, 132, 135, and 213)
- [81] M. P. Backlund, A. Arbabi, P. N. Petrov, E. Arbabi, S. Saurabh, A. Faraon, and W. E. Moerner. Removing orientation-induced localization biases in single-molecule microscopy using a broadband metasurface mask. *Nat. Photonics*, 10:459–462, 2016. (cited on pp. 13 and 79)
- [82] A. S. Backer and W. E. Moerner. Determining the rotational mobility of a single molecule from a single image: A numerical study. *Opt. Express*, 23(4):4255–4276, 2015. (cited on pp. 13, 22, 42, 88, 93, 117, 118, and 122)
- [83] M. D. Lew. *Engineering new capabilities into optical microscopes: Toward measuring the three-dimensional position and orientation of single molecules in living cells*. PhD thesis, Stanford University, 2015. (cited on p. 13)
- [84] O. Zhang and M. D. Lew. Fundamental limits on measuring the rotational constraint of single molecules using fluorescence microscopy. *Phys. Rev. Lett.*, 122:198301, 2019. (cited on pp. 13, 20, 42, 80, 126, and 214)
- [85] O. Zhang, J. Lu, T. Ding, and M. D. Lew. Imaging the three-dimensional orientation and rotational mobility of fluorescent emitters using the tri-spot point spread function. *Appl. Phys. Lett.*, 113(3):031103, 2018. (cited on pp. 13, 19, 20, 22, 42, 43, 80, 88, 122, and 214)
- [86] O. Zhang and M. D. Lew. Quantum limits for precisely estimating the orientation and wobble of dipole emitters. *arXiv*, 2020. (cited on p. 13)
- [87] M. Minsky. Microscopy apparatus, 1957. (cited on p. 14)
- [88] M. Minsky. Memoir on inventing the confocal scanning microscope. *Scanning*, 10(4):128–138, 1988. (cited on p. 14)
- [89] T. Wilson and C. J. R. Sheppard. *Theory and practice of scanning optical microscopy*. Academic Press, 1984. (cited on p. 14)
- [90] J. G. White, W. B. Amos, and M. Fordham. An evaluation of confocal versus conventional imaging of biological structures by fluorescence light microscopy. *J. Cell Biol.*, 105(1):41–48, 1987. (cited on p. 14)
- [91] C. J. R. Sheppard. Super-resolution in confocal imaging. *Optik - Int. J. for Light Electron Opt.*, 80:53, 1988. (cited on p. 14)
- [92] C. J. R. Sheppard, S. B. Mehta, and R. Heintzmann. Superresolution by image scanning microscopy using pixel reassignment. *Opt. Lett.*, 38(15):2889–2892, 2013. (cited on p. 14)

- [93] A. G. York, S. H. Parekh, D. D. Nogare, R. S. Fischer, K. Temprine, M. Mione, A. B. Chitnis, C. A. Combs, and H. Shroff. Resolution doubling in live, multicellular organisms via multifocal structured illumination microscopy. *Nat. Methods*, 9(7):749–754, 2012. (cited on pp. 14 and 224)
- [94] A. G. York, P. Chandris, D. D. Nogare, J. Head, P. Wawrzusin, R. S. Fischer, A. Chitnis, and H. Shroff. Instant super-resolution imaging in live cells and embryos via analog image processing. *Nat. Methods*, 10:1122–1126, 2013. (cited on pp. 14 and 224)
- [95] A. H. Voie, D. H. Burns, and F. A. Spelman. Orthogonal-plane fluorescence optical sectioning: Three-dimensional imaging of macroscopic biological specimens. *J. Microsc.*, 170(3):229–236, 1993. (cited on p. 14)
- [96] E. H. K. Stelzer and S. Lindek. Fundamental reduction of the observation volume in far-field light microscopy by detection orthogonal to the illumination axis: Confocal theta microscopy. *Opt. Commun.*, 111(5):536–547, 1994. (cited on p. 14)
- [97] J. Huisken, J. Swoger, F. Del Bene, J. Wittbrodt, and E. H. K. Stelzer. Optical sectioning deep inside live embryos by selective plane illumination microscopy. *Science*, 305(5686):1007–1009, 2004. (cited on p. 14)
- [98] P. J. Keller, A. D. Schmidt, J. Wittbrodt, and E. H. K. Stelzer. Reconstruction of zebrafish early embryonic development by scanned light sheet microscopy. *Science*, 322(5904):1065–1069, 2008. (cited on p. 14)
- [99] U. Krzic. *Multiple-view microscopy with light-sheet based fluorescence microscope*. PhD thesis, University of Heidelberg, 2009. (cited on p. 14)
- [100] U. Krzic, S. Gunther, T. E. Saunders, S. J. Streichan, and L. Hufnagel. Multiview light-sheet microscope for rapid *in toto* imaging. *Nat. Methods*, 9(7):730–733, 2012. (cited on p. 14)
- [101] Y. Wu, P. Wawrzusin, J. Senseney, R. S. Fischer, R. Christensen, A. Santella, A. G. York, P. W. Winter, C. M. Waterman, Z. Bao, D. A. Colón-Ramos, M. McAuliffe, and H. Shroff. Spatially isotropic four-dimensional imaging with dual-view plane illumination microscopy. *Nat. Biotechnol.*, 31(11):1032–1038, 2013. (cited on pp. 14, 172, and 224)
- [102] Y. Wu, P. Chandris, P. W. Winter, E. Y. Kim, V. Jaumouillé, A. Kumar, M. Guo, J. M. Leung, C. Smith, I. Rey-Suarez, H. Liu, C. M. Waterman, K. S. Ramamurthi, P. J. La Rivière, and H. Shroff. Simultaneous multiview capture and fusion improves spatial resolution in wide-field and light-sheet microscopy. *Optica*, 3(8):897–910, 2016. (cited on pp. 14 and 172)
- [103] Y. Wu, A. Kumar, C. Smith, E. Ardiel, P. Chandris, R. Christensen, M. Rey-Suarez, Ivan pand Guo, H. D. Vishwasrao, J. Chen, J. Tang, A. Upadhyaya, P. J. La Rivière, and H. Shroff. Reflective imaging improves spatiotemporal resolution and collection efficiency in light sheet microscopy. *Nat. Commun.*, 8(1):1452, 2017. (cited on p. 14)

- [104] B.-C. Chen, W. R. Legant, K. Wang, L. Shao, D. E. Milkie, M. W. Davidson, C. Jane-topoulos, X. S. Wu, J. A. Hammer, Z. Liu, B. P. English, Y. Mimori-Kiyosue, D. P. Romero, A. T. Ritter, J. Lippincott-Schwartz, L. Fritz-Laylin, R. D. Mullins, D. M. Mitchell, J. N. Bembeneck, A.-C. Reymann, R. Böhme, S. W. Grill, J. T. Wang, G. Seydoux, U. S. Tulu, D. P. Kiehart, and E. Betzig. Lattice light-sheet microscopy: Imaging molecules to embryos at high spatiotemporal resolution. *Science*, 346(6208):1257998, 2014. (cited on p. 14)
- [105] B.-J. Chang, M. Kittisopkul, K. M. Dean, P. Roudot, E. S. Welf, and R. Fiolka. Universal light-sheet generation with field synthesis. *Nat. Methods*, 16(3):235–238, 2019. (cited on p. 14)
- [106] P. N. Hedde, S. Ranjit, and E. Gratton. 3D fluorescence anisotropy imaging using selective plane illumination microscopy. *Opt. Express*, 23(17):22308, 2015. (cited on p. 15)
- [107] M. L. Markwardt, N. E. Snell, M. Guo, Y. Wu, R. Christensen, H. Liu, H. Shroff, and M. Rizzo. A genetically encoded biosensor strategy for quantifying non-muscle myosin II phosphorylation dynamics in living cells and organisms. *Cell Rep.*, 24(4):1060 – 1070.e4, 2018. (cited on p. 15)
- [108] A. Rose. *Vision: Human and electronic*. Optical Physics and Engineering. Springer US, 2012. (cited on p. 15)
- [109] J. C. Dainty and R. Shaw. *Image science: Principles, analysis and evaluation of photographic-type imaging processes*. Academic Press, 1974. (cited on p. 15)
- [110] H. H. Barrett and W. Swindell. *Radiological imaging: The theory of image formation, detection, and processing*. Elsevier Science, 1981. (cited on p. 15)
- [111] T. Chandler, H. Shroff, R. Oldenbourg, and P. J. La Rivière. Spatio-angular fluorescence microscopy I. Basic theory. *J. Opt. Soc. Am. A*, 36(8):1334–1345, 2019. (cited on p. 17)
- [112] T. Chandler, H. Shroff, R. Oldenbourg, and P. J. La Rivière. Spatio-angular fluorescence microscopy II. Paraxial $4f$ imaging. *J. Opt. Soc. Am. A*, 36(8):1346–1360, 2019. (cited on p. 17)
- [113] T. Chandler, H. Shroff, R. Oldenbourg, and P. J. La Rivière. Spatio-angular fluorescence microscopy III. Constrained angular diffusion, polarized excitation, and high-NA imaging. *arXiv*, 2020. (cited on p. 18)
- [114] M. McQuilken, M. S. Jentzsch, A. Verma, S. B. Mehta, R. Oldenbourg, and A. S. Gladfelter. Analysis of septin reorganization at cytokinesis using polarized fluorescence microscopy. *Front. Cell Dev. Biol.*, 5:42, 2017. (cited on pp. 19 and 22)

- [115] K. Zhanghao, X. Chen, W. Liu, M. Li, Y. Liu, Y. Wang, S. Luo, X. Wang, C. Shan, H. Xie, J. Gao, X. Chen, D. Jin, X. Li, Y. Zhang, Q. Dai, and P. Xi. Super-resolution imaging of fluorescent dipoles via polarized structured illumination microscopy. *Nat. Commun.*, 10(4694):1–10, 2019. (cited on pp. 19, 22, 44, 78, 80, 88, 121, and 224)
- [116] A. Agrawal, S. Quirin, G. Grover, and R. Piestun. Limits of 3D dipole localization and orientation estimation for single-molecule imaging: Towards Green’s tensor engineering. *Opt. Express*, 20(24):26667–26680, 2012. (cited on pp. 19, 20, 41, and 79)
- [117] M. R. Foreman and P. Török. Fundamental limits in single-molecule orientation measurements. *New J. Phys.*, 13(9):093013, 2011. (cited on pp. 19 and 126)
- [118] J. Chao, E. S. Ward, and R. J. Ober. Fisher information theory for parameter estimation in single molecule microscopy: Tutorial. *J. Opt. Soc. Am. A*, 33(7):B36–B57, 2016. (cited on p. 19)
- [119] F. Aguet, S. Geissbühler, I. Märki, T. Lasser, and M. Unser. Super-resolution orientation estimation and localization of fluorescent dipoles using 3-D steerable filters. *Opt. Express*, 17(8):6829–6848, 2009. (cited on pp. 20, 42, and 88)
- [120] K. I. Mortensen, L. S. Churchman, J. A. Spudich, and H. Flyvbjerg. Optimized localization analysis for single-molecule tracking and super-resolution microscopy. *Nat. Methods*, 7:377–381, 2010. (cited on p. 20)
- [121] M. Born and E. Wolf. *Principles of optics: electromagnetic theory of propagation, interference and diffraction of light*. Elsevier Science Limited, 1980. (cited on p. 21)
- [122] S. F. Gibson and F. Lanni. Diffraction by a circular aperture as a model for three-dimensional optical microscopy. *J. Opt. Soc. Am. A*, 6(9):1357–1367, 1989. (cited on pp. 21 and 79)
- [123] B. Richards and E. Wolf. Electromagnetic diffraction in optical systems, II. Structure of the image field in an aplanatic system. *Proc. R. Soc. Lond. A*, 253(1274):358–379, 1959. (cited on p. 21)
- [124] A. G. T. Ruiter, J. A. Veerman, M. F. Garcia-Parajo, and N. F. van Hulst. Single molecule rotational and translational diffusion observed by near-field scanning optical microscopy. *J. Phys. Chem. A*, 101(40):7318–7323, 1997. (cited on p. 22)
- [125] S. Bhattacharya, D. K. Sharma, S. Saurabh, S. De, A. Sain, A. Nandi, and A. Chowdhury. Plasticization of poly(vinylpyrrolidone) thin films under ambient humidity: Insight from single-molecule tracer diffusion dynamics. *J. Phys. Chem. B*, 117(25):7771–7782, 2013. (cited on p. 22)
- [126] M. Gu. *Advanced optical imaging theory*. Springer Series in Optical Sciences. Springer, 2000. (cited on pp. 27, 55, and 59)

- [127] E. J. Botcherby, R. Juškaitis, M. J. Booth, and T. Wilson. An optical technique for remote focusing in microscopy. *Opt. Commun.*, 281(4):880–887, 2008. (cited on p. 27)
- [128] M. Descoteaux, E. Angelino, S. Fitzgibbons, and R. Deriche. Apparent diffusion coefficients from high angular resolution diffusion imaging: Estimation and applications. *Magn. Reson. Med.*, 56(2):395–410, 2006. (cited on pp. 43 and 44)
- [129] J. R. Driscoll and D. M. Healy. Computing Fourier transforms and convolutions on the 2-sphere. *Adv. Appl. Math.*, 15(2):202–250, 1994. (cited on p. 43)
- [130] A. S. Backer, M. Y. Lee, and W. E. Moerner. Enhanced DNA imaging using super-resolution microscopy and simultaneous single-molecule orientation measurements. *Optica*, 3(6):659–666, 2016. (cited on p. 44)
- [131] P. J. Basser, J. Mattiello, and D. Le Bihan. MR diffusion tensor spectroscopy and imaging. *Biophys. J.*, 66(1):259–267, 1994. (cited on p. 44)
- [132] J.-D. Tournier, F. Calamante, D. G. Gadian, and A. Connelly. Direct estimation of the fiber orientation density function from diffusion-weighted MRI data using spherical deconvolution. *NeuroImage*, 23(3):1176–1185, 2004. (cited on p. 44)
- [133] N. Schaeffer. Efficient spherical harmonic transforms aimed at pseudospectral numerical simulations. *Geochem. Geophys. Geosystems*, 14(3):751–758, 2013. (cited on p. 46)
- [134] J. W. Goodman. *Introduction to Fourier optics*. McGraw-Hill, 1996. (cited on pp. 57, 84, and 218)
- [135] D. Axelrod. Fluorescence excitation and imaging of single molecules near dielectric-coated and bare surfaces: A theoretical study. *J. Microsc.*, 247 2:147–60, 2012. (cited on p. 57)
- [136] C. J. R. Sheppard, M. Gu, Y. Kawata, and S. Kawata. Three-dimensional transfer functions for high-aperture systems. *J. Opt. Soc. Am. A*, 11(2):593–598, 1994. (cited on p. 59)
- [137] M. R. Arnison and C. J. R. Sheppard. A 3D vectorial optical transfer function suitable for arbitrary pupil functions. *Opt. Commun.*, 211(1):53–63, 2002. (cited on p. 59)
- [138] M. R. Foreman and P. Török. Computational methods in vectorial imaging. *J. Mod. Opt.*, 58(5-6):339–364, 2011. (cited on p. 59)
- [139] R. N. Bracewell. *Fourier analysis and imaging*. Springer US, 2004. (cited on pp. 59 and 84)
- [140] P. N. Petrov, Y. Shechtman, and W. E. Moerner. Measurement-based estimation of global pupil functions in 3D localization microscopy. *Opt. Express*, 25(7):7945–7959, 2017. (cited on p. 60)

- [141] M. P. Backlund, Y. Shechtman, and R. L. Walsworth. Fundamental precision bounds for three-dimensional optical localization microscopy with Poisson statistics. *Phys. Rev. Lett.*, 121:023904, 2018. (cited on p. 60)
- [142] A. G. Curto, T. H. Taminiau, G. Volpe, M. P. Kreuzer, R. Quidant, and N. F. van Hulst. Multipolar radiation of quantum emitters with nanowire optical antennas. *Nat. Commun.*, 4(1750):1–7, 2013. (cited on p. 78)
- [143] C. Zhao and J. H. Burge. Orthonormal vector polynomials in a unit circle, part I: Basis set derived from gradients of Zernike polynomials. *Opt. Express*, 15(26):18014–18024, 2007. (cited on p. 79)
- [144] X. Xu, W. Huang, and M. Xu. Orthogonal polynomials describing polarization aberration for rotationally symmetric optical systems. *Opt. Express*, 23(21):27911–27919, 2015. (cited on p. 79)
- [145] R. A. Chipman. Polarization analysis of optical systems. *Opt. Eng.*, 28(2):90–99, 1989. (cited on p. 79)
- [146] D. Patra, I. Gregor, and J. Enderlein. Image analysis of defocused single-molecule images for three-dimensional molecule orientation studies. *The J. Phys. Chem. A*, 108(33):6836–6841, 2004. (cited on p. 79)
- [147] A. S. Backer, M. P. Backlund, M. D. Lew, and W. E. Moerner. Single-molecule orientation measurements with a quadrated pupil. *Opt. Lett.*, 38(9):1521–1523, 2013. (cited on pp. 79 and 213)
- [148] N. Karedla, S. C. Stein, D. Hähnel, I. Gregor, A. Chizhik, and J. Enderlein. Simultaneous measurement of the three-dimensional orientation of excitation and emission dipoles. *Phys. Rev. Lett.*, 115(17):173002, 2015. (cited on p. 79)
- [149] S. Khadir, P. C. Chaumet, G. Baffou, and A. Sentenac. Quantitative model of the image of a radiating dipole through a microscope. *J. Opt. Soc. Am. A*, 36(4):478–484, 2019. (cited on p. 80)
- [150] I. S. Gradshteyn and I. M. Ryzhik. *Table of integrals, series, and products*. Elsevier/Academic Press, Amsterdam, 2007. (cited on pp. 81 and 85)
- [151] J. C. Mertz. *Introduction to optical microscopy*. W. H. Freeman, 2009. (cited on p. 84)
- [152] R. Ramamoorthi. Modeling illumination variation with spherical harmonics. In *Face Processing: Advanced Modeling and Methods*, pages 385–424. Academic Press, 2005. (cited on p. 85)
- [153] D. M. Jameson and J. A. Ross. Fluorescence polarization/anisotropy in diagnostics and imaging. *Chem. Rev.*, 110(5):2685–2708, 2010. (cited on pp. 87 and 88)

- [154] R. B. Jones. Adiabatic change in the Smoluchowski equation: Orientational diffusion of polar particles. *J. Chem. Phys.*, 119(3):1517–1532, 2003. (cited on pp. 89 and 99)
- [155] K. Schulten and I. Kosztin. Lectures in theoretical biophysics. Technical report, University of Illinois at Urbana-Champaign, 2000. (cited on pp. 89, 93, 94, and 96)
- [156] H. Risken. *The Fokker-Planck equation*. Springer, Berlin, Heidelberg, 1996. (cited on p. 93)
- [157] W. T. Coffey, Y. P. Kalmykov, and J. T. Waldron. *The Langevin equation: With applications to stochastic problems in physics, chemistry and electrical engineering*. World Scientific series in contemporary chemical physics. World Scientific, 2012. (cited on p. 93)
- [158] A. Loman, I. Gregor, C. Stutz, M. Mund, and J. Enderlein. Measuring rotational diffusion of macromolecules by fluorescence correlation spectroscopy. *Photochem. Photobiol. Sci.*, 9:627–636, 2010. (cited on p. 93)
- [159] W.-K. Tung. *Group theory in physics*. World Scientific Publishing Company, 1985. (cited on pp. 99 and 157)
- [160] M. Hamermesh. *Group theory and its application to physical problems*. Courier Corporation, 1989. (cited on p. 99)
- [161] M. G. L. Gustafsson. Nonlinear structured-illumination microscopy: Wide-field fluorescence imaging with theoretically unlimited resolution. *Proc. Natl. Acad. Sci.*, 102(37):13081–13086, 2005. (cited on pp. 102 and 120)
- [162] M. G. L. Gustafsson. Surpassing the lateral resolution limit by a factor of two using structured illumination microscopy. *J. Microsc.*, 198(2):82–87, 2000. (cited on pp. 105 and 209)
- [163] H. H. H. Homeier and E. O. Steinborn. Some properties of the coupling coefficients of real spherical harmonics and their relation to Gaunt coefficients. *J. Mol. Struct. THEOCHEM*, 368:31–37, 1996. (cited on pp. 111 and 133)
- [164] S. Shirdhonkar and D. W. Jacobs. Non-negative lighting and specular object recognition. In *Tenth IEEE International Conference on Computer Vision (ICCV'05) Volume 1*, volume 2, pages 1323–1330 Vol. 2, 2005. (cited on p. 111)
- [165] K. V. Mardia and P. E. Jupp. *Directional statistics*. Wiley series in probability and statistics. Wiley, 1999. (cited on p. 112)
- [166] D. Li, L. Shao, B.-C. Chen, X. Zhang, M. Zhang, B. Moses, D. E. Milkie, J. R. Beach, J. A. Hammer, M. Pasham, T. Kirchhausen, M. A. Baird, M. W. Davidson, P. Xu, and E. Betzig. Extended-resolution structured illumination imaging of endocytic and cytoskeletal dynamics. *Science*, 349(6251):aab3500, 2015. (cited on p. 120)

- [167] N. Hafi, M. Grunwald, L. S. van den Heuvel, T. Aspelmeier, J.-H. Chen, M. Zagrebelsky, O. M. Schütte, C. Steinem, M. Korte, A. Munk, and P. J. Walla. Fluorescence nanoscopy by polarization modulation and polarization angle narrowing. *Nat. Methods*, 11(5):579–584, 2014. (cited on p. 121)
- [168] L. Frahm and J. Keller. Polarization modulation adds little additional information to super-resolution fluorescence microscopy. *Nat. Methods*, 13(1):7–8, 2015. (cited on p. 121)
- [169] W. Becker. *Advanced time-correlated single photon counting techniques*. Springer Science & Business Media, 2005. (cited on p. 121)
- [170] A. J. Bowman, B. B. Klopfer, T. Juffmann, and M. A. Kasevich. Electro-optic imaging enables efficient wide-field fluorescence lifetime microscopy. *Nat. Commun.*, 10(4561):1–8, 2019. (cited on p. 121)
- [171] I. Goodfellow, Y. Bengio, and A. Courville. *Deep learning*. MIT Press, 2016. (cited on p. 123)
- [172] A.-M. Legendre. *Nouvelles méthodes pour la détermination des orbites des comètes*. Firmin Didot, 1805. (cited on p. 126)
- [173] S. M. Stigler. Gauss and the invention of least squares. *Ann. Stat.*, 9(3):465–474, 1981. (cited on p. 126)
- [174] E. Schmidt. Zur theorie der linearen und nichtlinearen integralgleichungen. i. teil: entwicklung willkürlicher funktionen nach systemen vorgeschrifbener. *Math. Ann.*, 63:433–476, 1907. (cited on p. 126)
- [175] G. W. Stewart. On the early history of the singular value decomposition. *SIAM Rev.*, 35(4):551–566, 1993. (cited on p. 126)
- [176] A. N. Tikhonov. Solution of incorrectly formulated problems and the regularization method. *Doklady Akademii Nauk SSSR*, 151:501–504, 1963. (cited on p. 126)
- [177] H. H. Barrett, J. N. Aarsvold, and T. J. Roney. Null functions and eigenfunctions: tools for the analysis of imaging systems. *Prog. Clin. Biol. Res.*, 363:211–226, 1991. (cited on p. 126)
- [178] J. N. Aarsvold and H. H. Barrett. Symmetries of single-slice multiple-pinhole tomographs. In *IEEE Nuclear Science Symposium and Medical Imaging Conference*, pages 1673–1677. IEEE, 1996. (cited on p. 126)
- [179] A. Burvall, H. H. Barrett, C. Dainty, and K. J. Myers. Singular-value decomposition for through-focus imaging systems. *J. Opt. Soc. Am. A*, 23(10):2440–2448, 2006. (cited on p. 126)

- [180] A. Burvall, H. H. Barrett, K. J. Myers, and C. Dainty. Singular-value decomposition of a tomosynthesis system. *Opt. Express*, 18(20):20699–20711, 2010. (cited on p. 126)
- [181] E. Clarkson, R. Palit, and M. A. Kupinski. SVD for imaging systems with discrete rotational symmetry. *Opt. Express*, 18(24):25306–25320, 2010. (cited on pp. 126 and 170)
- [182] A. K. Jha, H. H. Barrett, E. C. Frey, E. Clarkson, L. Caucci, and M. A. Kupinski. Singular value decomposition for photon-processing nuclear imaging systems and applications for reconstruction and computing null functions. *Phys. Med. Biol.*, 60(18):7359–7385, 2015. (cited on p. 126)
- [183] Y. Ding, L. Caucci, and H. H. Barrett. Null functions in three-dimensional imaging of alpha and beta particles. *Sci. Rep.*, 7(1):15807, 2017. (cited on p. 126)
- [184] D. Modgil, P. J. La Rivière, and B. E. Treeby. Photoacoustic image reconstruction in an attenuating medium using singular-value decomposition. *J. Biomed. Opt.*, 17(6):061204, 2012. (cited on p. 126)
- [185] L. Pfister. *Parsimonious models for inverse problems*. PhD thesis, University of Illinois at Urbana-Champaign, 2019. (cited on p. 126)
- [186] T. Chandler, S. Mehta, H. Shroff, R. Oldenbourg, and P. J. La Rivière. Single-fluorophore orientation determination with multiview polarized illumination: Modeling and microscope design. *Opt. Express*, 25(25):31309–31325, 2017. (cited on p. 126)
- [187] A. T. Blanchard, J. Brockman, K. Salaita, and A. L. Mattheyses. Variable incidence angle linear dichroism (VALiD): A technique for unique 3D orientation measurement of fluorescent ensembles. *Opt. Express*, 2020. (cited on p. 126)
- [188] D. S. Sabatke, M. R. Descour, E. L. Dereniak, W. C. Sweatt, S. A. Kemme, and G. S. Phipps. Optimization of retardance for a complete Stokes polarimeter. *Opt. Lett.*, 25(11):802–804, 2000. (cited on pp. 126 and 149)
- [189] K. M. Twietmeyer and R. A. Chipman. Optimization of Mueller matrix polarimeters in the presence of error sources. *Opt. Express*, 16(15):11589–11603, 2008. (cited on p. 126)
- [190] M. R. Foreman, A. Favaro, and A. Aiello. Optimal frames for polarization state reconstruction. *Phys. Rev. Lett.*, 115(26):263901, 2015. (cited on pp. 126, 149, and 150)
- [191] M. D. Lew and W. E. Moerner. Azimuthal polarization filtering for accurate, precise, and robust single-molecule localization microscopy. *Nano Lett.*, 14(11):6407–6413, 2014. (cited on p. 135)
- [192] R. P. Stanley. *Enumerative Combinatorics*, volume 1 of *Cambridge Studies in Advanced Mathematics*. Cambridge University Press, 2nd edition, 2011. (cited on p. 146)

- [193] W. Fulton and J. Harris. *Representation theory*. Springer, New York, NY, 2004. (cited on p. 148)
- [194] P. Delsarte, J. M. Goethals, and J. J. Seidel. Spherical codes and designs. *Geom. Dedicata*, 6(3):363–388, 1977. (cited on p. 150)
- [195] R. H. Hardin and N. J. A. Sloane. McLaren’s improved snub cube and other new spherical designs in three dimensions. *Discret. Comput. Geom.*, 15(4):429–441, 1996. (cited on p. 150)
- [196] D. Hughes and S. Waldron. Spherical (t, t) -designs with a small number of vectors. *arXiv*, 2018. (cited on p. 151)
- [197] G. H. Golub and C. F. Van Loan. *Matrix computations*. Johns Hopkins Studies in the Mathematical Sciences. Johns Hopkins University Press, 2013. (cited on p. 161)
- [198] Á. González. Measurement of areas on a sphere using Fibonacci and latitude-longitude lattices. *Math. Geosci.*, 42(1):49–64, 2010. (cited on p. 165)
- [199] R. Marques, C. Bouville, M. Ribardière, L. P. Santos, and K. Bouatouch. Spherical Fibonacci point sets for illumination integrals. *Comput. Graph. Forum*, 32(8):134–143, 2013. (cited on p. 165)
- [200] S. Pajevic and C. Pierpaoli. Color schemes to represent the orientation of anisotropic tissues from diffusion tensor data: Application to white matter fiber tract mapping in the human brain. *Magn. Reson. Med.*, 42(3):526–540, 1999. (cited on p. 166)
- [201] Ç. Demiralp, J. F. Hughes, and D. H. Laidlaw. Coloring 3D line fields using Boy’s real projective plane immersion. *IEEE Trans. Vis. Comput. Graph.*, 15(6):1457–1464, 2009. (cited on p. 166)
- [202] D. S. Tuch. Q-ball imaging. *Magn. Reson. Med.*, 52(6):1358–1372, 2004. (cited on p. 166)
- [203] J. Cheng and P. J. Basser. Director field analysis (DFA): Exploring local white matter geometric structure in diffusion MRI. *Med. Image Anal.*, 43:112–128, 2018. (cited on p. 166)
- [204] K. Åhlander. Einstein summation for multidimensional arrays. *Comput. Math. with Appl.*, 44(8):1007–1017, 2002. (cited on p. 167)
- [205] P. Virtanen, R. Gommers, T. E. Oliphant, M. Haberland, T. Reddy, D. Cournapeau, E. Burovski, P. Peterson, W. Weckesser, J. Bright, S. J. van der Walt, M. Brett, J. Wilson, K. Jarrod Millman, N. Mayorov, A. R. J. Nelson, E. Jones, R. Kern, E. Larson, C. Carey, İ. Polat, Y. Feng, E. W. Moore, J. VanderPlas, D. Laxalde, J. Perktold, R. Cimrman, I. Henriksen, E. A. Quintero, C. R. Harris, A. M. Archibald, A. H. Ribeiro, F. Pedregosa, and P. van Mulbregt. SciPy 1.0: Fundamental algorithms for scientific computing in Python. *Nat. Methods*, 2020. (cited on p. 167)

- [206] V. S. Sunder. *Operators on Hilbert space*. Springer Singapore, 2016. (cited on p. 169)
- [207] K. Åhlander and H. Munthe-Kaas. Applications of the generalized Fourier transform in numerical linear algebra. *BIT Numer. Math.*, 45(4):819–850, 2005. (cited on p. 170)
- [208] D. K. Maslen and D. N. Rockmore. Generalized FFTs—a survey of some recent results. Technical report, Dartmouth College, USA, 1996. (cited on p. 170)
- [209] J. Kautz, P.-P. Sloan, and J. Snyder. Fast, arbitrary BRDF shading for low-frequency lighting using spherical harmonics. In *Proceedings of the 13th Eurographics Workshop on Rendering*, EGRW ’02, pages 291–296, Aire-la-Ville, Switzerland, Switzerland, 2002. Eurographics Association. (cited on p. 180)
- [210] D. Pinchon and P. E. Hoggan. Rotation matrices for real spherical harmonics: General rotations of atomic orbitals in space-fixed axes. *J. Phys. A: Math. Theor.*, 40(7):1597–1610, 2007. (cited on p. 180)
- [211] T. Bhatia, P. Husen, J. Brewer, L. A. Bagatolli, P. L. Hansen, J. H. Ipsen, and O. G. Mouritsen. Preparing giant unilamellar vesicles (GUVs) of complex lipid mixtures on demand: Mixing small unilamellar vesicles of compositionally heterogeneous mixtures. *Biochimica et Biophys. Acta*, 1848(12):3175–3180, 2015. (cited on p. 192)
- [212] E. M. Schmid, D. L. Richmond, and D. A. Fletcher. Reconstitution of proteins on electroformed giant unilamellar vesicles. In J. Ross and W. F. Marshall, editors, *Building a Cell from its Component Parts*, volume 128 of *Methods in Cell Biology*, pages 319–338. Academic Press, 2015. (cited on p. 192)
- [213] J. E. Reeve, A. D. Corbett, I. Boczarow, T. Wilson, H. Bayley, and H. L. Anderson. Probing the orientational distribution of dyes in membranes through multiphoton microscopy. *Biophys. J.*, 103(5):907–917, 2012. (cited on p. 192)
- [214] M. G. L. Gustafsson, L. Shao, P. M. Carlton, C. J. R. Wang, I. N. Golubovskaya, W. Z. Cande, D. A. Agard, and J. W. Sedat. Three-dimensional resolution doubling in wide-field fluorescence microscopy by structured illumination. *Biophys. J.*, 94(12):4957–4970, 2008. (cited on p. 209)
- [215] F. Ströhle and C. F. Kaminski. A concept for single-shot volumetric fluorescence imaging via orthogonally polarized excitation lattices. *Sci. Rep.*, 9(1):6425, 2019. (cited on p. 210)
- [216] R. C. Jones. A new calculus for the treatment of optical systems I. Description and discussion of the calculus. *J. Opt. Soc. Am. A*, 31(7):488–493, 1941. (cited on p. 210)
- [217] W. A. Shurcliff. *Polarized light; production and use*. Harvard University Press, 1962. (cited on p. 210)
- [218] R. M. A. Azzam. Three-dimensional polarization states of monochromatic light fields. *J. Opt. Soc. Am. A*, 28(11):2279–2283, 2011. (cited on p. 210)

- [219] N. Ortega-Quijano and J. L. Arce-Diego. Generalized Jones matrices for anisotropic media. *Opt. Express*, 21(6):6895–6900, 2013. (cited on pp. 210 and 229)
- [220] A. S. Backer. *Extending single-molecule microscopy using optical processing techniques*. PhD thesis, Stanford University, 2016. (cited on p. 213)
- [221] K. Spehar, T. Ding, Y. Sun, N. Kedia, J. Lu, G. R. Nahass, M. D. Lew, and J. Bieschke. Super-resolution imaging of amyloid structures over extended times by using transient binding of single thioflavin T molecules. *ChemBioChem*, 19(18):1944–1948, 2018. (cited on p. 214)
- [222] M. Broxton, L. Grosenick, S. Yang, N. Cohen, A. Andelman, K. Deisseroth, and M. Levoy. Wave optics theory and 3-D deconvolution for the light field microscope. *Opt. Express*, 21(21):25418–25439, 2013. (cited on pp. 215, 216, and 218)
- [223] M. Broxton. *Volume reconstruction and resolution limits for three dimensional snapshot microscopy*. PhD thesis, Stanford University, 2019. (cited on p. 215)
- [224] P. Quicke. *Improved methods for functional neuronal imaging with genetically encoded voltage indicators*. PhD thesis, Imperical College London, 2019. (cited on p. 215)
- [225] D. Voelz. *Computational Fourier optics: a MATLAB tutorial*. SPIE Press monograph. SPIE Press, 2011. (cited on p. 218)
- [226] K. Zhanghao, L. Chen, X.-S. Yang, M.-Y. Wang, Z.-L. Jing, H.-B. Han, M. Q. Zhang, D. Jin, J.-T. Gao, and P. Xi. Super-resolution dipole orientation mapping via polarization demodulation. *Light. Sci. Appl.*, 5(10):e16166–e16166, 2016. (cited on p. 224)
- [227] C. J. R. Sheppard and M. Gu. The three-dimensional (3-D) transmission cross-coefficient for transmission imaging. *Optik*, 100:155–158, 1995. (cited on p. 229)

Index

- 4f* imaging, 52, 89
- Abbe's sine condition, 11
Abbe, Ernst, 11, 26
Abelian group, 170
absolute value coloring, 166
accidental degeneracy, 159
actin, 12, 13, 172, 196, 202
adjoint operator, 92, 96
Airy pattern, 4, 62, 65
Albrecht, Andreas, 10
alternating group, 148
angular bandlimit, 181
angular diffusion, 12, 87, 88, 92, 93, 104, 117, 128
angular rank, 156, 163
anisotropy, 9, 10, 15
multiple meanings of, 10
anisotropy imaging, 12, 15
aplanatic condition, 11, 19, 26, 57, 61
asymmetric rotor, 93
Axelrod, Daniel, 12, 88, 121
Aztecs, 6
- Backer, Adam, 13, 20, 44, 62, 63, 79, 88, 117, 122, 135, 213
Backlund, Mikael, 13, 19, 60, 79, 213
Barrett, Harrison, xi, 15, 16, 27, 37, 56, 81, 95, 98, 99, 121, 123, 126, 140, 145, 170, 171
Bayesian prior, 126
Bessel function, 4, 59, 81
bilinear transfer functions, 229
biorthogonal set, 96
Boltzmann distribution, 95, 98, 130, 207
Born, Max, 21, 22
Boyle, Robert, 7
Bracewell, Ronald, 59
Brewster, David, 11
- calibration, 160
Chalfie, Martin, 12
chat function, 60, 81, 82
- circular harmonics, 44
coherence, 207
coherent transfer function, 39
compact operator, 6, 126, 145, 169
condition number, 188
Condon–Shortley phase, 47
confocal microscopy, 14
convolution-multiplication theorem, 28, 38, 206
Coons, Albert, 11
- Dainty, John Christopher, 15
Danube river, 8
de L'Écluse, Charles, 6
developmental biology, 14
diffusion MRI, 44, 229
dipole vs. monopole, 3
diSPIM, 173, 176, 185, 196
DNA, 13
dose, 14
double cone, 72, 73, 84, 119
- `einsum`, 167, 168
electromagnetic radiation, 5
emission tomography, 1
Enderlein, Jörg, 13, 20, 62
Eysenhardtia polystachya, 7
- Föster resonance energy transfer, 12
Fibonacci lattice, 165
Fisher information, 44
fluorescence
applications, 7, 8, 11–14, 19, 172, 192, 202, 227–229
early history, 7, 8
fluorescence lifetime, 9, 12, 87, 121
force sensing, 228
Fourier–Legendre transform, 203
free orbits, 170
Fresnel propagation, 218
fundamental anistropy, 10
fundamental polarization, 9

- Göppelsröder, Friedrich, 8
 Galilei, Galileo, 11
 Garrison, Fielding Hudson, 7
 Gaunt coefficients, 111, 133, 206
 Gauss, Carl Friedrich, 126
 generalized fractional anisotropy, 164, 166
 giant unilamellar vesicles, 172, 192, 197–201
 Gibson, Sarah Frisken, 21, 22, 79
 glyph coloring, 166
 green fluorescent protein, 12, 93
 Grimaldi, Francesco Maria, 7
 group theory, 16, 98, 146, 148, 159, 169, 170, 180, 184, 216, 229
- Ha, Taekjip, 13, 88
 Haitinger, Max, 11
 Heimstädt, Oskar, 11
 Hermitian operator, 95
 Herschel, John Frederick William, 8
 Hilbert space, 23, 90, 91, 94, 96, 100, 108, 124, 128, 145
 Hilbert–Schmidt test, 145
 Hofstadter, Douglas, iv
 homogeneous polynomial, 6, 41, 146, 151
 Hooke, Robert, 11
- icosahedral group, 148
 icosahedron, 141, 147–149, 153, 169
 immunofluorescence, 11
 incoherence, 207
 infinity-corrected objective, 59
 Inoué, Shinya, 11, 12
 integrin, 12
 inverse problem, 127, 129, 159, 171, 189
 practical, 167, 168
 irreducible representation, 99, 146, 148
- Jabłoński, Aleksander, 9
 Jefferson, Thomas, 52
 jinc function, 59, 81, 82
 Jones vector, 210
 Joubert, Joseph, 206
- Keller, Philipp J., 14
- Kepler, Johannes, 141
 Knuth, Donald E., 123
- Lakowicz, Joseph R., 10, 93
 Lanni, Frederick, 21, 22, 79
 Legendre polynomial, 47, 86, 143, 203
 Legendre, Adrien-Marie, 126
 Lew, Matthew, 13, 19, 79, 88, 117, 122, 135, 213, 214
Lignum nephriticum, 7
 misattribution of, 7
 light-field microscopy, 215
 inverse problem, 223
 challenges, 225
 modeling, 216, 218
 reconstruction, 223
 singular value decomposition, 222
 symmetries, 216
 light-sheet microscopy, 14, 172
 field synthesis, 14
 lattice, 14
 modeling, 172
 multiview, 14
 optimization, 184
 reconstruction, 189
 singular value decomposition, 182
 light-sheet tilting, 189
 lipid rafts, 12
- magnified coordinates, 54, 58
 maximum likelihood, 125, 171
 measurement space, 16, 121, 124, 126
 meta-surface masks, 13
 Mexico, 7
 Minsky, Marvin, 14, 172
 mitosis, 11
 Moerner, William Esco, 13, 19, 44, 62, 63, 79, 88, 117, 122, 135, 213
 molecular motors, 13
 Monardes, Nicolás Bautista, 6
 monopole approximation, 5, 20, 22, 26, 53, 78
 monopole vs. dipole, 3
 multiplet, 99, 146, 159
 multiview microscopy, 172, 215
 Myers, Kyle, xi, 15, 16, 27, 37, 56, 81, 95, 98,

- 99, 121, 123, 126, 140, 145, 170, 171
 narra, 7
 Newton, Isaac, 7
 noise, 15, 122
 non-Abelian group, 170
 Novotny, Lukas, 13, 62, 65, 79
 nuclear pore complex, 12
 null space, 16, 124, 126, 152
`numpy`, 167, 168
 numerical aperture, 4
 Nyquist sampling, 67, 77, 120, 150, 214
- $\mathbb{O}(2)$, 159, 170
 octahedron, 147
 optical sectioning, 14, 172
 optimal sampling, 144, 184, 188, 190, 214
 orientation distribution function, 164, 165
- paraxial approximation, 52, 55, 59, 61, 63, 176
 Perrin equation, 9, 10
 Perrin plot, 9
 Perrin, Francis, 8–10, 88, 228
 PET, 1
 pH sensor, 7
 Phillipines, 7
 Plancherel theorem, 37, 38
 Plato, 19
 Ploem, Johan Sebastiaan, 11
 polarization
 fundamental, 9
 multiple meanings of, 9
 optical, 5, 20
 spectroscopic, 8
 splitter, 210
 protein conformation, 13
Pterocarpus indicus, 7
- quadrupole emitters, 78
 quantum mechanics, 2
 quinine, 8, 87
- reconstruction, 9, 46, 125–127, 159, 169–171,
 189
 practical, 167, 168, 186, 189
 rect function, 59, 81, 82
 resolution
 angular, 77, 78, 172, 225
 spatial, 3, 5, 14, 52, 172
 Richardson–Lucy algorithm, 171
 Rieger, Bernd, 13
 Rose, Albert, 15
- Safford, William Edwin, 7
 scalar approximation, 2, 5, 20–22, 57
 Schatten norm, 169, 185, 188
 Schmidt, W. J., 11
 Schulten, Klaus, 94
 second moments, 41, 42, 44
 sectoral harmonics, 135
 seismic tomography, 1
 septin, 12, 19
 Shakespeare, William, 87
 Shulten, Klaus, 89
 single molecule localization microscopy, 13,
 15, 20
 angular bias, 13
 singular value decomposition, 16, 123, 126,
 131, 139, 141, 146, 159, 170
 computation, 161
 detection operator, 131
 diSPIM, 182
 illumination operator, 144
 light field, 222
 single-view, 153
 Smoluchowski equation, 93, 94, 96, 98, 117,
 128
 Snell’s law, 4
 $\mathbb{SO}(2)$, 85, 97, 98, 170
 $\mathbb{SO}(3)$, 92, 97, 98, 146, 148, 159
 Spain, 7
 SPECT, 1, 15
 spherical t -design, 150
 spherical Fourier transform, 46, 75, 84, 91, 179
 fast, 43
 spherical harmonics, 41, 42, 48, 71, 74, 77, 84,
 98, 120, 146, 166
 addition theorem, 143, 204
 complex-valued, 76
 definition, 46

- interpretation, 75
- real-valued, 45
- visualization, 45
- spherical rotor, 9, 93, 130
- spherical sampling, 165
- split detection, 210
- stable orbits, 170
- Stallinga, Sjoerd, 13, 51, 110, 117, 122
- STED, 121
- Stokes shift, 8
- Stokes, George Gabriel, 8, 87
- structured illumination, 6, 78, 102, 207, 209, 224
 - angular, 119
 - light sheet, 14, 172
 - multifocal, 14
 - nonlinear, 120
- $SU(3)$, 229
- symmetry, 16, 17, 169, 170
 - discrete, 216
 - mirror, 140, 159
 - rotational, 10, 15, 77, 85, 97, 98, 119, 131, 136, 140, 159, 169, 184
 - spatial, 27, 57, 216
- Talbot, Henry Fox, 11
- tesseral harmonics, 135, 141
- three-dimensional imaging, 133, 172
- Tikhonov regularization, 125, 126, 163, 170, 223
- topology, 6
- total-internal reflection microscopy, 12
- transitive action, 170
- transmission microscopy, 11, 229
- tube lens, 55, 59, 132
- two-photon excitation, 12, 78, 121
- van Leeuwenhoek, Antonie, 11
- vector space, 6, 146
- visualization, 164, 166, 168, 197, 200, 201
- voltage sensing, 229
- Webb, Watt, 12
- Weber, Gregorio, 10, 88
- Weigert, Fritz, 8, 88
- Weiss, Shimon, 13
- Wigner D-matrices, 99, 179, 191, 206
 - real-valued, 180
- Wolf, Emil, 21, 22
- Xi, Peng, 19, 44, 80, 121
- Zernike polynomials, 79
- zonal harmonics, 135, 203